



UNIVERSITAT<sup>DE</sup>  
BARCELONA

# Molecular-based Magnetoresistance Devices at Room Temperature

Alejandro Martín Rodríguez



Aquesta tesi doctoral està subjecta a la llicència **Reconeixement 4.0. Espanya de Creative Commons.**

Esta tesis doctoral está sujeta a la licencia **Reconocimiento 4.0. España de Creative Commons.**

This doctoral thesis is licensed under the **Creative Commons Attribution 4.0. Spain License.**

Doctoral thesis

**Molecular-based Magnetoresistance  
Devices at Room Temperature**

Alejandro Martín Rodríguez



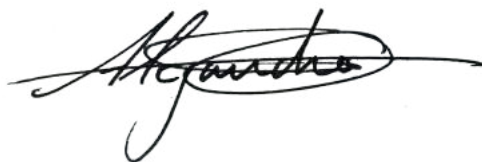
UNIVERSITAT DE  
BARCELONA



# Molecular-based Magnetoresistance Devices at Room Temperature

Programa de Doctorat en Nanociències

Autor: Alejandro Martín Rodríguez



Directors: Dr. Eliseo Ruiz Sabín

*Departament de Química Inorgànica i Orgànica, Facultat de Química*

Dr. Ismael Díez Pérez

*Departament de Ciència dels Materials i Química Física, Facultat de Química*

Tutor: Dr. Pere Alemany i Cahner

*Departament de Ciència dels Materials i Química Física, Facultat de Química*



Institut de Química Teòrica  
i Computacional  
UNIVERSITAT DE BARCELONA



UNIVERSITAT DE  
BARCELONA



*Ad astra per aspera*



## RESUM

En aquesta tesi doctoral es presenta una sèrie d'estudis computacionals i experimentals sobre dispositius moleculars magnetoresistents a temperatura ambient. Aquesta mena de dispositius s'engloben dins de l'electrònica molecular, que té com a objectiu l'estudi de sistemes moleculars per l'elaboració de components electrònics. Particularment, els sistemes moleculars amb electrons desaparellats són candidats potencials a mimetitzar i miniaturitzar les actuals vàlvules d'espí, àmpliament emprades en memòries magnètiques, a més de poder afegir noves funcionalitats a través de la modificació química d'aquests dispositius. Trobar candidats funcionals a temperatura ambient és crucial per a la posterior aplicació en dispositius electrònics.

En el primer capítol s'introdueix la fenomenologia típica de l'electrònica molecular i les tècniques experimentals més emprades en el seu estudi. S'explica en profunditat el formalisme de Landauer en conjunció amb el formalisme de Green, que permet la descripció de l'electró com a una ona viatjant d'un elèctrode a un altre per mitjà d'una diferència de voltatge. Es discuteixen diferents codis d'estructura electrònica i de transport quàntic que s'utilitzen per realitzar càlculs teòrics.



En el segon capítol, es proposen, a través de càlculs computacionals, diferents interaccions supramoleculares de la  $\text{Co}^{\text{II}}$ -5,15-difenilporfirina (CoDPP) i  $\text{Co}^{\text{II}}$ -porfirina (CoP) per explicar les altes conductàncies observades en experiments *STM-Break Junction* quan els elèctrodes d'or es funcionalitzen amb piridina-4-yl-metantiol (PyrMT) i 4-mercaptopiridina (PyrT). Posteriorment, la discussió s'amplia a les metal·lodifenilporfirines de  $\text{Co}^{\text{II}}$ ,  $\text{Ni}^{\text{II}}$ ,  $\text{Cu}^{\text{II}}$  i  $\text{Zn}^{\text{II}}$  per explorar la magnetoresistència d'aquests sistemes en el capítol tercer. Els càlculs teòrics permeten comprendre qualitativament la magnetoresistència observada en les metal·loporfirines de  $\text{Co}^{\text{II}}$  i  $\text{Cu}^{\text{II}}$ .

El quart capítol abandona els dispositius unimoleculares i aborda, en dues col·laboracions, l'estudi computacional de juntes moleculars monocapa. La primera col·laboració es va dur a terme amb el grup del Dr. Monakhov (IOM, Leipzig), en la qual s'estudia la junta monocapa  $[\text{CuLn}(\text{L SMe})_2(\text{OOCMe})_2(\text{NO}_3)]$  ( $\text{Ln} = \text{Gd}, \text{Tb}, \text{Dy}$  i  $\text{Y}$ ,  $x = 0.75-1$ ) mitjançant un elèctrode eutèctic de gal·li i indi (EGaIn). La independència experimental de la corrent respecte del lantànid queda corroborada en l'estudi computacional. Una segona col·laboració amb el Dr. Nijhuis (NUS, Singapur) i el Dr. Harding (Walailak University) estudia el primer sistema de  $\text{Fe}^{\text{III}}$  amb propietats de transició d'espí a temperatura ambient:  $[\text{Fe}^{\text{III}}(\text{qsal-I})_2]\text{NTf}_2$  (qsal-I = 4-iodo-2-[(8-quinolilimino)metilfenolat]). En aquest estudi s'inclou un model explícit de l'elèctrode EGaIn que explica la conductància observada segons l'estat d'espín del  $\text{Fe}^{\text{III}}$ .

El cinquè capítol afronta, tant experimental com teòricament, la formació de dispositius espintrònics basats en monocapes de tipus clatrat de Hofmann  $\{\text{Co}^{\text{II}}(\text{PyrT})_2\text{Pt}(\text{CN})_4\}$  (PyrT = 4-mercaptopiridina). En la secció experimental, s'explica la síntesi i caracterització de la monocapa mitjançant XPS, elipsometria i imatges AFM i C-AFM. Resultats preliminars de la conductància a nivell molecular s'obtenen mitjançant

experiments de *blinking* STM. L'estudi teòric permet entendre les senyals de conductància observades i, a més, explicar de manera qualitativa la magnetoresistència observada.

En l'últim capítol es retorna a les nanojuntes unimoleculares per estudiar les propietats termoelèctriques de complexos magnètics. En aquest capítol s'exploren teòricament metal·locens de  $V^{II}$ ,  $Fe^{II}$ ,  $Co^{II}$  i  $Ni^{II}$ , compostos tipus sandvitx de  $Gd^{III}$  i  $Eu^{II}$  i complexos de  $Co^{II}$  i  $Fe^{II}$  de la mena  $[M^{II}(SCN)_{2+x}(py)_{4-x}]$  ( $x = 0-2$ ,  $py =$  piridina) per trobar característiques comunes a potencials candidats per futurs experiments.



## SUMMARY

In this doctoral thesis a series of computational and experimental studies of molecular magnetoresistance devices at room temperature is presented. This sort of devices is included in the molecular electronics framework with the objective of studying molecular systems to build up molecular devices. Particularly, molecular systems with unpaired electrons are potential candidates to mimic and miniaturizing nowadays spin valves, widely employed in magnetic memories, besides adding new functionalities through chemical modification. Finding out functional candidates at room temperature is crucial to the posterior application on electronic devices.

The first chapter introduces common molecular electronics phenomenology and the most used experimental techniques. Landauer's formalism is explained in detail along with Green's function formalism, which permits to describe the electron as a traveling wave from one electrode to the other via an applied bias. Different electronic structure and quantum transport codes employed to perform theoretical calculations are discussed.

In the second chapter, a supramolecular landscape of Co<sup>II</sup>-5,15-diphenylporphyrin (CoDPP) and Co<sup>II</sup>-Porphyrin (CoP) is proposed to explain the high conductance signatures observed in *STM-Break Junction* experiments when both gold electrodes are functionalised with pyridine-4-yl-metanthiol (PyrMT) and 4-mercaptopyridine (PyrT). Afterwards, the discussion is expanded to Co<sup>II</sup>, Ni<sup>II</sup>, Cu<sup>II</sup> and Zn<sup>II</sup> metallodiphenylporphyrins to explore the magnetoresistance of these systems in the third chapter. Theoretical calculations allow understanding qualitatively the observed magnetoresistance on Co<sup>II</sup> and Cu<sup>II</sup> metalloporphyrins.

The fourth chapter leaves unimolecular devices and tackles, in two collaborations, the computational study of molecular monolayer junctions. The first contribution was in collaboration with Dr. Monakhov's group (IOM, Leipzig), in which the monolayer junction CuLn(L·SMe)<sub>2</sub>(OOCMe)<sub>2</sub>(NO<sub>3</sub>) (Ln = Gd, Tb, Dy i Y, x = 0.75-1) is studied employing an eutectic gallium and indium electrode (EGaIn). The experimental current independence of the lanthanide is corroborated in the computational study. A second collaboration with Dr. Nijhuis (NUS, Singapore) and Dr. Harding (Walailak University) studies the first Fe<sup>III</sup> spin crossover system at room temperature: [Fe<sup>III</sup>(qsal-I)<sub>2</sub>]NTf<sub>2</sub> (qsal-I = 4-iodo-2-[(8-quinolylimino)methyl]phenolate). In this study an explicit model of EGaIn electrode is included to explain the observed conductance according to the Fe<sup>III</sup> spin state.

The fifth chapter faces, both computational and experimentally, the building of spintronic devices based on Hofmann-type clathrate monolayers {Co<sup>II</sup>(PyrT)<sub>2</sub>Pt(CN)<sub>4</sub>} (PyrT = 4-mercaptopyridine). In the experimental section, the synthesis and characterisation of the monolayer using XPS, ellipsometry, AFM and C-AFM images is explained. Preliminary results about conductance at the molecular level were

obtained in *blinking* STM experiments. The theoretical study permits the understanding of the observed conductance signatures and gives a qualitative explanation to the observed magnetoresistance.

The last chapter goes back to unimolecular nanojunctions to study the thermoelectric properties of magnetic complexes. In this chapter, V<sup>II</sup>, Fe<sup>II</sup>, Co<sup>II</sup> and Ni<sup>II</sup> metallocenes, Gd<sup>III</sup> and Eu<sup>II</sup> sandwich compounds and Co<sup>II</sup> and Fe<sup>II</sup> complexes of the form  $[M^{II}(SCN)_{2+x}(py)_{4-x}]$  ( $x = 0-2$ , py = pyridine) are theoretically explored to find out common characteristics for potential candidates to future experiments.



# TABLE OF CONTENTS

<b>1</b>	<b>Introduction</b>	<b>21</b>
1.1	Physical phenomena in molecular devices	23
1.1.1	Energy level diagram	23
1.1.2	Transport regimes	25
1.1.3	Molecular wires	29
1.1.4	Molecular rectification	30
1.1.5	Molecular switching	32
1.1.6	Molecular spintronics	35
1.1.7	Molecular thermoelectrics	40
1.1.8	Quantum interference	43
1.2	Experimental techniques	44
1.2.1	STM Break Junction (STM-BJ)	46
1.2.2	Mechanically Controlled Break Junction (MCBJ)	49
1.2.3	Electromigration Break Junction (EMBJ)	50
1.2.4	Data collection and analysis	51
1.2.5	Eutectic Gallium Indium electrode (EGaIn)	56
1.2.6	Conducting Atomic Force Microscopy (C-AFM)	58
1.3	Landauer Formalism	59



1.3.1	Previous considerations	60
1.3.2	Definition of the isolated electrodes	61
1.3.3	Scattering in the nanojunction	62
1.3.4	Total current	63
1.3.5	Green's function operator as a propagator	65
1.3.6	Partition of the system	67
1.3.7	Landauer Formula	69
1.4	Green's function formalism	71
1.4.1	Equilibrium Green's function	72
1.4.2	Non-equilibrium Green's function	73
1.5	Computational flow charts	78
1.6	References	81
<b>2</b>	<b>Supramolecular landscape of CoDPP</b>	<b>99</b>
2.1	Motivation	99
2.2	Previous work	100
2.3	Results	105
2.3.1	Computational details	105
2.3.2	Characterisation of functionalised electrodes	106
2.3.3	Metal related conductance signatures	108
2.3.4	Through-backbone conductance signatures	113
2.3.5	Supramolecular landscape	118
2.4	Conclusions	121
2.5	References	123
<b>3</b>	<b>Study of magnetoresistance on metalloporphyrin devices</b>	<b>127</b>
3.1	Motivation	127
3.2	Previous work	128

3.3	Results	133
3.3.1	Computational details	134
3.3.2	Theoretical study of the magnetoresistance	134
3.4	Conclusions	142
3.5	References	144
<b>4</b>	<b>Study of large area EGaIn magnetic junctions</b>	<b>151</b>
4.1	Binuclear Cu <sup>II</sup> -Ln <sup>III</sup> complexes	152
4.1.1	Motivation	152
4.1.2	Previous work	153
4.1.3	Computational details	156
4.1.4	Results	157
4.1.5	Conclusions	160
4.1.6	References	162
4.2	Iron (III) spin crossover conductance switching	165
4.2.1	Motivation	165
4.2.2	Previous work	166
4.2.3	Computational details	171
4.2.4	Results	172
4.2.5	Conclusions	178
4.2.6	References	180
<b>5</b>	<b>Spintronic devices based on Hofmann-type clathrate monolayer</b>	<b>187</b>
5.1	Introduction	187
5.2	Results	189
5.2.1	Synthesis and characterisation	189
5.2.2	C-AFM measurements	193
5.2.3	Blinking STM experiments	194

5.2.4	Computational details	198
5.2.5	Theoretical study of $\{\text{Co}^{\text{II}}(\text{PyrI})_2\text{Pt}(\text{CN})_4\}$ monolayer	199
5.3	Conclusions	202
5.4	References	205
<b>6</b>	<b>Systematic study of thermoelectric properties on magnetic complexes</b>	<b>209</b>
6.1	Introduction	209
6.2	Results	212
6.2.1	Computational details	212
6.2.2	Metallocenes ( $\text{V}^{\text{II}}$ , $\text{Fe}^{\text{II}}$ , $\text{Co}^{\text{II}}$ and $\text{Ni}^{\text{II}}$ )	213
6.2.3	Sandwich compounds of $\text{Gd}^{\text{III}}$ and $\text{Eu}^{\text{II}}$	216
6.2.4	$[\text{Co}^{\text{II}}(\text{SCN})_{2+x}(\text{py})_{4-x}]$ and $[\text{Fe}^{\text{II}}(\text{SCN})_{2+x}(\text{py})_{4-x}]$ families	220
6.3	Conclusions	223
6.4	References	226
	<b>Final Conclusions</b>	<b>229</b>





# 1 INTRODUCTION

It is hard to imagine nowadays life without all the electronic devices that surround us. From the first computers (ENIAC, 1947) to our powerful modern laptops there is a paramount improvement in computer power, efficiency and, of course, size. The key to understand this huge and astonishingly fast betterment is the reduction of the size of the different electronic devices that compose our gadgets.

Traditionally, the Moore's Law<sup>1</sup> has ruled the exponential reduction of the size of the transistors and an increase in the complexity of the electronic devices. However, to keep up with the trend with silicon electronics requires an enormous effort both technologically and economically. Hence, new technologies "More than Moore"<sup>2</sup> and "beyond CMOS"<sup>3</sup> (Complementary Metal-Oxide semiconductor) are required to achieve future generations of electronic devices.

Following Richard Feynman's intuition,<sup>4</sup> the electronic devices may ultimately be reduced to single molecules or a very few of them. The vast richness of molecular chemistry suggests that the traditional electronic devices could be mimicked and new functions could appear by combining its properties.<sup>5-7</sup> The first serious attempt to do so was devised by Aviram and Ratner (1974).<sup>8</sup> A molecule such as a hemiquinone with two clearly

## 1 Introduction

---

separated donor and acceptor groups could reproduce a classical rectifier based on an n-p junction. They conceptually placed the molecule between two metallic electrodes to apply a bias to let electrons flow and calculated the I(V) characteristics expected for a rectifier.

In the wake of that, Carter proposed a series of molecules that may work as wires, switches, amplifiers and other electronic devices.<sup>9,10</sup> Although molecular electronics does not change dramatically the concepts already known in silicon electronics, the quantum nature of molecules introduces new fascinating phenomena. A remarkable case is quantum interference<sup>11</sup> (QI) where two current paths can cancel each other giving a final current not equal to the sum of the current on each path. Other interesting phenomena such as magnetoresistance and spin filtering yield spin-polarised electron currents.<sup>12–16</sup>

Unluckily, it was not before the 1990s when scientists were able to manipulate molecules at single molecule level. Among the pioneers, Gimzewski and Joachim measured the electrical conductance of a single fullerene (C<sub>60</sub>) trapped between two gold electrodes using a STM (Scanning Tunnelling Microscope).<sup>17</sup> A few years later, Martin<sup>18</sup> and Metzger<sup>19</sup> published an experimental proof of unimolecular rectification behaviour in an Aviram-Ratner type molecule. In 2003, Tao introduced the use of STM to measure the electrical characteristics of molecules, which allow the imaging of single molecules during the experiment.<sup>20</sup>

Since then, molecular electronics has reached maturity. Molecular materials such as liquid crystals<sup>21</sup>, polymers for lithographic photoresists<sup>22</sup> and OLEDs<sup>23</sup> are now used in a daily basis. Lately, there is a special interest in the use of magnetic molecules as spin transfer torque magnetic random access memory (STT-MRAM),<sup>24</sup> its newer derivative spin-orbit torque MRAM (SOT-MRAM)<sup>25</sup> and as memristors.<sup>26,27</sup> Such devices should combine the cost benefits of a Dynamic RAM (DRAM), the speed

of a Static RAM (SRAM) and the non-volatility of a flash memory along with infinite durability. Therefore, they are potential candidates to be universal memory devices.

On the cutting-edge, memristors have been also employed to implement neuronal plasticity on neuromorphic computing.<sup>28–30</sup> This new field has the objective of imitating the neural structure and operation mechanisms of the human brain to create new algorithms dealing with uncertainty, ambiguity and contradiction.

## 1.1 Physical phenomena in molecular devices

In this section the most representative physical phenomena observed in molecular junctions<sup>31–33</sup> will be briefly discussed from a qualitative point of view. As Aviram and Ratner did,<sup>8</sup> a molecule will be conceptually placed between two metallic electrodes. From there, the different transport regimes and some of the most representative physical phenomena observed, along with some examples, will be shown.

### 1.1.1 Energy level diagram

The key to understand and predict the behaviour of a molecular junction is to draw an energy level diagram and locate the Fermi energy ( $E_F$ ). Consider a molecule sandwiched between two metallic contacts at the zero limit interaction. In this situation the electrodes can be understood as a continuum of energy levels (orbitals) with a given work function (WF) and the frontier orbitals of the molecule are related with its electron affinity (EA) and ionisation potential (IP). It is expected that the molecule stay in its neutral state (although there is no actual limitation in that sense) as long as  $IP - WF$  and  $WF - EA$  are much larger than  $k_B T$ , a condition that is



## 1 Introduction

---

most of the times fulfilled (Figure 1.1, left). The Fermi energy can then be located at the work function of the electrodes.

Whenever the interaction with the leads is not zero (Figure 1.1, right), the molecular orbitals are shifted by a contact potential because of the hybridisation with the continuum of orbitals of the electrodes. Hence, there might be a fractional charge transfer and the molecule may not be completely neutral.

The definition of the Fermi energy is now much more slippery. Below the Fermi energy, the number of states must be equal to the number of electrons in the molecule. Due to the interaction with the electrodes, the integer occupation number of the molecule can be a fractional number instead. However, the amount of charge transferred is usually less than one electron. Thus, the Fermi energy can be placed somewhere inside the HOMO-LUMO gap.

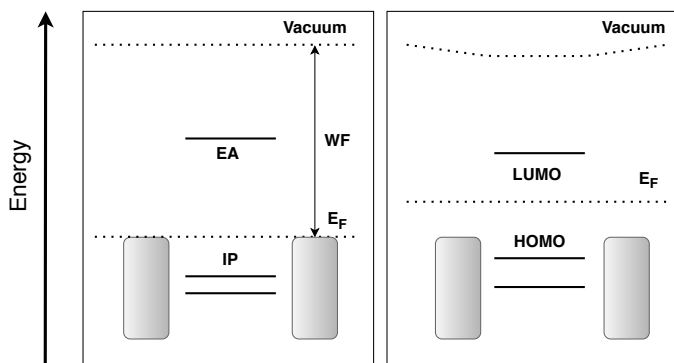


Figure 1.1. Equilibrium energy level diagram for a metal-molecule-metal junction at zero interaction limit (left) and once the interaction is turned on (right).

Related to the hybridisation with the electrodes, molecular orbital energies are broadened (Figure 1.2). This broadening ( $\Gamma$ ) is as well due to the interaction with the continuum of the electrodes molecular orbitals and may be different for each molecular orbital and each electrode. Depending

on how the molecule is anchored to the electrode, the energy difference in relation to the Fermi energy ( $E - E_F$ ) and the broadening can be strongly affected.

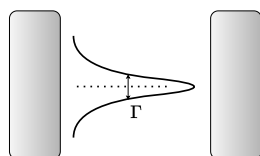


Figure 1.2. Energy broadening of a molecular orbital due to interaction with the electrode.

Under bias, the Fermi level of the electrodes becomes mismatched and electrons start flowing to restore the equilibrium (Figure 1.3). The interaction of the molecule with the electrodes is modified and  $E - E_F$  and  $\Gamma$  are thus dependent of the applied bias.

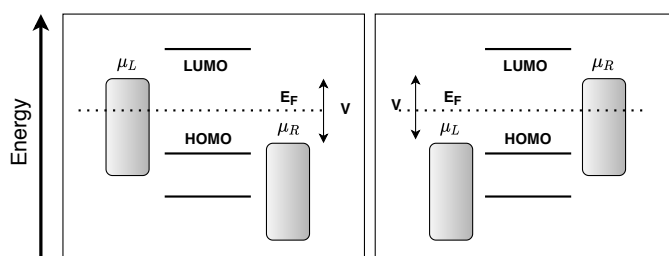


Figure 1.3. Schematic energy representation of a metal-molecule-metal nanojunction under bias.

Additionally, a third electrode, known as gate electrode, can be used to tune the energy position of the molecular orbitals. By applying a positive voltage, the molecular orbitals are shifted down in energy, while the opposite happens for negative voltages. In this manner, it is possible to tune the  $E - E_F$  expense.

### 1.1.2 Transport regimes

Once a bias is applied, it is possible to distinguish two main transport processes:

## 1 Introduction

---

In 1-step transport, the electron flows directly from one electrode to the other with no significant residence time in the molecule. The electron behaves as a wave moving with (elastic transport) or without (inelastic transport) energy exchange and phase-coherence. If the energy of the moving electron matches the energy of a molecular orbital, the electron charge transport efficiency increases. This phenomenon is known as resonant tunnelling. When the mean free path of the electron (average length that a particle travels freely) is longer than the interelectrode distance, the electron transport is called ballistic and the conductance is equal to  $G_0$  ( $7.748 \cdot 10^{-5}$  S).

On the other hand, in 2-step transport an electron or hole spends some time in the molecule before moving to the electrode. Hence, the molecule is charged during the residence time. The electron loses its phase-coherence and can exchange energy. This sort of transport is temperature-dependent in opposition to 1-step mechanisms.

Loosely speaking, 1-step transport can be related to the wave nature of the electron whilst 2-step transport shows the particle behaviour. Using the parameters  $E - E_F$  and  $\Gamma$  shown in section 1.1.1, it is possible to further characterise the different transport mechanisms. The first two are 2-step transport while the last two belong to 1-step transport mechanisms.

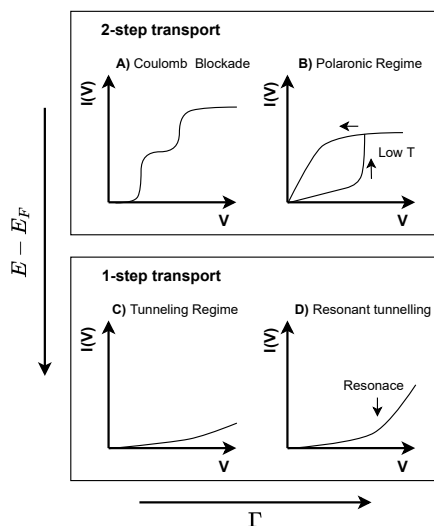


Figure 1.4. Transport regimes depending on the broadening of the molecular orbital and its energy difference to the Fermi energy. Adapted figure.<sup>31</sup>

If  $E - E_F$  is small and the broadening of the molecular orbital ( $\Gamma$ ) is low, the zero-interaction limit applies (Figure 1.1, left). Under these conditions, the molecule is barely affected by the electrodes but can be oxidised or reduced because of the applied bias. Once the molecule has lost or gained an electron, it is impossible to lose or add another electron until it has left the molecule. When the bias is further increased, the current is blocked for a certain bias difference corresponding to the charging energy of the molecule ( $E_{\text{add}}$ ). This yields a staircase-like current plot ( $I(V)$ ) corresponding to the transmission of a single electron (Figure 1.4A). This regime is known as Coulomb staircase or Coulomb blockade. It is usually modelled using a master equation that governs the probability rates to move from/to source electrode, molecule and drain electrode.<sup>34–37</sup> Experimentally, bias and gate voltages can be employed to map the stability diagram of the junction (Figure 1.5).

## 1 Introduction

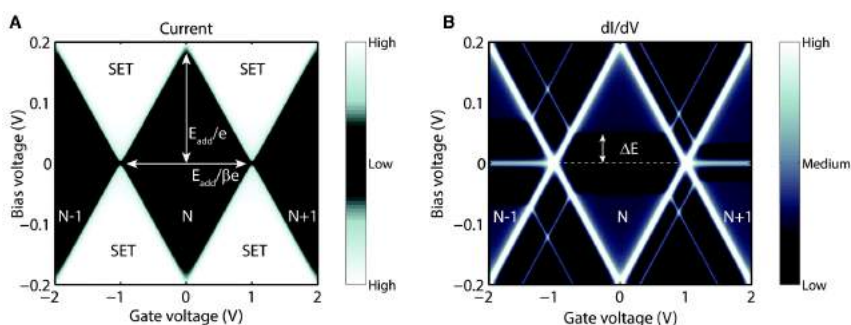


Figure 1.5. Idealised Coulomb blockade stability diagram (A) showing high current regions of single electron tunnelling (SET). The differential current map (B) shows the molecular orbital as bright diamond edges. Resonant tunnelling through excited states is observed as well as thin bright lines. N: Charge of the molecule.  $E_{add}$ : charging energy,  $\beta$ : Gate coupling,  $\Delta E$ : Excitation energy.<sup>38</sup>

If  $E - E_F$  is low but  $\Gamma$  is high, the electron is travelling in the Marcus or *Hopping* regime. This case is very similar to a chemical reaction and can be related to Marcus-Hush theory of electron transfer. The transmitted electron tunnels sequentially from site to site, usually this happens for large interelectrode distance. If the interelectrode gap is small and the bias is high enough, polarisation changes in the geometry can occur as the electron is transmitted triggering the so-called polaronic regime. The polaronic regime is a temperature-dependent mechanism in which the electron couples with the phonon/vibron modes of the electrode/molecule. Hysteresis is observed for low temperatures (Figure 1.4B).

When  $E - E_F$  is high, the electron flows as a wave in a tunnelling regime. For two different molecules with same size and sufficiently high  $E - E_F$  and low  $\Gamma$ , the measured current observed will be essentially tunnelling current through space (Figure 1.4C). Instead, if  $\Gamma$  is high, the tail of the broadened molecular level can reach the Fermi energy and then result in a molecule-dependent current (Figure 1.4D). These last two regimes are modelled under the Landauer and non-equilibrium Green's function formalisms and constitute the core of this thesis (sections 1.3 and 1.4).

### 1.1.3 Molecular wires

The simplest electronic and molecular device is a wire. It must let electrons travel easily, thereby having a high conductance ( $G$ ) in the 1-step regime (section 1.1.2).

Technically, any molecule with high conductance can work as a molecular wire. Nevertheless, it will be restricted to molecules without unpaired electrons and no asymmetry. These characteristics give rise to different phenomena that will be discussed in the following subsections.

There are many examples of molecular wires, but simple organic polymeric molecules may be the largest family and the most studied until today.<sup>39,40</sup> They are commonly characterised by their  $\beta$  value, which corresponds to the exponential factor in the exponential decay of the conductance in respect to length (1.1).<sup>41</sup> When a molecule is mediating the electron transport, higher conductance and smaller decays are obtained. Figure 1.6 shows the tunnelling current decay for a junction with a molecular wire compared to the expected exponential decay for vacuum.<sup>42</sup>

$$G = G_0 e^{-\beta d} \quad 1.1$$

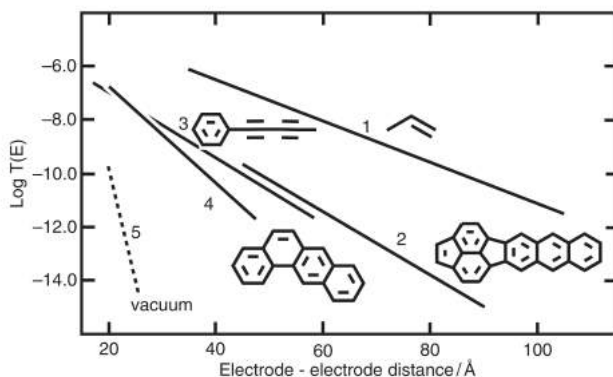


Figure 1.6. Molecular wires current decay compared to the vacuum decay.<sup>42</sup>

## 1 Introduction

---

Common decay rates ( $\beta$ ) are 0.75-0.94  $\text{\AA}^{-1}$  for alkanedithiols and 0.28-0.67  $\text{\AA}^{-1}$  for oligophenylenedithiols. Recently, ultralow, zero or even inverted attenuation rates in the range of -0.21 to 0.4  $\text{\AA}^{-1}$  have been reported for a large variety of molecules.<sup>43-50</sup> Particularly, diketopyrrolopyroles and fused porphyrins oligomers have shown almost zero and inverted attenuation in the range of -0.21 and -0.12  $\text{\AA}^{-1}$ .

### 1.1.4 Molecular rectification

A rectifier or diode is an electronic device capable of transforming an alternating current into a direct current. In other words, it lets electrons to flow in only one direction.

As it was mentioned before, Arieh Aviram and Mark Ratner introduced the idea of a molecular rectifier back in 1974.<sup>8</sup> The Aviram-Ratner type rectifiers consist of an electron donor moiety separated by an aliphatic chain from an electron acceptor moiety (Figure 1.7). In this way, the whole molecule is able to mimic the n-p junction of a rectifier.

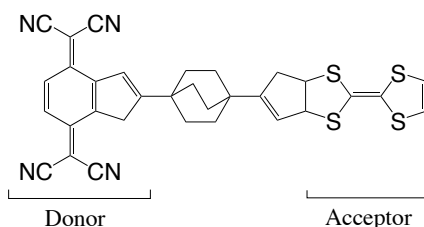


Figure 1.7. Aviram-Ratner type rectifier: donor and acceptor moieties work as an n-p junction.

Rectification occurs because the tunnelling barrier from acceptor to donor is higher than that from donor to acceptor (Figure 1.8, left). To quantify rectification, one measures the rectification ratio (RR), which is defined as the absolute value of the ratio of currents with reversed polarities at a given bias (1.2).

$$RR(V) = \left| \frac{I(V)}{I(-V)} \right| \quad 1.2$$

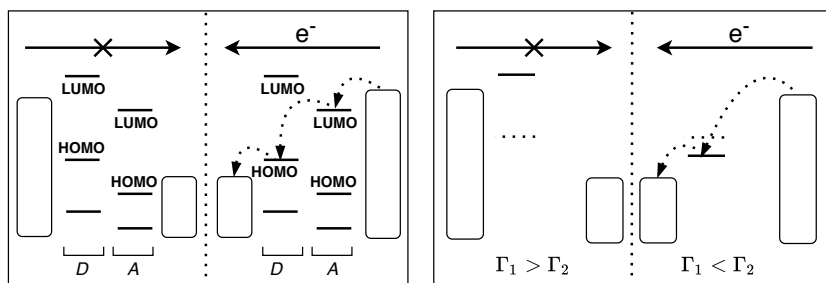


Figure 1.8. Rectification mechanisms. Aviram-Ratner rectification mechanism is analogue to an n-p junction (left). Asymmetry in the junction ( $\Gamma_1 \neq \Gamma_2$ ) also introduces rectification effects (right). Dashed molecular orbitals represent its energy at zero interaction.

More subtle rectification can occur if the broadening is different for each electrode ( $\Gamma_1 \neq \Gamma_2$ ) or due to an asymmetry in the junction. If  $\Gamma_1 > \Gamma_2$  and a bias is applied to electrode 1, the molecular orbitals will shift along with the electrode orbitals. If the same is done to electrode 2, the molecular orbitals will follow the applied bias but with a smaller shift because  $\Gamma_1 > \Gamma_2$ . In the case of an asymmetric molecule, that asymmetry is reflected in  $\Gamma_1$  and  $\Gamma_2$  and the same reasoning follows (Figure 1.8, right). Implicit rectification will be observed if two different materials are employed as electrodes.

Thus, rectifiers come in very different flavours. Perrin *et al.* presented a gate-tuneable diphenylethyne (DPE)-based diode, DPE-2F with  $RR > 600$  (Figure 1.9A).<sup>51</sup> Capozzi showed that the shape of the electrodes can also introduce rectification up to 200 in thiophene-1,1-dioxide (TDO<sub>n</sub>) junctions (Figure 1.9B).<sup>52</sup> Based on the asymmetry of the molecule, Yuan and co-workers formed a HS(CH<sub>2</sub>)<sub>11</sub>Fc<sub>2</sub> junction that reached a rectification ratio of  $10^3$  (Figure 1.9C).<sup>53</sup> In Chen's work, a similar junction of HS(CH<sub>2</sub>)<sub>15</sub>Fc-C≡C-Fc driven by electrostatic interactions exhibited a



## 1 Introduction

remarkable  $RR > 10^5$ , a value comparable to those of conventional diodes (Figure 1.9D).<sup>54</sup>

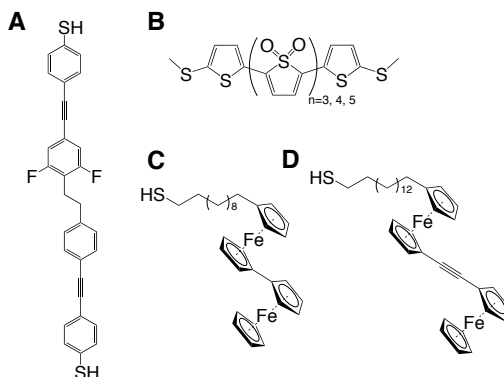


Figure 1.9. High RR molecular rectifiers. A) Aviram-Ratner type rectifier DPE-2F. B) TDO<sub>n</sub> presents rectification with asymmetric electrode shapes. C) and D) Nijhuis rectifiers based on the asymmetry of the molecule.

### 1.1.5 Molecular switching

A switch is an electronic device that can turn on and off the current. It is a very appealing functionality because a transistor is, ultimately, a gate-controlled switch. Changes in the molecular geometry or in the electronic structure can lead to an abrupt change in the measured conductance. Hence, molecules showing *cis-trans* isomerism<sup>55,56</sup> or spin crossover compounds<sup>57–60</sup> are excellent molecular switch candidates because of its intrinsic bistability. The switching between these two states can be triggered by a gate voltage, bias, pH, temperature, pressure or light. The main difficulty to design a molecular switch is to keep the bistability intact once the molecule is placed between the electrodes. Strong coupling with the electrodes can be detrimental for the bistability of the isolated molecule, making impossible the switching process.

Ideally, the molecule should switch from a zero conductance state (OFF) to an infinite conductance state (ON). In practice, intermediate situations

are found, and those can be characterized by their calculated ON/OFF conductance ratio, which is a quality measure of the switching device.

An elegant switch example is the graphene – diarylethene – graphene junction (Figure 1.10, left). This molecule presents switching behaviour that can be controlled by light irradiation.<sup>61</sup> The diarylethene molecule, directly placed between the electrodes, lost its switching capability. To overcome this, three methylene units were incorporated between the diarylethene moiety and the electrode to reduce the coupling. When diarylethene is irradiated with ultraviolet (UV) light a new C-C bond is created, leading to the ON state. The current can be switched OFF when visible light is employed (Figure 1.10, right) producing a switching ratio of 100.

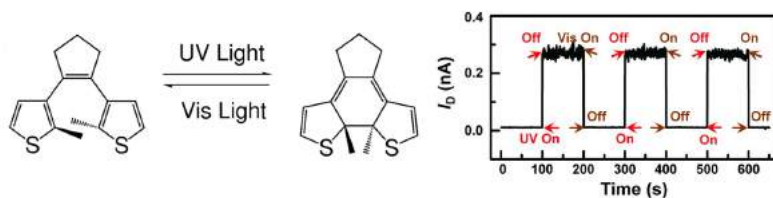


Figure 1.10. Photoswitch by Xu, Nitzan, Guo *et al.* The creation of a C-C bond in the ON state opens a new current pathway. The pathway is destroyed when visible light is used. Adapted figure.<sup>61</sup>

In 2015 Van der Zant and Mayor reported an Fe<sup>II</sup> spin crossover unimolecular switch triggered by voltage<sup>62</sup> (Figure 1.11). For low biases the Fe<sup>II</sup> complex remains in the low-spin state (Figure 1.11, left). When the applied voltage is high, the electric field induces a distortion in the coordination sphere triggering the high-spin state (Figure 1.11, right).

# 1 Introduction

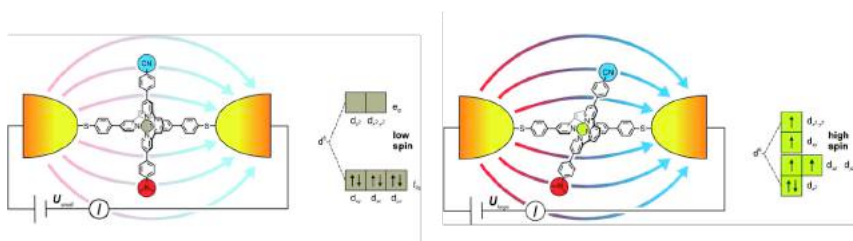


Figure 1.11. Voltage-triggered Fe<sup>II</sup> spin crossover junction by Van der Zant and Mayor. Adapted figure.<sup>62</sup>

More recently, Mosey has proposed a non-volatile spin crossover molecular switch based on an ensemble of 40-50 molecular layers thick [Fe{H<sub>2</sub>B(pz)<sub>2</sub>}(bipy)] (pz = tris(pyrazol-1-yl)-borohydride, bipy = 2,2'-bipyridine).<sup>63</sup> The high-spin state works as ON state and the low-spin state as the OFF state. An increase of the temperature triggers the switch due to a spin crossover process (Figure 1.12, left). The molecular layer also exhibits polarisation-dependent conductance at room temperature. When the polarisation is pointed towards the [Fe{H<sub>2</sub>B(pz)<sub>2</sub>}(bipy)] layer, the high-spin state is dominant and higher conductance is observed (Figure 1.12, right). The polarisation of the ferroelectric PVDF-HFP substrate can be controlled by a gate voltage and is non-volatile, creating a straightforward route towards a three terminal molecular device.

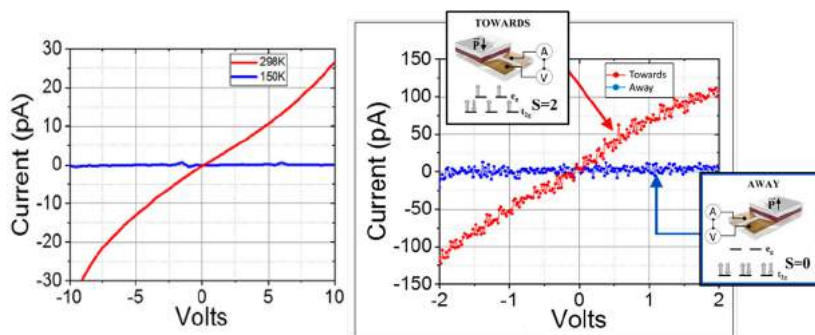


Figure 1.12. Cheng [Fe{H<sub>2</sub>B(pz)<sub>2</sub>}(bipy)] molecular switch characteristics controlled with temperature (left). Memristive behaviour is observed when a ferroelectric is polarised towards (red) and away (blue) the SCO layer (right). Adapted figure.<sup>63</sup>

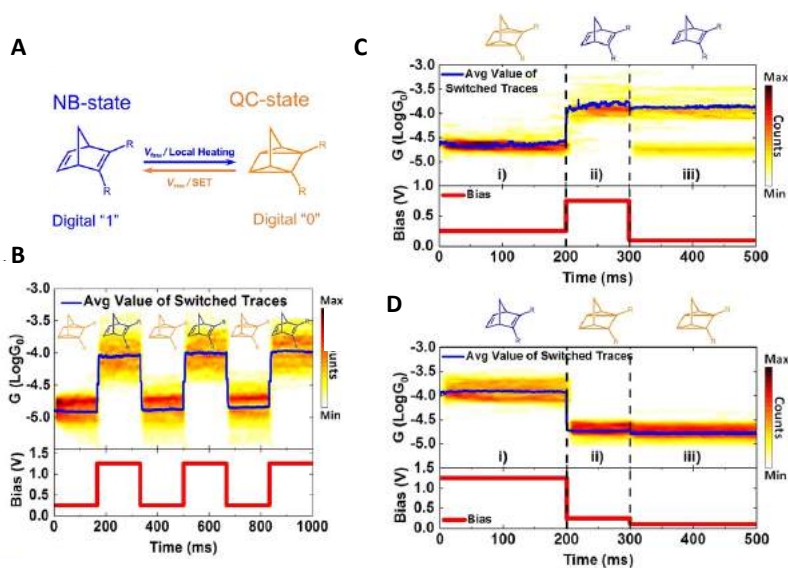


Figure 1.13. Molecular switch by Hihath between NB and QC state (A and B) can work as a memristor (C and D). Adapted figure.<sup>64</sup>

Lately, molecular switches have been focused towards their use in memristive devices. Hypothetically, a memristor is an electronic device whose resistance is dependent on the previous electronic current, the so-called non-volatile property. A memristor-like molecular switch between a cyclic norbornadiene (NB) derivative with oligo(phenylene-ethynylene) (OPE) side groups state and its quadricyclane (QC) state (Figure 1.13A) was designed by Li and co-workers (Figure 1.13B).<sup>64</sup> The QC-state (“0” state) is detected at 0.25 V, the NB-state (“1” state) is written at 0.75 V and finally read at 0.1 V (Figure 1.13C). In the case of NB-state, it is detected, written and read at 1.25, 0.25 and 0.1 V (Figure 1.13D).

### 1.1.6 Molecular spintronics

In the previous sections the discussion was focused on the transport of the electron charge, completely ignoring the spin magnetic moment. To include the spin, two different transport channels must be considered for

## 1 Introduction

alpha and beta electrons. Achieving control over the spin of travelling electrons gave rise the field of molecular spintronics.<sup>65–67</sup> The Kondo effect and giant magnetoresistance (GMR) are the two most important spintronic effects.

The Kondo effect on bulk conductors arises at very low temperatures when magnetic impurities are found in the sample, introducing unpaired electrons. Those electrons interact with the conducting electrons reducing the conductance at temperatures below the Kondo temperature ( $T_K$ ), in honour of Jun Kondo who first described the phenomenon in 1964.<sup>68</sup> The magnetic impurity has been shown to be successfully described in Anderson model.<sup>69</sup>

For paramagnetic molecules, the Kondo effect can be observed at temperatures below  $T_K$  because they show an increase of the conductance, contrary to bulk Kondo effect. In the molecular case, the flowing electrons interact with the unpaired electrons via spin-spin interactions forming a weakly bound many-body single state. Because of that, Kondo states are always on the Fermi energy level and on resonance. By applying a magnetic field, it is possible to distinguish spin up and spin down electrons as shown in Figure 1.14.

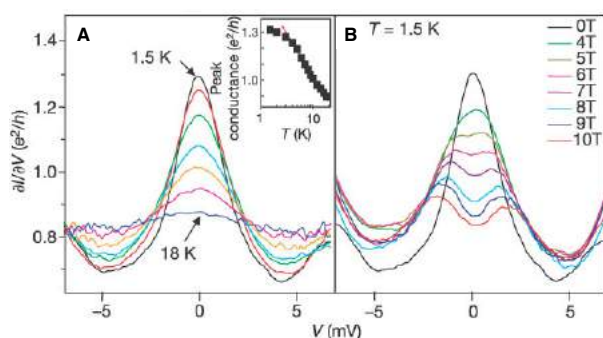


Figure 1.14. (A) Differential current measurements of  $[\text{Co}(\text{tpy-SH})_2]^{2+}$  (tpy = terpyridi-nyl) showing an increasing current as long as the temperature is diminished. (B) Applying a magnetic field the differential current peak is split into two different peaks related to alpha and beta electrons.<sup>66</sup>

Giant magnetoresistance (GMR) was first observed in metallic multilayers, in which a thin conductive non-magnetic layer separates two ferromagnetic layers.<sup>70,71</sup> The resistance increases when the polarisation of the ferromagnetic layers is antiparallel, conversely parallel ferromagnets produce a low resistance state. The magnetisation of the ferromagnets can be controlled via an external magnetic field. Such device is known as spin valve (Figure 1.15).<sup>72</sup> Magnetic-RAMs, magnetic heads and hard disks are some of the utilities of this sort of valves.

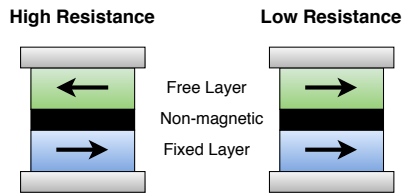


Figure 1.15. Scheme of a spin valve device.

In modern MRAM, the external magnetic field is no longer used in favour of spin transfer torque-magnetic random access memory (STT-MRAM) and spin-orbit torque-MRAM (SOT-MRAM)<sup>24,25,73,74</sup> based on spin Hall<sup>75</sup> and Rashba<sup>76</sup> effects (Figure 1.16). STT-MRAM has lower power consumption in comparison to applying an external magnetic field, is non-volatile and has near-zero power leakage consumption.

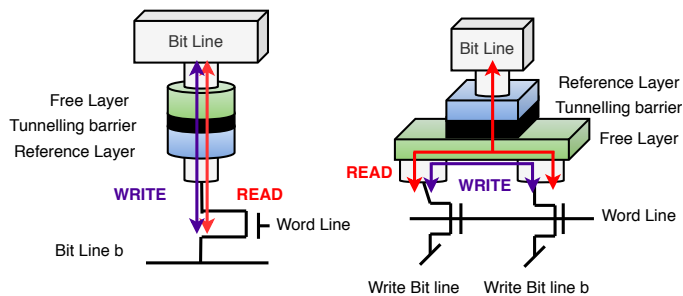


Figure 1.16. A spin transfer torque (STT) device (left) and the newer spin-orbit torque (SOT) device (right).

## 1 Introduction

The weakness of STT devices is that to set (write) the ferromagnets either parallel or antiparallel a high-density current is needed. This can damage the non-magnetic layer and hence potentially destroy the device besides requiring high power consumption. To avoid this issue, spin-orbit torque devices are a promising way to separate the writing and reading paths. In SOT devices, a perpendicular current is applied to write the alignment of the ferromagnetic layers, thus keeping the non-magnetic layer safe. Despite of this, SOT-devices require two transistors whilst STT-devices require only one, limiting the use of SOT-MRAM in high-density memory.

Molecules with unpaired electrons may work as molecular spin valves.<sup>12,77,78</sup> If the molecular orbital closer to the Fermi energy is an alpha spinorbital, it is expected to observe a larger conductance when alpha electrons are injected. If the injected electrons are beta-polarised, then the conductance is lower because the first beta spinorbital lies far away of the Fermi energy. Such effect is often called magnetoresistance. A notable example is the paramagnetic molecule  $[\text{Fe}(\text{tzpy})_2(\text{NCS})_2]$ <sup>79,80</sup> (tzpy = 3-(2-pyridyl)-[1,2,3]triazolo[1,5-*a*]pyridine) that presents a magnetoresistance of 100-fold under opposite nickel magnetic polarisation at room temperature (Figure 1.17, left). The homologous diamagnetic complex  $[\text{Fe}(\text{L}^{\text{A}})_2(\text{NCS})_2]$  ( $\text{L}^{\text{A}} = \text{N}, \text{N}'\text{-bis}(1\text{-pyridin-2-yl-ethylidene)-2,2\text{-dimethylpropane-1,3-diamine}$ ) shows almost the same conductance value (Figure 1.17, right).

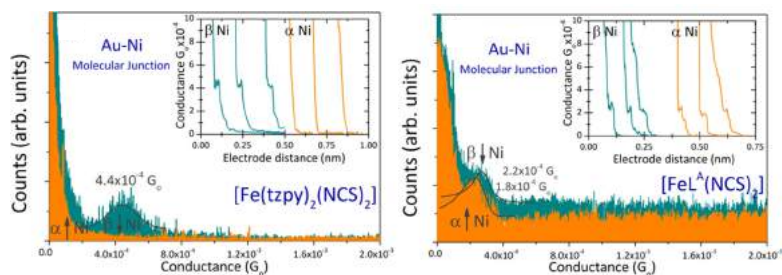


Figure 1.17. Conductance histogram of paramagnetic  $[\text{Fe}(\text{tzpy})_2(\text{NCS})_2]$  and an homologous diamagnetic  $[\text{Fe}(\text{L}^{\text{A}})_2(\text{NCS})_2]$  complex. The former case presents a strong magnetoresistance. Adapted figure.<sup>81</sup>

In the case that the injected electrons are a mixture of alpha and beta electrons, and assuming that the molecule keeps a fixed polarisation (alpha and beta states are not degenerated), the injected electrons will be spin-filtered because one polarisation will have a larger conductance.

However, diamagnetic molecules cannot be ruled out from spintronics. Applying a gate voltage on a diamagnetic junction can lead to a reduction/oxidation of the molecule and, hence, creating a radical with unpaired electrons.<sup>82</sup> Plus, spin-orbit coupling (SOC) can introduce a refined way of magnetoresistance.<sup>83</sup> Chirality induced spin selectivity (CISS)<sup>84-87</sup> effect opens a door to spintronics to diamagnetic molecules such as DNA or peptides: When a spin-polarised current is injected through a molecule with helical chirality, the conductance is different for alpha and beta electrons. Ron Naaman and David Waldeck introduced the concept when the spin selectivity in electron transmission through self-assembled monolayers of double-stranded DNA was observed.<sup>88</sup> The spin selectivity is often studied using cyclic voltammetry, where one of the electrodes is coated with a monolayer of the molecule under study and the electrons are injected from a polarised nickel electrode (Figure 1.18).<sup>89</sup> Other techniques such as STM Break Junction (section 1.2.1) have been employed as well.<sup>90</sup>

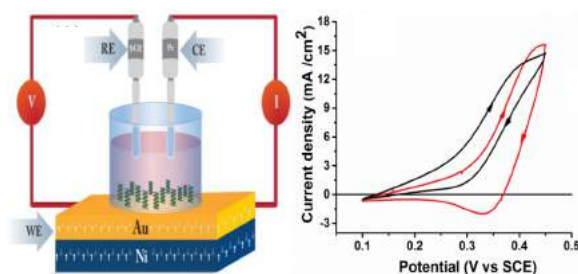


Figure 1.18. On the left, Scheme of a cyclic voltammetry set-up. L-poly{[methyl N-(tert-butoxycarbonyl)-S-3-thienyl-L cysteinyl]-cothiophene} is coating the gold electrode (working electrode). The cyclic voltammogram of ferrocene (right) reveals a difference response for alpha (red) and beta electrons (black). Adapted figure.<sup>89</sup>



## 1 Introduction

---

Although CISS effect is widely demonstrated experimentally,<sup>91–93</sup> there is still no theoretical consensus.<sup>87</sup> Molecular orbitals of two enantiomers are exactly the same and differences in their SOC properties seem difficult to understand. Even more, molecules usually contain light atoms, and thus their SOC should be small.<sup>94</sup> Luckily, some methodologies based on a perturbative approach to the spin-orbit interaction have been published to settle the basis of a correct analysis.<sup>95–100</sup>

### 1.1.7 Molecular thermoelectrics

All electric machines generate heat because of Joule effect. Up to 80% of industrial waste heat is released as heated gas.<sup>101</sup> In the case of electronics, removing the produced heat to keep the devices in good conditions is a priority.

A temperature difference between two electrodes will break the equilibrium of the system. To restore it, electrons carry thermal energy from one electrode to the other. Thermoelectric devices are, thus, an excellent way to recycle waste heat and transform it back into electricity.

This time, however, apart of electrons there is a second significant actor: Phonon thermal conductance can be comparable to electronic thermal conductance. In a successful thermoelectric device, the electronic contribution must greatly surpass the phonon thermal conductance. Otherwise, vibrations will be the preferred mechanism and small current will flow.

The figure of merit ( $ZT$ ) is the main parameter to rate the performance of a thermoelectric device (**1.3**), where  $S$  is the thermopower or Seebeck coefficient,  $G$  is the electric conductance and  $k_e$  and  $k_{ph}$  is the electron and phonon thermal conductance.

$$ZT = \frac{S^2GT}{k_{el} + k_{ph}} \quad 1.3$$

There are commercial thermoelectric devices based in a great variety of inorganic compounds.<sup>102-107</sup> Among them, Bi<sub>2</sub>Te<sub>3</sub> exhibits a ZT of 1 near room temperature (350-450K), making it an excellent thermoelectric material. However, the low abundance of Bi and Te, the working temperature range, the stability and the scalability at the industrial level stimulates the search of alternatives.<sup>108</sup>

Paulsson and Datta were among the first to study thermoelectric properties in a molecular junction of benzenedithiol (BDT).<sup>109</sup> In that work, they suggested that the Seebeck coefficient could indicate whether the electronic transport were through the HOMO or LUMO orbitals. The thermopower is given by equation 1.4.<sup>110</sup>

$$S = -\frac{\pi^2 k_B^2 T}{3|e|} \frac{\partial \text{Ln}[T(E)]}{\partial E} \quad 1.4$$

Where  $k_B$  is the Boltzmann constant, T is temperature and T(E) is the transmission function. Since thermopower depends on the derivative of Ln[T(E)], a positive thermopower value indicates HOMO mediated transport, while negative thermopower is due to LUMO mediated transport.

## 1 Introduction

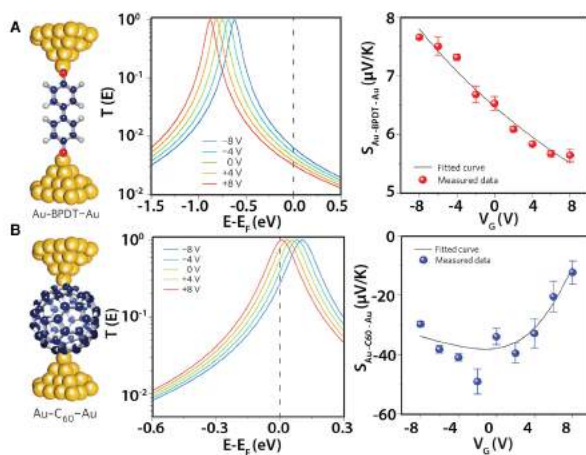


Figure 1.19. Thermoelectric properties of 4,4'-dibenzenedithiol (DBDT) (A) and  $C_{60}$  (B) under gate voltage potential.<sup>111</sup>

Many simple organic molecules have been studied to gain more insight in thermoelectricity.<sup>111,112</sup> Nevertheless, while theoretical calculations of thermoelectric properties are easily accessible,<sup>113–117</sup> experimental measuring is still limited. A voltage-gate is frequently employed to improve the ZT of the junction (Figure 1.19). As it happens for conductance, ZT is enhanced when a molecular orbital is mediating the electron transport (in fact, when the derivative is maximum).

Sign and magnitude of thermoelectric properties depend strongly on the orientation of the molecule in the molecular junction. Agraït and co-workers<sup>118,119</sup> have shown that endohedral fullerene  $Sc_3N@C_{60}$  is a bi-thermoelectric material, displaying positive or negative thermopower depending on the orientation of the molecule in the junction. The orientation of the endohedral fullerene can be controlled by applying pressure with a STM tip.

Beyond the purely figure of merit improvement, thermoelectric properties have been also used to directly probe ground and excited states of Gd(tpy-

SH)<sub>2</sub>(SCN)<sub>3</sub> complex, showing that thermoelectric measurements can be used as well as a spectroscopic tool.<sup>120</sup>

### 1.1.8 Quantum interference

All the aforementioned physical phenomena count on with a classical analogue in electronics. It is worth mentioning a purely quantum phenomenon that arises from the wave nature of electrons: Quantum interference (QI). When electrons are coherently travelling across a nanojunction through two (or more) molecular orbitals, they can interfere either constructively or destructively, resulting in molecules not following classic electrical circuit rules. Controlling QI effect offers an opportunity to build up molecular sensors/switches<sup>121,122</sup> and thermoelectric devices.<sup>123,124</sup>

Conjugated organic rings<sup>125,126</sup> and cages<sup>127</sup> have been used intensively in the last years to study quantum interference. A canonical example is *ortho*, *meta* and *para* substitution of benzene in a molecular wire, often related to Mach-Zehnder interferometer in physics.<sup>128</sup> A simple tight binding model of the benzene ring is capable to deduce that a *meta* connection triggers a destructive QI whereas *ortho* and *para* connections generate constructive QI.<sup>11</sup> Other QI effects of interest are Breit-Wigner interference (the broadening of a molecular orbital shown in 1.1.1) and Fano resonance, composed of both a destructive and a nearby constructive interference. This last one is of strong interest in thermoelectrics since it can lead to great thermopowers and figures of merit in single molecule devices.<sup>129</sup>

In the last years a growing complexity in the aromatic rings used to explore quantum interference has arised.<sup>130–132</sup> Venkataraman and Evers<sup>133</sup> introduced a mechanically controlled quantum interference case of two ferrocene derivatives (Figure 1.20A). A broad peak with maximum around

## 1 Introduction

$3 \cdot 10^{-5} G_0$  for both derivatives is shown (Figure 1.20B). The broadening of the conductance peaks is related to the relative angle of the Cp rings, theoretically confirmed in the calculated transmission (Figure 1.20C).

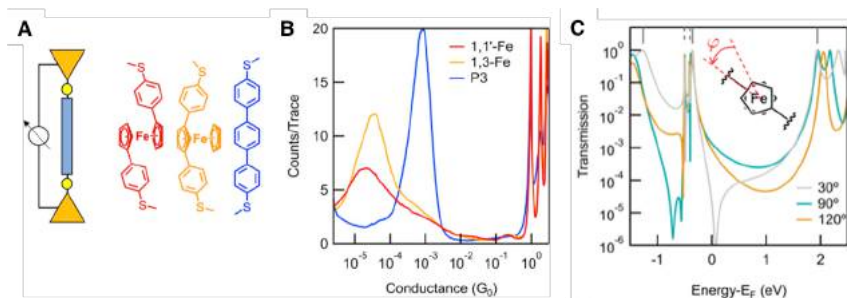


Figure 1.20. Mechanically controlled quantum interference of two ferrocene derivatives. A) STM-BJ scheme and molecular systems considered B) Conductance histogram obtained C) Calculated transmission dependence with angle. Adapted figure.<sup>133</sup>

## 1.2 Experimental techniques

The art of catching a molecule between two electrodes lies in the assumption that there is a certain probability that molecules eventually will bridge both electrodes once a nanogap is created. How this gap is created is the most important distinction between the different experimental techniques.

Generally speaking, there is no limitation in the environment in which these measurements can be performed. Vacuum, air, organic solvents, even aqueous electrolyte and ionic liquids have been used to place a molecule between electrodes. Low temperature measurements in ultrahigh vacuum (UHV) gives the most reproducible results but lately, there is a growing interest in the scientific community to study how the environment modifies the electrical properties of molecules.<sup>134–137</sup> The solvent-molecule interactions introduce slight shifts on the energy of the

molecular orbitals (section 1.1.1), hence, the measured conductance can be modulated depending on which solvent is employed.

The most usual electrode material is gold, which remains inert under experimental conditions. In the vast majority of metals a natural oxide layer is formed under exposure to air. The formation of such layer disrupts the tunnelling current, making impossible the measurement. Moreover, the inert nature of gold facilitates the cleaning of the electrodes before the experiment in which strong acids are often used. Although the non-reactive nature of gold may be counterintuitive in terms of forming a nanojunction, there are a large variety of so-called anchoring groups that strongly bind to gold. The most common groups are thiols and its derivatives because they covalently bond to gold. Other anchors of this sort are Au-C<sup>138</sup> and Au-N,<sup>139</sup> frequently used as well. Even though a covalent anchoring group is usually the preferred manner to bind a molecule in the nanojunction,<sup>140</sup> weak bonds such as  $\pi$ -interactions have been reported to be a convenient way to form a nanojunction.<sup>141</sup>

Of course, depending on the experiment, a different metal might be a better choice. Pt/Ir electrode is the chosen one to obtain STM images because of its toughness, producing high quality images.<sup>142</sup> Nickel can be easily magnetised to study the magnetoresistance response of molecules with unpaired electrons.<sup>143</sup> However, special care must be taken to avoid the aforementioned oxide layer. Even more, other conductive materials as graphene are employed in a daily basis.<sup>144</sup>

In the previous section (section 1.1), the physical phenomena in a molecular junction, obviating how this is done, was discussed. In this section the main experimental techniques employed in the study of single molecules is reviewed. STM-Break Junction (STM-BJ), Mechanically Controlled Break Junction (MCBJ) and Electromigration Break Junction

(EMBJ) are used to study the electrical properties at the single molecule level.<sup>145</sup> These techniques are as well the most flexible ones in terms of variety of experiments and allow a quite deep understanding of the target molecular system. The statistical data obtained is compiled in a conductance histogram, which is the main output of these techniques. Traditionally, the construction of this histogram can be slightly human-biased<sup>146–156</sup> but in the last years, machine-learning algorithms have been introduced to overcome this issue.<sup>157–160</sup>

A more natural way to investigate extensive systems is to use Conductive Atomic Force Microscopy (C-AFM) or an Eutectic-GaIn (EGaIn) electrode, as proposed by Nijhuis and Whitesides.<sup>161</sup> Notwithstanding, STM-BJ can explore extensive systems such as monolayers in its *blinking* mode. Hence, a clear line between unimolecular and extensive experiments cannot be drawn.

### 1.2.1 STM Break Junction (STM-BJ)

The Scanning Tunnelling Microscopy (STM) is a well established technique that can be used to access to the properties of molecules either adsorbed on a conductive substrate or in solution. It allows the precise control of the tip-substrate distance, thus controlling the contact spacing and tilt angle. STM-BJ experiments can be easily carried out under electrochemical conditions. Also, STM experiments can be combined with high-resolution STM-imaging to extract structural information of the substrate.

The most common way for creating single molecule junctions is the STM-Break Junction technique or *tapping* mode,<sup>20</sup> demonstrated by Tao and collaborators in 2003 in which the tip is crashed into and driven out of contact in a substrate covered in molecules (Figure 1.21).

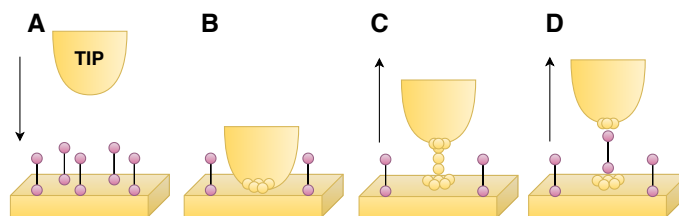


Figure 1.21. Typical STM-Break Junction cycle.

Initially, the molecules under study are either adsorbed on the substrate or in solution. The solvents employed are usually 1,3,5-trimethylbenzene (mesitylene) and 1,3,5-trichlorobenzene (TCB) because they have very low oxygen and water solubility. Nevertheless, any solvent can be potentially used. Then, a bias voltage is set between the tip and the substrate, and the tip is drifted away from the surface a certain distance set by a feedback tunnelling current control (Figure 1.21A).

The feedback is switched off and the break-junction cycle starts: the tip is crashed to the substrate at constant x-y position (Figure 1.21B). In fact, the tip is approached until a pre-set upper limit of current. This limit usually corresponds to the metal-metal contact. The tip is then withdrawn from the surface at a chosen rate (Figure 1.21C). During the withdrawing process, a molecule eventually can bridge the substrate and the tip. In such cases, a plateau in the expected exponential decay of the tunnelling current is observed (Figure 1.21D). The withdrawing rate must be slow enough to lengthen the current plateau as much as possible. However, a too slow rate can snag the tip in the surface. Finally, the junction is broken and the cycle starts again.

The cycle is repeated thousands of times, being 3000-5000 conductance traces a typical value. These traces are recorded for the subsequent statistical analysis (Figure 1.22).



## 1 Introduction

---

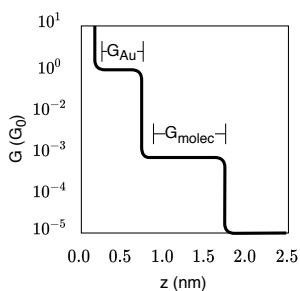


Figure 1.22. Idealised  $I(z)$  trace obtained in a STM-BJ experiment. Conductance plateaus indicate the formation of a nanojunction mediating the electron current.

Another possibility to catch a molecule is to wait for the spontaneous junction formation, a technique demonstrated by Haiss and co-workers.<sup>162</sup> Instead of crashing the tip against the substrate, the tip is approached up to a certain tip-substrate distance (interelectrode distance) and then the feedback control is switched off (Figure 1.23,  $t_1$ ). Without feedback, the tip drifts freely at a given x-y position. Then the current as a function of time ( $I(t)$ ) is recorded. Eventually, a molecule jumps into the nanogap giving a conductance jump or *blink* (Figure 1.23,  $t_2$ ). Afterwards, the molecule spontaneously detaches from the tip (Figure 1.23,  $t_3$ ).

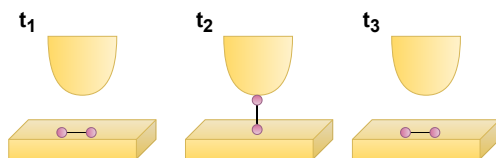


Figure 1.23. Spontaneous junction formation or *blinking* technique.

As in the *tapping* mode, hundreds to thousands of *blinks* are recorded for statistical analysis (Figure 1.24).

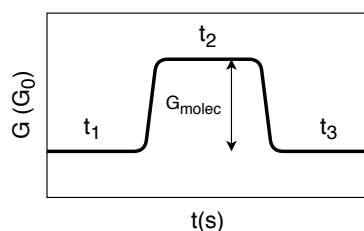


Figure 1.24. Current jumps or *blinks* during spontaneous junction formation technique.

In opposition of these two “fishing” techniques, at sufficiently low temperatures it is possible to image an individual molecule before it is contacted.<sup>163</sup> This way, it can be indisputably agreed that one molecule is studied.

In addition to the explained above, the use of a STM tip as an electrode permits its easy functionalization. This allows the creation of junctions based on supramolecular interactions. Moreover, if a nickel tip is used to perform the experiment, it can be magnetised to explore the effect of the magnetic polarisation of the electrode on the molecule current signature.

### 1.2.2 Mechanically Controlled Break Junction (MCBJ)

Similar to the STM-BJ, the MCBJ permits the automated cyclic formation/breaking of a target single molecule junction. A notched metal wire is placed in a bendable substrate and elongated until it is fractured using a piezo-controlled pushing rod. Two sharp electrodes are thus formed separated by a nanogap (Figure 1.25). Before or after the rupture, the molecule under study is introduced to link both electrodes. MCBJ was introduced by Moreland<sup>164</sup> and Muller<sup>165</sup> and further developed by Reed and colleagues.<sup>166</sup>

In comparison with STM-BJ, MCBJ has a high mechanical and vibrational stability, up to two orders of magnitude more stable. It allows a very fine control of the nanogap size formed down to the picometer range even at

## 1 Introduction

---

room temperature. The slower stretching velocity of the electrodes makes it a more precise technique. Furthermore, it can be combined with Raman Spectroscopy to access *in situ* monitoring of the molecular junction formation along with the charge transport measurements.<sup>167–170</sup>

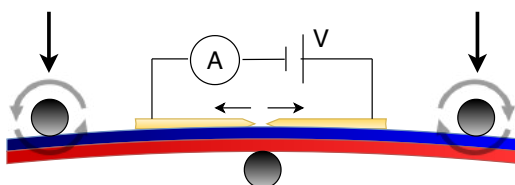


Figure 1.25. Schematic representation of a Mechanically Controlled Break Junction (MCBJ).

However, certain drawbacks arise. MCBJ measurements require an elaborate preparation and changing the electrode material effectively involves the creation of a complete new device. Plus, obtaining the desired molecular presence between the electrodes is often hard to accomplish.<sup>145,171</sup> As in STM-BJ, similar current traces are obtained and recorded for future analysis.

### 1.2.3 Electromigration Break Junction (EMBJ)

The first report of the fabrication of two metallic electrodes by electromigration was by Park in 1999<sup>172</sup> (Figure 1.26). First, a metallic nanowire is defined by electron-beam lithography. Then, metal atoms evaporate due to Joule effect by the effect of an applied electric field, which results in the breakage of the nanowire. Monitoring the current-voltage response in real time follows the breaking process, until a tunnelling signal is observed.

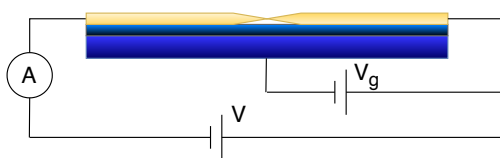


Figure 1.26. Electromigration Break Junction (EMBJ) scheme.

Although STM-BJ and MCBJ can incorporate a gate electrode, in EMBJ is already present before the creation of the nanogap, making it an excellent choice to build three-terminal devices. A gate voltage can shift up and down in energy the molecular orbitals, thus modulating the current.

As a drawback, it is often required to rebuild the junction when a large number of metal-molecule geometries are needed for statistical analysis. Furthermore, EMBJ shares the lack of direct observation of the nanojunction with MCBJ. Luckily, in both techniques *in situ* STM, AFM or transmission electron microscopy (TEM) can be employed to circumvent the problem.

## 1.2.4 Data collection and analysis

Regardless of which technique was employed to obtain the experimental data, the current, or more typically the conductance, is analysed to build a histogram that reflects the most common conductance values observed during the measurement.

To do that, it is essential to know the anatomy of a conductance-distance trace ( $G(z)$ ), the main output of a BJ experiment. These traces are usually plotted in units of the conductance quantum  $G_0$  ( $77.5 \mu\text{S}$ ). Note that actually conductance ( $G$ ) is not a quantized magnitude. Instead,  $G_0$  describes the conductance of two quantum channels (one spin up and one spin down) when the transport through them is ballistic. In other words: It

## 1 Introduction

is the conductance observed in a quantum point contact (QPC). The first definition will become clearer in the following sections.

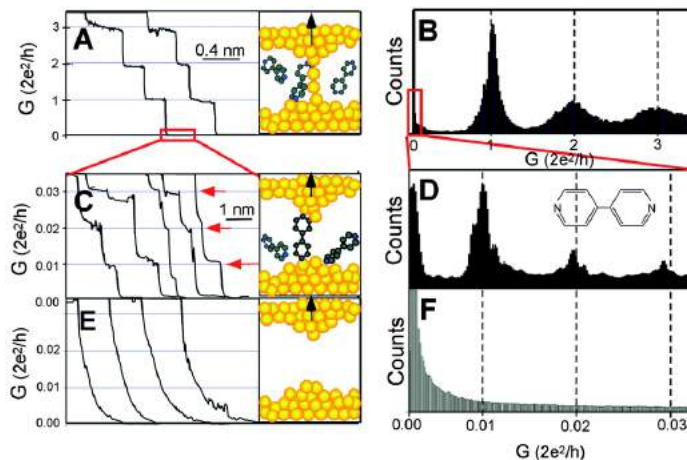


Figure 1.27. Conductance traces of 4,4'-bipyridine (left) obtained in a break-junction experiment are recorded to construct a histogram of the accumulated  $G(z)$  traces (right).<sup>173</sup>

Figure 1.27 shows some traces and the resulting histogram of a break-junction experiment on 4,4'-bipyridine using gold electrodes.<sup>173</sup> As previously mentioned, during the BJ cycle if no junction is created, observing a clean exponential decay of the conductance should be expected. This is because the tunnelling current between the two electrodes decays in that manner (Figure 1.27E).

However, most of the traces will show a plateau at  $G_0$  (around 70-90%). When the tip is driven into the gold substrate and retracted, a gold nanowire is formed. It mostly consists of a single gold atom bridging both electrodes. If the withdrawing rate is slow enough, it is possible to see plateaus at  $2G_0$  and  $3G_0$  (Figure 1.27A). The integer multiplicity of  $G_0$  is interpreted as one, two or three gold atoms bridging the nanojunction at the same time in parallel.

While the tip is being withdrawn a molecule in the vicinity may jump into the nanogap creating a new junction. Thus, some new plateaus are shown

in the  $G(z)$  trace (Figure 1.27C). The lowest value is  $0.01 G_0$  and the rest are integer multiples of this value. As happened with gold, one, two or three 4,4'-bipyridines can be trapped in the junction at the same time. The presence of these plateaus implies that the molecule provides a relative constant pathway for the electron current. In a molecular junction, there is never a completely flat plateau. It may contain sudden jumps and may even possess a gentle slope. The reason why is difficult to underpin, but these characteristics are commonly related with vibrations, slight conformational changes and stress during the junction lifetime. In that context, the length of the plateau is normally related with the junction stability.

Finally, there are no more conductance plateaus and the exponential decay appears (Figure 1.27E).

Although this can be experimentally observed, only a very few traces will show the whole story. Most of the traces will show only the  $G_0$  plateau. Some others  $G_0$  and  $0.01 G_0$ , or just  $0.01 G_0$ . All traces are accumulated to create a histogram that reveals the most usual conductance values observed. Figure 1.27B shows three conductance peaks in the histogram corresponding to  $G_0$ ,  $2 G_0$  and  $3 G_0$ . As one should expect, the number of counts for  $G_0$  is larger than  $2 G_0$  and so on. The same is true for the conductance peaks related to 4,4'-bipyridine. Catching a single 4,4'-bipyridine is statistically more probable than catching two or three at once, as shown in Figure 1.27D. Of course, when there is no molecule in the junction, no peak is shown in the histogram (Figure 1.27F).

Further analysis can be done building 2D conductance-displacement histograms. These sorts of histograms correlate the conductance, displacement and number of counts. They permit to elucidate the “plasticity” of a junction. If the junction is very rigid, a lot of counts will

## 1 Introduction

be shown for specific conductance and displacement values with little dispersion. If not, both parameters will show larger scattering. In the case of benzenediamide (BDA), di- and tribenzenediamide (DBDA, TBDA) the dispersion in the conductance-displacement plot increases with the number of benzene units. It is a somehow intuitive result, because a longer junction can have a wider range of tilt angle (Figure 1.28).

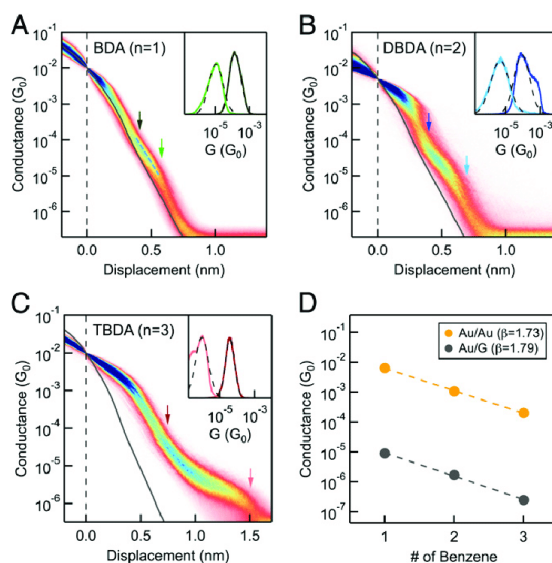


Figure 1.28. 2D Conductance-displacement histograms for A) BDA, B) DBDA and C) TBDA. The dependency of the conductance with the length of the chain is shown in D.<sup>174</sup>

More subtle features can be inferred considering the correlation between conductance plateaus. For example, the molecular junction plateau is usually observed in the same trace as the gold nanowire plateau. Thus, these two events are intimately related. First the gold nanowire is created and right after breaking, the molecule jumps into the gap.

If a molecule shows different conductance plateaus and are observed at the same time, a reasonable model may be that the molecule slightly changes its conformation during the retraction of the electrode. Otherwise, two completely independent peaks for the same molecule can

be related with two different spin states or two different anchoring groups, ruling out the possibility of molecular conformational changes.

To build up the conductance histograms (Figure 1.27 and Figure 1.28) the number of times every conductance value appears in a current trace that presents a conductance plateau is recorded. To do so, it is necessary to define what can be considered as a plateau. This seemingly innocent definition hides a possible big human bias. For very long and very different conductance plateaus, an easy consensus can be achieved. Nevertheless, when the conductance plateaus are close to each other it may be possible to consider them as a single broad conductance peak or several smaller ones. Even more: how long a conductance plateau must be to be considered as a genuine molecular plateau?

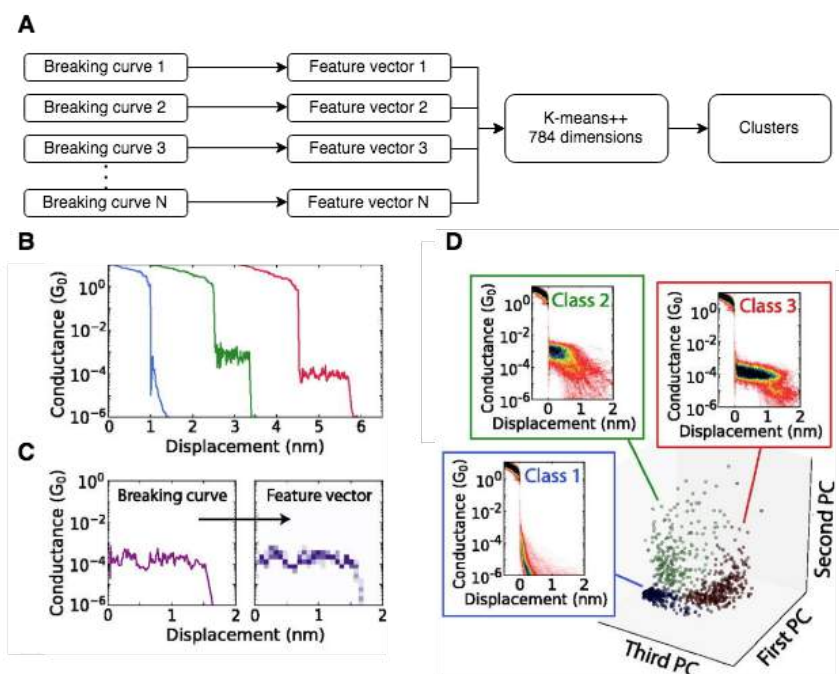


Figure 1.29. A) Schematic of the K-means algorithm B) Conductance traces of OPE3 C) Transformation of the breaking trace into individual 2D histogram D) Reduced feature space using principal component analysis (PCA). Adapted figure.<sup>158</sup>



## 1 Introduction

In order to reduce the human bias, machine-learning methods have proliferated recently.<sup>175–178</sup> They are usually based on the K-means method (Figure 1.29), in which a number of clusters parameter is chosen and the different conductance plateaus are sorted into those clusters.

Although in machine-learning methods the number of parameters subject to the human bias is largely reduced, the number of clusters considered is still a human choice and critical for the posterior analysis.

### 1.2.5 Eutectic Gallium Indium electrode (EGaIn)

Self-assembled monolayer (SAM) devices are a very good approximation to actual molecular devices. In the previous sections, techniques focused on the study of single molecule devices have been discussed. To measure the conductance of a thin-film as a whole with low defects and in a non-invasive way, it is needed to create a top electrode that is able to adapt its shape to the topological characteristics of a molecular layer.

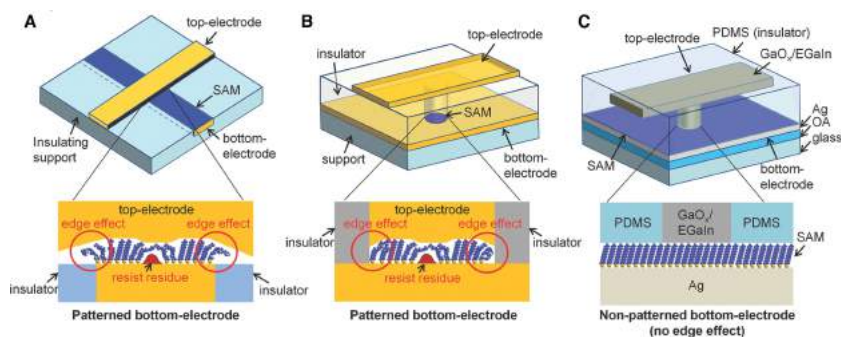


Figure 1.30. A) Crossbar configuration B) micro/nanopore configuration C) EGaIn electrode.<sup>179</sup>

Intuitively, the use of Hg as a top electrode seems an excellent choice because a liquid metal can adapt to any shape the SAM may have. In fact, the Hg-drop technique has been employed successfully but has certain drawbacks, for instance, Hg can filter through the SAM short-circuiting the junction.<sup>180–183</sup> Thus, the yield of successful junctions is low.

Other approaches relying on crossbar (Figure 1.30A) or nano/micropore (Figure 1.30B) configurations require patterning of the bottom electrode. Nonetheless, the use of patterned electrodes requires a photoresist that may contaminate the sample. Plus, the edges of the electrodes can hinder the packing of the SAM.<sup>184–187</sup>

Nijhuis and Whitesides presented a new top-electrode based on the use of non-Newtonian liquid-metal  $\text{GaO}_x/\text{EGaIn}$  stabilised in a microfluidic-based device (Figure 1.30C).<sup>179</sup> Unlike Hg, EGaIn forms a self-limiting 0.7 nm thickness layer of  $\text{GaO}_x$  in air, preventing the formation of alloys with the bottom electrode. A detailed description of the construction of the EGaIn electrode can be found in Nijhuis work.

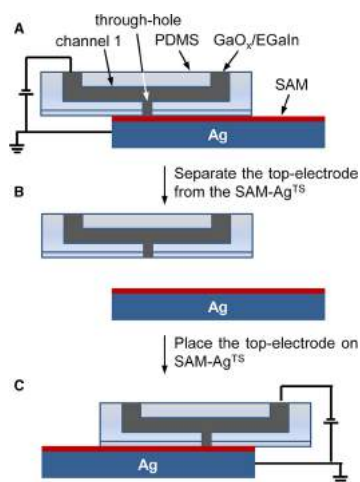


Figure 1.31. Formation of reversible contacts with  $\text{GaO}_x/\text{EGaIn}$  electrode on a SAM.<sup>179</sup>

$\text{GaO}_x/\text{EGaIn}$  electrode forms a reversible contact with the substrate via Van der Waals interactions (Figure 1.31). When the junction is set, current density curves ( $J(V)$ ) are run. Up to 15–25 different junctions with around 78% of successful junctions (non short-circuited) with a single  $\text{GaO}_x/\text{EGaIn}$  electrode can be built. Even more, excellent electrical stability is achieved and thousands of  $J(V)$  curves can be performed in a single junction.

### 1.2.6 Conducting Atomic Force Microscopy (C-AFM)

Atomic Force Microscope (AFM) was developed by Binnig, Quate and Gerber in 1986.<sup>188</sup> Nowadays this technique is widely employed to obtain high-resolution images of a large variety of materials from solid-state systems to biomolecules.<sup>189,190</sup> Similar to STM images, where the current is used as a feedback to place the tip into a certain distance of the surface, AFM uses the deflection of a cantilever when interacting with a surface as it passes through the topography. The deflection is controlled reflecting a laser on the cantilever and checking the reflected ray over a photodiode (Figure 1.32).

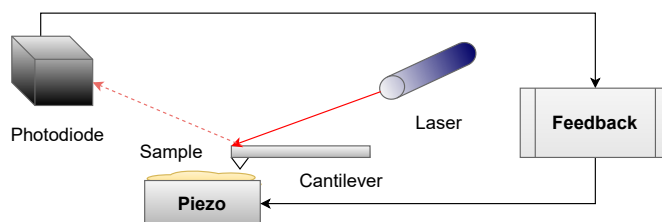


Figure 1.32. Scheme of an Atomic Force Microscope. Adapted figure.<sup>191</sup>

Electrical feedback is used to control a piezo, which maintains a constant cantilever deflection and hence, a constant force. Usually, contact mode is used to record the topology of hard surfaces. Soft materials, however, can be easily damaged because of the applied load and usually an intermittent contact (or *tapping*) mode is preferred.

While the cantilever is following the topology of the surface in contact mode, it is possible to record the current in the range of nA or even pA. This makes possible the correlation between topology and current images (Figure 1.33). Thereafter,  $I(V)$  curves can be recorded over a selected area, in contrast to EGAIn top electrode where large ensembles of molecules are contacted. Notice that in C-AFM images the magnitude of the current is not of fundamental interest, since it can be modulated by the force

applied during the topology measurement. Plus, the current strongly depends on contact area,<sup>192</sup> which is most of the times difficult to estimate, and tip contamination.<sup>193</sup>

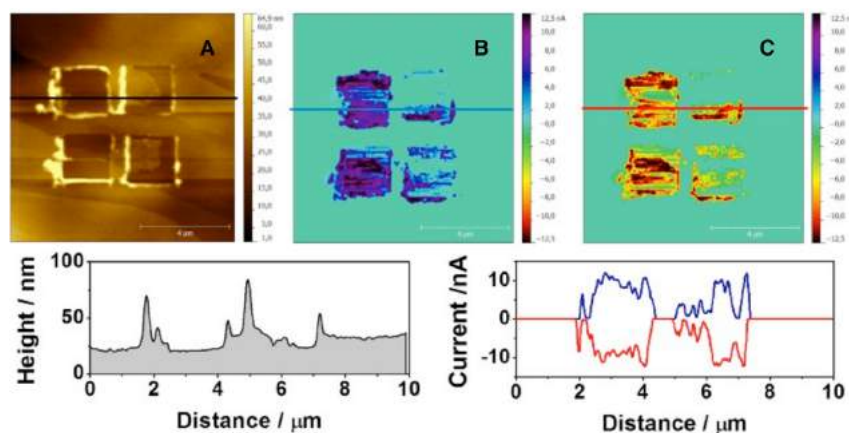


Figure 1.33. A) Topology image of aryl diazonium salts on HOPG. The image shows four scratched squares with the AFM tip to obtain uncovered HOPG, as shown in the section line. C-AFM current images obtained under 0.5 V (B) and -0.5 V (C) show higher conductance on the scratched areas (uncovered HOPG) and very low conductance on the covered regions,<sup>194</sup>

### 1.3 Landauer Formalism

In the next two sections, it will be mathematically described how an electron travelling from a source electrode can go through the molecular junction and be transmitted to the drain electrode in a coherent regime.<sup>195–197</sup> To this end, concepts from scattering theory will be used and will be related to the Green's function formalism. To make it accessible, only the highlights will be reviewed keeping the underlying physical concepts as simple as possible.

# 1 Introduction

---

## 1.3.1 Previous considerations

As announced in section 1.1.1, the electron will be strictly treated as a wave and travelling in an elastic tunnelling regime. This corresponds to large  $E-E_F$ . Further approximations needed are:

1. As Aviram and Ratner imagined, a nanoscale junction sandwiched between two electrodes, each open to a reservoir of electrons, will be employed.
2. Existing an ideal steady state of the current is assumed (1.5).

$$\langle \hat{I} \rangle_t = \text{Tr}\{\hat{\rho}_S(t)\hat{I}\} \rightarrow \text{Tr}\{\hat{\rho}_S^{SS}\hat{I}\} = \langle \hat{I} \rangle = \text{constant} \quad 1.5$$

Where  $\hat{\rho}_S$  is the density matrix written in the Schrödinger picture.

3. The “openness” of the system is replaced by scattering boundary conditions. The open system is transformed in a closed by infinite quantum system composed of the sample sandwiched between two leads (Figure 1.34).

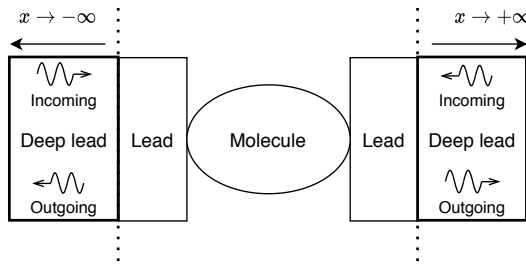


Figure 1.34. Scheme of the system in the Landauer Formalism.

4. The Hamiltonian can be written within the mean-field approximation. This approximation will be revisited in section 1.4.
5. Independent conduction channels. That is, electrons are assumed to be in a pure state. In the left/right reservoirs, electrons are in a

local equilibrium corresponding to a Fermi-Dirac distribution (1.6).

$$f_{L(R)}(E) = \frac{1}{e^{(E-\mu_{L(R)})/k_B T} + 1} \quad 1.6$$

Hence, if  $|\Psi^{L(R)}$  are electrons injected from the left (right) it is possible to write the statistical operator in 1.5 as

$$\hat{\rho}_S^{SS} = \sum_L |\Psi^L\rangle f_L \langle \Psi^L| + \sum_R |\Psi^R\rangle f_R \langle \Psi^R| \quad 1.7$$

### 1.3.2 Definition of the isolated electrodes

It will be assumed that electrons travel only along the x direction and are confined in the y-z directions (Figure 1.34). The Hamiltonian for left and right leads is

$$H_L = -\frac{\hbar^2}{2m} \nabla^2 + V_L(r_\perp) \quad 1.8$$

$$H_R = -\frac{\hbar^2}{2m} \nabla^2 + V_R(r_\perp) \quad 1.9$$

Where  $V(r_\perp)$  corresponds to a single-particle potential that confines electrons in the transverse direction of the propagation. The solutions of 1.8 and 1.9 have the form

$$\psi_{\alpha k}(r) = \sqrt{\frac{1}{L_x}} u_\alpha(r_\perp) e^{ikx} \quad -\infty < k < \infty \quad 1.10$$

## 1 Introduction

---

In equation **1.10**,  $u_\alpha(\mathbf{r}_\perp)$  is the transverse wavefunction. Along the  $x$  direction the electron behaves as a plane wave.  $L_x$  is just a normalisation length. These states satisfy the continuum orthonormality condition:

$$\langle \psi_{\alpha k}(r) | \psi_{\alpha' k'}(r) \rangle = \frac{2\pi}{L_x} \delta(k' - k) \delta_{\alpha\alpha'} \quad 1.11$$

### 1.3.3 Scattering in the nanojunction

When the full system is considered (Figure 1.34), the Hamiltonian is

$$\left[ -\frac{\hbar^2}{2m} \nabla^2 + V(r) \right] \Psi_{\alpha k}(r) = E \Psi_{\alpha k}(r) \quad 1.12$$

$\Psi_{\alpha k}$  in the nanojunction can have a very complicated form. However, it is expected that deep into the electrodes  $x \rightarrow \pm\infty$ ,  $\Psi_{\alpha k}$  must be somehow related with that shown in equation **1.10**. Lets imagine a right-moving electron from deep into the left lead. When the electron hits the nanojunction, part of the wave is reflected and scattered into the left lead. The rest is scattered and transmitted deep into the right electrode. Thus it is possible to write  $\Psi_{\alpha k}$  as

$$\Psi_{ik_i}(r) \rightarrow \sum_{f=1}^{N_e^R} \mathcal{T}_{if} \psi_{fk_f}(r) \quad x \rightarrow +\infty \quad 1.13$$

$$\Psi_{ik_i}(r) \rightarrow \psi_{ik_i}(r) + \sum_{f=1}^{N_e^L} \mathcal{R}_{if} \psi_{fk_f}(r) \quad x \rightarrow -\infty \quad 1.14$$

The subscript  $i$  is used for incoming states and  $f$  to the outgoing states. An incoming state is a wave that travels towards the nanojunction. Waves travelling away of the nanojunction are named outgoing states. Incoming states in the left lead have positive momentum  $+\hbar k_i$  while outgoing states have negative momentum  $-\hbar k_f$ . The opposite signs are used for the right lead, in which the same reasoning can be done for left moving electrons. Hence, deep into the electrodes the asymptotic form of the wavefunction is a linear combination of outgoing states with complex coefficients  $\mathcal{T}_{if}$  and  $\mathcal{R}_{if}$ .

### 1.3.4 Total current

The average current state by a single channel in the nanojunction is expressed as

$$\begin{aligned}
 I(E_i) &= e \langle \Psi_{ik_i} | \hat{I} | \Psi_{ik_i} \rangle = e \text{Tr} \{ \hat{\rho}_S^{ss} \hat{I} \} = \\
 &= \frac{e\hbar}{i2m} \int_{-\infty}^{\infty} dy \int_{-\infty}^{\infty} dz \left[ \Psi_{ik_i}^*(r) \frac{\partial \Psi_{ik_i}(r)}{\partial x} - \Psi_{ik_i} \frac{\partial \Psi_{ik_i}^*(r)}{\partial x} \right]
 \end{aligned} \tag{1.15}$$

As it was referred before,  $\Psi_{ik_i}$  has a complicated form. Luckily, as it is assumed ideal steady state (1.5), the current measured in a random pair of points in the system must be the same regardless of the chosen points. Hence, the current is calculated, for example, deep into the right electrode. Since independent channels are assumed, the total current is the sum of the individual current of all channels. Therefore, it is needed to multiply by the density of states  $D_i(E_i)$  of the system and integrate over the all the range of energies.

For a one-dimensional problem (electrons are chosen to move strictly along x axis), the density of states per spin is simply



$$D_i(E_i) = \frac{L_x}{2\pi\hbar v_i(k_i)} \quad 1.16$$

Then, the total current is calculated using **1.7**, **1.13**, **1.14** (for the right electrode), **1.15** and **1.16**

$$\begin{aligned} I &= 2e \int dE D_i(E_i) \text{Tr}\{\hat{\rho}_S^{ss} \hat{I}\} = \\ &= 2e \int dE \left\{ \sum_L^{N_e^L} D_L(E_L) f_L \langle \Psi_L | \hat{I} | \Psi_L \rangle + \sum_R^{N_e^R} D_R(E_R) f_R \langle \Psi_R | \hat{I} | \Psi_R \rangle \right\} \\ &= 2e \int dE \left\{ \sum_{i=1}^{N_e^L} \sum_{f=1}^{N_e^R} D_i(E_i) f_L T_{if} \frac{v_i}{L_x} \right. \\ &\quad \left. - \sum_{i=1}^{N_e^R} D_i(E_i) f_R \frac{v_i}{L_x} \left[ 1 - \sum_{f=1}^{N_e^R} R_{if}(E_i) \right] \right\} \quad 1.17 \\ &= \frac{e}{\hbar\pi} \int dE (f_L - f_R) \sum_{i=1}^{N_e^L} \sum_{f=1}^{N_e^R} T_{if} = \frac{e}{\hbar\pi} \int_{-\infty}^{\infty} dE (f_L - f_R) T(E) \end{aligned}$$

Where it was defined  $T_{if} = |\mathcal{T}_{if}|^2 \frac{v_f(E_i)}{v_i(E_i)}$  and  $R_{if} = |\mathcal{R}_{if}|^2 \frac{v_f(E_i)}{v_i(E_i)}$ . Notice that to write the last equality, it was considered that the transmission from left to right must be equal to the transmission from right to left:  $T_{LR}(E) = T_{RL}(E) = T(E)$ . An expression for the current is given in Equation **1.17**. Nevertheless,  $T(E)$  obviously depends on the molecule in the nanojunction. In the following, the discussion will turn to obtain an expression to  $T(E)$ .

### 1.3.5 Green's function operator as a propagator

From the general theory of differential equations, a Green's function is a function that solves the Schrödinger equation such as

$$\left(i\hbar \frac{\partial}{\partial t} - \widehat{H}_S\right) \widehat{G}^{\pm}(t - t_0) = \widehat{1}\delta(t - t_0) \quad 1.18$$

With formal solutions

$$\begin{aligned} \widehat{G}^+(t - t_0) &= -\frac{i}{\hbar} e^{-\frac{i\widehat{H}_S t}{\hbar}} & \widehat{G}^-(t - t_0) &= 0 & t - t_0 > 0 \\ \widehat{G}^+(t - t_0) &= 0 & \widehat{G}^-(t - t_0) &= \frac{i}{\hbar} e^{-\frac{i\widehat{H}_S t}{\hbar}} & t - t_0 < 0 \end{aligned} \quad 1.19$$

The Green's function works as a propagator of a state vector over time in the way

$$\begin{aligned} |\Psi(t)\rangle &= i\hbar \widehat{G}^+(t - t_0) \Psi(t_0)\rangle & t - t_0 > 0 \\ |\Psi(t)\rangle &= -i\hbar \widehat{G}^-(t - t_0) \Psi(t_0)\rangle & t - t_0 < 0 \end{aligned} \quad 1.20$$

where  $\widehat{G}^+(t)$  is the retarded Green's function and propagates the state vector into the future after  $t_0$ .  $\widehat{G}^-(t)$  is the advanced Green's function and backtracks the state vector to a time before  $t_0$ . Notice the pole of the function at  $t = 0$ . The Green's function associated with Hamiltonian  $\widehat{H}_S$  can be related to a free Hamiltonian  $\widehat{H}_0$  (without scattering because of potential  $\widehat{V}$ ) using the well-known Lippmann-Schwinger relation:

## 1 Introduction

---

$$\begin{aligned}
 \hat{G}^\pm(t - t_0) &= \hat{G}_0^\pm(t - t_0) + \int_{t_0}^t dt' \hat{G}_0^\pm(t - t') \hat{V} \hat{G}^\pm(t' - t_0) \\
 &= \hat{G}_0^\pm(t - t_0) + \int_{t_0}^t dt' \hat{G}^\pm(t - t') \hat{V} \hat{G}_0^\pm(t' - t_0)
 \end{aligned}
 \tag{1.21}$$

As it can be seen, equation 1.21 is recursive. If the series expansion converge, it is possible to condense it all as

$$\begin{aligned}
 \hat{G}^\pm(t - t_0) &= \hat{G}_0^\pm(t - t_0) + \\
 &+ \int_{t_0}^t dt' \int_{t_0}^{t'} dt'' \hat{G}_0^\pm(t - t') \hat{\Sigma}^\pm(t' - t'') \hat{G}^\pm(t'' - t_0)
 \end{aligned}
 \tag{1.22}$$

This equation is known as the Dyson equation. Notwithstanding, in the mean-field approximation:  $\hat{\Sigma}^\pm(t' - t'') = \hat{V} \delta(t' - t'')$ . Hence, the Dyson equation is identical to the Lippmann-Schwinger equation. This will not be further true when many-body interactions are taken into account (section 1.4).

Equations 1.19 can be Fourier transformed as

$$\hat{G}^\pm(E) = \frac{\hat{1}}{E \pm i\varepsilon - \hat{H}_S}
 \tag{1.23}$$

In which  $\varepsilon$  is an infinitesimal number needed to get around the pole at  $t = 0$ . Similarly, for equation 1.22

$$\hat{G}^\pm(E) = \frac{\hat{1}}{E \pm i\varepsilon - \hat{H}_0 - \Sigma^\pm(E)}
 \tag{1.24}$$

The eigenstates of  $\widehat{H}_S$  satisfy the resolution of the identity. Thus, the spectral representation of the Green's function **1.23** is

$$\widehat{G}^\pm(z) = \sum_{E_i, \alpha} \frac{|\Psi_{E_i, \alpha}\rangle \langle \Psi_{E_i, \alpha}|}{z - E_i} + \sum_{\alpha} \int_0^{\infty} dE \frac{|\Psi_{E, \alpha}\rangle \langle \Psi_{E, \alpha}|}{z - E} \quad 1.25$$

The spectral representation is a clear link between the wavefunction of the system of interest and the Green's function. Furthermore, note that the local density of states is

$$\begin{aligned} D(r, E) &= \langle r | \widehat{D}(E) | r \rangle = i \lim_{\varepsilon \rightarrow 0} \left\langle r \left| \frac{\widehat{G}^+(E) - \widehat{G}^-(E)}{2\pi} \right| r \right\rangle = \\ &= -\frac{1}{\pi} \text{Im}[G^+(r, r, E)] \end{aligned} \quad 1.26$$

Which is an ingredient needed for calculating the total current **1.17**.

### 1.3.6 Partition of the system

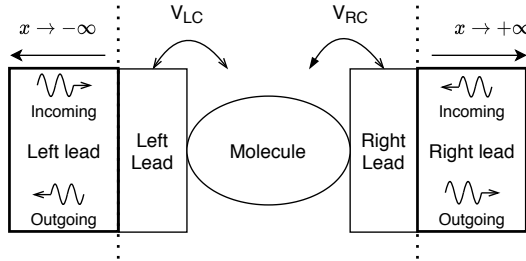


Figure 1.35. Partition of the system. The central region is coupled to the electrodes but no direct interaction is considered between both leads.

If a partition like the one shown in Figure 1.35 is considered, the Schrödinger equation can be written in matrix form such as

$$\begin{bmatrix} \hat{H}_L & \hat{V}_{LC} & 0 \\ \hat{V}_{LC}^\dagger & \hat{H}_C & \hat{V}_{CR}^\dagger \\ 0 & \hat{V}_{CR} & \hat{H}_R \end{bmatrix} \begin{bmatrix} |\phi_L\rangle \\ |\phi_C\rangle \\ |\phi_R\rangle \end{bmatrix} = E \begin{bmatrix} |\phi_L\rangle \\ |\phi_C\rangle \\ |\phi_R\rangle \end{bmatrix} \quad 1.27$$

Solving the system of equations produces

$$[E - \hat{H}_C - \hat{V}_{LC}^\dagger \hat{G}_L(z) \hat{V}_{LC} - \hat{V}_{CR}^\dagger \hat{G}_R(z) \hat{V}_{CR}] |\phi_C\rangle = 0 \quad 1.28$$

As it was done for equation 1.18, for 1.28 it can be written

$$\hat{G}(z) = \frac{\hat{1}}{E - \hat{H}_C - \hat{\Sigma}_L(z) - \hat{\Sigma}_R(z)} \quad 1.29$$

Where it was defined  $\hat{\Sigma}_L(z) = \hat{V}_{LC}^\dagger \hat{G}_L(z) \hat{V}_{LC}$  and  $\hat{\Sigma}_R(z) = \hat{V}_{CR}^\dagger \hat{G}_R(z) \hat{V}_{CR}$ . If  $\hat{\Sigma}_{L,R}(z)$  is split into its real and imaginary parts

$$\hat{G}(z) = \frac{\hat{1}}{E - \hat{H}_C - \text{Re}[\hat{\Sigma}_L(E) + \hat{\Sigma}_R(E)] - i\text{Im}[\hat{\Sigma}_L(E) + \hat{\Sigma}_R(E)]} \quad 1.30$$

The density of states 1.26 is

$$D_i(E) = \frac{2}{\pi\Gamma(E)} \frac{(\Gamma(E)/2)^2}{(E - E_i - \text{Re}[\Sigma_L(E) + \Sigma_R(E)])^2 + (\Gamma(E)/2)^2} \quad 1.31$$

With  $\Gamma(E) = \Gamma_L(E) + \Gamma_R(E)$  and  $\Gamma_{L,R}(E) = -2\text{Im}[\Sigma_{L,R}(E)]$ .

Equation 1.31 has a Lorentzian shape with the eigenvalues of the isolated molecular Hamiltonian  $\hat{H}_C$  shifted by  $\text{Re}[\hat{\Sigma}_L(E) + \hat{\Sigma}_R(E)]$  and broadened at half maximum by  $\Gamma(E)$ , a result expected in section 1.1.1. Even more, if  $\Gamma(E) \rightarrow 0$  then  $D_i(E) \rightarrow \delta(E - E_i)$ , which is the picture imagined in Figure 1.1, left.

### 1.3.7 Landauer Formula

In sections 1.3.5 and 1.3.6 the Green's functions were introduced. In a similar fashion as that used to obtain equation **1.17** from the wavefunctions of the isolated electrodes (**1.10**) and the full system (in fact, the asymptotic forms **1.13** and **1.14**), it is possible to obtain an expression for  $T(E)$  from the Green's function of the isolated electrodes and the asymptotic form of the full system Green's function.

The retarded Green's function in the position basis of the isolated lead can be obtained from the spectral representation **1.25** and the wavefunction **1.10**.

$$G_{L,R}^+(r, r', E) \equiv G_0^+(r, r', E) = \frac{1}{i\hbar} \sum_{\alpha} u_{\alpha}^*(r_{\perp}) \frac{e^{ik_{\alpha}|x-x'|}}{v_{\alpha}(k_{\alpha})} u_{\alpha}(r'_{\perp}) \quad \mathbf{1.32}$$

From scattering theory, the position representation of the Lippmann-Schwinger equation for a scattered wavefunction is

$$\Psi_{ik_i}^+(r) = \psi_{ik_i}(r) + \int dr' G_0^+(r, r', E) V(r') \Psi_{ik_i}^+(r') \quad \mathbf{1.33}$$

Working out equations **1.32** and **1.33**, it can be rewritten equations **1.13** and **1.14** from deep into the left and right leads as

$$\Psi_{i,L}^+(r) \rightarrow \begin{cases} \psi_{ik_i}(r) + \sum_{f=1}^{N_e^L} r_{if} \sqrt{\frac{|v_i|}{|v_f|}} \psi_{fk_f}(r), & x \rightarrow -\infty \\ \sum_{f=1}^{N_e^R} \tau_{if} \sqrt{\frac{|v_i|}{|v_f|}} \psi_{fk_f}(r), & x \rightarrow +\infty \end{cases} \quad \mathbf{1.34}$$

$$\Psi_{i,R}^+(r) \rightarrow \begin{cases} \sum_{f=1}^{N_e^L} \tilde{t}_{if} \sqrt{\frac{|v_i|}{|v_f|}} \psi_{fk_f}(r), & x \rightarrow -\infty \\ \psi_{i(-k_i)}(r) + \sum_{f=1}^{N_e^R} \tilde{r}_{if} \sqrt{\frac{|v_i|}{|v_f|}} \psi_{fk_f}(r), & x \rightarrow +\infty \end{cases} \quad 1.35$$

The transmission  $T(E)$  defined in **1.17** is now redefined as

$$T(E) = \sum_{i=1}^{N_e^L} \sum_{f=1}^{N_e^R} T_{if} = \sum_{i=1}^{N_e^L} \sum_{f=1}^{N_e^R} \tau_{if} \tau_{if}^* = \text{Tr}[\tau\tau^\dagger] \quad 1.36$$

If a point  $r_L$  sufficiently deep into the left electrode and an equivalent point  $r_R$  in the right electrode are taken into account, the Green's function that propagates an electron from left to right electrode  $G^+(r_R, r_L, E)$  can be calculated using the spectral representation **1.25** and equations **1.34** and **1.35**.

$$G^+(r_R, r_L, E) = - \sum_{i=1}^{N_e^L} \sum_{f=1}^{N_e^R} \frac{i}{\hbar \sqrt{v_i v_f}} u_f^*(r_{\perp,R}) \tau_{if} u_i(r_{\perp,L}) e^{i(k_i x_L - k_f x_R)} \quad 1.37$$

The transmission amplitude  $\tau_{if}$  can be obtained inverting **1.37**

$$\tau_{if} = i \hbar \sqrt{v_i v_f} \int dr_{\perp,L} \int dr_{\perp,R} u_f^*(r_{\perp,R}) G^+(r_R, r_L, E) u_i(r_{\perp,L}) \quad 1.38$$

Combining **1.36** and **1.38**

$$\begin{aligned}
 T(E) &= Tr[\tau\tau^\dagger] = \\
 &= \int dr_{\perp,L} \int dr_{\perp,R} \int dr'_{\perp,L} \int dr'_{\perp,R} \Gamma_R(r'_{\perp,R}, r_{\perp,R}) G^+(r_{\perp,R}, r_{\perp,L}, E) \times \\
 &\quad \times \Gamma_L(r_{\perp,L}, r'_{\perp,L}) G^-(r'_{\perp,L}, r'_{\perp,R}, E)
 \end{aligned} \tag{1.39}$$

where it was defined  $\Gamma_R(r'_{\perp,R}, r_{\perp,R}) = \sum_{f=1}^{N_R^e} u_f(r'_{\perp,R}) \hbar v_f u_f^*(r_{\perp,R})$  and  $\Gamma_L(r_{\perp,L}, r'_{\perp,L}) = \sum_{i=1}^{N_L^e} u_i(r_{\perp,L}) \hbar v_i u_i^*(r'_{\perp,L})$ .

Finally, if a discrete-space representation is used, equation 1.39 is

$$T(E) = T_{LR} = T_{RL} = Tr[\hat{\Gamma}_R G^+ \hat{\Gamma}_L G^-] = Tr[\hat{\Gamma}_L G^+ \hat{\Gamma}_R G^-] \tag{1.40}$$

Known as the Caroli formula.<sup>198,199</sup> Substituting 1.40 into 1.17 we get

$$I = \frac{e}{\hbar\pi} \int_{-\infty}^{\infty} dE (f_L - f_R) Tr[\hat{\Gamma}_R G^+ \hat{\Gamma}_L G^-] \tag{1.41}$$

Which is the Landauer formula, valid for single electrons travelling in a mean-field potential.<sup>200</sup>

## 1.4 Green's function formalism

Within the Landauer formalism, electron transport is treated as a steady-state phenomenon happening at equilibrium and picturing electrons moving in a mean-field potential (section 1.3.1). Although a big piece of the physics are understood with this simple image, the electron transport is intrinsically a non-equilibrium phenomenon. Moreover, electrons are actually interacting in a many-body potential. To take into account many-body effects, switching into to second-quantisation formulation of the



## 1 Introduction

---

wavefunction is convenient. In the following discussion, these two approximations considered in the Landauer approach will be overcome.

### 1.4.1 Equilibrium Green's function

Before heading the non-equilibrium problem, the equilibrium assumption will be kept and introduced the many-body interactions in the nanojunction. The leads are limited to the mean-field approximation; otherwise no closed form of the Green's function can be obtained.

The many-body equilibrium Green's function is defined as

$$\begin{aligned}
 G(r, t; r', t') &= -\frac{i}{\hbar} \langle T[\hat{\psi}_H(r, t)\hat{\psi}_H^\dagger(r', t')] \rangle = \\
 &= -\frac{i}{\hbar} Tr\{\hat{\rho}_c^{eq} T[\hat{\psi}_H(r, t)\hat{\psi}_H^\dagger(r', t')]\}
 \end{aligned}
 \tag{1.42}$$

Where  $T[\dots]$  is the time-ordering operator that sorts the field operators earlier in time to the right. For fermions (electrons) it is

$$\begin{aligned}
 T[\hat{\psi}_H(r, t)\hat{\psi}_H^\dagger(r', t')] &= \\
 &= \theta(t - t')\hat{\psi}_H(r, t)\hat{\psi}_H^\dagger(r', t') - \theta(t' - t)\hat{\psi}_H^\dagger(r', t')\hat{\psi}_H(r, t)
 \end{aligned}
 \tag{1.43}$$

The many-body Green's function is no longer a Green's function in the mathematical sense (1.18) except for the free-particle case.<sup>195</sup> Other useful Green's functions are defined as

$$\begin{aligned}
G^+(r, t; r', t') &= -\frac{i}{\hbar} \theta(t - t') \langle [\hat{\psi}_H(r, t), \hat{\psi}_H^\dagger(r', t')] \rangle \\
G^-(r, t; r', t') &= \frac{i}{\hbar} \theta(t' - t) \langle [\hat{\psi}_H(r, t), \hat{\psi}_H^\dagger(r', t')] \rangle \\
G^<(r, t; r', t') &= \frac{i}{\hbar} \langle \hat{\psi}_H^\dagger(r', t') \hat{\psi}_H(r, t) \rangle \\
G^>(r, t; r', t') &= -\frac{i}{\hbar} \langle \hat{\psi}_H(r, t) \hat{\psi}_H^\dagger(r', t') \rangle
\end{aligned} \tag{1.44}$$

Which are, in order, the retarded, advanced, lesser and greater many-body equilibrium Green's functions that are related via

$$G^+ - G^- = G^> - G^< \tag{1.45}$$

The equilibrium Green's function formalism is formally equivalent to the Landauer approach, except that the Dyson equation 1.22 is now holding the many-body interactions in the nanojunction. Equations 1.26, 1.40 and 1.41 are valid under the equilibrium approximation. In the next section the non-equilibrium is introduced via time-dependent perturbation theory.

### 1.4.2 Non-equilibrium Green's function

The time-dependent perturbation of the electrodes is introduced adiabatically for  $t > t_0$  so that the total Hamiltonian is

$$\hat{H}(t) = \hat{H}_0 + \hat{H}'(t) \tag{1.46}$$

Assuming the system is in global canonical equilibrium at initial time  $t = t_0$ , the canonical statistical operator is

## 1 Introduction

$$\hat{\rho}(\leq t_0) = \frac{e^{-\hat{H}_0/k_B T}}{Z_C} \equiv \hat{\rho}_C^{eq} \quad 1.47$$

Within these considerations, the expectation value of an operator written in the Heisenberg picture is, similarly to **1.15**

$$\langle \hat{A}_H(t) \rangle = Tr\{\hat{\rho}_C^{eq} \hat{A}_H\} = \frac{Tr\{e^{-\hat{H}_0/k_B T} \hat{U}(t_0, t) \hat{A}_H \hat{U}(t, t_0)\}}{Tr\{e^{-\hat{H}_0/k_B T}\}} \quad 1.48$$

Notice that  $\hat{\rho}_C^{eq}$  can be reinterpreted as the evolution operator of the system from time  $t_0$  to complex time  $t_0 - i\hbar/k_B T$ ,  $\hat{U}(t_0 - i\hbar/k_B T, t_0)$ . Thus, **1.48** can be understood as the propagation of the system in a time contour from  $t_0$  to  $t$ , then going back from  $t$  to  $t_0$  and finally moving to complex time  $t_0 - i\hbar/k_B T$  (Figure 1.36).

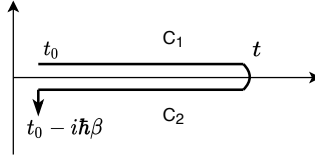


Figure 1.36. Time contour to evaluate the expectation value of an operator. This contour is also known as the Keldysh contour.

Then, the operator  $\hat{A}_H(t)$  can be written as the contour time ordering

$$\hat{A}_H(t) = T_C \left\{ \exp \left[ -\frac{i}{\hbar} \int_C dt' \hat{H}_{H_0}(t') \right] \hat{A}_{H_0}(t) \right\} \quad 1.49$$

Where  $C$  is the piece of the contour  $t_0 \rightarrow t \rightarrow t_0$  (Figure 1.36).

Since **1.49** is written in the equilibrium Hamiltonian  $H_0$ , many-body perturbation techniques can be applied. In such time-dependent perturbation the non-equilibrium effects are introduced.

Likewise for the equilibrium case (1.42), the contour ordered non-equilibrium Green's function is defined as

$$\begin{aligned}
 G(r, t; r', t') &= -\frac{i}{\hbar} \langle T_C [\hat{\psi}_H(r, t) \hat{\psi}_H^\dagger(r', t')] \rangle = \\
 &= -\frac{i}{\hbar} Tr \{ \hat{\rho}(t = t_0) T [\hat{\psi}_H(r, t) \hat{\psi}_H^\dagger(r', t')] \}
 \end{aligned}
 \tag{1.50}$$

Other Green's functions definitions in reference to Figure 1.36

$$G(r, t; r', t') = \begin{cases} G^C(r, t; r', t'), & t, t' \in C_1 \\ G^>(r, t; r', t'), & t \in C_2, t' \in C_1 \\ G^<(r, t; r', t'), & t \in C_1, t' \in C_2 \\ G^{\bar{C}}(r, t; r', t'), & t, t' \in C_2 \end{cases}
 \tag{1.51}$$

Where the new  $G^C$  and  $G^{\bar{C}}$  are the contour-ordered and anti-contour ordered Green's function. Retarded and advanced Green's function in 1.44 and the relation 1.45 can be used as well.

The Dyson equation 1.22 for non-equilibrium is now transformed to

$$\begin{aligned}
 G(1; 1') &= G_0(1; 1') + \int_{C'} d2 G(1; 2) H'(2) G_0(2; 1') + \\
 &+ \int_{\bar{C}} d2 \int_{\bar{C}} d3 G(1; 2) \Sigma(2; 3) G_0(3; 1')
 \end{aligned}
 \tag{1.52}$$

To compact the notation,  $n = r_n, t_n$  was defined. Contour  $C$  runs along the whole contour (Figure 1.36) and  $C'$  along the real time axis  $t_0 \rightarrow t \rightarrow t_0$ . Analogous definitions of  $G$  are applicable to  $\Sigma$  (1.51). To calculate the transport properties, the same partition of the system employed in the Landauer approach (section 1.3.6) is used but, this time introducing the interaction of the electrodes after  $t_0$  (Figure 1.37).

## 1 Introduction

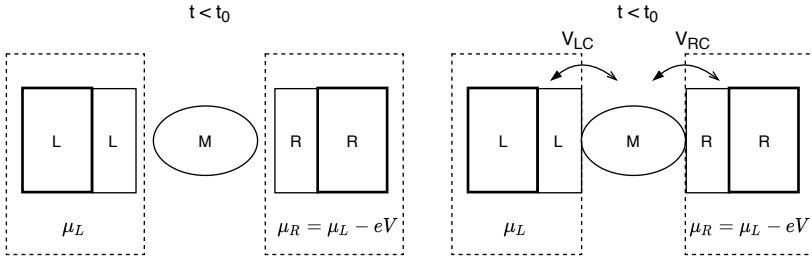


Figure 1.37. Scheme of the system in which the perturbation of the system is turned on after  $t_0$ .

The full Hamiltonian of the partition is

$$\hat{H} = \hat{H}_L + \hat{H}_R + \hat{H}_C + \hat{V}_{LC} + \hat{V}_{RC} + \hat{V}_{LC}^\dagger + \hat{V}_{RC}^\dagger \quad 1.53$$

The isolated leads lesser Green's function is considered under a mean-field potential in equilibrium. From 1.44 the Fourier transform expressed in an eigenfunction basis is

$$g_{L(R),k}^<(E) = 2\pi f_{L(R)}(E)\delta(E - E_{L(R),k}) \quad 1.54$$

For convenience, the current will be defined as the expectation value of the rate of change of the total number operator in the left electrode

$$I_L = -e \left\langle \frac{d\hat{N}_L}{dt} \right\rangle = -\frac{ie}{\hbar} \langle [\hat{H}, \hat{N}_L] \rangle = \frac{-ie}{\hbar} \langle [\hat{V}_{LC} + \hat{V}_{LC}^\dagger, \hat{N}_L] \rangle \quad 1.55$$

Replacing in 1.55 the definition of the operator  $\hat{V}_{LC} = \sum_{nk,L} V_{nk,L} \hat{a}_{k,L}^\dagger \hat{c}_n$  and  $\hat{N}_L = \sum_{k,L} \hat{a}_{k,L}^\dagger \hat{a}_{k,L}$  gives

$$I_L = \frac{2ie}{\hbar} \text{Re} \left( \sum_{nk,L} V_{nk,L} \langle \hat{a}_{k,L}^\dagger(t') \hat{c}_n(t) \rangle \right) \quad 1.56$$

Where  $\hat{a}_{k,L}^\dagger$  is the creation operator in the lead and  $\hat{c}_n$  is the annihilation operator in the central region. Plus, it can be defined  $G_{nk,L}^<(t - t') = \frac{i}{\hbar} \langle \hat{a}_{k,L}^\dagger(t') \hat{c}_n(t) \rangle$ . Fourier transforming **1.56**

$$I_L = \frac{2e}{\hbar} \int \frac{dE}{2\pi} \text{Re} \left( \sum_{nk,L} V_{nk,L} G_{nk,L}^<(E) \right) \quad 1.57$$

After a long derivation, starting from the equation of motion of  $G_{nk,L}^<(t - t')$ , defining the contour-ordered version of  $G_{nk,L}^<$  and obtaining the lesser Green's function from the correct segments of the contour (Haug and Jauho)<sup>201</sup> one finds

$$G_{nk,L}^<(E) = \sum_m V_{mk,L}^* [G_{nm}^+(E) g_{k,L}^< + G_{nm}^+(E) g_{k,L}^-] \quad 1.58$$

Where  $n$  and  $m$  states are arbitrary states of the central region and  $k$  are states from the left lead.

Defining the matrix

$$\Gamma_L = \{\Gamma_L(E_k)\}_{mn} = 2\pi \sum_L D_L(E_k) V_{n,L}(E_k) V_{L,m}^*(E_k) \quad 1.59$$

And introducing **1.58** into **1.57** produces

$$I_L = \frac{ie}{\hbar} \int \frac{dE}{2\pi} \text{Tr} \{ \Gamma_L(E) [G^<(E) + f_L(E)(G^+(E) - G^-(E))] \} \quad 1.60$$

With the lesser, retarded and advanced Green's function single-particle Green's function of the central region in the presence of the leads. The same procedure can be done for the right electrode.

## 1 Introduction

---

In an ideal steady state,  $I_L = -I_R$ . The symmetrised version of the current  $I = (I_L - I_R)/2$  is finally

$$I_L = 2 \frac{ie}{2\hbar} \int \frac{dE}{2\pi} \text{Tr}\{[\Gamma_L(E) - \Gamma_R(E)]G^<(E) + [f_L(E)\Gamma_L(E) - f_R(E)\Gamma_R(E)](G^+(E) - G^-(E))\} \quad 1.61$$

In which the factor of 2 appears for spin degeneracy.

Note that, comparing **1.61** and **1.41**, in the presence of interactions, and taking into account the non-equilibrium nature of electron transport, the concept of transmission is lost. Furthermore, the Green's functions involved are generally not known.

Despite the effort to obtain a very fine description of current in the non-equilibrium Green's function formalism, whenever the Green's functions are calculated within the mean-field approximation, the Landauer formula **1.41** can be recovered from equation **1.61**.

## 1.5 Computational flow charts

In the last sections, three different approaches to calculate the current of a nanojunction were discussed. Figure 1.38 summarizes the main constrictions when calculating electronic properties.

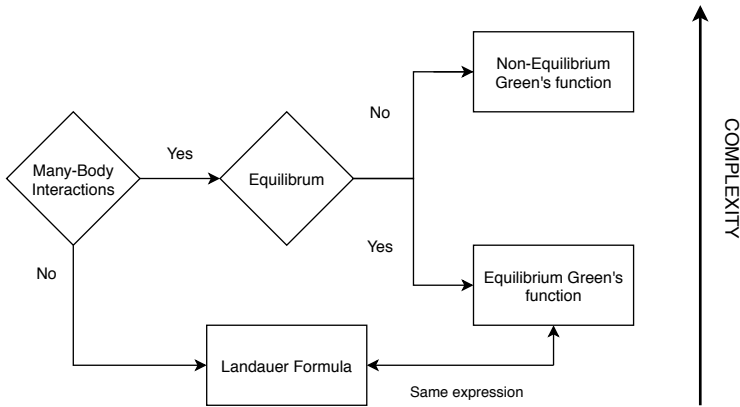


Figure 1.38. Flow chart summary of the three main approaches to calculate electron transport properties.

Essentially, to compute the current of a nanojunction the Hamiltonian and overlap matrix of the isolated leads ( $H_{L(R)}, S_{L(R)}$ ) and the nanojunction ( $H_{\text{junc}}, S_{\text{junc}}$ ) are needed (Figure 1.39). Luckily, there are many codes that provide the electronic structure compatible with electronic transport codes. Among those, SIESTA,<sup>202,203</sup> ATK,<sup>204</sup> FHI-AIMS<sup>205</sup> and ADF<sup>206</sup> are widely employed. These four packages have a native module to calculate electrical properties ( $\Sigma_{L(R)}, \Gamma_{L(R)}, G_{\text{junc}}, T(E), I$ ). SIESTA/TranSIESTA<sup>207</sup> and ATK calculate the electronic structure with LDA and GGA functionals, and the transport properties can be modelled within the NEGF formalism. It is possible to include the Hubbard correction to amend self-interaction error. Hybrid functionals are included in FHI-AIMS and ADF quantum codes. Nonetheless, transport calculations are restricted to zero voltage in FHI-AIMS/AITRANS<sup>208–210</sup> and the self-energies of the electrodes are calculated within the wide-band limit (WBL) in ADF. This approximation assumes that the density of states of gold in approximately constant in the surroundings of the Fermi energy (1.26).



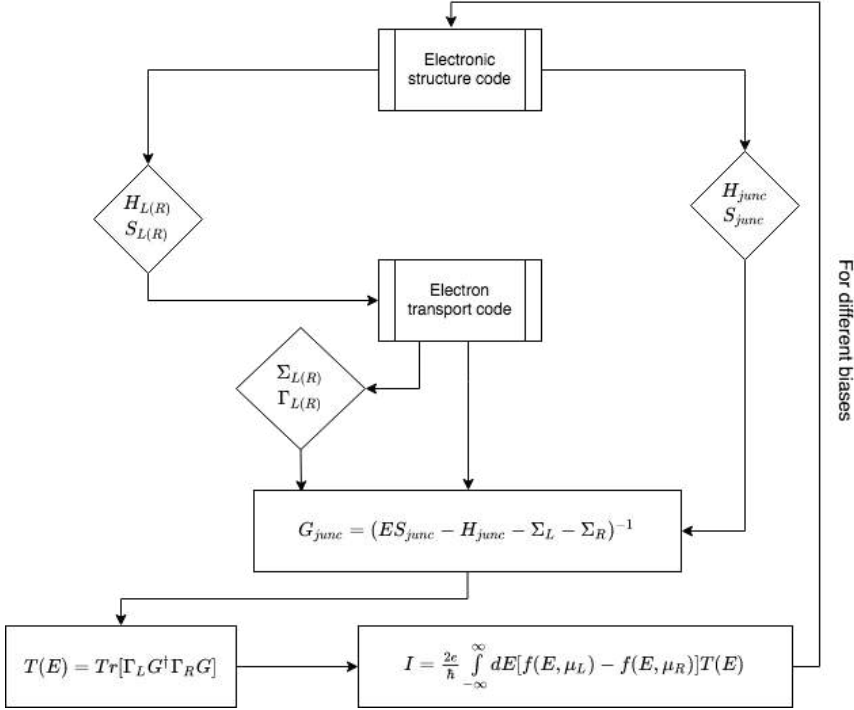


Figure 1.39. Flowchart to calculate the electron transport in a nanojunction.

Post-processing tools as GOLLUM<sup>211</sup> and ARTAIOS<sup>212,213</sup> produce excellent results and open the range of quantum codes. Gollum obtains the transport properties within the EGF formalism and is compatible with Wannier90,<sup>214</sup> Castep,<sup>215</sup> VASP,<sup>216–218</sup> ABINIT,<sup>219,220</sup> Quantum Espresso<sup>221</sup> and SIESTA. ARTAIOS permits the use of hybrid functionals being compatible with Gaussian<sup>222</sup> and ADF. In this case, the transmission is obtained at zero voltage and within the WBL approximation.

Although many-body interactions and non-equilibrium can be included in the calculations, the electronic structure of the leads and nanojunction are most of the time calculated within the mean-field approximation. Many-body interactions can be introduced via GW approximation,<sup>223</sup> but this procedure is still too costly for taking them into account in a regular basis. Hence, the current is *de facto* restricted to the Landauer formula (1.41).

## 1.6 References

- 1 Gordon E. Moore, *Electronics* **1965**, *38*, 114.
- 2 M. M. Waldrop, *Nature* **2016**, *530*, 144.
- 3 A. Chen, J. Hutchby, V. V. Zhirnov, G. Bourianoff, *Emerging Nanoelectronic Devices*, John Wiley & Sons Ltd, **2015**.
- 4 R. Feynman, in *Feynman Comput.*, **2018**, pp. 63–76.
- 5 R. M. Metzger, *J. Mater. Chem.* **2008**, *18*, 4364.
- 6 L. Sun, Y. A. Diaz-Fernandez, T. A. Gschneidtner, F. Westerlund, S. Lara-Avila, K. Moth-Poulsen, *Chem. Soc. Rev.* **2014**, *43*, 7378.
- 7 D. Xiang, X. Wang, C. Jia, T. Lee, X. Guo, *Chem. Rev.* **2016**, 4318.
- 8 A. Aviram, M. A. Ratner, *Chem. Phys. Lett.* **1974**, *29*, 277.
- 9 F. L. Carter, *Molecular Electronic Devices I*, M. Dekker, **1982**.
- 10 F. L. Carter, *Molecular Electronic Devices II*, M. Dekker, **1987**.
- 11 C. J. Lambert, *Chem. Soc. Rev.* **2015**, *44*, 875.
- 12 S. Schmaus, A. Bagrets, Y. Nahas, T. K. Yamada, A. Bork, M. Bowen, E. Beaupair, F. Evers, W. Wulfhekel, *Nat. Nanotechnol.* **2011**, *6*, 185.
- 13 L. Bogani, W. Wernsdorfer, *Nat. Mater.* **2008**, *7*, 179.
- 14 I. Zutic, J. Fabian, S. Das Sarma, *Rev. Mod. Phys.* **2004**, *76*, 323.
- 15 S. Sanvito, *Chem. Soc. Rev.* **2011**, *40*, 3336.
- 16 S. Fusil, V. Garcia, A. Barthelemy, M. Bibes, *Annu. Rev. Mater. Res.* **2014**, *44*, 91.
- 17 C. Joachim, J. K. Gimzewski, R. R. Schlittler, C. Chavy, *Phys. Rev. Lett.* **1995**, *74*, 2102.
- 18 A. S. Martin, J. R. Sambles, G. J. Ashwell, *Phys. Rev. Lett.* **1993**, *70*, 218.
- 19 R. M. Metzger, B. Chen, U. Höpfner, M. V. Lakshmikantham, D. Vuillaume, T. Kawai, X. Wu, H. Tachibana, T. V. Hughes, H. Sakurai, J. W. Baldwin, C. Hosch, M. P. Cava, L. Brehmer, G. J.

- Ashwell, *J. Am. Chem. Soc.* **1997**, *119*, 10455.
- 20 B. Xu, N. J. Tao, *Science* **2003**, *301*, 1221.
- 21 C. K. Ober, *J. Am. Chem. Soc.* **1998**, *120*, 2693.
- 22 J. E. Mark, Ed. , *Physical Properties of Polymers Handbook*, Springer, **2007**.
- 23 A. Buckley, Ed. , *Organic Light-Emitting Diodes (OLEDs)*, Woodhead Publishing, **2013**.
- 24 K. C. Chun, H. Zhao, J. D. Harms, T. H. Kim, J. P. Wang, C. H. Kim, *IEEE J. Solid-State Circuits* **2013**, *48*, 598.
- 25 C. Bi, N. Sato, S. X. Wang, in *Adv. Non-Volatile Mem. Storage Technol.*, **2019**, pp. 203–235.
- 26 L. Chua, *Appl. Phys. A Mater. Sci. Process.* **2011**, *102*, 765.
- 27 P. Pfeiffer, I. L. Egusquiza, M. DI Ventra, M. Sanz, E. Solano, *Sci. Rep.* **2016**, *6*, 29507.
- 28 K. Roy, A. Jaiswal, P. Panda, *Nature* **2019**, *575*, 607.
- 29 Y. Wang, G. Wang, Y. Shen, H. H. C. Iu, *Circuits, Syst. Signal Process.* **2020**, *39*, 3496.
- 30 C. Merkel, D. Kudithipudi, in *Proc. IEEE Comput. Soc. Annu. Symp. VLSI, ISVLSI*, **2014**, pp. 77–82.
- 31 J.-P. Launay, M. Verdaguer, *Electrons in Molecules*, Oxford University Press, **2014**.
- 32 I. Bâldea, Ed. , *Molecular Electronics: An Experimental and Theoretical Approach*, Jenny Stanford Publishing, **2016**.
- 33 J. C. Cuevas, E. Scheer, *Molecular Electronics: An Introduction to Theory and Experiment*, World Scientific Publishing Company Pte Limited, **2010**.
- 34 B. Song, D. A. Ryndyk, G. Cuniberti, *Phys. Rev. B - Condens. Matter Mater. Phys.* **2007**, *76*, 45408.
- 35 M. H. Hettler, W. Wenzel, M. R. Wegewijs, H. Schoeller, *Phys. Rev. Lett.* **2003**, *90*, 4.

- 36 E. Bonet, M. M. Deshmukh, D. C. Ralph, *Phys. Rev. B - Condens. Matter Mater. Phys.* **2002**, *65*, 1.
- 37 B. Muralidharan, A. W. Ghosh, S. Datta, *Phys. Rev. B - Condens. Matter Mater. Phys.* **2006**, *73*, 155410.
- 38 M. L. Perrin, E. Burzurí, H. S. J. Van Der Zant, *Chem. Soc. Rev.* **2015**, *44*, 902.
- 39 D. M. Guldi, H. Nishihara, L. Venkataraman, *Chem. Soc. Rev.* **2015**, *44*, 842.
- 40 D. K. James, J. M. Tour, *Top. Curr. Chem.* **2005**, *257*, 33.
- 41 M. Magoga, C. Joachim, *Phys. Rev. B - Condens. Matter Mater. Phys.* **1997**, *56*, 4722.
- 42 M. Magoga, C. Joachim, *Phys. Rev. B - Condens. Matter Mater. Phys.* **1998**, *57*, 1820.
- 43 H. J. Lee, S. J. Cho, H. Kang, X. He, H. J. Yoon, *Small* **2021**, *17*, 2005711.
- 44 Y. S. Wu, Y. C. Lin, S. Y. Hung, C. K. Chen, Y. C. Chiang, C. C. Chueh, W. C. Chen, *Macromolecules* **2020**, *53*, 4968.
- 45 J. Y. Back, H. Yu, I. Song, I. Kang, H. Ahn, T. J. Shin, S. K. Kwon, J. H. Oh, Y. H. Kim, *Chem. Mater.* **2015**, *27*, 1732.
- 46 A. Omidvar, A. Mohajeri, *J. Mol. Liq.* **2020**, *312*, 113403.
- 47 P. B. Shea, L. R. Pattison, M. Kawano, C. Chen, J. Chen, P. Petroff, D. C. Martin, H. Yamada, N. Ono, J. Kanicki, *Synth. Met.* **2007**, *157*, 190.
- 48 R. R. Burch, Y. H. Dong, C. Fincher, M. Goldfinger, P. E. Rouviere, *Synth. Met.* **2004**, *146*, 43.
- 49 A. Liess, L. Huang, A. Arjona-Esteban, A. Lv, M. Gsänger, V. Stepanenko, M. Stolte, F. Würthner, *Adv. Funct. Mater.* **2015**, *25*, 44.
- 50 W. Xu, Y. He, I. Murtaza, D. Zhang, A. Li, Z. Hu, X. Zeng, Y. Guo, Y. Zhu, M. Liu, H. Meng, *J. Mater. Chem. C* **2017**, *5*, 2852.
- 51 M. L. Perrin, E. Galán, R. Eelkema, J. M. Thijssen, F. Grozema, H.

- S. J. Van Der Zant, *Nanoscale* **2016**, *8*, 8919.
- 52 B. Capozzi, J. Xia, O. Adak, E. J. Dell, Z. F. Liu, J. C. Taylor, J. B. Neaton, L. M. Campos, L. Venkataraman, *Nat. Nanotechnol.* **2015**, *10*, 522.
- 53 L. Yuan, R. Breuer, L. Jiang, M. Schmittel, C. A. Nijhuis, *Nano Lett.* **2015**, *15*, 5506.
- 54 X. Chen, M. Roemer, L. Yuan, W. Du, D. Thompson, E. Del Barco, C. A. Nijhuis, *Nat. Nanotechnol.* **2017**, *12*, 797.
- 55 S. Jan Van Der Molen, P. Liljeroth, *J. Phys. Condens. Matter* **2010**, *22*, 133001.
- 56 S. Lara-Avila, A. Danilov, V. Geskin, S. Bouzakraoui, S. Kubatkin, J. Cornil, T. Bjørnholm, *J. Phys. Chem. C* **2010**, *114*, 20686.
- 57 E. Ruiz, *Phys. Chem. Chem. Phys.* **2014**, *16*, 14.
- 58 M. A. Halcrow, *Spin-Crossover Materials: Properties and Applications*, Wiley, Chichester, **2013**.
- 59 F. Prins, M. Monrabal-Capilla, E. A. Osorio, E. Coronado, H. S. J. van der Zant, *Adv. Mater.* **2011**, *23*, 1545.
- 60 T. Miyamachi, M. Gruber, V. Davesne, M. Bowen, S. Boukari, L. Joly, F. Scheurer, G. Rogez, T. K. Yamada, P. Ohresser, E. Beaurepaire, W. Wulfhekel, *Nat. Commun.* **2012**, *3*, 938.
- 61 C. Jia, A. Migliore, N. Xin, S. Huang, J. Wang, Q. Yang, S. Wang, H. Chen, D. Wang, B. Feng, Z. Liu, G. Zhang, D. H. Qu, H. Tian, M. A. Ratner, H. Q. Xu, A. Nitzan, X. Guo, *Science* **2016**, *352*, 1443.
- 62 G. D. Harzmann, R. Frisenda, H. S. J. Van Der Zant, M. Mayor, *Angew. Chemie - Int. Ed.* **2015**, *54*, 13425.
- 63 A. Mosey, A. S. Dale, G. Hao, A. N'Diaye, P. A. Dowben, R. Cheng, *J. Phys. Chem. Lett.* **2020**, *11*, 8231.
- 64 H. B. Li, B. E. Tebikachew, C. Wiberg, K. Moth-Poulsen, J. Hihath, *Angew. Chemie - Int. Ed.* **2020**, *59*, 11641.

- 65 S. A. Wolf, D. D. Awschalom, R. A. Buhrman, J. M. Daughton, S. von Molnar, M. L. Roukes, A. Y. Chtchelkanova, D. M. Treger, *Science* **2001**, *294*, 1488.
- 66 J. Park, A. N. Pasupathy, J. I. Goldsmith, C. Chang, Y. Yalsh, J. R. Petta, M. Rinkoski, J. P. Sethna, H. D. Abruña, P. L. McEuen, D. C. Ralph, *Nature* **2002**, *417*, 722.
- 67 W. Liang, M. P. Shores, M. Bockrath, J. R. Long, H. Park, *Nature* **2002**, *417*, 725.
- 68 J. Kondo, *Prog. Theor. Phys.* **1964**, *32*, 37.
- 69 P. W. Anderson, *Phys. Rev.* **1961**, *124*, 41.
- 70 M. N. Baibich, J. M. Broto, A. Fert, F. N. Van Dau, F. Petroff, P. Eitenne, G. Creuzet, A. Friederich, J. Chazelas, *Phys. Rev. Lett.* **1988**, *61*, 2472.
- 71 G. Binasch, P. Grünberg, F. Saurenbach, W. Zinn, *Phys. Rev. B* **1989**, *39*, 4828.
- 72 R. Jansen, in *Spintron. Mater. Technol.*, **2006**, pp. 371–413.
- 73 C. Baraduc, M. Chshiev, B. Dieny, in *Smart Sensors, Meas. Instrum.*, **2013**, pp. 1–30.
- 74 G. Prenat, K. Jabeur, G. Di Pendina, O. Boulle, G. Gaudin, in *Spintron. Comput.*, **2015**, pp. 145–158.
- 75 A. Hirohata, K. Yamada, Y. Nakatani, L. Prejbeanu, B. Diény, P. Pirro, B. Hillebrands, *J. Magn. Magn. Mater.* **2020**, *509*, 166711.
- 76 H. C. Koo, S. B. Kim, H. Kim, T. E. Park, J. W. Choi, K. W. Kim, G. Go, J. H. Oh, D. K. Lee, E. S. Park, I. S. Hong, K. J. Lee, *Adv. Mater.* **2020**, *32*, 2002117.
- 77 M. Urdampilleta, S. Klyatskaya, J. P. Cleuziou, M. Ruben, W. Wernsdorfer, *Nat. Mater.* **2011**, *10*, 502.
- 78 J. Devkota, R. Geng, R. C. Subedi, T. D. Nguyen, *Adv. Funct. Mater.* **2016**, *26*, 3881.
- 79 A. C. Aragonès, D. Aravena, J. I. Cerdá, Z. Acís-Castillo, H. Li, J.

- A. Real, F. Sanz, J. Hihath, E. Ruiz, I. Díez-Pérez, *Nano Lett.* **2016**, *16*, 218.
- 80 D. Aravena, E. Ruiz, *J. Am. Chem. Soc.* **2011**, *134*, 777.
- 81 A. C. Aragonès, D. Aravena, F. J. Valverde-Muñoz, J. A. Real, F. Sanz, I. Díez-Pérez, E. Ruiz, *J. Am. Chem. Soc.* **2017**, *139*, 5768.
- 82 M. Oltscher, F. Eberle, T. Kuczmik, A. Bayer, D. Schuh, D. Bougeard, M. Ciorga, D. Weiss, *Nat. Commun.* **2017**, *8*, 1807.
- 83 Y. Sheng, T. D. Nguyen, G. Veeraraghavan, Ö. Mermer, M. Wohlgenannt, *Phys. Rev. B - Condens. Matter Mater. Phys.* **2007**, *75*, 35202.
- 84 K. Ray, S. P. Ananthavel, D. H. Waldeck, R. Naaman, *Science* **1999**, *283*, 814.
- 85 K. Michaeli, V. Varade, R. Naaman, D. H. Waldeck, *J. Phys. Condens. Matter* **2017**, *29*, 103002.
- 86 R. Naaman, C. Fontanesi, D. H. Waldeck, *Curr. Opin. Electrochem.* **2019**, *14*, 138.
- 87 R. Naaman, Y. Paltiel, D. H. Waldeck, *Nat. Rev. Chem.* **2019**, *3*, 250.
- 88 B. Göhler, V. Hamelbeck, T. Z. Markus, M. Kettner, G. F. Hanne, Z. Vager, R. Naaman, H. Zacharias, *Science* **2011**, *331*, 894.
- 89 P. C. Mondal, C. Fontanesi, D. H. Waldeck, R. Naaman, *Acc. Chem. Res.* **2016**, *49*, 2560.
- 90 A. C. Aragonès, E. Medina, M. Ferrer-Huerta, N. Gimeno, M. Teixidó, J. L. Palma, N. Tao, J. M. Ugalde, E. Giralt, I. Díez-Pérez, V. Mujica, *Small* **2017**, *13*, 1602519.
- 91 R. Torres-Cavanillas, G. Escorcia-Ariza, I. Brotons-Alcázar, R. Sanchis-Gual, P. C. Mondal, L. E. Rosaleny, S. Giménez-Santamarina, M. Sessolo, M. Galbiati, S. Tatay, A. Gaita-Ariño, A. Forment-Aliaga, S. Cardona-Serra, *J. Am. Chem. Soc.* **2020**, *142*, 17572.
- 92 G. Bullard, F. Tassinari, C. H. Ko, A. K. Mondal, R. Wang, S.

- Mishra, R. Naaman, M. J. Therien, *J. Am. Chem. Soc.* **2019**, *141*, 14707.
- 93 K. Michaeli, N. Kantor-Uriel, R. Naaman, D. H. Waldeck, *Chem. Soc. Rev.* **2016**, *45*, 6478.
- 94 W. S. Veeman, J. H. Van Der Waals, *Mol. Phys.* **1970**, *18*, 1.
- 95 S. Dalum, P. Hedegård, *Nano Lett.* **2019**, *19*, 5253.
- 96 R. Fandreyer, D. Thompson, K. Blum, *J. Phys. B At. Mol. Opt. Phys.* **1990**, *23*, 3031.
- 97 S. Yeganeh, M. A. Ratner, E. Medina, V. Mujica, *J. Chem. Phys.* **2009**, *131*, 14707.
- 98 A. M. Guo, Q. F. Sun, *Phys. Rev. Lett.* **2012**, *108*, 218102.
- 99 R. Gutierrez, E. Díaz, C. Gaul, T. Brumme, F. Domínguez-Adame, G. Cuniberti, *J. Phys. Chem. C* **2013**, *117*, 22276.
- 100 J. Gersten, K. Kaasbjerg, A. Nitzan, *J. Chem. Phys.* **2013**, *139*, 114111.
- 101 D. M. Rowe, *Thermoelectr. Handb. Macro to Nano* **2005**, *80*, 1014.
- 102 S. Hébert, D. Berthebaud, R. Daou, Y. Bréard, D. Pelloquin, E. Guilmeau, F. Gascoin, O. Lebedev, A. Maignan, *J. Phys. Condens. Matter* **2016**, *28*, 13001.
- 103 M. Rull-Bravo, A. Moure, J. F. Fernández, M. Martín-González, *RSC Adv.* **2015**, *5*, 41653.
- 104 E. S. Toberer, A. F. May, G. J. Snyder, *Chem. Mater.* **2010**, *22*, 624.
- 105 H. Kleinke, *Chem. Mater.* **2010**, *22*, 604.
- 106 J. W. G. Bos, R. A. Downie, *J. Phys. Condens. Matter* **2014**, *26*, 433201.
- 107 A. Nozariasbmarz, A. Agarwal, Z. A. Coutant, M. J. Hall, J. Liu, R. Liu, A. Malhotra, P. Norouzzadeh, M. C. Öztürk, V. P. Ramesh, Y. Sargolzaeiaval, F. Suarez, D. Vashae, *Jpn. J. Appl. Phys.* **2017**, *56*, 05DA04.
- 108 R. Freer, A. V. Powell, *J. Mater. Chem. C* **2020**, *8*, 441.



## 1 Introduction

---

- 109 M. Paulsson, S. Datta, *Phys. Rev. B - Condens. Matter Mater. Phys.* **2003**, *67*, 241403.
- 110 P. Reddy, S. Y. Jang, R. A. Segalman, A. Majumdar, *Science* **2007**, *315*, 1568.
- 111 L. Cui, R. Miao, C. Jiang, E. Meyhofer, P. Reddy, *J. Chem. Phys.* **2017**, *146*, 92201.
- 112 L. Cui, S. Hur, Z. A. Akbar, J. C. Klöckner, W. Jeong, F. Pauly, S. Y. Jang, P. Reddy, E. Meyhofer, *Nature* **2019**, *572*, 628.
- 113 C. C. Kaun, Y. C. Chen, *J. Phys. Chem. C* **2018**, *122*, 12185.
- 114 L. O. Jones, M. A. Mosquera, G. C. Schatz, M. A. Ratner, *J. Phys. Chem. B* **2019**, *123*, 8096.
- 115 N. Mosso, H. Sadeghi, A. Gemma, S. Sangtarash, U. Drechsler, C. Lambert, B. Gotsmann, *Nano Lett.* **2019**, *19*, 7614.
- 116 A. Droghetti, I. Rungger, *Phys. Chem. Chem. Phys.* **2020**, *22*, 1466.
- 117 R. Gupta, N. Kumar, P. Kaur, C. Bera, *Phys. Chem. Chem. Phys.* **2020**, *22*, 18989.
- 118 C. Evangeli, K. Gillemot, E. Leary, M. T. González, G. Rubio-Bollinger, C. J. Lambert, N. Agrait, *Nano Lett.* **2013**, *13*, 2141.
- 119 L. Rincón-García, A. K. Ismael, C. Evangeli, I. Grace, G. Rubio-Bollinger, K. Porfyrakis, N. Agrait, C. J. Lambert, *Nat. Mater.* **2016**, *15*, 289.
- 120 P. Gehring, J. K. Sowa, C. Hsu, J. de Bruijckere, M. van der Star, J. J. Le Roy, L. Bogani, E. M. Gauger, H. S. J. van der Zant, *Nat. Nanotechnol.* **2021**, *16*, 426.
- 121 T. Markussen, J. Schiötz, K. S. Thygesen, *J. Chem. Phys.* **2010**, *132*, 224104.
- 122 T. Tada, K. Yoshizawa, *ChemPhysChem* **2002**, *3*, 1035.
- 123 R. Stadler, T. Markussen, *J. Chem. Phys.* **2011**, *135*, 154109.
- 124 J. P. Bergfield, G. C. Solomon, C. A. Stafford, M. A. Ratner, *Nano Lett.* **2011**, *11*, 2759.

- 125 S. Naghibi, A. K. Ismael, A. Vezzoli, M. K. Al-Khaykane, X. Zheng, I. M. Grace, D. Bethell, S. J. Higgins, C. J. Lambert, R. J. Nichols, *J. Phys. Chem. Lett.* **2019**, *10*, 6419.
- 126 M. Baghernejad, Y. Yang, O. A. Al-Owaedi, Y. Aeschi, B. F. Zeng, Z. M. Abd Dawood, X. Li, J. Liu, J. Shi, S. Decurtins, S. X. Liu, W. Hong, C. J. Lambert, *Chem. - A Eur. J.* **2020**, *26*, 5264.
- 127 M. H. Garner, H. Li, M. Neupane, Q. Zou, T. Liu, T. A. Su, Z. Shangguan, D. W. Paley, F. Ng, S. Xiao, C. Nuckolls, L. Venkataraman, G. C. Solomon, *J. Am. Chem. Soc.* **2019**, *141*, 15471.
- 128 Y. C. Choi, W. Y. Kim, K. S. Park, P. Tarakeshwar, K. S. Kim, T. S. Kim, J. Y. Lee, *J. Chem. Phys.* **2005**, *122*, 94706.
- 129 D. Nozaki, S. M. Avdoshenko, H. Sevinçli, G. Cuniberti, *J. Appl. Phys.* **2014**, *116*, 74308.
- 130 X. Li, Z. Tan, X. Huang, J. Bai, J. Liu, W. Hong, *J. Mater. Chem. C* **2019**, *7*, 12790.
- 131 G. C. Solomon, D. Q. Andrews, T. Hansen, R. H. Goldsmith, M. R. Wasielewski, R. P. Van Duyne, M. A. Ratner, *J. Chem. Phys.* **2008**, *129*, 54701.
- 132 K. Okazawa, Y. Tsuji, K. Yoshizawa, *J. Phys. Chem. C* **2020**, *124*, 3322.
- 133 M. Camarasa-Gómez, D. Hernangómez-Pérez, M. S. Inkpen, G. Lovat, E. D. Fung, X. Roy, L. Venkataraman, F. Evers, *Nano Lett.* **2020**, *20*, 6381.
- 134 V. Fatemi, M. Kamenetska, J. B. Neaton, L. Venkataraman, *Nano Lett.* **2011**, *11*, 1988.
- 135 P. Chandra Mondal, U. M. Tefashe, R. L. McCreery, *J. Am. Chem. Soc.* **2018**, *140*, 7239.
- 136 D. C. Milan, O. A. Al-Owaedi, M. C. Oerthel, S. Marqués-González, R. J. Brooke, M. R. Bryce, P. Cea, J. Ferrer, S. J. Higgins, C. J. Lambert, P. J. Low, D. Z. Manrique, S. Martin, R. J.

- Nichols, W. Schwarzacher, V. M. García-Suárez, *J. Phys. Chem. C* **2016**, *120*, 15666.
- 137 M. Kotiuga, P. Darancet, C. R. Arroyo, L. Venkataraman, J. B. Neaton, *Nano Lett.* **2015**, *15*, 4498.
- 138 I. J. Olavarria-Contreras, M. L. Perrin, Z. Chen, S. Klyatskaya, M. Ruben, H. S. J. Van Der Zant, *J. Am. Chem. Soc.* **2016**, *138*, 8465.
- 139 Y. Sugita, A. Taninaka, S. Yoshida, O. Takeuchi, H. Shigekawa, *Sci. Rep.* **2018**, *8*, 5222.
- 140 P. Moreno-García, M. Gulcur, D. Z. Manrique, T. Pope, W. Hong, V. Kaliginedi, C. Huang, A. S. Batsanov, M. R. Bryce, C. Lambert, T. Wandlowski, *J. Am. Chem. Soc.* **2013**, *135*, 12228.
- 141 G. Gryn’Ova, C. Corminboeuf, *J. Phys. Chem. Lett.* **2018**, *9*, 2298.
- 142 C. J. Chen, *MRS Proc.* **1989**, *159*, 289.
- 143 M. Haze, H. H. Yang, K. Asakawa, N. Watanabe, R. Yamamoto, Y. Yoshida, Y. Hasegawa, *Rev. Sci. Instrum.* **2019**, *90*, 13704.
- 144 H. Zhu, F. Cui, X. Zhang, N. Ma, X. Hu, Z. Di, X. Xie, A. Li, *J. Appl. Phys.* **2019**, *126*, 75304.
- 145 P. Gehring, J. M. Thijssen, H. S. J. van der Zant, *Nat. Rev. Phys.* **2019**, *1*, 381.
- 146 C. A. Martin, D. Ding, J. K. Sørensen, T. Bjørnholm, J. M. Van Ruitenbeek, H. S. J. Van Der Zant, *J. Am. Chem. Soc.* **2008**, *130*, 13198.
- 147 M. Kamenetska, M. Koentopp, A. C. Whalley, Y. S. Park, M. L. Steigerwald, C. Nuckolls, M. S. Hybertsen, L. Venkataraman, *Phys. Rev. Lett.* **2009**, *102*, 126803.
- 148 A. Halbritter, P. Makk, S. MacKowiak, S. Csonka, M. Wawrzyniak, J. Martinek, *Phys. Rev. Lett.* **2010**, *105*, 266805.
- 149 P. Makk, D. Tomaszewski, J. Martinek, Z. Balogh, S. Csonka, M. Wawrzyniak, M. Frei, L. Venkataraman, A. Halbritter, *ACS Nano* **2012**, *6*, 3411.

- 150 A. Magyarkuti, K. P. Lauritzen, Z. Balogh, A. Nyáry, G. Mészáros, P. Makk, G. C. Solomon, A. Halbritter, *J. Chem. Phys.* **2017**, *146*, 92319.
- 151 A. Halbritter, S. Csonka, G. Mihály, E. Jurdik, O. Y. Kolesnychenko, O. I. Shklyarevskii, S. Speller, H. Van Kempen, *Phys. Rev. B - Condens. Matter Mater. Phys.* **2003**, *68*, 354171.
- 152 S. Y. Quek, L. Venkataraman, H. J. Choi, S. G. Louie, M. S. Hybertsen, J. B. Neaton, *Nano Lett.* **2007**, *7*, 3477.
- 153 P. Makk, Z. Balogh, S. Csonka, A. Halbritter, *Nanoscale* **2012**, *4*, 4739.
- 154 M. S. Inkpen, M. Lemmer, N. Fitzpatrick, D. C. Milan, R. J. Nichols, N. J. Long, T. Albrecht, *J. Am. Chem. Soc.* **2015**, *137*, 9971.
- 155 C. Huang, M. Jevric, A. Borges, S. T. Olsen, J. M. Hamill, J. T. Zheng, Y. Yang, A. Rudnev, M. Baghernejad, P. Broekmann, A. U. Petersen, T. Wandlowski, K. V. Mikkelsen, G. C. Solomon, M. Brøndsted Nielsen, W. Hong, *Nat. Commun.* **2017**, *8*, 15436.
- 156 R. Frisenda, D. Stefani, H. S. J. Van Der Zant, *Acc. Chem. Res.* **2018**, *51*, 1359.
- 157 M. Lemmer, M. S. Inkpen, K. Kornysheva, N. J. Long, T. Albrecht, *Nat. Commun.* **2016**, *7*, 12922.
- 158 D. Cabosart, M. El Abbassi, D. Stefani, R. Frisenda, M. Calame, H. S. J. Van der Zant, M. L. Perrin, *Appl. Phys. Lett.* **2019**, *114*, 143102.
- 159 J. M. Hamill, X. T. Zhao, G. Mészáros, M. R. Bryce, M. Arenz, *Phys. Rev. Lett.* **2018**, *120*, 16601.
- 160 K. P. Lauritzen, A. Magyarkuti, Z. Balogh, A. Halbritter, G. C. Solomon, *J. Chem. Phys.* **2018**, *148*, 84111.
- 161 C. A. Nijhuis, W. F. Reus, J. R. Barber, G. M. Whitesides, *J. Phys. Chem. C* **2012**, *116*, 14139.
- 162 W. Haiss, R. J. Nichols, H. van Zalinge, S. J. Higgins, D. Bethell, D. J. Schiffrin, *Phys. Chem. Chem. Phys.* **2004**, *6*, 4330.

- 163 X. D. Cui, A. Primak, X. Zarate, J. Tomfohr, O. F. Sankey, A. L. Moore, T. A. Moore, D. Gust, G. Harris, S. M. Lindsay, *Science* **2001**, *294*, 571.
- 164 J. Moreland, J. W. Ekin, *J. Appl. Phys.* **1985**, *58*, 3888.
- 165 C. J. Muller, J. M. Van Ruitenbeek, L. J. De Jongh, *Phys. Rev. Lett.* **1992**, *69*, 140.
- 166 M. A. Reed, C. Zhou, C. J. Muller, T. P. Burgin, J. M. Tour, *Science* **1997**, *278*, 252.
- 167 J. H. Tian, B. Liu, S. Jin, K. Dai, Z. Bin Chen, X. Li, H. Ke, S. T. Wu, Y. Yang, B. Ren, B. W. Mao, N. Tao, Z. Q. Tian, in *2007 7th IEEE Int. Conf. Nanotechnol. - IEEE-NANO 2007, Proc.*, **2007**, pp. 1302–1305.
- 168 T. Konishi, M. Kiguchi, M. Takase, F. Nagasawa, H. Nabika, K. Ikeda, K. Uosaki, K. Ueno, H. Misawa, K. Murakoshi, *J. Am. Chem. Soc.* **2013**, *135*, 1009.
- 169 Y. Yu, T.-H. Xiao, Y. Wu, W. Li, Q.-G. Zeng, L. Long, Z.-Y. Li, *Adv. Photonics* **2020**, *2*, 1.
- 170 M. Iwane, S. Fujii, M. Kiguchi, *Sensors (Switzerland)* **2017**, *17*, 1901.
- 171 M. L. Perrin, C. A. Martin, F. Prins, A. J. Shaikh, R. Eelkema, J. H. van Esch, J. M. van Ruitenbeek, H. S. J. van der Zant, D. Dulić, *Beilstein J. Nanotechnol.* **2011**, *2*, 714.
- 172 H. Park, A. K. L. Lim, A. P. Alivisatos, J. Park, P. L. McEuen, *Appl. Phys. Lett.* **1999**, *75*, 301.
- 173 S. V. Aradhya, M. Frei, M. S. Hybertsen, L. Venkataraman, *Nat. Mater.* **2012**, *11*, 872.
- 174 T. Kim, Z. F. Liu, C. Lee, J. B. Neaton, L. Venkataraman, *Proc. Natl. Acad. Sci. U. S. A.* **2014**, *111*, 10928.
- 175 F. Huang, R. Li, G. Wang, J. Zheng, Y. Tang, J. Liu, Y. Yang, Y. Yao, J. Shi, W. Hong, *Phys. Chem. Chem. Phys.* **2020**, *22*, 1674.
- 176 N. D. Bamberger, J. A. Ivie, K. N. Parida, D. V. McGrath, O. L.

- A. Monti, *J. Phys. Chem. C* **2020**, *124*, 18302.
- 177 A. Magyarkuti, N. Balogh, Z. Balogh, L. Venkataraman, A. Halbritter, *Nanoscale* **2020**, *12*, 8355.
- 178 B. Liu, S. Murayama, Y. Komoto, M. Tsutsui, M. Taniguchi, *J. Phys. Chem. Lett.* **2020**, *11*, 6567.
- 179 A. Wan, L. Jiang, C. S. S. Sangeeth, C. A. Nijhuis, *Adv. Funct. Mater.* **2014**, *24*, 4442.
- 180 R. L. York, P. T. Nguyen, K. Slowinski, *J. Am. Chem. Soc.* **2003**, *125*, 5948.
- 181 O. Yaffe, Y. Qi, L. Scheres, S. R. Puniredd, L. Segev, T. Ely, H. Haick, H. Zuilhof, A. Vilan, L. Kronik, A. Kahn, D. Cahen, *Phys. Rev. B - Condens. Matter Mater. Phys.* **2012**, *85*, 45433.
- 182 Y. Selzer, A. Salomon, D. Cahen, *J. Am. Chem. Soc.* **2002**, *124*, 2886.
- 183 E. A. Weiss, R. C. Chiechi, G. K. Kaufman, J. K. Kriebel, Z. Li, M. Duati, M. A. Rampi, G. M. Whitesides, *J. Am. Chem. Soc.* **2007**, *129*, 4336.
- 184 J. Cantone, Y. van Dommelen, A. Jiang, S. Dunn, T. Winter, K. Petrillo, R. Johnson, P. Lawson, W. Conley, R. Callahan, *J. Vac. Sci. Technol. B Microelectron. Nanom. Struct.* **2009**, *27*, 3014.
- 185 H. Mao, D. Wu, W. Wu, J. Xu, Y. Hao, *Nanotechnology* **2009**, *20*, 445304.
- 186 M. S. Chen, S. L. Brandow, W. J. Dressick, *Thin Solid Films* **2000**, *379*, 203.
- 187 M. Chen, S. L. Brandow, C. S. Dulcey, W. J. Dressick, G. N. Taylor, J. F. Bohland, J. H. Georger, E. K. Pavelchek, J. M. Calvert, *J. Electrochem. Soc.* **1999**, *146*, 1421.
- 188 G. Binnig, C. F. Quate, C. Gerber, *Phys. Rev. Lett.* **1986**, *56*, 930.
- 189 S. Maghsoudy-Louyeh, M. Kropf, B. R. Tittmann, *Open Neuroimag. J.* **2019**, *12*, 86.

## 1 Introduction

---

- 190 Y. Seo, W. Jhe, *Reports Prog. Phys.* **2008**, *71*, 16101.
- 191 J. M. Mativetsky, M. Palma, P. Samorì, *Top. Curr. Chem.* **2008**, *285*, 157.
- 192 A. Salomon, D. Cahen, S. Lindsay, J. Tomfohr, V. B. Engelkes, C. D. Frisbie, *Adv. Mater.* **2003**, *15*, 1881.
- 193 V. B. Engelkes, J. M. Beebe, C. D. Frisbie, *J. Phys. Chem. B* **2005**, *109*, 16801.
- 194 M. C. R. González, A. G. Orive, R. C. Salvarezza, A. H. Creus, *Phys. Chem. Chem. Phys.* **2016**, *18*, 1953.
- 195 M. Di Ventra, *Electrical Transport in Nanoscale Systems*, Cambridge University Press, **2008**.
- 196 D. Ryndyk, *Theory of Quantum Transport at Nanoscale*, Springer International Publishing, **2016**.
- 197 K. Hirose, N. Kobayashi, *Quantum Transport Calculations for Nanosystems*, Jenny Stanford Publishing, **2014**.
- 198 C. Caroli, R. Combescot, P. Nozieres, D. Saint-James, *J. Phys. C Solid State Phys.* **1971**, *4*, 916.
- 199 C. Caroli, R. Combescot, D. Lederer, P. Nozieres, D. Saint-James, *J. Phys. C Solid State Phys.* **1971**, *4*, 2598.
- 200 R. Landauer, *IBM J. Res. Dev.* **1957**, *1*, 223.
- 201 A.-P. Haug, Hartmut, Jauho, *Quantum Kinetics in Transport and Optics of Semiconductors*, Springer-Verlag Berlin Heidelberg, **2008**.
- 202 J. M. Soler, E. Artacho, J. D. Gale, A. García, J. Junquera, P. Ordejón, D. Sánchez-Portal, *J. Phys. Condens. Matter* **2002**, *14*, 2745.
- 203 A. García, N. Papior, A. Akhtar, E. Artacho, V. Blum, E. Bosoni, P. Brandimarte, M. Brandbyge, J. I. Cerdá, F. Corsetti, R. Cuadrado, V. Dikan, J. Ferrer, J. Gale, P. García-Fernández, V. M. García-Suárez, S. García, G. Huhs, S. Illera, R. Korytár, P. Koval, I. Lebedeva, L. Lin, P. López-Tarifa, S. G. Mayo, S. Mohr, P. Ordejón, A. Postnikov, Y. Pouillon, M. Pruneda, R. Robles, D.

- Sánchez-Portal, J. M. Soler, R. Ullah, V. W. Z. Yu, J. Junquera, *J. Chem. Phys.* **2020**, *152*, 204108.
- 204 S. Smidstrup, T. Markussen, P. Vancraeyveld, J. Wellendorff, J. Schneider, T. Gunst, B. Verstichel, D. Stradi, P. Khomyakov, U. Vej-Hansen, M.-E. Lee, S. Chill, F. Rasmussen, G. Penazzi, F. Corsetti, A. Ojanpera, K. Jensen, M. Palsgaard, U. Martinez, K. Stokbro, *J. Phys. Condens. Matter* **2019**, *32*, 15901.
- 205 V. Blum, R. Gehrke, F. Hanke, P. Havu, V. Havu, X. Ren, K. Reuter, M. Scheffler, *Comput. Phys. Commun.* **2009**, *180*, 2175.
- 206 G. te Velde, F. M. Bickelhaupt, E. J. Baerends, C. Fonseca Guerra, S. J. A. van Gisbergen, J. G. Snijders, T. Ziegler, *J. Comput. Chem.* **2001**, *22*, 931.
- 207 M. Brandbyge, J. L. Mozos, P. Ordejon, J. Taylor, K. Stokbro, *Phys. Rev. B* **2002**, *65*, 165401.
- 208 A. Arnold, F. Weigend, F. Evers, *J. Chem. Phys.* **2007**, *126*, 174101.
- 209 J. Wilhelm, M. Walz, M. Stendel, A. Bagrets, F. Evers, *Phys. Chem. Chem. Phys.* **2013**, *15*, 6684.
- 210 A. Bagrets, *J. Chem. Theory Comput.* **2013**, *9*, 2801.
- 211 J. Ferrer, C. J. Lambert, V. M. García-Suárez, D. Z. Manrique, D. Visontai, L. Oroszlany, R. Rodríguez-Ferradás, I. Grace, S. W. D. Bailey, K. Gillemot, H. Sadeghi, L. A. Algharagholy, *New J. Phys.* **2014**, *16*, 93029.
- 212 C. Herrmann, G. C. Solomon, M. A. Ratner, *J. Am. Chem. Soc.* **2010**, *132*, 3682.
- 213 C. Herrmann, G. C. Solomon, J. E. Subotnik, V. Mujica, M. A. Ratner, *J. Chem. Phys.* **2010**, *132*, 24103.
- 214 A. A. Mostofi, J. R. Yates, G. Pizzi, Y. S. Lee, I. Souza, D. Vanderbilt, N. Marzari, *Comput. Phys. Commun.* **2014**, *185*, 2309.
- 215 S. J. Clark, M. D. Segall, C. J. Pickard, P. J. Hasnip, M. I. J. Probert, K. Refson, M. C. Payne, *Zeitschrift für Krist.* **2005**, *220*, 567.



## 1 Introduction

---

- 216 G. Kresse, J. Hafner, *Phys. Rev. B* **1993**, *47*, 558.
- 217 G. Kresse, J. Furthmüller, *Phys. Rev. B - Condens. Matter Mater. Phys.* **1996**, *54*, 11169.
- 218 G. Kresse, J. Furthmüller, *Comput. Mater. Sci.* **1996**, *6*, 15.
- 219 X. Gonze, B. Amadon, G. Antonius, F. Arnardi, L. Baguet, J. M. Beuken, J. Bieder, F. Bottin, J. Bouchet, E. Bousquet, N. Brouwer, F. Bruneval, G. Brunin, T. Cavignac, J. B. Charraud, W. Chen, M. Côté, S. Cottenier, J. Denier, G. Geneste, P. Ghosez, M. Giantomassi, Y. Gillet, O. Gingras, D. R. Hamann, G. Hautier, X. He, N. Helbig, N. Holzwarth, Y. Jia, F. Jollet, W. Lafargue-Dit-Hauret, K. Lejaeghere, M. A. L. Marques, A. Martin, C. Martins, H. P. C. Miranda, F. Naccarato, K. Persson, G. Petretto, V. Planes, Y. Pouillon, S. Prokhorenko, F. Ricci, G. M. Rignanese, A. H. Romero, M. M. Schmitt, M. Torrent, M. J. van Setten, B. Van Troeye, M. J. Verstraete, G. Zérah, J. W. Zwanziger, *Comput. Phys. Commun.* **2020**, *248*, 107042.
- 220 A. H. Romero, D. C. Allan, B. Amadon, G. Antonius, T. Applencourt, L. Baguet, J. Bieder, F. Bottin, J. Bouchet, E. Bousquet, F. Bruneval, G. Brunin, D. Caliste, M. Côté, J. Denier, C. Dreyer, P. Ghosez, M. Giantomassi, Y. Gillet, O. Gingras, D. R. Hamann, G. Hautier, F. Jollet, G. Jomard, A. Martin, H. P. C. Miranda, F. Naccarato, G. Petretto, N. A. Pike, V. Planes, S. Prokhorenko, T. Rangel, F. Ricci, G. M. Rignanese, M. Royo, M. Stengel, M. Torrent, M. J. Van Setten, B. Van Troeye, M. J. Verstraete, J. Wiktor, J. W. Zwanziger, X. Gonze, *J. Chem. Phys.* **2020**, *152*, 124102.
- 221 P. Giannozzi, S. Baroni, N. Bonini, M. Calandra, R. Car, C. Cavazzoni, D. Ceresoli, G. L. Chiarotti, M. Cococcioni, I. Dabo, A. Dal Corso, S. De Gironcoli, S. Fabris, G. Fratesi, R. Gebauer, U. Gerstmann, C. Gougoussis, A. Kokalj, M. Lazzeri, L. Martin-

- Samos, N. Marzari, F. Mauri, R. Mazzarello, S. Paolini, A. Pasquarello, L. Paulatto, C. Sbraccia, S. Scandolo, G. Sclauszero, A. P. Seitsonen, A. Smogunov, P. Umari, R. M. Wentzcovitch, *J. Phys. Condens. Matter* **2009**, *21*, 395502.
- 222 M. J. Frisch, G. W. Trucks, H. B. Schlegel, G. E. Scuseria, M. A. Robb, J. R. Cheeseman, G. Scalmani, V. Barone, B. Mennucci, G. A. Petersson, H. Nakatsuji, M. Caricato, X. Li, H. P. Hratchian, A. F. Izmaylov, J. Bloino, G. Zheng, J. L. Sonnenberg, M. Hada, M. Ehara, K. Toyota, R. Fukuda, J. Hasegawa, M. Ishida, T. Nakajima, Y. Honda, O. Kitao, H. Nakai, T. Vreven, J. A. Montgomery Jr., J. E. Peralta, F. Ogliaro, M. Bearpark, J. J. Heyd, E. Brothers, K. N. Kudin, V. N. Staroverov, R. Kobayashi, J. Normand, K. Raghavachari, A. Rendell, J. C. Burant, S. S. Iyengar, J. Tomasi, M. Cossi, N. Rega, J. M. Millam, M. Klene, J. E. Knox, J. B. Cross, V. Bakken, C. Adamo, J. Jaramillo, R. Gomperts, R. E. Stratmann, O. Yazyev, A. J. Austin, R. Cammi, C. Pomelli, J. W. Ochterski, R. L. Martin, K. Morokuma, V. G. Zakrzewski, G. A. Voth, P. Salvador, J. J. Dannenberg, S. Dapprich, A. D. Daniels, Ö. Farkas, J. B. Foresman, J. V. Ortiz, J. Cioslowski, D. J. Fox, *Gaussian, Inc. Wallingford CT* **2009**.
- 223 L. Reining, *Wiley Interdiscip. Rev. Comput. Mol. Sci.* **2018**, *8*, e1344.



## 2 SUPRAMOLECULAR LANDSCAPE OF CoDPP

### 2.1 Motivation

The aim of this chapter is to find highly conductive magnetoresistance molecular junctions at room temperature. This sort of junctions is a necessity to built spin valves (section 1.1.6) based on molecular nanojunctions, which constitutes the core of spintronics.

Taking a look at section 1.1.1, reducing the parameter  $E - E_F$  and/or increasing the broadening of the molecular level  $\Gamma$  as much as possible is needed to obtain highly conductive molecular junctions. To reduce  $E - E_F$  energy difference, nanojunctions based on supramolecular interactions such as  $\pi$ - $\pi$  stacking are excellent candidates. Weak interactions do not push molecular orbitals far away from the Fermi level, thus obtaining better conductance, a priori. However, in this kind of junctions the broadening of the molecular levels is usually low. Luckily, increasing the electrode-molecule contact area and reducing the interelectrode distance, as shown in the results of this chapter, can counterbalance this.

Porphyrins have been extensively studied as molecular wires because of their high chemical stability, conjugation and very rich supramolecular

## 2 Supramolecular Landscape of CoDPP

---

chemistry.<sup>1-5</sup> Furthermore, metalloporphyrins are an amazing testbed to introduce magnetoresistance and tune the response by changing the metal centre (chapter 3). In previous studies, metalloporphyrins have been connected to metal electrodes by directly lying flat on the metal surfaces via  $\pi$  orbital interaction or by covalently anchoring the porphyrin through ring substituents,<sup>6-9</sup> obtaining conductance values of around  $10^{-5} G_0$ . In this chapter, the conductance landscape of a metalloporphyrin-based supramolecular wire under mechanical stress will be studied by systematically introducing structural changes of both the axial coordinative ligands and the porphyrin chemical substitution.<sup>9-13</sup> The axial ligands will act as anchoring groups or linkers, mimicking the common natural schemes exploited in the chemistry of photosynthetic and transmembrane electron transport.<sup>14,15</sup> Magnetoresistance of metalloporphyrins will be faced in the next chapter.

### 2.2 Previous work

In 2014, Aragonès and co-workers presented a new approach to form single molecule junctions with porphyrin molecules.<sup>16,17</sup> Essentially, they functionalised both the tip and the substrate with pyridine-4-yl-methanethiol (from now on, PyrMT) which is anchored to gold through a covalent Au-S bond. With the modified gold tip and monocrystalline Au(111) surface, they run STM-BJ experiments (section 1.2.1) on a free base porphyrin 5,15-diphenylporphyrin (DPP) with no metal centre and on Co<sup>II</sup>-5,15-diphenylporphyrin (CoDPP). In the latter case, the formation of a junction due to PyrMT-Co<sup>II</sup> coordination should be expected.

The accumulation of hundreds of STM-BJ<sup>18</sup>  $I(z)$  traces (section 1.2.4) yields the conductance histograms shown in Figure 2.1.

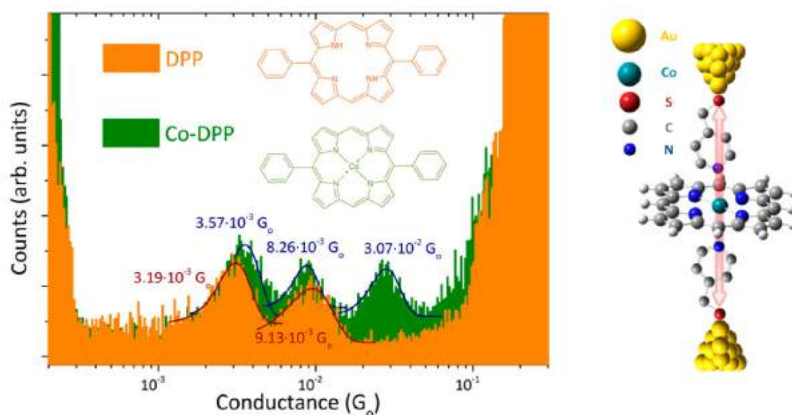


Figure 2.1. STM-BJ conductance histograms for DPP and CoDPP employing functionalised gold tip and substrate with PyrMT (left). Aragonès proposed junction for the high conductance peak (right).

Adapted figure.<sup>16</sup>

As may be observed, CoDPP and DPP share the two lowest conductance peaks at  $9 \cdot 10^{-3} G_0$  and  $3 \cdot 10^{-3} G_0$ . Strikingly, CoDPP exhibits an additional conductance peak at  $3 \cdot 10^{-2} G_0$ , presumably metal-related, 3 orders of magnitude higher than those found previously from porphyrin molecules of similar length but directly connected to the electrodes. It is worth mentioning that the three conductance signatures can be seen during the same trace, suggesting an interelectrode distance correlation between them.

It is well known that STM-BJ (*tapping*) may lead to stretch-dependent conductance because of the force applied when the tip is driven in and out of the surface.<sup>19</sup> To rule out this, and to understand the origin of the multiple conductance peaks, *blinking* experiments were carried out, which also gave insight on the lifetime of the different nanojunctions.<sup>20</sup> Figure 2.2A shows the typical *blinking* traces at different tip-surface distances. The accumulation of such traces is then plotted into 2D maps and compared to those obtained in STM-BJ mode. The conductance values obtained for medium (MC) and low conductance (LC) peaks are consistent between

## 2 Supramolecular Landscape of CoDPP

both methods for CoDPP and DPP (Figure 2.2B). Moreover, the former also presents the additional high conductance peak (HC). The absence of either the porphyrin molecule or the PyrMT linker shows no *blinking* events under the same experimental conditions.

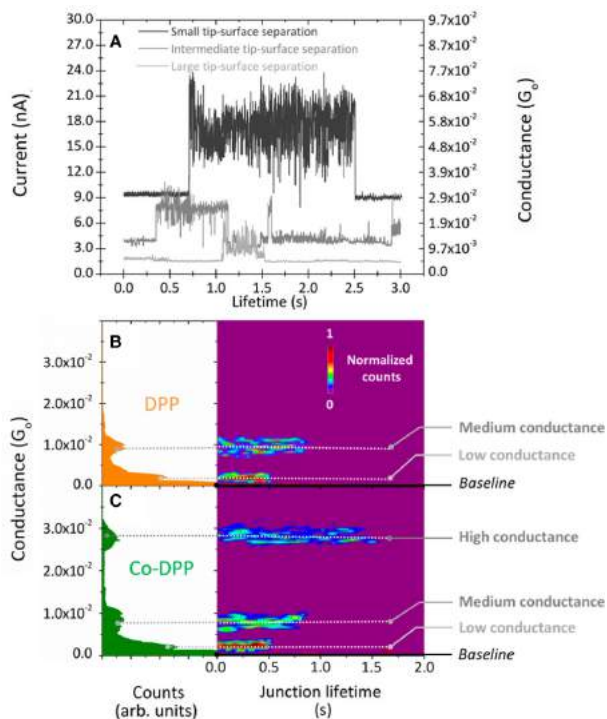


Figure 2.2. Individual *blinks* for DPP and CoDPP (A) and accumulation of *blinking* experiments (B and C).<sup>16</sup>

From the *blinking* traces (Figure 2.2A) it is readily observed that the tip-surface separation increases as the conductance diminishes. Moreover, the lifetimes of the junctions formed are larger for HC and decrease as the conductance is reduced. The existence of the HC peak in both kinds of experiments evidences that  $\text{Co}^{\text{II}}$  is involved directly in the molecular junction for that peak. These results seem to point to a hexacoordinated  $\text{Co}^{\text{II}}$  centre for the HC peak<sup>21</sup> and a stretched analogue or hydrogen bond related conformations for MC and LC peaks.

Although some theoretical efforts have been done to explain the observed experimental features, no adequate rationalisation was found.<sup>22</sup>

To gain more insight, the discussion was extended to include two new linkers: pyridine-4-yl-methanethiol (PyrMT) and 4-pyridinethiol (PyrT). Following the same procedure, the employed electrodes were functionalised *ex situ* exposing them to a 5 mM ethanolic solution of PyrT (or PyrMT) for 24h. Afterwards they were washed with ethanol and dried under an argon stream.

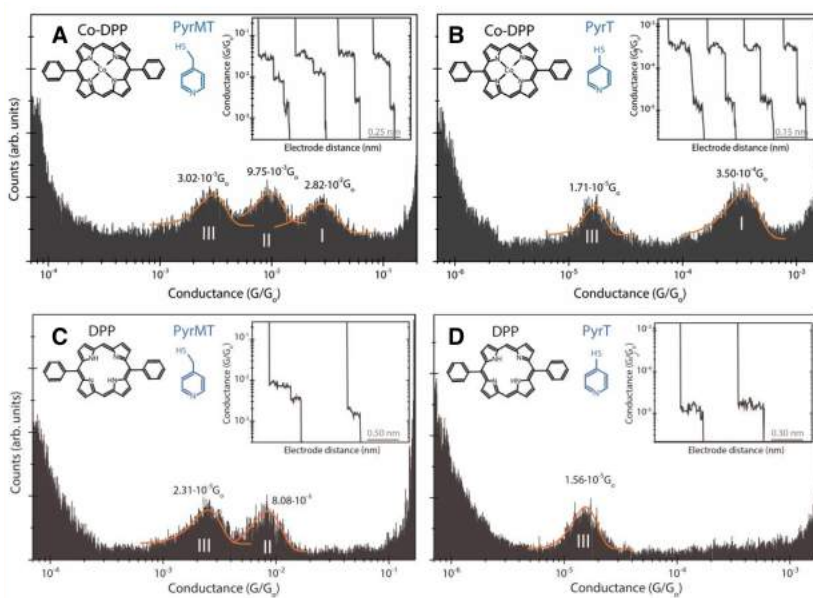


Figure 2.3. Semi-log conductance histograms for CoDPP/PyrMT function (A) and CoDPP/PyrT (B). The same experiment is performed over DPP/PyrMT (C) and DPP/PyrT (D) junctions. Insets show individual I(z) traces of the STM-BJ. These traces show strong correlation between peaks I, II and III (consecutive appearance). Adapted figure.<sup>23</sup>

Junctions of 5,15-diphenylporphyrin (DPP) and its  $\text{Co}^{\text{II}}$  analogue (CoDPP) were measured with functionalised gold tip and substrate with both linkers independently (Figure 2.3). Comparing DPP and CoDPP junctions it can be observed that peak I is missing for both linkers. Hence, the notion of a metal-dependent conductance peak is reinforced.



## 2 Supramolecular Landscape of CoDPP

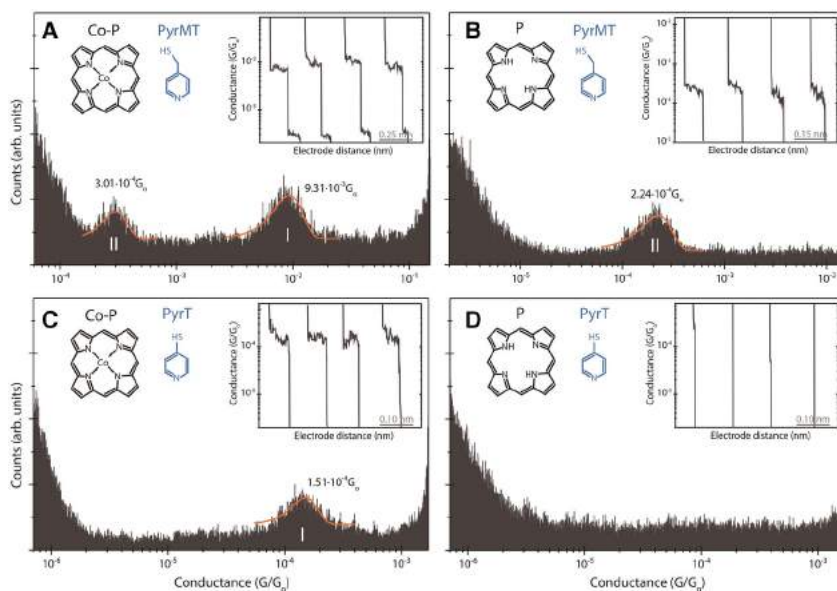


Figure 2.4. Semi-log conductance histograms for CoP/PyrMT function (A) and its free base analogue P/PyrMT (B). The same experiment is performed over CoP/PyrMT (C) and P/PyrT (D) junctions. Insets show individual  $I(z)$  traces of the STM-BJ.<sup>23</sup>

Beyond the role of  $\text{Co}^{\text{II}}$  centre and the linker employed, one last actor left is the lateral phenyl ring of DPP. This side group is capable of forming  $\pi$ - $\pi$  stacking-based nanojunctions. To obtain more information related with conductance features II and III in Figure 2.3, additional experiments were carried out on unsubstituted  $\text{Co}^{\text{II}}$  porphyrin (CoP) and its free base analogue (P) with both linkers (Figure 2.4). The elimination of the plausible phenyl ring interactions results in the removal of one conductance signature (Figure 2.3A and Figure 2.4A, for example), as observed when the tip functionalization is changed from PyrMT to PyrT (Figure 2.3A and B).

The experiments above show that CoDPP exhibits a rich supramolecular landscape of high conductance junctions ranging from  $10^{-4} G_0$  to more than  $10^{-2} G_0$ . Note, however, that the actual geometry of the nanojunction is still unknown.

## 2.3 Results

Regarding the previous work of Aragonès, a full rationalisation of the supramolecular landscape of Co<sup>II</sup>-diphenilporphyrin junction (Figure 2.5) is provided herein. Theoretical work along with experimental corroborations based on XPS and ellipsometry measurements is done.



Figure 2.5. Summary of the nanojunctions studied to resolve the supramolecular scenario of CoDPP molecular junctions.<sup>23</sup>

### 2.3.1 Computational details

The proposed nanojunctions were sandwiched between five Au layers of 5x4 surface unit cell. The electronic structure of this system was obtained with the SIESTA<sup>24,25</sup> code along with the PBE+U ( $U = 4.0$  eV)<sup>26</sup> functional. The transmission spectra was obtained by employing the GOLLUM<sup>27</sup> quantum transport code (section 1.5). To obtain the conductance values from transmission,  $G$  was computed as  $G = T(E_F)G_0$ , which is a valid approximation for small biases.<sup>28</sup>

The nanojunction geometries were optimised up to atomic forces below  $0.04$  eV/Å, the last three layers of gold electrode on both ends were only allowed to move along the axis as a rigid block. In this manner, the electrode is well described to obtain the incoming states (section 1.3.3) while optimising the interelectrode distance. Van Voorhis functional<sup>29,30</sup>

## 2 Supramolecular Landscape of CoDPP

---

was chosen to include dispersion effects and a Hubbard correction ( $U = 4.0$  eV) was added to obtain semiquantitative conductance values, which provide a better description of the frontier orbital energies.

The wavefunction was expanded using double- $\zeta$  polarised (DZP) basis set with valence pseudopotentials for all atoms, except Co, in which semicore 3p orbitals were considered. In the case of Au, the most abundant atom in the calculations, 11e<sup>-</sup> pseudopotential was used for optimisations whilst 1e<sup>-</sup> pseudopotential and single- $\zeta$  polarised (SZP) basis set were chosen in the transport calculations to manage a 21x27x1 k-point grid for the whole system and 21x27x51 for the isolated electrode.<sup>31</sup>

In the case of the optimisation of pyridine-4-yl-methanethiol (PyrMT) and 4-pyridinethiol (PyrT) on the Au(111) surface, pair dispersion models such as the van Voorhis functional fail to properly describe the system. In those cases, FHI-AIMS<sup>32</sup> was employed to compare the relative energies for lying down and standing up conformations within a many-body approach<sup>33</sup> implemented in the code using PBE functional and a tight basis set.<sup>34,35</sup>

### 2.3.2 Characterisation of functionalised electrodes

The substrate and the tip were functionalised prior to the experiments with either pyridine-4-yl-methanethiol (PyrMT) or 4-pyridinethiol (PyrT), as shown in section 2.2. In the case of PyrT on Au in ethanol, the decomposition of the monolayer has been reported under the presence of O<sub>2</sub>.<sup>36</sup> To keep the functionalised surface under anaerobic conditions, the PyrT/Ethanol solution was purged with N<sub>2</sub> and the substrate was preserved under N<sub>2</sub> and kept away of direct light exposure to avoid photo-generation of radical species.<sup>37</sup>

The X-ray photoelectron spectroscopy (XPS) data demonstrates that the procedure to build up the PyrT monolayer produces a fairly stable self-assembled monolayer when immersed overnight. As shown in Figure 2.6, there are significant amounts of N, C and S in the sample. The high-resolution scans show a 3:1 relation of S:N elements, demonstrating that although part of the monolayer may decompose, there is a significant amount of PyrT on the Au surface (Figure 2.6).

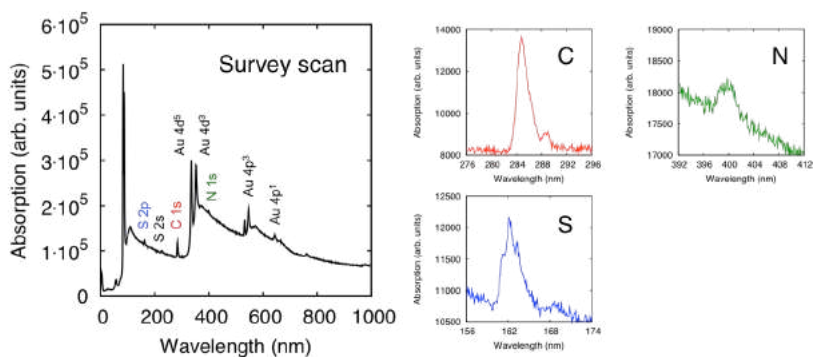


Figure 2.6. XPS characterisation of the PyrT-functionalised Au(111) surface (left) and the high-resolution scans for C, N and S elements (right).<sup>23</sup>

Further characterisation was done using ellipsometry to elucidate how PyrT and PyrMT interact with CoDPP. A solution of 3 mg of CoDPP and 2 mg of linker in 20 mL of chloroform was prepared. The solubility of CoDPP is rather low at room temperature, thus the solution was first filtered before use. After filtration, the resultant solution has a CoDPP concentration around  $1 \cdot 10^{-4}$  M. Then, a Au(111) monocrystal is dipped during 20 min and dried afterwards under dry  $N_2$ . The Au(111) monocrystal was previously cleaned under piranha solution (3:1 of  $H_2SO_4:H_2O_2$  concentrated) for three cycles of 20 minutes, rinsed with water and annealed with  $H_2$  flame.

These measurements were carried out with an alpha-SE Ellipsometer from J.A. Woollam Ellipsometry Solutions. The data was acquired within a

## 2 Supramolecular Landscape of CoDPP

wavelength range of 380-900 nm and angles of incidence of 65, 70 and 75°. The monolayers were modelled as a Cauchy optical layer with an Urbach absorption tail on a Au(111) and fitted with the CompleteEASE software to obtain the layer thickness (Figure 2.7).

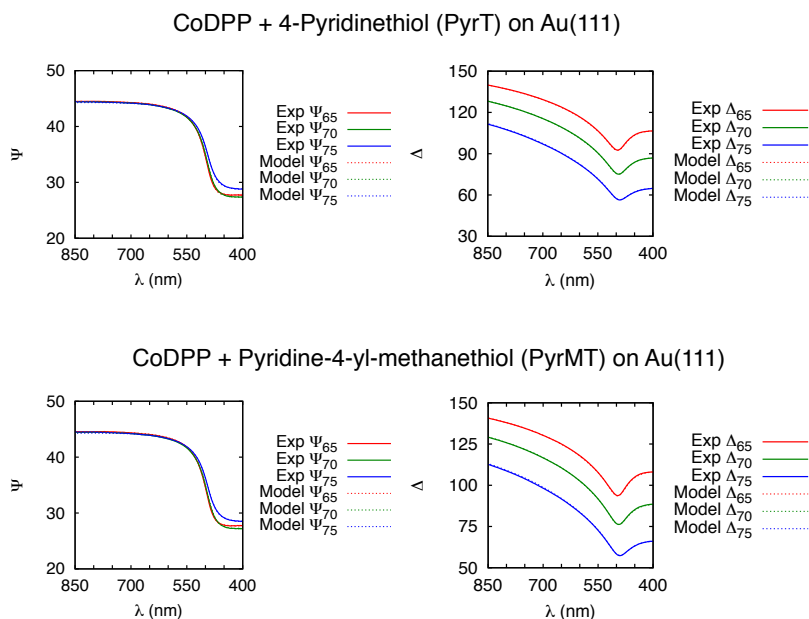


Figure 2.7. Ellipsometry data for CoDPP/PyrT (top) and CoDPP/PyrMT (bottom). Both monolayers are described as a Cauchy layer. For PyrT  $n(\lambda)=1.754 \pm 0.025$  and Urbach absorption tail of  $k = 0.202 \pm 0.008$  with  $MSE = 2.451$ . For PyrMT,  $n(\lambda)=1.516 \pm 0.042$  and  $k = 0.156 \pm 0.012$  with  $MSE = 2.889$ .<sup>23</sup>

From these experiments, a  $13.0 \pm 0.3 \text{ \AA}$  layer thickness for CoDPP/PyrT and  $11.6 \pm 0.6 \text{ \AA}$  for CoDPP/PyrMT were found. Further discussion of these results can be found in the next section.

### 2.3.3 Metal related conductance signatures

Due to the lack of direct observation of the created junctions, theoretical calculations are crucial for the complete understanding of STM-BJ experiments. The discussion in this section will be restricted to resolve a

sensible junction for peak I. Peaks II and III are common for both CoDPP and DPP, thus related with a linker/DPP interaction. These two peaks will be discussed in the next section.

As Aragonès *et al.* proposed, from a coordination chemistry point of view, that the most common educated guess for a nanojunction through the Co<sup>II</sup> centre should be a hexacoordinated metal centre (Figure 2.8). However, the calculated conductance using a PBE+U approach with this structural arrangement is  $7.5 \cdot 10^{-5} G_0$ , diverging three orders of magnitude from the experimental value.

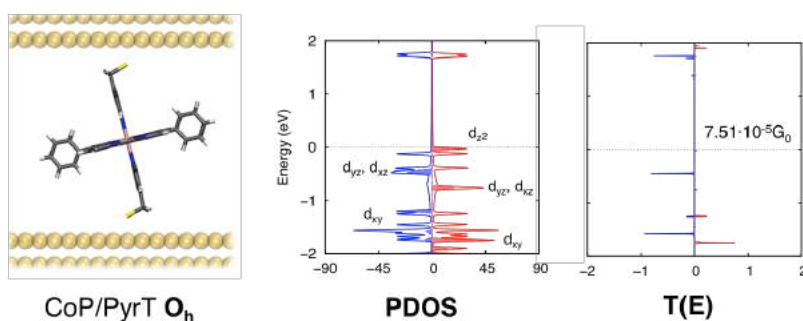


Figure 2.8. CoDPP/PyMT hexacoordinated junction (left), Projected Density of States (centre) and transmission spectrum (right). Adapted figure.<sup>23</sup>

Such discrepancy is too large to be associated with the approximations used in the DFT calculations or in the transport formalism itself. DFT is well known to underestimate the HOMO-LUMO gap, and thus the conductance value should be overestimated. For this reason, the Hubbard correction stated previously was applied.

To face the structural analysis of the linker/CoDPP/linker adduct constrained in a tunnelling gap, it is reasonable to go back to basics and optimise both linkers on a Au(111) surface. In this case, a many-body approach is chosen to obtain accurate energies for comparison. As a result, two main optimised geometries were found: a standing up and a lying down conformation for each linker (Figure 2.9).

## 2 Supramolecular Landscape of CoDPP

---

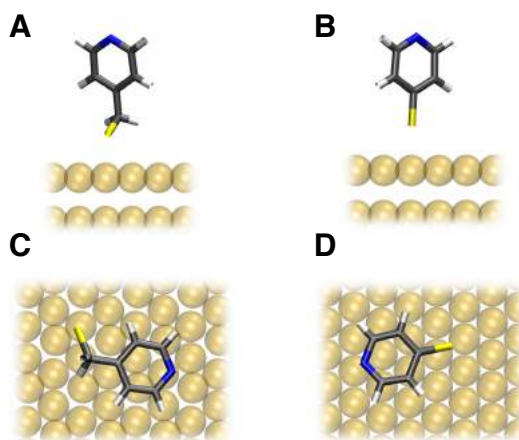


Figure 2.9. (A) PyrMT standing up, (B) PyrT standing up, (C) PyrMT lying down and (D) PyrT lying down geometries. Adapted figure.<sup>23</sup>

The lying down PyrMT (Figure 2.9C) is 14.0 kcal/mol more stable than the standing up PyrMT conformer (Figure 2.9A). The same happens for the lying down PyrT (Figure 2.9D), although it is only 6.0 kcal/mol more stable than its lying-up counterpart. This suggests a more pronounced tendency of PyrT to be standing up (Figure 2.9B) when forming a part of a compact monolayer, as the one prepared for the experiments. STM imaging previously reported suggests a lifted conformation for the PyrT monolayer.<sup>36,38</sup>

These computational results suggest that PyrMT might interact with CoDPP via a  $\pi$ - $\pi$  interaction, whilst PyrT is expected to form the Co<sup>II</sup> hexacoordinated junction. To corroborate this, ellipsometry measurements have been done on a linker/CoDPP/linker molecular layer on Au(111). The resulting thickness for PyrMT/CoDPP/PyrMT is 11.6 Å and 13.0 Å is scored for PyrT/CoDPP/PyrT. As the linker employed is in excess in both cases, the measured thickness will be underestimated. The obtained thicknesses support the idea of a lying down PyrMT when interacting with CoDPP and a standing up PyrT coordinating the Co<sup>II</sup> centre (Figure 2.10).

If both linkers were to be standing up or lying down, PyrMT adducts should be expected to be thicker. The experimental results, nonetheless, point out that PyrMT adducts are thinner. Thus, only a lying down PyrMT and a standing up PyrT seem to explain the obtained results.

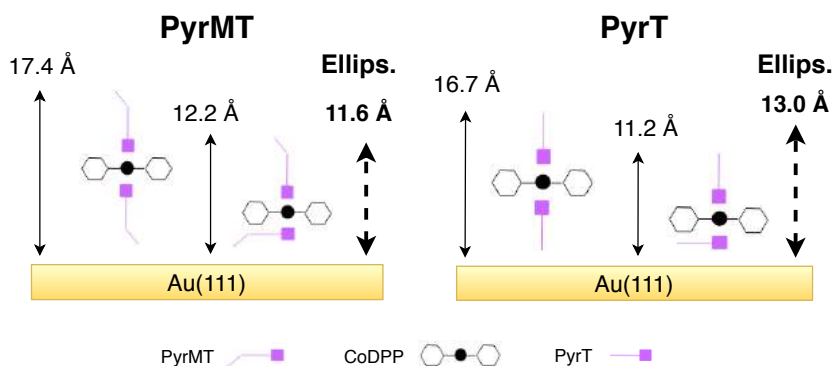


Figure 2.10. Scheme of the ellipsometry measurements of lying down and standing up linker/CoDPP/linker adducts for PyrMT and PyrT. The ellipsometric thickness is represented as a bold dashed line. Adapted figure.<sup>23</sup>

Note that the ellipsometry analysis might differ from the actual nanojunctions. When the two electrodes are considered, it is expected to have both axial PyrMT in a lying down configuration. Notwithstanding, the ellipsometry measurements highlight that PyrT is a more rigid linker and significantly decoupled from the metal (thicker measured layer) while PyrMT is flexible, providing thinner layers despite of its larger molecular length.

Guided by the ellipsometry data, the PyrMT/CoDPP/PyrMT and PyrT/CoDPP/PyrT adducts were optimised with PyrMT lying down and PyrT standing up but keeping the axial N-Co bond, as suggested by the experiments (Figure 2.11).



## 2 Supramolecular Landscape of CoDPP

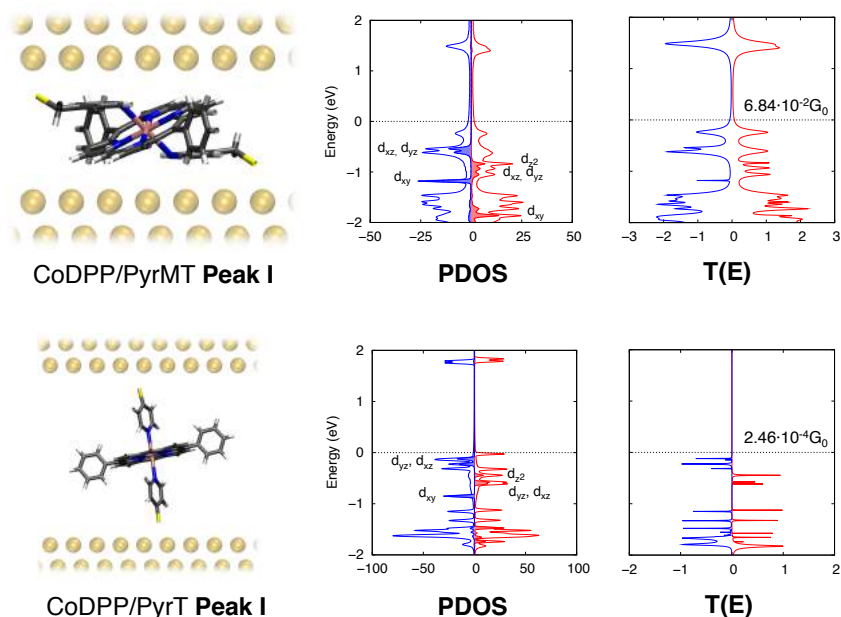


Figure 2.11. On top panel, proposed nanojunction of CoDPP/PyrMT peak I (top left), projected density of states on the molecule (top centre) and transmission spectrum (top right). On the bottom panel, the corresponding to CoDPP/PyrT. Adapted figure.<sup>23</sup>

The computed conductances at zero bias are  $6.84 \cdot 10^{-2} G_0$  and  $2.46 \cdot 10^{-4} G_0$  for the PyrMT and PyrT junctions, respectively, in excellent agreement to peak I (Figure 2.3A and Figure 2.3B). Although PyrMT and PyrT linkers are very similar, surprisingly different nanojunctions are obtained. The extra methylene group in PyrMT allows the successful combination of covalent Au-S and Co-N bonds plus  $\pi$ -interaction of the ring with the gold surface. PyrT, on the contrary, prefers to keep a solid Au-S bond and tends to adopt a more orthogonal coordinative geometry. The much shorter junction length of PyrMT/CoDPP/PyrMT junction readily explains the higher conductance observed.

Peak I of CoP/PyrMT (Figure 2.4A) and CoP/PyrT (Figure 2.4C) junctions can be related to equivalent junctions regarding CoDPP/PyrMT and CoDPP/PyrT peak I (Figure 2.3A and B). The calculated conductance

for these junctions is  $3.67 \cdot 10^{-2} G_0$  and  $2.11 \cdot 10^{-4} G_0$ , respectively, in good agreement with the experimental values of  $9.31 \cdot 10^{-2} G_0$  and  $1.51 \cdot 10^{-4} G_0$  (Figure 2.12). As observed in the analogous peak I for CoDPP and DPP, the PyrMT junctions exhibit broader transmission peaks than those for PyrT, which should be expected from the ellipsometry measurements because of the decoupling introduced by the rigid linker.

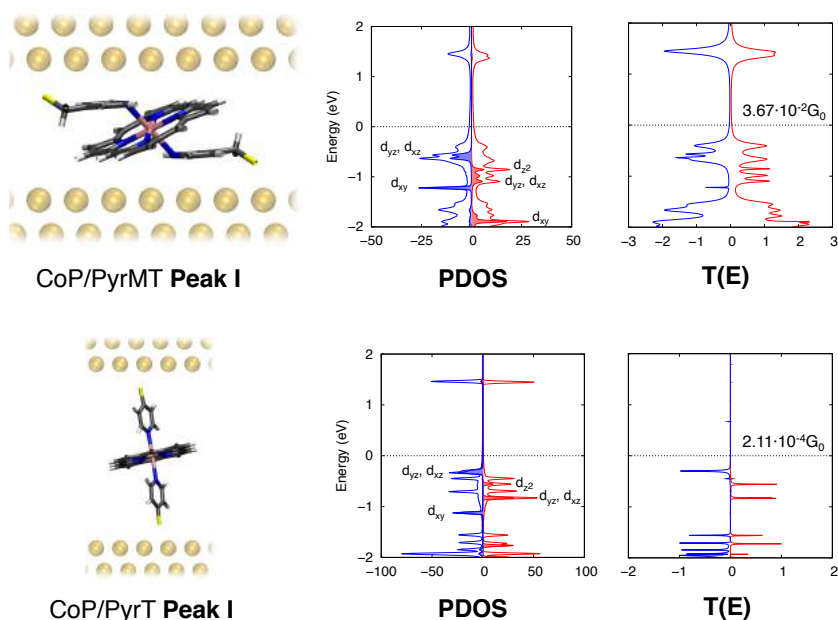


Figure 2.12. On top panel, proposed nanojunction of CoP/PyrMT peak I (top left), projected density of states on the molecule (top centre) and transmission spectrum (top right). On the bottom panel, the corresponding to CoP/PyrT. Adapted figure.<sup>23</sup>

### 2.3.4 Through-backbone conductance signatures

Turning the attention to features II and III, the absence of metal centre and lateral phenyl rings along with the rigid PyrT linker on P/PyrT junction yields a silent conductance histogram (Figure 2.4D). Probably, no stable junction can be formed in the explored conductance window. However, P/PyrMT shows a single peak at  $2.24 \cdot 10^{-4} G_0$  (Figure 2.4B). A

## 2 Supramolecular Landscape of CoDPP

similar value appears again for CoP/PyrMT peak II (Figure 2.4A). A sensible junction for P/PyrMT might be a  $\pi$ - $\pi$  stacking of PyrMT-P-PyrMT moieties. The flexibility of the PyrMT linker allows the formation of such junction for the free base porphyrin, whilst PyrT cannot be accommodated to furnish this sort of interaction (Figure 2.13).

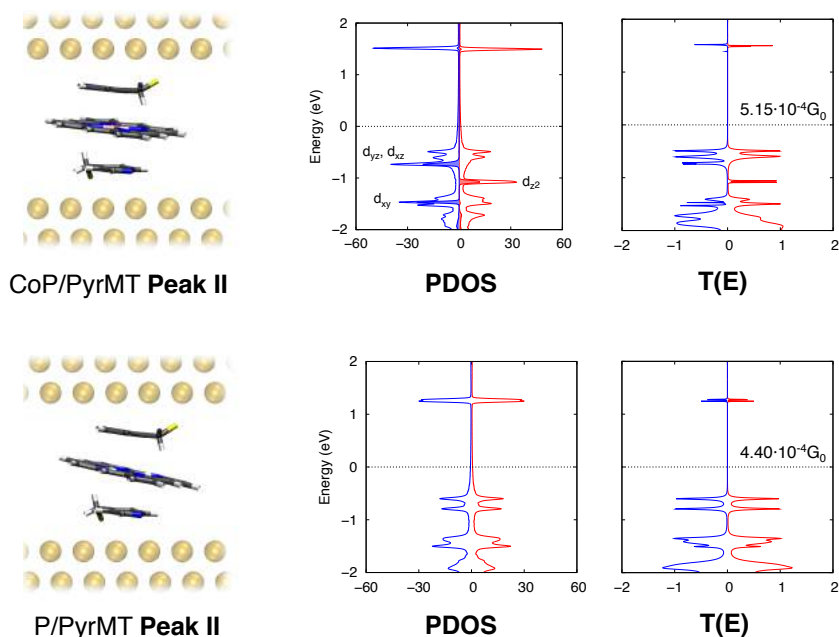


Figure 2.13. On top panel, proposed nanojunction of CoP/PyrMT peak II (top left), projected density of states on the molecule (top centre) and transmission spectrum (top right). On the bottom panel, the corresponding to P/PyrT. Adapted figure.<sup>23</sup>

The calculated conductances for both junctions are  $5.15 \cdot 10^{-4} G_0$  and  $4.40 \cdot 10^{-4} G_0$  for CoP/PyrMT and P/PyrMT, in close agreement with the experimental values  $3.01 \cdot 10^{-4} G_0$  and  $2.24 \cdot 10^{-4} G_0$ . Despite that there is no direct interaction between the linkers and the  $\text{Co}^{\text{II}}$  centre, a small effect on the conductance is observed both in experiments and calculations. The metal centre slightly increases the conductance because of the proximity of  $d_{yz}$  and  $d_{xz}$  orbitals (Figure 2.13, top centre), which constitute a successful

transmission channel (Figure 2.13, top right). These two orbitals are, of course, missing in the P/PyrMT junction (Figure 2.13, bottom centre).

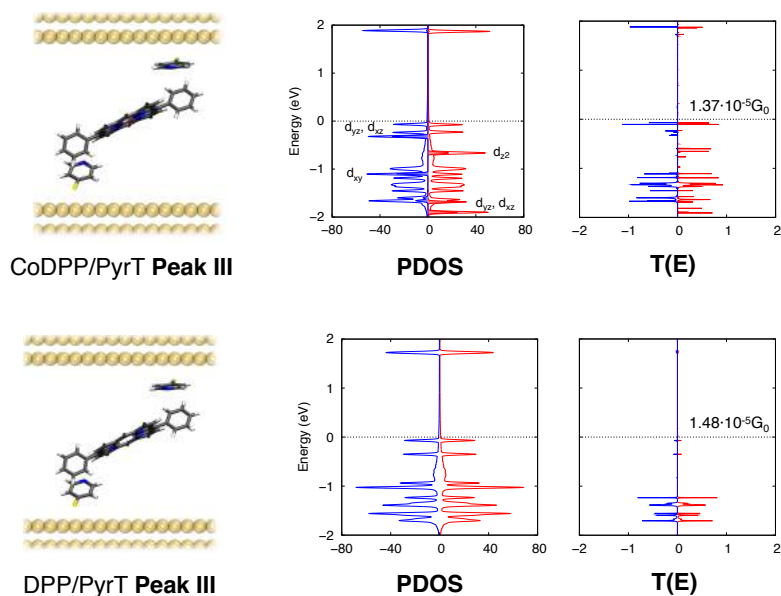


Figure 2.14. On top panel, proposed nanojunction of CoDPP/PyrT peak III (top left), projected density of states on the molecule (top centre) and transmission spectrum (top right). On the bottom panel, the corresponding to DPP/PyrT. Adapted figure.<sup>23</sup>

Knowing that  $\pi$ - $\pi$  supramolecular interactions are effective to form nanojunctions, CoDPP/PyrMT and CoDPP/PyrT conductance peaks II and III (Figure 2.3) are now considered. Focusing first on feature III of DPP/PyrT (Figure 2.3D), it can be easily noticed that this junction and P/PyrT junction (Figure 2.4D) peak III must be related to the phenyl rings. Two analogous junctions are found for CoDPP/PyrT (Figure 2.14) and CoDPP/PyrMT peak III (Figure 2.15).

## 2 Supramolecular Landscape of CoDPP

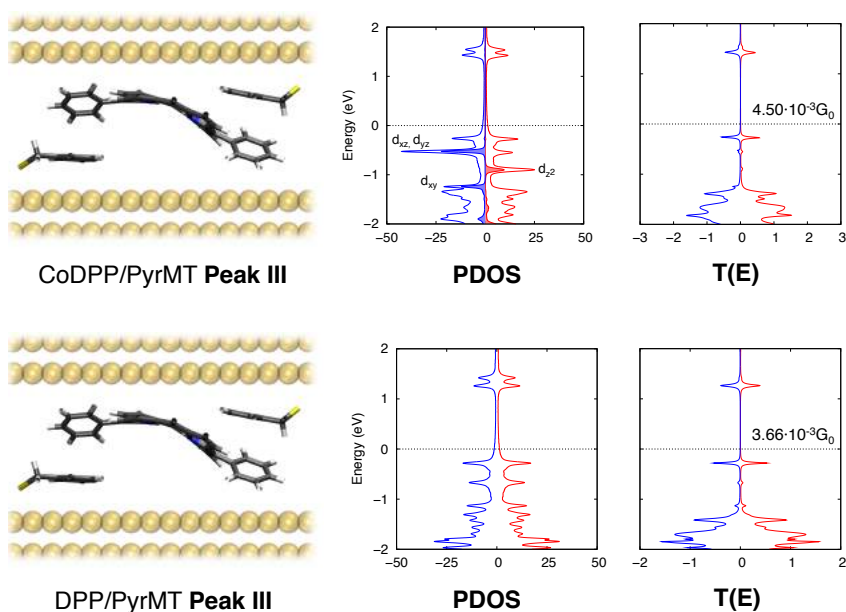


Figure 2.15. On top panel, proposed nanojunction of CoDPP/PyrMT peak III (top left), projected density of states on the molecule (top centre) and transmission spectrum (top right). On the bottom panel, the corresponding to DPP/PyrMT. Adapted figure.<sup>23</sup>

In this junction, PyrT can interact with the lateral phenyl rings keeping a tilted standing up arrangement. The calculated conductance for peak III for CoDPP/PyrT and DPP/PyrT are almost the same  $1.37 \cdot 10^{-5} G_0$  and  $1.48 \cdot 10^{-5} G_0$  in very good agreement with the experimental conductance  $1.71 \cdot 10^{-5} G_0$  and  $1.56 \cdot 10^{-5} G_0$ , respectively. Another feasible conformation for this peak could be a pentacoordinated junction. However, the geometry shown in Figure 2.14 is 12.6 kcal/mol more stable than this pentacoordinated geometry. Furthermore, the experimental data indicate that the DPP/PyrT peak III exists even in the absence of the metal centre, thus highlighting the metal-independent character of peak III.

The DPP/PyrMT Peak III junction (Figure 2.15) scores a conductance value two orders magnitude larger than the DPP/PyrT analogue. Again, the flexibility of PyrMT linker permits a higher coupling and a larger

contact area with the electrodes as deduced from the comparison of the transmission peaks broadening in Figure 2.14 and Figure 2.15.

Finally, peak II of Figure 2.3 could be tentatively related with the junction presented in Figure 2.13. However, this conformation seems to be hindered by the phenyl rings of DPP. Instead, an intermediate conformation in which one PyrMT is interacting with the pyrrolic ring of the DPP is obtained while the second PyrMT linker interacts directly with the phenyl ring (Figure 2.16).

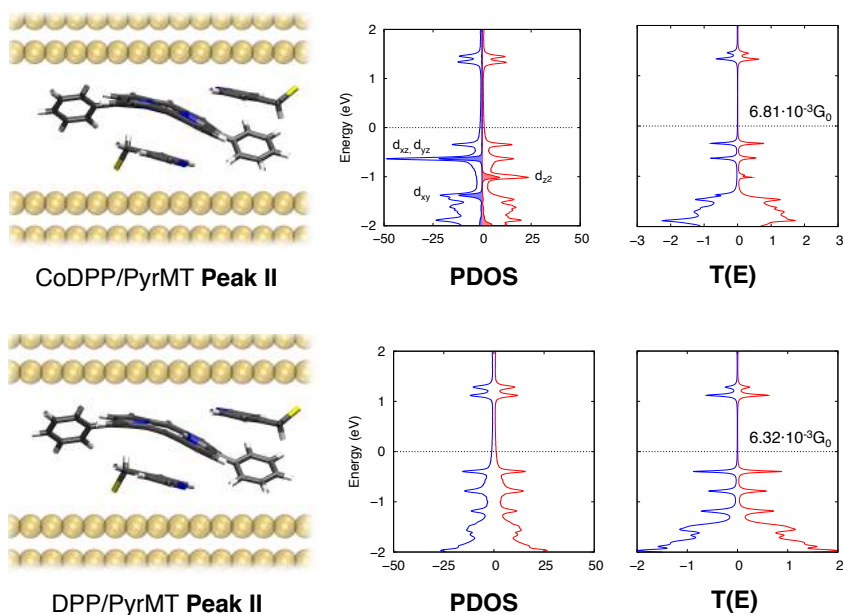


Figure 2.16. On top panel, proposed nanojunction of CoDPP/PyrMT peak II (top left), projected density of states on the molecule (top centre) and transmission spectrum (top right). On the bottom panel, the corresponding to DPP/PyrMT. Adapted figure.<sup>23</sup>

The calculated Peak II conductance values are  $6.81 \cdot 10^{-3} G_0$  for CoDPP/PyrMT and  $6.32 \cdot 10^{-3} G_0$  for DPP/PyrMT, respectively, in fair agreement with the experimental observation.

As a final remark, the overall conductance decreases for CoP and P

## 2 Supramolecular Landscape of CoDPP

---

junctions. Although there is no straightforward reasoning to explain such behaviour, it can be tentatively ascribed to two different electrical contributions. On one hand, the phenyl substitution might bring the energy of the HOMO orbital closer to the Fermi energy *via* electron donation by resonance,<sup>39–42</sup> hence increasing the conductance value. Such resonance is expected to be larger for the pyridine/porphyrin ring interaction, as shown for feature II. On the other hand, the presence of the phenyl rings enlarges the electrical contact area, producing an increased conductance.

### 2.3.5 Supramolecular landscape

Along the previous section, several junctions that explain successfully the experimental data are presented and allow creating a picture of the rich supramolecular landscape when building nanojunctions based on diphenylporphyrins (DPP). The richness of this sort of junctions lies on the chosen metal centre and the interplay between the lateral substitutions of the porphyrin and the chosen linker.

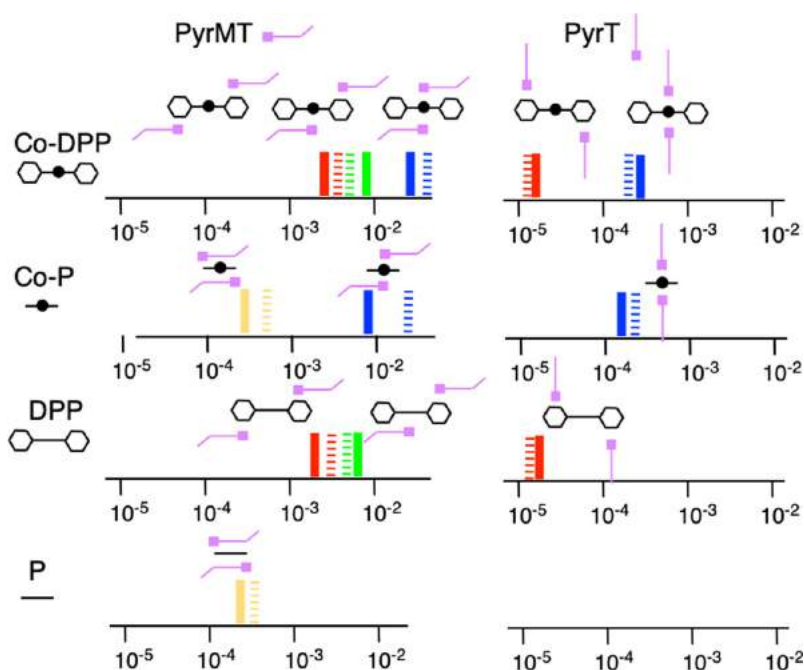


Figure 2.17. Cartoon diagram of the supramolecular landscape of all the nanojunctions studied along the study. Representations of the structural DFT models are drawn for each conductance signature. The conductance values are displayed in the x-axis in  $G_0$  units. Blue colour corresponds to both axial linkers interacting with the metal centre. Green stands for junctions interacting with one phenyl ring and red when interacting with both phenyl rings. Yellow is for pyrrolic link interactions. Dashed lines represent calculated values and the solid ones the measured value.<sup>23</sup>

Figure 2.17 serves as a summary of plausible molecular junctions and allows the comparison between the experimental observations and the proposed computed molecular junctions. As it can be observed, the overall agreement between experimental and calculated conductance values is usually very good. Furthermore, the proposed geometries are respectful with the dynamic picture of the STM measurement: consecutive plateaus in the individual conductance traces pairing peaks I-II and peaks I-III show a very good agreement between the experimental interelectrode distance and the calculated separation. The measured separations for CoDPP/PyrMT junction are 6.98, 8.00 and 8.14 Å for features I, II and III, respectively, when the 5 Å gold snap-back is added.<sup>43</sup> The calculated



## 2 Supramolecular Landscape of CoDPP

electrode-electrode separation follows the same trend: 9.36, 10.5 and 10.7 Å. The small discrepancy can be a manifestation of the out-of-equilibrium nature of the STM measurements. Still, the correlation between interaction energies and plateau length (Figure 2.18) is very good, indicating that equilibrium geometries should be reliable to understand the dynamic supramolecular wire formation.

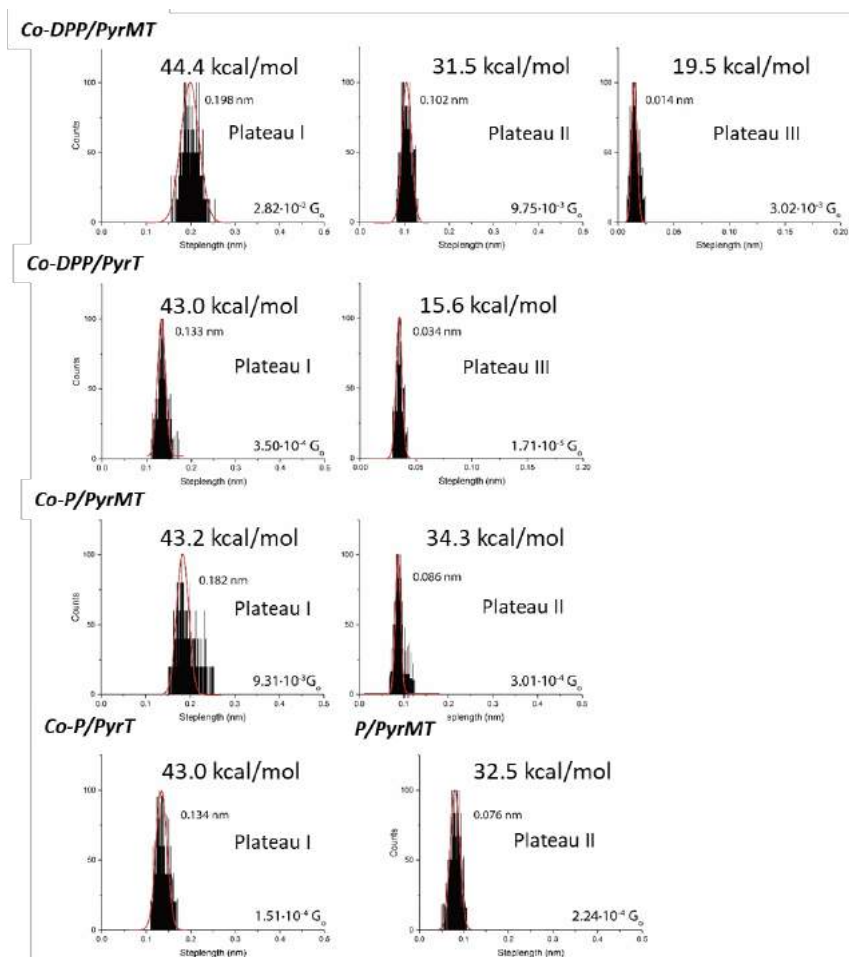


Figure 2.18. Plateau length histograms of the main observed junctions and the calculated interaction energy. There is a good correlation between larger plateaus and stronger interaction.<sup>23</sup>

## 2.4 Conclusions

In this chapter, the supramolecular landscape of Co<sup>II</sup>-5,15-diphenylporphyrin (CoDPP) when forming electrical wires with two different linkers, pyridine-4-yl-methanethiol (PyrMT) and 4-pyridinethiol (PyrT), has been studied. In this test bed, it has been demonstrated that new supramolecular wires can be designed by exploiting transition metal coordination chemistry or through weak interactions such as  $\pi$ -stacking, with conductance values ranging from  $10^{-4} G_0$  to  $10^{-2} G_0$ .

The flexibility of the PyrMT linker, when compared to the rigid PyrT analogue, yields strikingly different junctions with much shorter interelectrode distances. Weak interactions are expected to reduce the  $E - E_F$  energy difference and the broadening  $\Gamma$ . In general, this assumption was found to be true. However, a well-designed  $\pi$ -stacked nanojunction permits a large contact surface area with the electrodes, noticeably increasing the broadening of the orbital energies and hence the resultant conductance value, as found for CoDPP/PyrMT peak I.

Many orbitals can mediate the electron flow, but the highest occupied molecular orbital (HOMO) and/or the lowest unoccupied molecular orbital (LUMO) position are the principal conductive channels. The PBE+U (4.0 eV) DFT calculations produced very good results when modelling the electron transport properties. The Hubbard correction, which readjusts the HOMO-LUMO gap, increases the accuracy of the calculations.

A suitable dynamic picture of the observed plateaus was found. For CoDPP, short interelectrode distances forces peak I through metal junction with a very high conductance of  $2.82 \cdot 10^{-2} G_0$ . As the interelectrode distance increases, peaks II and III are observed. Good

## 2 Supramolecular Landscape of CoDPP

---

correlation was also obtained between the DFT calculated interaction energies and the observed plateau length of each conductance signature.

Supramolecular interactions are an exciting way to form nanojunctions, paving the way to Supramolecular Electronics. The results presented here demonstrate the large formability of a molecular wire via tweaking the internal degrees of freedom of weak interactions.

## 2.5 References

- 1 Z. F. Liu, S. Wei, H. Yoon, O. Adak, I. Ponce, Y. Jiang, W. D. Jang, L. M. Campos, L. Venkataraman, J. B. Neaton, *Nano Lett.* **2014**, *14*, 5365.
- 2 K. S. Suslick, N. A. Rakow, M. E. Rosal, J.-H. Chou, *J. Porphyrins Phthalocyanines* **2000**, *4*, 407.
- 3 S. Mohnani, D. Bonifazi, *Coord. Chem. Rev.* **2010**, *254*, 2342.
- 4 I. Beletskaya, V. S. Tyurin, A. Y. Tsivadze, R. Guilard, C. Stern, *Chem. Rev.* **2009**, *109*, 1659.
- 5 M. Jurow, A. E. Schuckman, J. D. Batteas, C. M. Drain, *Coord. Chem. Rev.* **2010**, *254*, 2297.
- 6 G. Sedghi, K. Sawada, L. J. Esdaile, M. Hoffmann, H. L. Anderson, D. Bethell, W. Haiss, S. J. Higgins, R. J. Nichols, *J. Am. Chem. Soc.* **2008**, *130*, 8582.
- 7 J. E. Lovett, M. Hoffmann, A. Cnossen, A. T. J. Shutter, H. J. Hogben, J. E. Warren, S. I. Pascu, C. W. M. Kay, C. R. Timmel, H. L. Anderson, *J. Am. Chem. Soc.* **2009**, *131*, 13852.
- 8 H. Ozawa, M. Kawao, S. Uno, K. Nakazato, H. Tanaka, T. Ogawa, *J. Mater. Chem.* **2009**, *19*, 8307.
- 9 G. Sedghi, V. M. García-Suárez, L. J. Esdaile, H. L. Anderson, C. J. Lambert, S. Martín, D. Bethell, S. J. Higgins, M. Elliott, N. Bennett, J. E. MacDonald, R. J. Nichols, *Nat. Nanotechnol.* **2011**, *6*, 517.
- 10 M. L. Perrin, C. A. Martin, F. Prins, A. J. Shaikh, R. Eelkema, J. H. van Esch, J. M. van Ruitenbeek, H. S. J. van der Zant, D. Dulić, *Beilstein J. Nanotechnol.* **2011**, *2*, 714.
- 11 Z. Li, M. Smeu, M. A. Ratner, E. Borguet, *J. Phys. Chem. C* **2013**, *117*, 14890.
- 12 Z. Li, E. Borguet, *J. Am. Chem. Soc.* **2011**, *134*, 63.

- 13 M. El Abbassi, P. Zwick, A. Rates, D. Stefani, A. Prescimone, M. Mayor, H. S. J. Van Der Zant, D. Dulić, *Chem. Sci.* **2019**, *10*, 8299.
- 14 J. Puigmartí-Luis, W. J. Saletta, A. González, D. B. Amabilino, L. Pérez-García, *Chem. Commun. (Camb)*. **2014**, *50*, 82.
- 15 J. J. Regan, B. E. Ramirez, J. R. Winkler, H. B. Gray, B. G. Malmström, *J. Bioenerg. Biomembr.* **1998**, *30*, 35.
- 16 A. C. Aragonès, N. Darwish, W. J. Saletta, L. Pérez-García, F. Sanz, J. Puigmartí-Luis, D. B. Amabilino, I. Díez-Pérez, *Nano Lett.* **2014**, *14*, 4751.
- 17 I. Ponce, A. C. Aragonès, N. Darwish, P. Pla-Vilanova, R. Oñate, M. C. Rezende, J. H. Zagal, F. Sanz, J. Pavez, I. Díez-Pérez, *Electrochim. Acta* **2015**, *179*, 611.
- 18 B. Xu, N. J. Tao, *Science* **2003**, *301*, 1221.
- 19 J. M. Artés, I. Díez-Pérez, P. Gorostiza, *Nano Lett.* **2012**, *12*, 2679.
- 20 W. Haiss, R. J. Nichols, H. van Zalinge, S. J. Higgins, D. Bethell, D. J. Schiffrin, *Phys. Chem. Chem. Phys.* **2004**, *6*, 4330.
- 21 S. Dey, S. A. Iqbal, S. P. Rath, *New J. Chem.* **2014**, *38*, 1458.
- 22 M. Noori, A. C. Aragonès, G. Di Palma, N. Darwish, S. W. D. Bailey, Q. Al-Galiby, I. Grace, D. B. Amabilino, A. González-Campo, I. Díez-Pérez, C. J. Lambert, *Sci. Rep.* **2016**, *6*, 37352.
- 23 A. C. Aragonès, A. Martín-Rodríguez, D. Aravena, J. Puigmartí-Luis, D. B. Amabilino, N. Aliaga-Alcalde, A. González-Campo, E. Ruiz, I. Díez-Pérez, *Angew. Chemie - Int. Ed.* **2020**, *59*, 19193.
- 24 J. M. Soler, E. Artacho, J. D. Gale, A. García, J. Junquera, P. Ordejón, D. Sánchez-Portal, *J. Phys. Condens. Matter* **2002**, *14*, 2745.
- 25 A. García, N. Papior, A. Akhtar, E. Artacho, V. Blum, E. Bosoni, P. Brandimarte, M. Brandbyge, J. I. Cerdá, F. Corsetti, R. Cuadrado, V. Dikan, J. Ferrer, J. Gale, P. García-Fernández, V. M. García-Suárez, S. García, G. Huhs, S. Illera, R. Korytár, P. Koval, I. Lebedeva, L. Lin, P. López-Tarifa, S. G. Mayo, S. Mohr, P.

- Ordejón, A. Postnikov, Y. Pouillon, M. Pruneda, R. Robles, D. Sánchez-Portal, J. M. Soler, R. Ullah, V. W. Z. Yu, J. Junquera, *J. Chem. Phys.* **2020**, *152*, 204108.
- 26 J. P. Perdew, K. Burke, M. Ernzerhof, *Phys. Rev. Lett.* **1996**, *77*, 3865.
- 27 J. Ferrer, C. J. Lambert, V. M. García-Suárez, D. Z. Manrique, D. Visontai, L. Oroszlany, R. Rodríguez-Ferradás, I. Grace, S. W. D. Bailey, K. Gillemot, H. Sadeghi, L. A. Algharagholy, *New J. Phys.* **2014**, *16*, 93029.
- 28 M. Di Ventra, *Electrical Transport in Nanoscale Systems*, Cambridge University Press, **2008**.
- 29 O. A. Vydrov, T. Van Voorhis, *J. Chem. Phys.* **2010**, *133*, 244103.
- 30 J. Hermann, R. A. DiStasio, A. Tkatchenko, *Chem. Rev.* **2017**, *117*, 4714.
- 31 C. Toher, S. Sanvito, *Phys. Rev. B* **2008**, *77*, 155402.
- 32 V. Blum, R. Gehrke, F. Hanke, P. Havu, V. Havu, X. Ren, K. Reuter, M. Scheffler, *Comput. Phys. Commun.* **2009**, *180*, 2175.
- 33 X. Ren, P. Rinke, V. Blum, J. Wieferink, A. Tkatchenko, A. Sanfilippo, K. Reuter, M. Scheffler, *New J. Phys.* **2012**, *14*, 53020.
- 34 K. Lejaeghere, G. Bihlmayer, T. Björkman, P. Blaha, S. Blügel, V. Blum, D. Caliste, I. E. Castelli, S. J. Clark, A. Dal Corso, S. De Gironcoli, T. Deutsch, J. K. Dewhurst, I. Di Marco, C. Draxl, M. Dułak, O. Eriksson, J. A. Flores-Livas, K. F. Garrity, L. Genovese, P. Giannozzi, M. Giantomassi, S. Goedecker, X. Gonze, O. Grånäs, E. K. U. Gross, A. Gulans, F. Gygi, D. R. Hamann, P. J. Hasnip, N. A. W. Holzwarth, D. Iușan, D. B. Jochym, F. Jollet, D. Jones, G. Kresse, K. Koepnik, E. Küçükbenli, Y. O. Kvashnin, I. L. M. Locht, S. Lubeck, M. Marsman, N. Marzari, U. Nitzsche, L. Nordström, T. Ozaki, L. Paulatto, C. J. Pickard, W. Poelmans, M. I. J. Probert, K. Refson, M. Richter, G. M. Rignanese, S. Saha, M.

## 2 Supramolecular Landscape of CoDPP

---

- Scheffler, M. Schlipf, K. Schwarz, S. Sharma, F. Tavazza, P. Thunström, A. Tkatchenko, M. Torrent, D. Vanderbilt, M. J. Van Setten, V. Van Speybroeck, J. M. Wills, J. R. Yates, G. X. Zhang, S. Cottenier, *Science* **2016**, *351*, aad3000.
- 35 S. R. Jensen, S. Saha, J. A. Flores-Livas, W. Huhn, V. Blum, S. Goedecker, L. Frediani, *J. Phys. Chem. Lett.* **2017**, *8*, 1449.
- 36 E. A. Ramírez, E. Cortés, A. A. Rubert, P. Carro, G. Benítez, M. E. Vela, R. C. Salvarezza, *Langmuir* **2012**, *28*, 6839.
- 37 S. Stoyanov, I. Petkov, L. Antonov, T. Stoyanova, P. Karagiannidis, P. Aslanidis, *Can. J. Chem.* **1990**, *68*, 1482.
- 38 S. Herrera, F. Tasca, F. J. Williams, E. J. Calvo, P. Carro, R. C. Salvarezza, *Langmuir* **2017**, *33*, 9565.
- 39 C. Hansch, A. Leo, R. W. Taft, *Chem. Rev.* **1991**, *91*, 165.
- 40 A. C. Aragonès, N. Darwish, J. Im, B. Lim, J. Choi, S. Koo, I. Díez-Pérez, *Chem. - A Eur. J.* **2015**, *21*, 7716.
- 41 X. Xiao, L. A. Nagahara, A. M. Rawlett, N. Tao, *J. Am. Chem. Soc.* **2005**, *127*, 9235.
- 42 L. Venkataraman, Y. S. Park, A. C. Whalley, C. Nuckolls, M. S. Hybertsen, M. L. Steigerwald, *Nano Lett.* **2007**, *7*, 502.
- 43 C. Huang, A. V. Rudnev, W. Hong, T. Wandlowski, *Chem. Soc. Rev.* **2015**, *44*, 889.

### Work published in

A. C. Aragonès, A. Martín-Rodríguez, D. Aravena, J. Puigmartí-Luis, D. B. Amabilino, N. Aliaga-Alcalde, A. González-Campo, E. Ruiz, I. Díez-Pérez, *Angew. Chemie - Int. Ed.* 2020, *59*, 19193.

## 3 STUDY OF MAGNETORESISTANCE ON METALLOPORPHYRIN DEVICES

### 3.1 Motivation

Magnetoresistance is a crucial property to create any spintronic device.<sup>1,2</sup> This property is well understood in multi-layered inorganic materials, in which a non-magnetic layer is sandwiched between two ferromagnetic layers,<sup>3-5</sup> also known as spin valve (section 1.1.6). Beyond the ultimate miniaturisation of the device that a molecule represents, it offers an opportunity to tune and improve the electrical properties by introducing small variations in the chemical structure.<sup>6-9</sup>

Magnetoresistance in single molecule devices can be originated when the surroundings of the Fermi energy is spin-polarised. To study the interplay between the ferromagnet and the molecule is crucial to understand the phenomenon.<sup>10</sup> In this context, phthalocyanines have been extensively studied as ferromagnet/molecule bilayers<sup>11-13</sup> and at single molecule level.<sup>14-20</sup> Magnetoresistance has been also observed in diamagnetic molecules as  $C_{60}$  under the influence of a ferromagnetic electrode.<sup>21</sup> The effect of the magnetisation orientation is studied as well, leading to tuneable anisotropic magnetoresistance.<sup>22,23</sup> However, many of these examples must be kept at cryogenic temperatures in order to preserve



### 3 Study of Magnetoresistance on Metalloporphyrin Devices

---

their magnetic properties. Room temperature magnetoresistance devices are thus highly desirable to open up to realistic technological applications.<sup>24–26</sup>

Magnetoresistance at room temperature can be achieved using small molecules with unpaired electrons such as the transition metal triazole-pyridine complexes  $[M(\text{tzpy})_2(\text{NCX})_2]$ , (M: Fe or Co; X: S or Se) in the high-spin configuration.<sup>27</sup> In these cases, the magnetic molecule is placed between a Au(111) bottom electrode and a ferromagnetic top electrode as Ni or Co.<sup>28</sup> The conductance obtained is dependent of the direction of the magnetic polarisation, potentially mimicking the response of a spin valve.

In the previous chapter it was studied the supramolecular landscape of CoDPP. In that, a metal-dependent high conductance peak was observed. Intimately related with this study, the discussion is now extended to NiDPP, CuDPP and ZnDPP to explore the magnetoresistance of these highly conductive metalloporphyrins.

## 3.2 Previous work

Aragonès *et al* carried out the magnetoresistance measurements of  $M^{\text{II}}$ DPP ( $M^{\text{II}} = \text{Co}^{\text{II}}, \text{Ni}^{\text{II}}, \text{Cu}^{\text{II}}$  and  $\text{Zn}^{\text{II}}$ ) as a natural continuation of their previous work. CoDPP supramolecular landscape was studied through the rationalisation of the conductance features when the electrodes are functionalised with two different ligands (PyrMT and PyrT). For the magnetoresistance experiments, the set of junctions is restricted to the  $M^{\text{II}}$ DPP/PyrMT case, in which it is observed the highest conductance features with a metal-dependent high conductance peak.

STM-BJ experiments were run in the same fashion as explained in section 2.3 but with a spin-polarised tip. A freshly cut Ni tip was magnetically polarised *ex situ* by exposing it to a 1 T NdFeB magnet for 2h in an Ar

atmosphere. The inert atmosphere is needed to avoid the formation of insulating nickel oxide on the tip. After the magnetisation, both the Au(111) substrate and the nickel tip were functionalised with pyridine-4-yl-methanethiol (PyrMT) under anaerobic conditions.

The analysis of individual  $G(z)$  STM-BJ traces for  $M^{\text{II}}\text{DPP}/\text{PyrMT}$  junctions with polarised (alpha and beta) and non-polarised Ni tip shows three clearly distinct conductance plateaus, as previously observed for  $\text{CoDPP}/\text{PyrMT}$  (section 2.2) with a Au tip (Figure 3.1). The experiments have been done for positive and negative bias, showing very similar results.

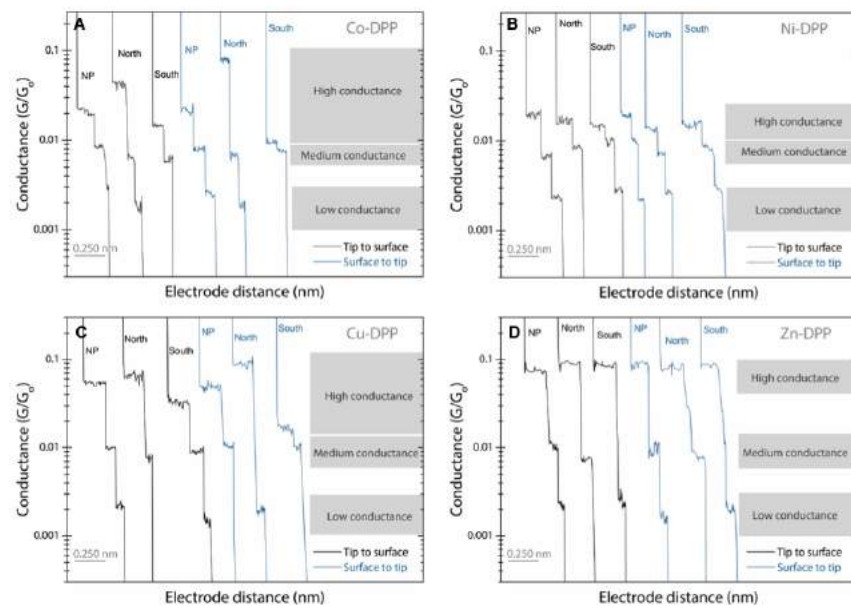


Figure 3.1. Individual STM-BJ conductance traces for A)  $\text{CoDPP}/\text{PyrMT}$  B)  $\text{NiDPP}/\text{PyrMT}$  C)  $\text{CuDPP}/\text{PyrMT}$  and D)  $\text{ZnDPP}/\text{PyrMT}$  junctions with Ni tip. The applied bias is  $-7.5$  mV for the black curves and  $+7.5$  mV for the blue curves.

### 3 Study of Magnetoresistance on Metalloporphyrin Devices

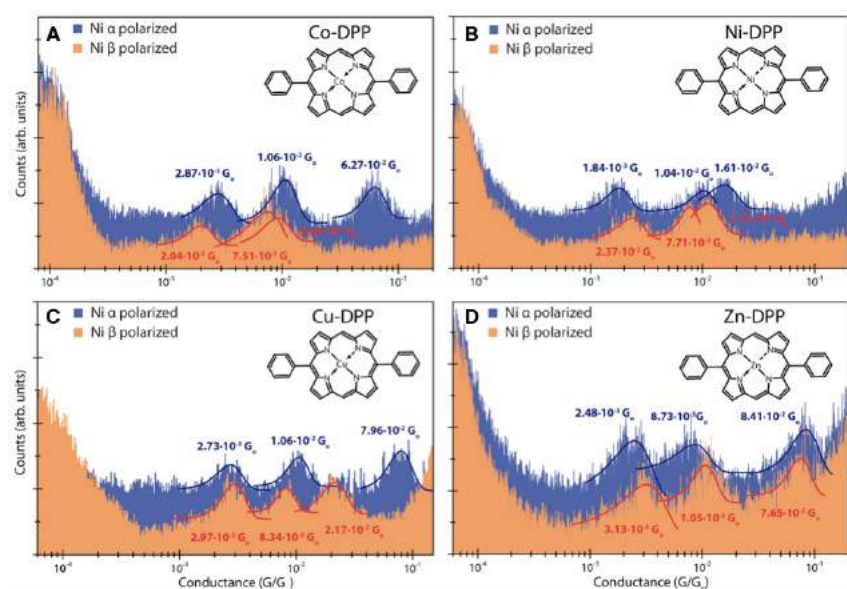


Figure 3.2. Conductance histograms of A) CoDPP/PyrMT B) NiDPP/PyrMT C) CuDPP/PyrMT and D) ZnDPP/PyrMT junctions. Blue and orange histograms are obtained with alpha and beta-polarised Ni tip, respectively from applied voltage set to -7.5 mV.

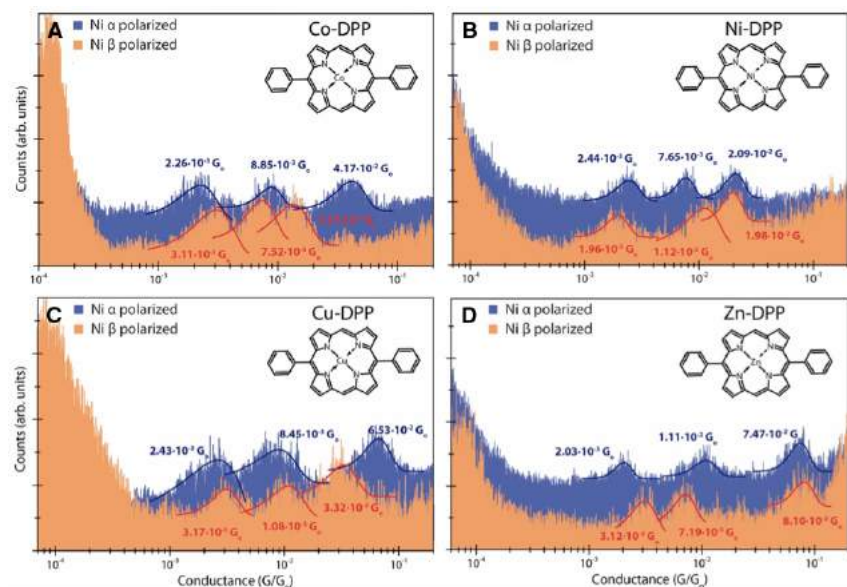


Figure 3.3. Conductance histograms of A) CoDPP/PyrMT B) NiDPP/PyrMT C) CuDPP/PyrMT and D) ZnDPP/PyrMT junctions. Blue and orange histograms are obtained with alpha and beta-polarised Ni tip, respectively from applied voltage set to +7.5 mV.

The resulting histogram of the accumulation of thousands of  $G(z)$  traces for MDPP/PyrMT junctions when the nickel tip is polarised (alpha and beta) and the electrons are injected from the substrate is shown in Figure 3.2 and when injected from the substrate in Figure 3.3.

For all MDPP junctions, low conductance (LC) and medium conductance (MC) signatures display a poor dependence of the magnetisation. LC and MC peaks are within  $2\text{-}3 \cdot 10^{-3} G_0$  and  $0.8\text{-}1 \cdot 10^{-2} G_0$  ranges, respectively. The high conductance (HC) peak, however, is dependent of the magnetisation of the Ni tip and the metal centre. The paramagnetic  $\text{Co}^{\text{II}}\text{DPP}(\text{PyrMT})_2$  and  $\text{Cu}^{\text{II}}\text{DPP}(\text{PyrMT})_2$  complexes (Figure 3.2 and Figure 3.3, A and C) show larger conductance value under alpha polarisation than for beta tip polarisation. The conductance ratios with the inversion of the polarisation are approximately 3-fold and 2-fold for CoDPP and CuDPP for positive biases and 6-fold and 4-fold for negative biases (Figure 3.4).

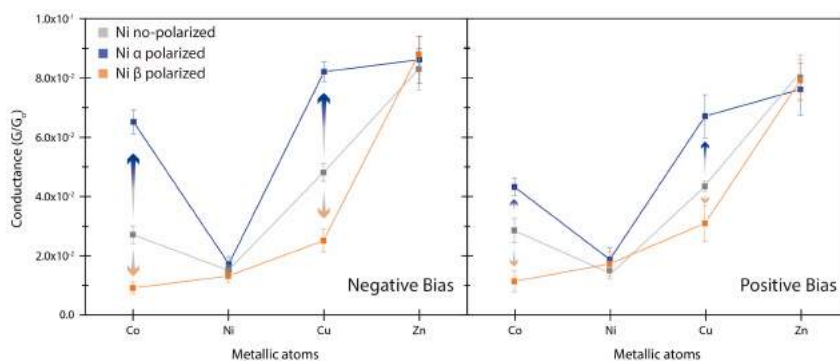


Figure 3.4. Effect of the Ni tip magnetic polarisation over the observed conductance of MDPP/PyrMT HC peak. Grey curve represents the conductance value for a non-polarised Ni tip. Blue and orange curves stands for alpha and beta-polarised Ni tip. Error bars show the standard deviation from different experiments.

NiDPP (Figure 3.2 and Figure 3.3, B) does not present significant variations of the HC conductance peak. Bulk hexacoordinated  $\text{Ni}^{\text{II}}\text{DPP}(\text{PyrMT})_2$  complex is expected to have a high-spin ( $S=1$ ) ground

### 3 Study of Magnetoresistance on Metalloporphyrin Devices

---

state. Therefore, it should exhibit magnetoresistance. The absence of magnetoresistance indicates that  $\text{Ni}^{\text{II}}\text{DPP}(\text{PyrMT})_2$  within electrodes might be in a low-spin (LS) state with  $S=0$ .

Finally,  $\text{ZnDPP}/\text{PyrMT}$  junction presents no magnetoresistance, as it expected for a diamagnetic junction without helical chirality. Surprisingly,  $\text{ZnDPP}$  scores the highest conductance of all junctions considering the closed d-shell of  $\text{Zn}^{\text{II}}$  centre.

*Blinking* STM experiments were also carried out to avoid the disruptive mechanical pulling introduced during the STM-BJ cycle (section 1.2.1). Although *blinking* experiments brings less statistical information in comparison to break junction, information about the lifetime of the formed junctions is obtained. Few hundreds of these *blinks* are analysed and accumulated into a 2D histogram or *blinking* map. As an example, Figure 3.5 shows the *blinking* histograms of paramagnetic  $\text{CuDPP}/\text{PyrMT}$  ( $S=1/2$ ) for different Ni tip magnetisations. In the same fashion as in the previous chapter, the three conductance features were found for all  $\text{M}^{\text{II}}\text{DPP}$ . The stability of the junction goes as  $\text{HC} > \text{MC} > \text{LC}$ , in agreement with what is shown for  $\text{CoDPP}$  (Figure 2.18).

Spin-polarised STM-BJ and *blinking* experiments are in agreement with the LC and MC conductance values being insensitive of the magnetisation of the nickel tip. For the HC value, it is observed a 4-fold conductance difference between alpha (Figure 3.5B) and beta (Figure 3.5C) magnetisation, being the alpha larger. The non-polarised (Figure 3.5A) conductance value lies in between these two, as intuitively expected.

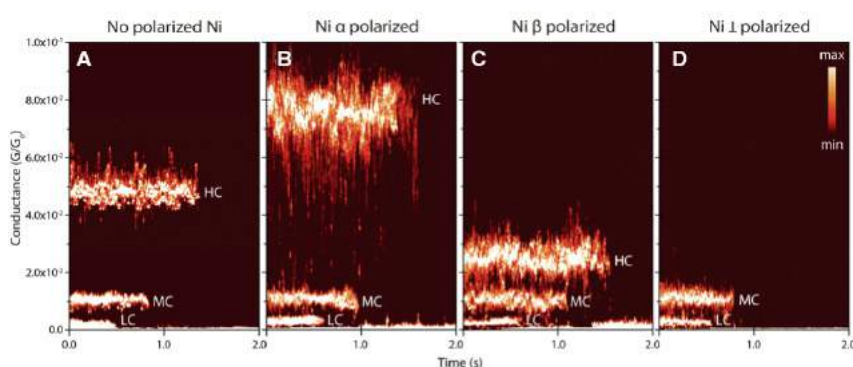


Figure 3.5. *Blinking* STM 2D histograms for CuDPP/PyrMT with A) Non-polarised B) Alpha C) Beta and D) orthogonal Ni tip. Lifetime of each junction s directly related with its stability.

Up to now, it was only considered parallel or antiparallel magnetisation of the tip. The anisotropy of the magnetoresistance effect was also studied by applying and orthogonal magnetisation to the Ni tip (Figure 3.5D). While LC and MC conductance values had no response to the orthogonal magnetisation, the HC value exhibits a remarkable response to the magnetisation falling below the detection limit of the amplifier ( $10^{-6}$  G<sub>0</sub>), evidencing a strong anisotropy of the spin-dependent transport.

### 3.3 Results

The STM-BJ experiments have shown that the three conductance features observed for CoDPP/PyrMT are present for NiDPP, CuDPP and ZnDPP, as well. Here, it will be checked if the conformations proposed in the previous chapter are valid for the rest of the metalloporphyrins considered.

The magnetoresistance of the high conductance feature is rationalised. Although the polarised nickel tip is not introduced in the theoretical results, the spin polarisation of the metalloporphyrin around the Fermi energy is enough to understand the experimental data. The larger

### 3 Study of Magnetoresistance on Metalloporphyrin Devices

---

conductance for paramagnetic CoDPP and CuDPP when an alpha Ni tip is employed in the STM-BJ experiment can be easily understood qualitatively.

#### 3.3.1 Computational details

The optimisation and charge transport properties of the different conformations found for CoDPP were carried out in the same fashion as in the previous chapter for Ni, Cu and Zn (section 2.3.1).

In any charge transport calculation, the position of the molecular orbitals is crucial. For magnetoresistance studies, this is especially true since the response to the alpha or beta-polarised tip depends on the polarisation of the surrounding of the Fermi energy. To check this, the PBE+U (4.0 eV)<sup>29</sup> periodic calculations carried out in SIESTA<sup>30,31</sup> and GOLLUM<sup>32</sup> are opposed to hybrid meta-GGA TPSSh<sup>33,34</sup> functional using Gaussian<sup>35</sup> and LANL2DZ basis set<sup>36–39</sup> to expand the wavefunction and ARTAIOS<sup>40</sup> to calculate the charge transport properties. TPSSh functional has been chosen to calculate accurately spin states of first row transition metal complexes.<sup>41</sup>

ARTAIOS is a non-periodic charge transport code within the Wide Band Limit (WBL). In this approximation, the density of states of the bulk gold electrode is approximated to a continuum of energy levels. Despite it is well known that it suffers of so-called ghost transmission,<sup>42</sup> it yields good results regarding the relative position of the molecular spinorbitals.

#### 3.3.2 Theoretical study of the magnetoresistance

The structures proposed for LC, MC and HC features of CoDPP were optimised for NiDPP, CuDPP and ZnDPP. It is found an excellent

agreement for metal independent LC and MC features (see annex A for PDOS and  $T(E)$  curves) and a fairly good concordance for HC feature. (Figure 3.6).

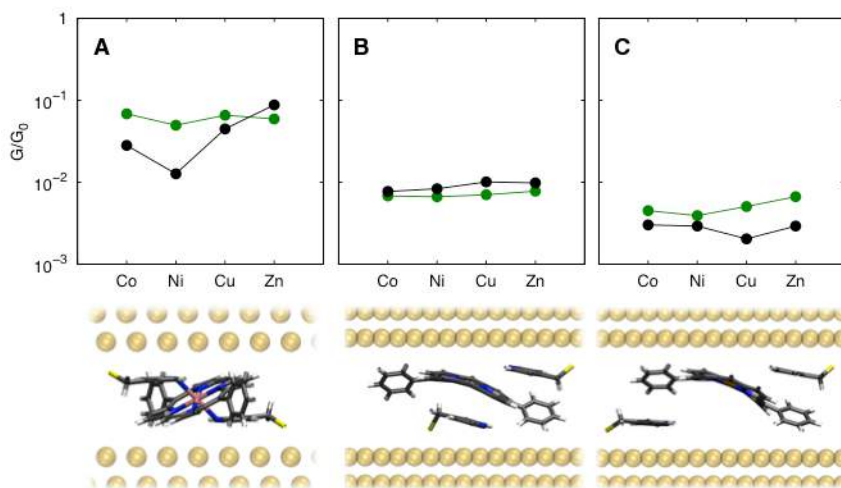


Figure 3.6. A) High conductance B) Medium conductance and C) Low conductance MDPP/PyMT ( $M = \text{Co, Ni, Cu}$  and  $\text{Zn}$ ) features. Green and black dots stand for computational and experimental data.

The highest conductance value found within the four metalloporphyrins considered is the metal-dependent HC peak of ZnDPP/PyMT (Figure 3.4). As before mentioned, it is striking that a diamagnetic metal ion as  $\text{Zn}^{\text{II}}$  scores the largest conductance feature. However, there is experimental evidence that supports such observation because of the strong pentacoordinating character of ZnDPP,<sup>43–45</sup> This would lead to a shorter interelectrode distance and hence, to a larger conductance, at least, a priori.



### 3 Study of Magnetoresistance on Metalloporphyrin Devices

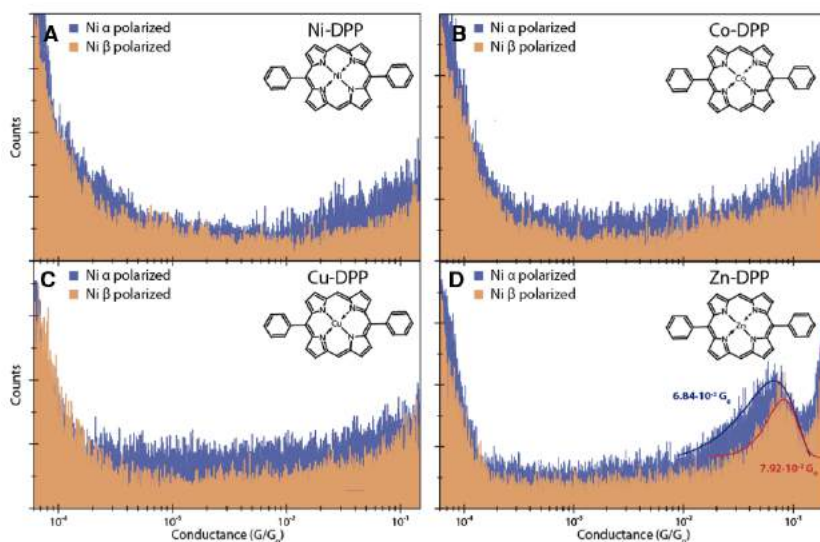


Figure 3.7. STM-BJ conductance histograms for A) NiDPP B) CoDPP C) CuDPP and D) ZnDPP for a functionalised bottom Au (111) substrate with PyrMT a pristine polarised Ni tip. Blue and orange histograms stand for alpha and beta-polarised tip.

In the wake of this, Aragonès run new STM-BJ experiments in which the spin-polarised nickel tip was left without PyrMT functionalization (Figure 3.7). The removal of PyrMT on the STM tip showed a completely silent conductance histogram for CoDPP, NiDPP and CuDPP. LC and MC peaks are absent for the four MDPP when the tip is not functionalised, highlighting that two PyrMT are needed to form any junction except for ZnDPP, which presents exclusively its HC peak. This strongly suggests that ZnDPP HC feature involves a pentacoordinated Zn<sup>II</sup> centre. The calculated conductance value of pentacoordinated ZnDPP is already shown in Figure 3.6A. Although there is a close quantitative agreement between calculated and observed conductance value, the relative trend is unluckily slightly distorted. Nevertheless, the qualitative picture is fairly well captured. The projected density of states (PDOS) and transmission spectra of Ni<sup>II</sup>(DPP)(PyrMT)<sub>2</sub> and Zn<sup>II</sup>(DPP)(PyrMT) are shown in Figure 3.8.

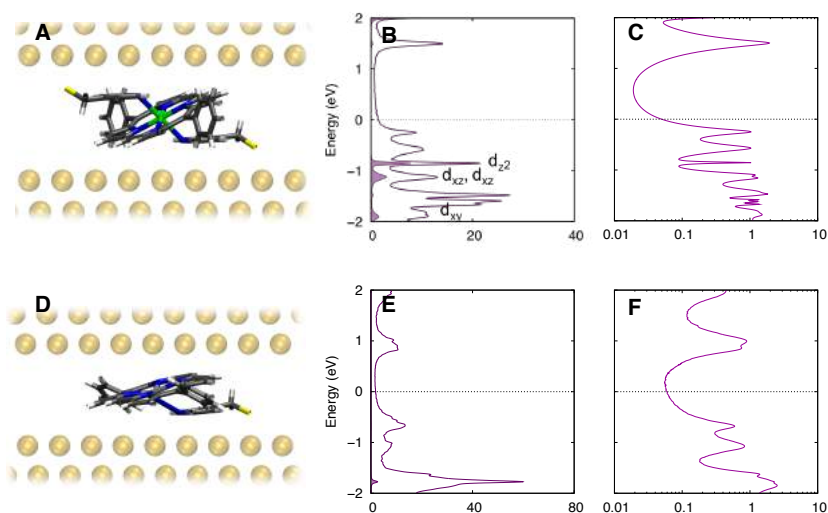


Figure 3.8. On top panel, scheme of Ni(DPP)(PyrMT)<sub>2</sub> HC feature (A), PDOS (B) and transmission spectrum (C). On the bottom panel, Zn(DPP)(PyrMT) (D), PDOS (E) and transmission spectrum (F).

Both Zn<sup>II</sup>(DPP)(PyrMT) and Ni<sup>II</sup>(DPP)(PyrMT)<sub>2</sub> present no dependence of the Ni tip magnetisation (Figure 3.4). For Zn<sup>II</sup> case, it is straightforward to see that a d<sup>10</sup> transition metal without chirality will not present magnetoresistance. For Ni<sup>II</sup> two possible spin states are available. The high-spin state is the ground state observed in bulk octahedral Ni<sup>II</sup> complexes (S=1). However, once Ni<sup>II</sup>(DPP)(PyrMT)<sub>2</sub> is formed within the electrodes, Ni<sup>II</sup> metal ion is in a highly distorted octahedral coordination sphere. The position of the axial ligand is strongly affected during the STM-BJ, probably stabilising the LS state with S=0. Single point TPSSh energy difference between high and low-spin states of Ni<sup>II</sup>(DPP)(PyrMT)<sub>2</sub> without electrodes scores a small preference of 6 kcal/mol for the high-spin state<sup>41</sup>. Qualitatively, the lone pair of N in PyrMT does not extensively overlap with the d<sub>z<sup>2</sup></sub> orbital in the junction, thus lying somewhere in between an actual octahedral and a square planar coordination. In the proposed geometries for HC feature, it is found larger M-N distances for Co (2.505 Å), Ni (2.752 Å), Cu (2.633 Å) and Zn (2.759

### 3 Study of Magnetoresistance on Metalloporphyrin Devices

Å) in comparison to common M-N values (2.00-2.20 Å). It all suggest that experimentally  $\text{Ni}^{\text{II}}(\text{DPP})(\text{PyrMT})_2$  is also a diamagnetic compound within electrodes and hence, not showing magnetoresistance.

The magnetoresistance systems have been measured under axial and perpendicular magnetisations (Figure 3.5). Although similar perpendicular magnetisation studies have been rationalised theoretically,<sup>22</sup> non-collinear spin calculations must be done to understand perpendicular magnetisation cases. This sort of calculations involves relativistic and spin-orbit contributions that are poorly introduced within the DFT+NEGF formalism. Therefore, the discussion is restricted to the axial magnetisation.

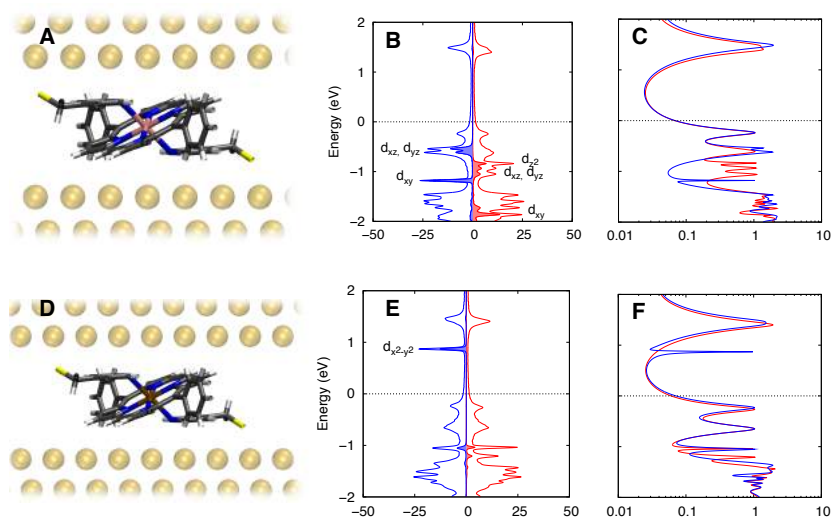


Figure 3.9. On top panel, scheme of  $\text{Co}(\text{DPP})(\text{PyrMT})_2$  HC feature, PDOS (b) and transmission spectrum (c). On the bottom panel,  $\text{Cu}(\text{DPP})(\text{PyrMT})_2$  (d), PDOS (e) and transmission spectrum (f). Red and blue curves represent alpha and beta spinorbitals. The filled curves of the same colours shows the contribution of the metal centre to the PDOS.

$\text{Co}(\text{DPP})(\text{PyrMT})_2$  and  $\text{Cu}(\text{DPP})(\text{PyrMT})_2$  have a common spin state with  $S=1/2$ . As shown in the previous chapter (section 2.3),  $\text{Co}^{\text{II}}$  centre is expected to be in the low-spin state. The unpaired electron breaks the

symmetry in the energy position of the alpha and beta spinorbitals, polarising the surroundings of the Fermi energy and leading to magnetoresistance. The PDOS and transmission spectra of both CoDPP and CuDPP junctions are shown in Figure 3.9.

Common to all metalloporphyrins, the main transmission channel is a porphyrinic orbital. For the paramagnetic cases, alpha and beta spinorbitals are slightly different in energy (Figure 3.9B and E). At first glance, CuDPP/PyrMT transmission (Figure 3.9F) spectrum presents a larger shift between alpha and beta spinorbitals in comparison to CoDPP/PyrMT (Figure 3.9C), thus suggesting that the former should present higher magnetoresistance, in opposition to experimental data. However, in the case of CoDPP/PyrMT, the  $\beta$   $d_{xz}$  and  $\beta$   $d_{yz}$  spinorbitals are relatively close to the Fermi level. Molecular orbitals with large metal contributions are very sensitive to the chosen DFT functional and their energy position can be slightly misplaced. Because those orbitals have some parallel contribution to the direction of charge transport, CoDPP/PyrMT might exhibit slightly larger magnetoresistance than CuDPP/PyrMT, in which perpendicular unoccupied  $\beta$   $d_{x^2-y^2}$  spinorbital is the closest metallic spinorbital to the Fermi energy. Moreover, the transmission spectrum of CuDPP/PyrMT (Figure 3.9F) presents a much narrower transmission peak for  $\beta$   $d_{x^2-y^2}$  than the peak observed for  $\beta$   $d_{xz}$  and  $\beta$   $d_{yz}$  in CoDPP/PyrMT junction (Figure 3.9C).

Given that both paramagnetic junctions share the same spin polarisation around the Fermi level, it follows that they will have the same response to the tip magnetisation, as it is observed experimentally (Figure 3.4).

### 3 Study of Magnetoresistance on Metalloporphyrin Devices

---

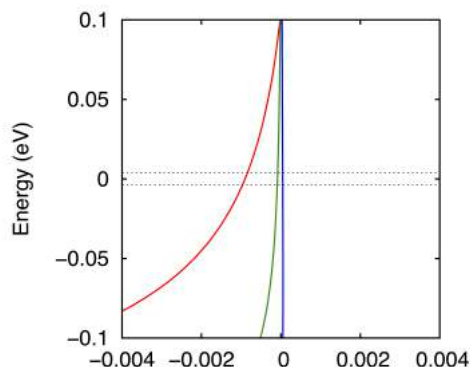


Figure 3.10. Alpha minus beta transmission around the Fermi energy for CoDPP/PyrMT for HC (red), MC (green) and LC (blue) junctions. Dotted lines represent the bias window applied. Negative x values represent an excess of beta transmission and positive values stand for an excess of alpha transmission. The area under each curve is proportional to the observed spin-polarised current.

Notwithstanding, the alpha/beta symmetry breaking of the unpaired electron on CoDPP/PyrMT and CuDPP/PyrMT junctions is observed on all three signatures because of the unpaired electron. The direct role of the metal centre on HC junction leads to a much higher asymmetry for this signature and almost unnoticeable asymmetry for MC and LC, as shown in Figure 3.10 for CoDPP/PyrMT.

In order to check the computed results using the PBE+U functional, the paramagnetic junctions are recalculated using TPSSh meta-hybrid functional. The transmission spectra are obtained using ARTAIOS code and shown in Figure 3.11 and Figure 3.12 along with the spinorbitals involved. The transmission obtained with TPSSh is fully consistent with the ones obtained with PBE+U. This indicates that the Hubbard correction removes the main deficiencies of the GGA functionals on the energy levels due to the self-interaction error.

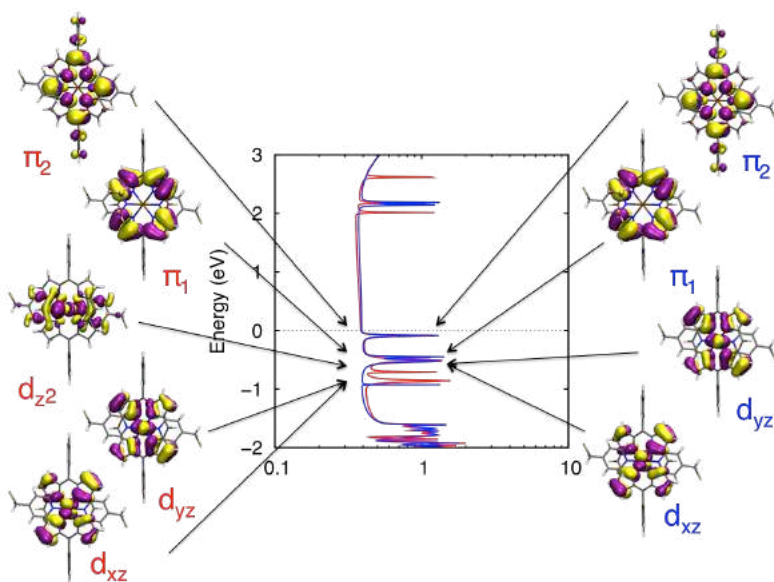


Figure 3.11. Transmission spectrum calculated using TPSSh meta-GGA functional using Gaussian and Artaios codes. The CoDPP orbitals involved close to the Fermi level are shown in the picture.

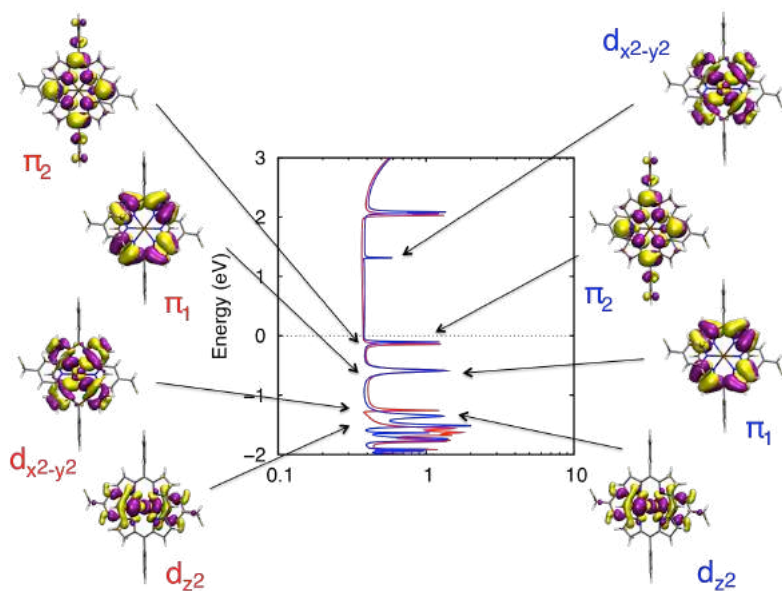


Figure 3.12. Transmission spectrum calculated using TPSSh meta-GGA functional using Gaussian and Artaios codes. The CuDPP orbitals involved close to the Fermi level are shown in the picture.

### 3 Study of Magnetoresistance on Metalloporphyrin Devices

---

The small asymmetry in the alpha and beta energy position is responsible of the modest magnetoresistance observed in the STM-BJ experiments for both paramagnetic metals. In  $M(\text{tzpy})_2(\text{NCX})_2$  complexes ( $M = \text{Fe}$  and  $\text{Co}$ ,  $X = \text{Se}$  and  $\text{S}$ ), for instance, the metal has a major role on the charge transport being a metallic  $\beta t_{2g}$  spinorbital the closest to the Fermi energy.<sup>46</sup> In such systems, a much larger asymmetry in the energy position is observed; hence leading to a greater magnetoresistance. Notwithstanding, it is worth to remark that CoDPP/PyrMT and CuDPP/PyrMT present the highest conductance value reported for a magnetoresistance system.

## 3.4 Conclusions

In this chapter, it was studied the magnetoresistance present in  $M^{\text{II}}\text{DPP}$  ( $M^{\text{II}} = \text{Co}^{\text{II}}$ ,  $\text{Ni}^{\text{II}}$ ,  $\text{Cu}^{\text{II}}$  and  $\text{Zn}^{\text{II}}$ ) junctions formed via supramolecular interactions between the metalloporphyrin and PyrMT, the latter attached to the bottom Au(111) electrode and to a polarised nickel tip as top electrode. The paramagnetic metalloporphyrins CoDPP and CuDPP showed magnetoresistance on their HC signature with their surroundings of the Fermi energy  $\beta$  polarised. The indirect role of the metallic centre in the mediation of the charge transport leads to a 3 and 2-fold magnetoresistance ratio when electrons are injected from the tip and 6 and 4-fold when injected from the substrate, being the alpha polarisation preferred. Remarkably, they exhibit the largest conductance reported for a room temperature magnetoresistance junction. The anisotropy of the magnetoresistance was also boarded experimentally by polarising the nickel tip orthogonally to the charge transport direction. In that case paramagnetic metalloporphyrins high conductance feature falls below the detection limit. Theoretical calculations aid to identify the expected magnitude of the magnetoresistance, but quantitative information seems

to be yet difficult to achieve, especially in the perpendicular magnetisation case.

NiDPP and ZnDPP are diamagnetic junctions, thus not showing magnetoresistance. The severely distorted octahedral coordination stabilises the low-spin of Ni<sup>II</sup> ( $S=0$ ). Zn<sup>II</sup> is a pentacoordinated closed-shell ion. This one shows the largest conductance of the studied metalloporphyrins due to the shorter transmission pathway.

Because of the aforementioned, the use of different transition metals and the chemical modification of the porphyrin may improve the magnetoresistance under a polarised tip, hence opening a way to obtain high conductance room temperature magnetoresistance junctions.



## 3.5 References

- 1 S. Sanvito, *Chem. Soc. Rev.* **2011**, *40*, 3336.
- 2 S. Sanvito, *Nat. Phys.* **2010**, *6*, 562.
- 3 A. Hirohata, K. Takanashi, *J. Phys. D-Applied Phys.* **2014**, *47*, 193001.
- 4 S. Fusil, V. Garcia, A. Barthelemy, M. Bibes, *Annu. Rev. Mater. Res.* **2014**, *44*, 91.
- 5 J. Sinova, S. O. Valenzuela, J. Wunderlich, C. H. Back, T. Jungwirth, *Rev. Mod. Phys.* **2015**, *87*, 1213.
- 6 D. Xiang, X. Wang, C. Jia, T. Lee, X. Guo, *Chem. Rev.* **2016**, 4318.
- 7 R. M. Metzger, *J. Mater. Chem.* **2008**, *18*, 4364.
- 8 D. K. James, J. M. Tour, *Top. Curr. Chem.* **2005**, *257*, 33.
- 9 S. V. Aradhya, L. Venkataraman, *Nat. Nanotechnol.* **2013**, *8*, 399.
- 10 S. Delprat, M. Galbiati, S. Tatay, B. Quinard, C. Barraud, F. Petroff, P. Seneor, R. Mattana, *J. Phys. D. Appl. Phys.* **2018**, *51*, 473001.
- 11 F. Djeghloul, F. Ibrahim, M. Cantoni, M. Bowen, L. Joly, S. Boukari, P. Ohresser, F. Bertran, P. Le Fevre, P. Thakur, F. Scheurer, T. Miyamachi, R. Mattana, P. Seneor, A. Jaafar, C. Rinaldi, S. Javaid, J. Arabski, J. P. Kappler, W. Wulfhekel, N. B. Brookes, R. Bertacco, A. Taleb-Ibrahimi, M. Alouani, E. Beaurepaire, W. Weber, *Sci. Rep.* **2013**, *3*, 1272.
- 12 S. Lach, A. Altenhof, K. Tarafder, F. Schmitt, M. E. Ali, M. Vogel, J. Sauther, P. M. Oppeneer, C. Ziegler, *Adv. Funct. Mater.* **2012**, *22*, 989.
- 13 A. Lodi Rizzini, C. Krull, A. Mugarza, T. Balashov, C. Nistor, R. Piqueret, S. Klyatskaya, M. Ruben, P. M. Sheverdyeva, P. Moras, C. Carbone, C. Stamm, P. S. Miedema, P. K. Thakur, V. Sessi, M. Soares, F. Yakhou-Harris, J. C. Cezar, S. Stepanow, P.

- Gambardella, *Surf. Sci.* **2014**, *630*, 361.
- 14 C. Iacovita, M. V. Rastei, B. W. Heinrich, T. Brumme, J. Kortus, L. Limot, J. P. Bucher, *Phys. Rev. Lett.* **2008**, *101*, 116602.
- 15 J. Brede, N. Atodiresei, S. Kuck, P. Lazić, V. Caciuc, Y. Morikawa, G. Hoffmann, S. Blügel, R. Wiesendanger, *Phys. Rev. Lett.* **2010**, *105*, 47204.
- 16 S. Schmaus, A. Bagrets, Y. Nahas, T. K. Yamada, A. Bork, M. Bowen, E. Beaupair, F. Evers, W. Wulfhekel, *Nat. Nanotechnol.* **2011**, *6*, 185.
- 17 T. Komeda, H. Isshiki, J. Liu, Y.-F. Zhang, N. Lorente, K. Katoh, B. K. Breedlove, M. Yamashita, *Nat. Commun.* **2011**, *2*, 217.
- 18 A. Lodi Rizzini, C. Krull, T. Balashov, J. J. Kavich, A. Mugarza, P. S. Miedema, P. K. Thakur, V. Sessi, S. Klyatskaya, M. Ruben, S. Stepanow, P. Gambardella, *Phys. Rev. Lett.* **2011**, *107*, 177205.
- 19 J. Schwobel, Y. S. Fu, J. Brede, A. Dilullo, G. Hoffmann, S. Klyatskaya, M. Ruben, R. Wiesendanger, *Nat. Commun.* **2012**, *3*.
- 20 S. Karan, C. García, M. Karolak, D. Jacob, N. Lorente, R. Berndt, *Nano Lett.* **2018**, *18*, 88.
- 21 S. L. Kawahara, J. Lagoute, V. Repain, C. Chacon, Y. Girard, S. Rousset, A. Smogunov, C. Barreteau, *Nano Lett.* **2012**, *12*, 4558.
- 22 J. J. Li, M. L. Bai, Z. Bin Chen, X. S. Zhou, Z. Shi, M. Zhang, S. Y. Ding, S. M. Hou, W. Schwarzacher, R. J. Nichols, B. W. Mao, *J. Am. Chem. Soc.* **2015**, *137*, 5923.
- 23 D. Rakhmilevitch, S. Sarkar, O. Bitton, L. Kronik, O. Tal, *Nano Lett.* **2016**, *16*, 1741.
- 24 R. Vincent, S. Klyatskaya, M. Ruben, W. Wernsdorfer, F. Balestro, *Nature* **2012**, *488*, 357.
- 25 M. Urdampilleta, S. Klyatskaya, J. P. Cleuziou, M. Ruben, W. Wernsdorfer, *Nat. Mater.* **2011**, *10*, 502.
- 26 S. Wagner, F. Kisslinger, S. Ballmann, F. Schramm, R.

### 3 Study of Magnetoresistance on Metalloporphyrin Devices

---

- Chandrasekar, T. Bodenstein, O. Fuhr, D. Secker, K. Fink, M. Ruben, H. B. Weber, *Nat. Nanotechnol.* **2013**, *8*, 575.
- 27 A. C. Aragonès, D. Aravena, J. I. Cerdá, Z. Acís-Castillo, H. Li, J. A. Real, F. Sanz, J. Hihath, E. Ruiz, I. Díez-Pérez, *Nano Lett.* **2016**, *16*, 218.
- 28 M. Johnson, *Handbook of Spin Transport and Magnetism*, Chapman And Hall/CRC, **2011**.
- 29 J. P. Perdew, K. Burke, M. Ernzerhof, *Phys. Rev. Lett.* **1996**, *77*, 3865.
- 30 J. M. Soler, E. Artacho, J. D. Gale, A. García, J. Junquera, P. Ordejón, D. Sánchez-Portal, *J. Phys. Condens. Matter* **2002**, *14*, 2745.
- 31 A. García, N. Papior, A. Akhtar, E. Artacho, V. Blum, E. Bosoni, P. Brandimarte, M. Brandbyge, J. I. Cerdá, F. Corsetti, R. Cuadrado, V. Dikan, J. Ferrer, J. Gale, P. García-Fernández, V. M. García-Suárez, S. García, G. Huhs, S. Illera, R. Korytár, P. Koval, I. Lebedeva, L. Lin, P. López-Tarifa, S. G. Mayo, S. Mohr, P. Ordejón, A. Postnikov, Y. Pouillon, M. Pruneda, R. Robles, D. Sánchez-Portal, J. M. Soler, R. Ullah, V. W. Z. Yu, J. Junquera, *J. Chem. Phys.* **2020**, *152*, 204108.
- 32 J. Ferrer, C. J. Lambert, V. M. García-Suárez, D. Z. Manrique, D. Visontai, L. Oroszlany, R. Rodríguez-Ferradás, I. Grace, S. W. D. Bailey, K. Gillemot, H. Sadeghi, L. A. Algharagholy, *New J. Phys.* **2014**, *16*, 93029.
- 33 J. Tao, J. P. Perdew, V. N. Staroverov, G. E. Scuseria, *Phys. Rev. Lett.* **2003**, *91*, 146401.
- 34 V. N. Staroverov, G. E. Scuseria, J. Tao, J. P. Perdew, *J. Chem. Phys.* **2003**, *119*, 12129.
- 35 M. J. Frisch, G. W. Trucks, H. B. Schlegel, G. E. Scuseria, M. A. Robb, J. R. Cheeseman, G. Scalmani, V. Barone, B. Mennucci, G. A. Petersson, H. Nakatsuji, M. Caricato, X. Li, H. P. Hratchian, A.

- F. Izmaylov, J. Bloino, G. Zheng, J. L. Sonnenberg, M. Hada, M. Ehara, K. Toyota, R. Fukuda, J. Hasegawa, M. Ishida, T. Nakajima, Y. Honda, O. Kitao, H. Nakai, T. Vreven, J. A. Montgomery Jr., J. E. Peralta, F. Ogliaro, M. Bearpark, J. J. Heyd, E. Brothers, K. N. Kudin, V. N. Staroverov, R. Kobayashi, J. Normand, K. Raghavachari, A. Rendell, J. C. Burant, S. S. Iyengar, J. Tomasi, M. Cossi, N. Rega, J. M. Millam, M. Klene, J. E. Knox, J. B. Cross, V. Bakken, C. Adamo, J. Jaramillo, R. Gomperts, R. E. Stratmann, O. Yazyev, A. J. Austin, R. Cammi, C. Pomelli, J. W. Ochterski, R. L. Martin, K. Morokuma, V. G. Zakrzewski, G. A. Voth, P. Salvador, J. J. Dannenberg, S. Dapprich, A. D. Daniels, Ö. Farkas, J. B. Foresman, J. V. Ortiz, J. Cioslowski, D. J. Fox, *Gaussian, Inc. Wallingford CT* **2009**.
- 36 T. H. J. Dunning, P. J. Hay, in *Mod. Theor. Chem.* (Ed: H.F. Schaefer III), Plenum Press, **1977**, pp. 1–28.
- 37 P. J. Hay, W. R. Wadt, *J. Chem. Phys.* **1985**, *82*, 270.
- 38 W. R. Wadt, P. J. Hay, *J. Chem. Phys.* **1985**, *82*, 284.
- 39 P. J. Hay, W. R. Wadt, *J. Chem. Phys.* **1985**, *82*, 299.
- 40 C. Herrmann, L. Groß, T. Steenbock, G. C. Solomon, **2015**.
- 41 J. Cirera, M. Via-Nadal, E. Ruiz, *Inorg. Chem.* **2018**, *57*, 14907.
- 42 C. Herrmann, G. C. Solomon, J. E. Subotnik, V. Mujica, M. A. Ratner, *J. Chem. Phys.* **2010**, *132*, 24103.
- 43 J. Mielke, F. Hanke, M. V. Peters, S. Hecht, M. Persson, L. Grill, *J. Am. Chem. Soc.* **2015**, *137*, 1844.
- 44 H. Kim, W. J. Son, W. J. Jang, J. K. Yoon, S. Han, S. J. Kahng, *Phys. Rev. B - Condens. Matter Mater. Phys.* **2009**, *80*, 245402.
- 45 T. Yokoyama, S. Yokoyama, T. Kamikado, S. Mashiko, *J. Chem. Phys.* **2001**, *115*, 3814.
- 46 A. C. Aragonès, D. Aravena, F. J. Valverde-Muñoz, J. A. Real, F. Sanz, I. Díez-Pérez, E. Ruiz, *J. Am. Chem. Soc.* **2017**, *139*, 5768.

## Annex A: Low and Medium conductance plots

The following figures correspond to scheme, projected density of states (PDOS) and transmission spectra of the medium conductance (MC) and low conductance (LC) features of MDPP/PyrMT (M = Co, Ni, Cu and Zn) junctions.

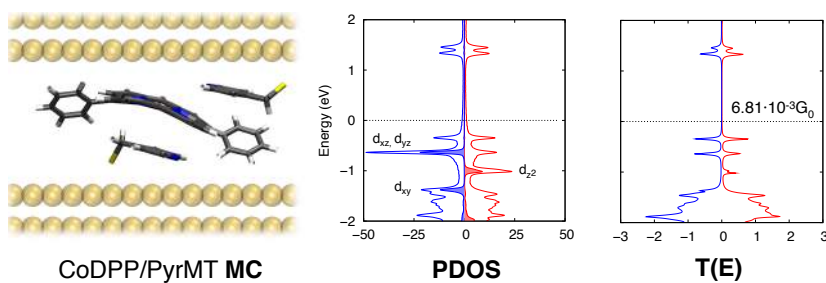


Figure A1. Representation of the junction (left), PDOS (centre) and transmission spectrum (right) of CoDPP/PyrMT MC feature. Alpha and beta contributions are represented in the red and blue curves, respectively. Filled curves of the same colours stand for the metal contribution.

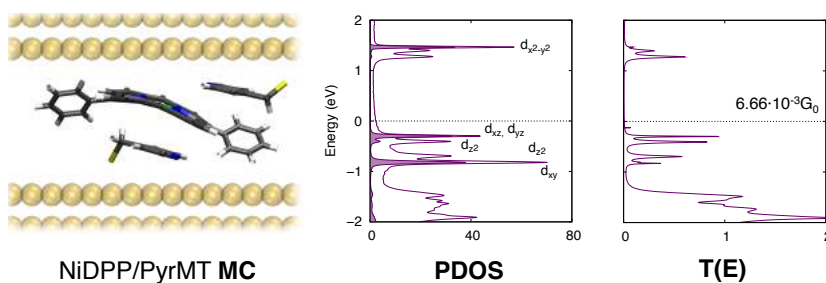


Figure A2. Representation of the junction (left), PDOS (centre) and transmission spectrum (right) of NiDPP/PyrMT MC feature. Filled curve stands for the metal contribution

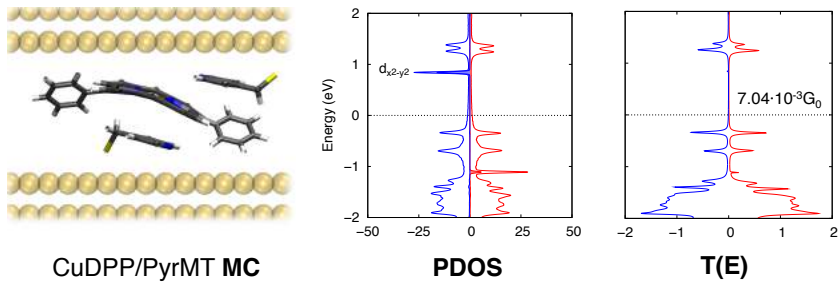


Figure A3. Representation of the junction (left), PDOS (centre) and transmission spectrum (right) of CuDPP/PyMT MC feature. Alpha and beta contributions are represented in the red and blue curves, respectively. Filled curves of the same colours stand for the metal contribution.

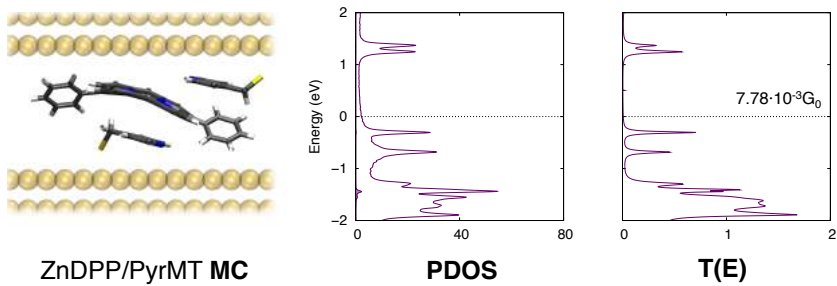


Figure A4. Representation of the junction (left), PDOS (centre) and transmission spectrum (right) of ZnDPP/PyMT MC feature. Filled curve stands for the metal contribution

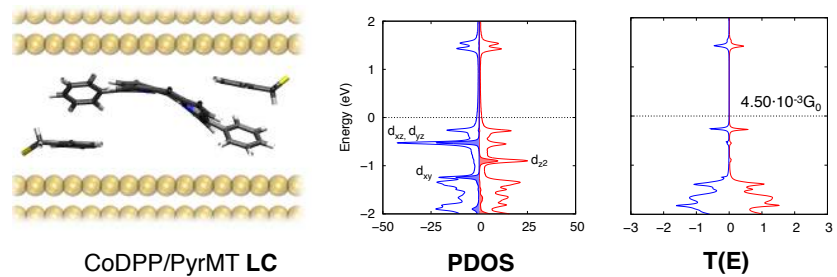


Figure A5. Representation of the junction (left), PDOS (centre) and transmission spectrum (right) of CoDPP/PyMT LC feature. Alpha and beta contributions are represented in the red and blue curves, respectively. Filled curves of the same colours stand for the metal contribution.

### 3 Study of Magnetoresistance on Metalloporphyrin Devices

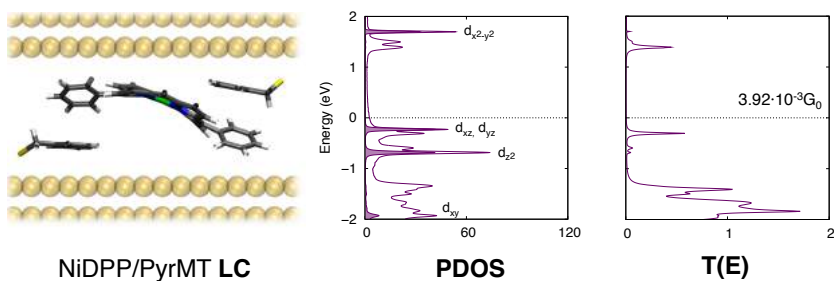


Figure A6. Representation of the junction (left), PDOS (centre) and transmission spectrum (right) of NiDPP/PyMT LC feature. Filled curve stands for the metal contribution

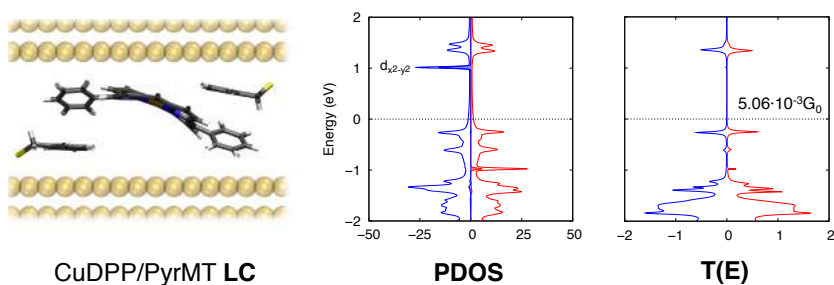


Figure A7. Representation of the junction (left), PDOS (centre) and transmission spectrum (right) of CuDPP/PyMT LC feature. Alpha and beta contributions are represented in the red and blue curves, respectively. Filled curves of the same colours stand for the metal contribution.

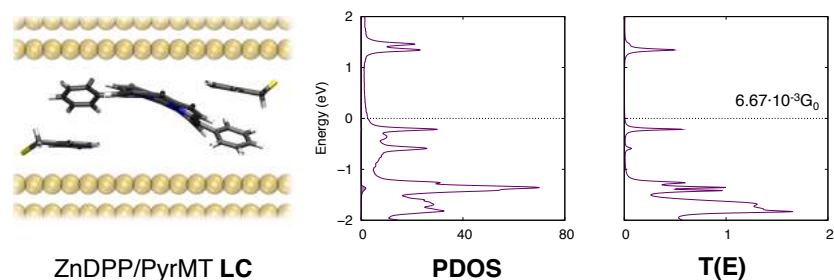


Figure A8. Representation of the junction (left), PDOS (centre) and transmission spectrum (right) of ZnDPP/PyMT LC feature. Filled curve stands for the metal contribution.

## 4 STUDY OF LARGE AREA EGAIN MAGNETIC JUNCTIONS

Up to now, the thesis was focused on single molecule nanojunctions. In the study over metalloporphyrins, it was shown that single molecule experiments along with theoretical calculations allow an unexpected deep understanding of the nanojunction despite the lack of *in situ* characterisation.

Now the attention is turned to extensive systems. These systems are usually closer to actual molecular devices. Notwithstanding, as it will be shown in this chapter, large area measurements are in detriment of the strong fundamental understanding that gives single molecule measurements. The conductance is measured on an ensemble of molecules that lies on a bottom electrode with many different conformations; hence the observed conductance is an average over the ensemble.

In this chapter it is presented two collaborations where DFT calculations are provided for the understanding of the electron transport phenomena using EGaIn electrodes. Although there are a few ways to measure large area nanojunctions, this one has been shown to be a robust methodology (section 1.2.5). The EGain electrode is based on the use of non-



Newtonian liquid-metal EGaIn/GaO<sub>x</sub>. The GaO<sub>x</sub> oxide is 0.7 nm thick preventing the GaIn to form alloys with the bottom electrode, but letting electrons tunnel through. Theoretical approximations to model EGaIn/GaO<sub>x</sub> electrode are often based on comparison of the HOMO/LUMO energy distance of the isolated molecule to the Fermi energy of the electrode,<sup>1</sup> tight-binding models<sup>2</sup> or simply picturing it between gold electrodes.<sup>3,4</sup> A more refined manner is to substitute EGaIn by Ag electrode because of the similarity of their Fermi energies.<sup>5</sup> However, no explicit model of the electrode has been published.

### 4.1 Binuclear Cu<sup>II</sup>-Ln<sup>III</sup> complexes

#### 4.1.1 Motivation

In collaboration with Dr. Monakhov group (IOM, Leipzig), here it is done a computational study of a Au-heterometal complex-EGaIn spin-polarised junction.<sup>6,7</sup> The heterometallic complex self-assembled monolayer consist of a binuclear Cu<sup>II</sup>-Ln<sup>III</sup> system of the type [CuLn(L-SMe)<sub>2</sub>(OOCMe)<sub>2</sub>(NO<sub>3</sub>)] · xMeOH (x = 0.75-1) and the chosen lanthanides (Ln) are Gd, Tb, Dy.<sup>8-16</sup> The same compound is also synthesised using Y<sup>III</sup> cation. This sort of systems has been shown to exhibit structural motifs of different complexity along with interesting magnetic and electrical conductivity properties.<sup>17</sup>

The challenge to deal with is to explain the observed indistinguishable charge transport properties of the Gd, Tb, Dy and Y compounds (further details on the next section). Unluckily, no realistic model of the junction can be calculated due to the lack of an X-ray structure of EGaIn electrode. Moreover, the single determinant nature of DFT calculations is not able to

describe properly Tb and Dy compounds because of their degenerated ground state.

#### 4.1.2 Previous work

In Monakhov's group, they provided a detailed description of the preparation, magnetochemistry, adsorption characteristics and electronic transport measurements of  $[\text{CuLn}(\text{L} \cdot \text{SMe})_2(\text{OOCMe})_2(\text{NO}_3)] \cdot x \text{MeOH}$  ( $x = 0.75 - 1$ ) with Ln = Gd (1), Tb (2), Dy (3) and also Y (4) (Figure 4.1). Here, a brief summary of the highlights is reported.<sup>18</sup>

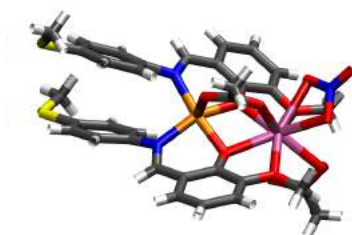


Figure 4.1. Molecular structure of Compounds 1-4.

Colours of the atoms are C: Grey, S: Yellow, H: White, N: Blue, Cu: Orange O: Red Ln: Mauve.

Adapted figure.<sup>18</sup>

As shown in Figure 4.1, X-ray diffraction shown that compounds **1-4** are quasi isostructural with  $P_1^2$  space group. The Ln<sup>III</sup> (and Y<sup>III</sup>) atoms are nine-coordinated while the Cu<sup>II</sup> centre is square pyramidal. The two metal centres are connected by two deprotonated tridentate Schiff base ligands (L · SMe<sup>-</sup>) and an acetate ligand, being 3.40 Å apart.

Regarding magnetism and magnetochemical modelling, the  $X_m T$  values for the four compounds are well within or close to the expected. In the case of Cu<sup>II</sup> and Gd<sup>III</sup> pair, the Gd<sup>III</sup> ion remains, to a very good

## 4 Study of Large Area EGaIn Magnetic Junctions

approximation, a pure  $S=7/2$  centre as indicates the molar magnetisation at 2.0 K and 5.0 T (Figure 4.2).

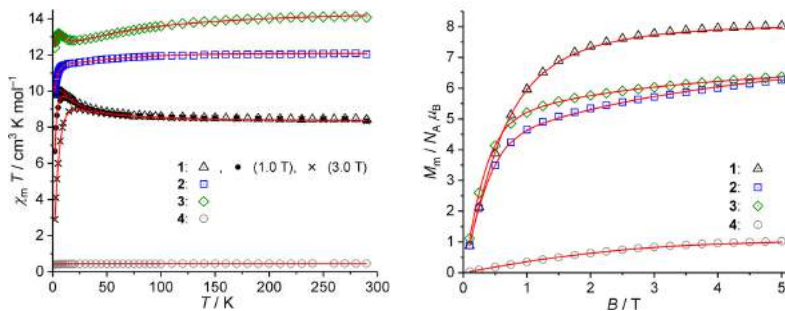


Figure 4.2.  $X_m T$  dependence with the temperature (left) and field dependence of molar magnetisation  $M_m$  (right) for 1-4 compounds. Open symbols: experimental data at 0.1 T (left) and 2.0 K (right), respectively. The least-square fit is represented as a solid red line. Adapted figure.<sup>18</sup>

The fitting of the data estimates the strength and magnitude of exchange interaction. In the case of CuGd pair, it was found a ferromagnetic interaction in the typical range for 3d-4f exchange interactions.<sup>19</sup> For the rest of lanthanides, ferromagnetic interactions of the same sort are obtained.

To know more about how the SAM is formed upon the gold substrate, Fourier Transform Infrared (FT-IR) and Fourier Transformed Infrared Reflection Absorption Spectroscopy (FT-IRRAS) characterisation was performed. The comparison of FT-IR and FT-IRRAS of HL-SMe ligand indicates that it remains essentially unchanged upon absorption.<sup>20</sup> The FT-IR of compounds **1-4** yields the same spectra except for small shifts; hence concluding that they are isostructural, as announced before. Figure 4.3 shows the FT-IR and FT-IRRAS of compound **2**.<sup>21</sup> The red curve shows a high-quality FT-IRRAS spectrum (IRRAS 1) obtained using a small amount of solvent for washing the Au substrate. Then, the same substrate is dipped into methanol and another FT-IRRAS is obtained (IRRAS 2). The intensity of the peaks diminishes (as expected) but the remaining

signals indicate that compound **2** still forms a thin layer – presumably a monolayer.

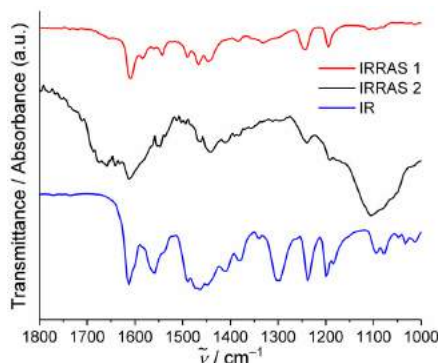


Figure 4.3. FT-IR (blue), FT-IRRAS spectra (red) and after dipping the SAM in methanol (black) of Compound **2**, Cu<sup>II</sup>-Tb<sup>III</sup> pair. Adapted figure.<sup>18</sup>

Further characterisation using STM and ellipsometry indicates that the monolayer is indeed formed with 1.3 nm thickness, but not as densely packed as the ones formed by, for example, alkanethiols.<sup>22–24</sup>

After the characterisation, large area charge transport measurements on compounds **1-4** were carried on. The SAM was constructed on Au<sup>TS</sup> (bottom electrode)<sup>25</sup> by immersion in a 0.1 mM methanolic solution of the target compound overnight. The EGaIn lead works as top electrode, employed in a wide variety of SAM measurements.

Figure 4.4 shows the density current  $J(V)$  of compounds **1-4**. Very slight differences in the shape and magnitude between the different compounds are found. Also, the error bars make impossible to distinguish between compounds.

## 4 Study of Large Area EGaIn Magnetic Junctions

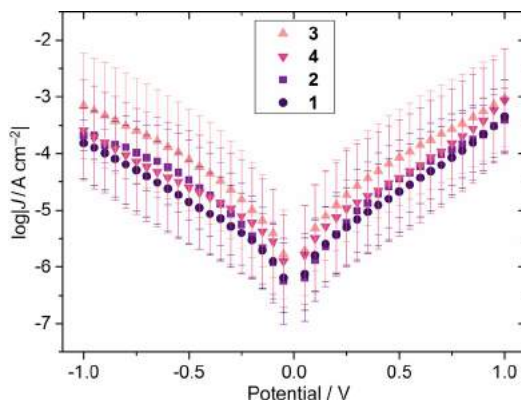


Figure 4.4. Plots of the current density vs applied voltage for compounds 1-4. Values at  $V=0$  V are omitted for clarity. Error bars represents the standard deviation of Gaussian fits.<sup>18</sup>

The above plot can be replotted in Fowler-Nordheim coordinates ( $\ln(\frac{1}{\sqrt{V}})$  vs  $\frac{1}{\sqrt{V}}$ ) to obtain the energy level alignment inside the junction.<sup>26</sup> For the four compounds, the transition voltage ( $V_T$ ) obtained is close to 0.3 V. This value can be attributed to  $\beta$   $d_{x^2-y^2}$  spinorbital of  $\text{Cu}^{\text{II}}$  centre, which lies close to the Fermi level and is present in all compounds. The same was proposed for ferrocene-containing molecules in which the  $\text{Fe}^{\text{II}}$  centre mediates the charge transport.<sup>27</sup>

### 4.1.3 Computational details

Transport properties of compounds **1** and **4** were studied using a combination of DFT+EGF (section 1.5). The mean-field electronic structure was obtained using SIESTA code.<sup>28,29</sup> The compounds **1** and **4** were placed between a bottom gold electrode consisting of 5 gold layers of  $5 \times 4$  unit cells and a top electrode of 3 gold layers and two shaped triangular shapes, in order to bond properly the methylthiol to the electrode (see Figure 4.5).

The wavefunction was expanded using the generalised-gradient approximation PBE<sup>30</sup> and valence pseudopotentials and double- $\zeta$  polarised

basis set for all atoms, except for gold, where one-electron pseudopotential and single- $\zeta$  polarised basis set was employed instead. This pseudopotential is not suitable for geometry optimisation but works smoothly for charge transport calculations.<sup>31</sup> A 20x26x1 k-point grid was chosen for the complete system and a 20x26x51 for the electrode calculation. Gollum code<sup>32</sup> employs the Equilibrium Green's function (EGF) to obtain the transmission spectra of compounds **1** and **4**.

#### 4.1.4 Results

To understand the  $J(V)$  characteristics of compounds **1-4**, it was performed DFT+EGF calculations to obtain the electronic structure and transmission spectra. First of all, the discussion is unluckily forced to be restricted to compounds **1** and **4**, CuGd and CuY systems. The single determinant nature of DFT cannot describe the degenerated ground states of Tb<sup>III</sup> and Dy<sup>III</sup>.<sup>33</sup> To tackle degenerated ground states it is needed to use a multideterminant description of the wavefunction. In such description, the concept of molecular orbital is lost, and hence the Green's function formulation cannot be applied. Gd<sup>III</sup> and Y<sup>III</sup> ions have, however, non-degenerated ground states.

To model the nanojunction, it was not found an X-ray structure for the EGaIn electrode. Nevertheless, in this sort of junctions the SAM itself and not the electrodes dominates the charge transport.<sup>5</sup> This is further supported by the experimental data: Monakhov's group proved with the IR and IRRAS measurements (section 4.1.2) that compounds **1-4** are weakly coupled with the electrodes and neighbouring molecules. From this, a gold electrode substitutes the EGaIn top lead and no intermolecular interactions are considered in the junction,<sup>34</sup> as shown in Figure 4.5.

## 4 Study of Large Area EGaIn Magnetic Junctions

---

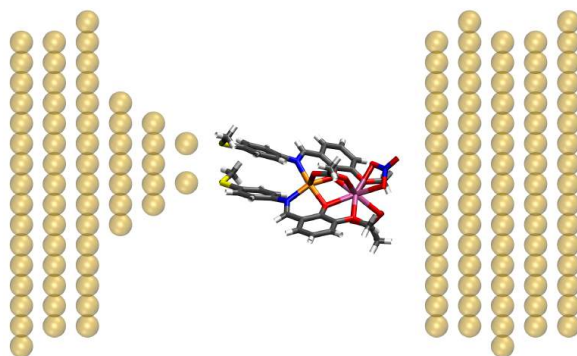


Figure 4.5. Model nanojunction for compounds **1** and **4**. The EGaIn top electrode is substituted with five layers of gold due to the weak interaction of the SAM with the electrode. Only a single molecule is considered in the junction because only weak intermolecular interactions are expected. Colours of the atoms are C: Grey, S: Yellow, H: White, N: Blue, Cu: Orange O: Red Ln: Mauve, Au: Golden. Adapted figure.<sup>18</sup>

The optimisation of the junction is very important to obtain conductance values as accurate as possible. However, it is the most expensive part of the workflow. To obtain the conductance value of a single molecule in a large area measurement involves the estimation of the density of molecules in the bottom electrode. Although it is possible to do such estimation, the substitution of the EGaIn top electrode by gold would distort the quantitative value by default. Fortunately, a qualitative discussion is enough to understand the undistinguishable  $J(V)$  curves.

Relying on the weak interactions with the electrodes, here it is elided the optimisation and the molecule is directly placed within electrodes keeping a typical Au-S distance of 2.2 Å and 2.6 Å for Au-O distance. The height of the molecule upon the bottom Au electrode scores 1.5 nm, in very good agreement with the value 1.3 nm obtained in the ellipsometry measurements (section 4.1.2).

The electronic structure calculation of **1** indicates a ferromagnetic ground state interaction between the Cu<sup>II</sup> and Gd<sup>III</sup> magnetic centres, in agreement with the experimental data. In the next two figures, it is shown

the projected density of states (PDOS) and transmission spectra ( $T(E)$ ) of compound **1** and **4** (Figure 4.6 and Figure 4.7).

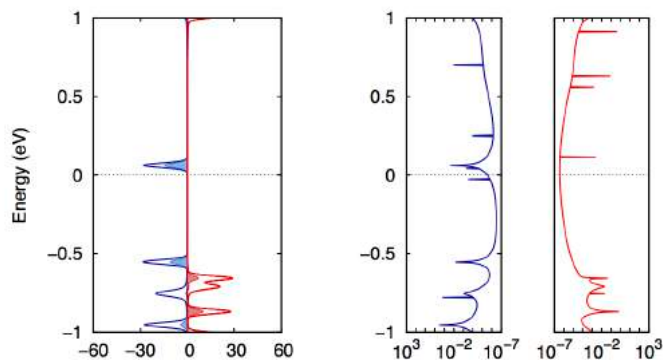


Figure 4.6. Projected Density of States (left) and logarithmic transmission spectrum (right) of CuGd system. Red and blue curves stand for alpha and beta contributions and filled curves represents the contribution of the  $\text{Cu}^{\text{II}}$  centre.<sup>18</sup>

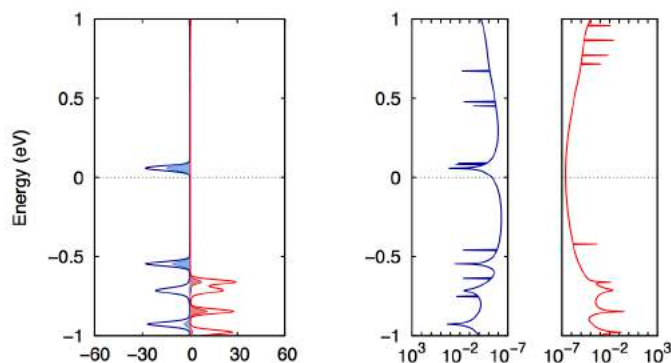


Figure 4.7. Projected Density of States (left) and logarithmic transmission spectrum (right) of CuY system. Red and blue curves stand for alpha and beta contributions and filled curves represents the contribution of the  $\text{Cu}^{\text{II}}$  centre.<sup>18</sup>

As it can be seen, the PDOS of Figure 4.6 and Figure 4.7 are very similar. Both PDOS show a single peak placed at 0.1 eV above the Fermi energy (set at  $E = E_{\text{F}} = 0$ ) with a high contribution of the  $\text{Cu}^{\text{II}}$  centre. This lonely orbital is, as Monakhov group suggested, the  $\beta d_{x^2-y^2}$  spinorbital of the  $\text{Cu}^{\text{II}}$ , present in both (presumably, all) compounds. The transmission



## 4 Study of Large Area EGaIn Magnetic Junctions

---

spectra show the corresponding transmission peak for this orbital. Because of its proximity to the Fermi energy, it constitutes the main conduction channel. The spinorbitals related with the lanthanides (and yttrium) are too deep in energy to become relevant transmission channels. Hence, it is clear that compounds **1-4** have indistinguishable  $J(V)$  curves, because their transmission spectra are to a large extent independent of the lanthanide atom for a wide energy range. The discrepancy between the  $E - E_F$  (0.1 V) and the experimental transition voltage (0.3 V) can be mainly related to the substitution of the EGaIn lead with a gold electrode. Nevertheless, the qualitative picture of the junction remains valid.

In sight of the spin-polarised main transmission channel, it is expected to observe magnetoresistance for all the set of compounds upon their contact with a magnetic electrode.

### 4.1.5 Conclusions

When thousands of molecules are measured at the same time, many possible configurations are measured. A single conductance value for a given bias is obtained for large area measurements unlike single molecule measurements, where it is possible to distinguish between conformations (conductance signatures).

Large area measurements can be evaluated using the same procedure as for single molecule junctions. To obtain quantitative results, the density of molecules per surface area must be determined. However, the qualitative picture may be sufficient to explain the experimental data. For interacting SAMs, it is needed to include more than one molecule in the junction. For weakly interacting SAMs, a single molecule model is enough to understand the charge transport.

In the case of CuLn compounds, the single molecule junction model is enough to qualitatively understand the indistinguishable  $J(V)$  curves observed experimentally. Cu<sup>II</sup>  $\beta$   $d_{x^2-y^2}$  spinorbital is the common transmission channel for compounds with different lanthanides (Gd, Tb, Dy and Y), giving a similar  $J(V)$  curve regardless of the lanthanide in the compound. Because of the spin-polarised orbital, magnetoresistance should be expected for these compounds when measured using magnetic electrodes.

To change the Cu<sup>II</sup> centre is expected to strongly affect the magnetic and charge transport properties of the selected compounds. The modification of the Ln<sup>III</sup> centre, however, should only modify the magnetic behaviour. Only early lanthanides with orbitals closer to the Fermi energy might modify the charge transport measurements.<sup>35</sup>

### 4.1.6 References

- 1 D. Fracasso, M. I. Muglali, M. Rohwerder, A. Terfort, R. C. Chiechi, *J. Phys. Chem. C* **2013**, *117*, 11367.
- 2 F. Mirjani, J. M. Thijssen, G. M. Whitesides, M. A. Ratner, *ACS Nano* **2014**, *8*, 12428.
- 3 M. Baghbanzadeh, C. M. Bowers, D. Rappoport, T. Zaba, M. Gonidec, M. H. Al-Sayah, P. Cyganik, A. Aspuru-Guzik, G. M. Whitesides, *Angew. Chemie - Int. Ed.* **2015**, *54*, 14743.
- 4 S. Kumar, J. T. Van Herpt, R. Y. N. Gengler, B. L. Feringa, P. Rudolf, R. C. Chiechi, *J. Am. Chem. Soc.* **2016**, *138*, 12519.
- 5 W. F. Reus, M. M. Thuo, N. D. Shapiro, C. A. Nijhuis, G. M. Whitesides, *ACS Nano* **2012**, *6*, 4806.
- 6 R. C. Chiechi, E. A. Weiss, M. D. Dickey, G. M. Whitesides, *Angew. Chemie - Int. Ed.* **2008**, *47*, 142.
- 7 A. Wan, C. S. Suchand Sangeeth, L. Wang, L. Yuan, L. Jiang, C. A. Nijhuis, *Nanoscale* **2015**, *7*, 19547.
- 8 J. Wu, X. L. Li, M. Guo, L. Zhao, Y. Q. Zhang, J. Tang, *Chem. Commun.* **2018**, *54*, 1065.
- 9 S. Biswas, P. Bag, S. Das, S. Kundu, J. van Leusen, P. Kögerler, V. Chandrasekhar, *Eur. J. Inorg. Chem.* **2017**, *2017*, 1129.
- 10 V. Baskar, K. Gopal, M. Helliwell, F. Tuna, W. Wernsdorfer, R. E. P. Winpenny, *Dalt. Trans.* **2010**, *39*, 4747.
- 11 Z. Y. Li, J. S. Yang, R. Bin Liu, J. J. Zhang, S. Q. Liu, J. Ni, C. Y. Duan, *J. Chem. Soc. Dalt. Trans.* **2012**, *41*, 13264.
- 12 Z. Y. Li, Y. X. Wang, J. Zhu, S. Q. Liu, G. Xin, J. J. Zhang, H. Q. Huang, C. Y. Duan, *Cryst. Growth Des.* **2013**, *13*, 3429.
- 13 G. Xiong, H. Xu, J. Z. Cui, Q. L. Wang, B. Zhao, *Dalt. Trans.* **2014**, *43*, 5639.
- 14 G. L. Zhuang, W. X. Chen, H. X. Zhao, X. J. Kong, L. S. Long, R.

- Bin Huang, L. S. Zheng, *Inorg. Chem.* **2011**, *50*, 3843.
- 15 J. J. Zhang, S. M. Hu, S. C. Xiang, T. Sheng, X. T. Wu, Y. M. Li, *Inorg. Chem.* **2006**, *45*, 7173.
- 16 T. Ueno, T. Fujinami, N. Matsumoto, M. Furusawa, R. Irie, N. Re, T. Kanetomo, T. Ishida, Y. Sunatsuki, *Inorg. Chem.* **2017**, *56*, 1679.
- 17 A. Kondinski, K. Y. Monakhov, *Chem. - A Eur. J.* **2017**, *23*, 7841.
- 18 S. Schmitz, A. Kovalchuk, A. Martín-Rodríguez, J. Van Leusen, N. V. Izarova, S. D. M. Bourone, Y. Ai, E. Ruiz, R. C. Chiechi, P. Kögerler, K. Y. Monakhov, *Inorg. Chem.* **2018**, *57*, 9274.
- 19 J. P. Sutter, M. L. Kahn, in *Magn. Mol. to Mater. V*, **2005**, pp. 161–187.
- 20 S. Schmitz, J. van Leusen, N. V. Izarova, S. D. M. Bourone, A. Ellern, P. Kögerler, K. Y. Monakhov, *Polyhedron* **2018**, *144*, 144.
- 21 G. Socrates, *Infrared and Raman Characteristic Group Frequencies*, Wiley, **2001**.
- 22 D. J. Lavrich, S. M. Wetterer, S. L. Bernasek, G. Scoles, *J. Phys. Chem. B* **1998**, *102*, 3456.
- 23 B. H. Huisman, D. M. Rudkevich, F. C. J. M. Van Veggel, D. N. Reinhoudt, *J. Am. Chem. Soc.* **1996**, *118*, 3523.
- 24 E. U. T. van Velzen, J. F. J. Engbersen, D. N. Reinhoudt, *J. Am. Chem. Soc.* **1994**, *116*, 3597.
- 25 E. A. Weiss, G. K. Kaufman, J. K. Kriebel, Z. Li, R. Schalek, G. M. Whitesides, *Langmuir* **2007**, *23*, 9686.
- 26 J. M. Beebe, B. Kim, J. W. Gadzuk, C. D. Frisbie, J. G. Kushmerick, *Phys. Rev. Lett.* **2006**, *97*, 26801.
- 27 A. R. Garrigues, L. Yuan, L. Wang, E. R. Mucciolo, D. Thompon, E. Del Barco, C. A. Nijhuis, *Sci. Rep.* **2016**, *6*, 26517.
- 28 J. M. Soler, E. Artacho, J. D. Gale, A. García, J. Junquera, P. Ordejón, D. Sánchez-Portal, *J. Phys. Condens. Matter* **2002**, *14*, 2745.
- 29 A. García, N. Papior, A. Akhtar, E. Artacho, V. Blum, E. Bosoni,

- P. Brandimarte, M. Brandbyge, J. I. Cerdá, F. Corsetti, R. Cuadrado, V. Dikan, J. Ferrer, J. Gale, P. García-Fernández, V. M. García-Suárez, S. García, G. Huhs, S. Illera, R. Korytár, P. Koval, I. Lebedeva, L. Lin, P. López-Tarifa, S. G. Mayo, S. Mohr, P. Ordejón, A. Postnikov, Y. Pouillon, M. Pruneda, R. Robles, D. Sánchez-Portal, J. M. Soler, R. Ullah, V. W. Z. Yu, J. Junquera, *J. Chem. Phys.* **2020**, *152*, 204108.
- 30 J. P. Perdew, K. Burke, M. Ernzerhof, *Phys. Rev. Lett.* **1996**, *77*, 3865.
- 31 C. Toher, S. Sanvito, *Phys. Rev. B* **2008**, *77*, 155402.
- 32 J. Ferrer, C. J. Lambert, V. M. García-Suárez, D. Z. Manrique, D. Visontai, L. Oroszlany, R. Rodríguez-Ferradás, I. Grace, S. W. D. Bailey, K. Gillemot, H. Sadeghi, L. A. Algharagholy, *New J. Phys.* **2014**, *16*, 93029.
- 33 M. Atanasov, D. Aravena, E. Suturina, E. Bill, D. Maganas, F. Neese, *Coord. Chem. Rev.* **2015**, *289*, 177.
- 34 M. Baghbanzadeh, F. C. Simeone, C. M. Bowers, K. C. Liao, M. Thuo, M. Baghbanzadeh, M. S. Miller, T. B. Carmichael, G. M. Whitesides, *J. Am. Chem. Soc.* **2014**, *136*, 16919.
- 35 S. Fahrenndorf, N. Atodiresei, C. Besson, V. Caciuc, F. Matthes, S. Blügel, P. Kögerler, D. E. Bürgler, C. M. Schneider, *Nat. Commun.* **2013**, *4*, 2425.

### Work published in

- S. Schmitz, A. Kovalchuk, A. Martín-Rodríguez, J. Van Leusen, N. V. Izarova, S. D. M. Bourone, Y. Ai, E. Ruiz, R. C. Chiechi, P. Kögerler, K. Y. Monakhov, *Inorg. Chem.* **2018**, *57*, 9274.

## 4.2 Iron (III) spin crossover conductance switching

### 4.2.1 Motivation

First row transition metals  $3d^n$  ( $n = 4-7$ ) can switch reversibly from low-spin (LS) to high-spin (HS) or viceversa, a phenomenon known as spin crossover. The switching between spin states can be triggered by temperature, pressure, voltage or light.<sup>1,2</sup>

Spin crossover (SCO) compounds are excellent candidates to have a major role on the development of molecular electronics, spintronics, information storage, micromechanics, sensing, switching and memristive properties.<sup>3-13</sup> In this sort of systems both charge and spin can be employed to build devices with greater efficiency in terms of power and performance.<sup>14-21</sup> However, to introduce this sort of compounds into nanojunctions is still challenging, as the SCO behaviour can be easily lost.<sup>22,23</sup> A balance between too weak and too strong coupling with the electrodes is paramount to design a successful spin crossover tunnelling junction.<sup>24-27</sup>

The SCO compounds used for nanojunctions par excellence are based on a  $Fe^{II}$  centre.<sup>28-30</sup> However, in many cases the crossover temperature  $T_{1/2}$  is very low.<sup>31-33</sup>  $Fe^{III}$  compounds are more stable, but almost entirely absent in SCO molecular junctions and not fully switchable.<sup>34</sup>

In collaboration with Dr. Nijhuis and Dr. Harding groups, it is studied the first  $Fe^{III}$  spin crossover (SCO) compound at room temperature.  $[Fe^{III}(qsal-I)_2]NTf_2$  ( $qsal-I = 4\text{-iodo-2-}[(8\text{-quinolyimino)methyl]phenolate$ ) was deposited on a Cu/SLG bottom electrode (SLG = Single layer graphene) and the charge transport as a function of bias and temperature was obtained using EGaIn top electrode. The spin crossover temperature

## 4 Study of Large Area EGaIn Magnetic Junctions

---

is a remarkable  $T_{1/2}=310$  K. DFT calculations will serve to understand the higher conductivity of the high-spin state in comparison to the low-spin state.

Furthermore, as a difference to the previous case (section 4.1), the complex structure of EGaIn electrode will be approached, in order to obtain a more realistic description of large-area measurements with this electrode.

### 4.2.2 Previous work

Similarly as in the previous section, here it is reported a summary of the detailed characterisation of  $[\text{Fe}^{\text{III}}(\text{qsal-I})_2]\text{NTf}_2$  junction.  $[\text{Fe}(\text{qsal-I})_2]\text{NTf}_2$  was selected because it shows strong spin transition hysteresis at room temperature<sup>35</sup>. The synthesis of this SCO compound is reported in a previous Nijhuis' work.<sup>35,36</sup>

The studied junction consist in physisorbed  $[\text{Fe}^{\text{III}}(\text{qsal-I})_2]\text{NTf}_2$  onto single layer graphene (SLG) by immersing a Cu/SLG substrate in a 1 mM solution of the compound. The graphene layer works as a screen to reduce the electrode-molecule coupling to keep a working SCO monolayer.<sup>37-42</sup> Afterwards, the junction in completed using EGaIn electrode.

Raman spectroscopy was employed to determine the quality of the graphene<sup>43</sup> in the substrate and to understand the interaction with the molecule (Figure 4.8A). The red plot shows the Raman spectrum of clean Cu/SLG substrate. The G and 2D bands ( $1587\text{ cm}^{-1}$  and  $2678\text{ cm}^{-1}$ ) without any satellite peaks indicates an ordered graphene. When the molecule is deposited on the substrate (black plot), both bands are blue-shifted. The shift reveals that  $[\text{Fe}^{\text{III}}(\text{qsal-I})_2]\text{NTf}_2$  interacts via Van der Waals interactions and moderate electrostatic interactions with the bottom electrode.

AFM images have been performed in a clean substrate (Figure 4.8B) showing a very smooth surface, in agreement with what is inferred in the Raman spectra. After the deposition of the SCO compound (Figure 4.8C), the observed surface is homogeneous without pinholes or big accumulations. The height profile of the AFM image (Figure 4.8D) presents islands of about 1.5-2.0 nm, in good agreement with the expected height of  $[\text{Fe}^{\text{III}}(\text{qsal-I})_2]\text{NTf}_2$ , 1.41 nm.

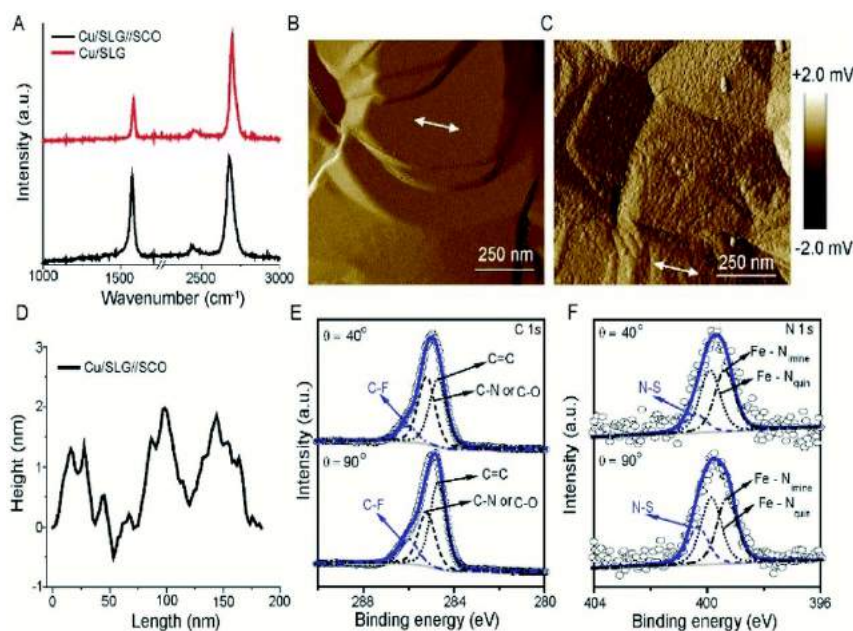


Figure 4.8. (A) Raman spectra of SLG before (red) and after adsorption (black) of  $[\text{Fe}^{\text{III}}(\text{qsal-I})_2]\text{NTf}_2$ . AFM images of clean graphene (B) and after deposition of  $[\text{Fe}^{\text{III}}(\text{qsal-I})_2]\text{NTf}_2$  (C) with its height profile (D). Angle-dependent XPS for C (E) 1s and N (F) 1s.<sup>44</sup>

To check the chemical composition and relative orientation of  $[\text{Fe}(\text{qsal-I})_2]\text{NTf}_2$ , angle-resolved XPS (ARXPS) of C 1s and N 1s orbitals are measured for 40 and 90° angle of incidence. The C 1s spectrum (Figure 4.8E) shows three peaks corresponding to CF<sub>3</sub> group and two more peaks corresponding to C=N and/or C-O and C=C groups present in the counterion. The relative intensity of CF<sub>3</sub> signal increases with the emission



## 4 Study of Large Area EGaIn Magnetic Junctions

angle (from 40 to 90), suggesting that the anion is adsorbed on the graphene surface.

Similar reasoning can be done for F 1s and I 3d spectra (Figure 4.9B and C). However, the angle dependence of I 3d spectrum indicates that  $[\text{Fe}(\text{qsal-I})_2]^+$  is interacting with the iodines towards the graphene layer.

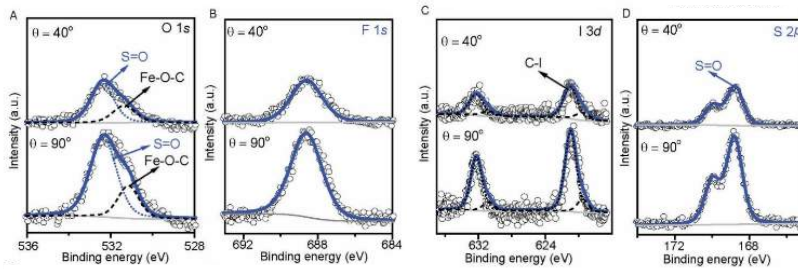


Figure 4.9. Angle dependent X-ray photoelectron spectra (ARXPS) of A) O 1s B) F 1s C) I 3d D) S 2p.

The spectra were obtained at room temperature. Adapted figure.<sup>44</sup>

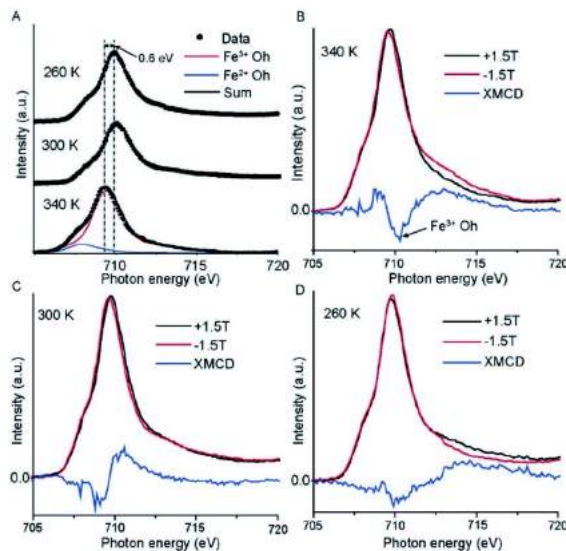


Figure 4.10. A) XAS spectra of the Fe L3 edge for a monolayer of  $[\text{FeIII}(\text{qsal-I})_2]\text{NTf}_2$  on Cu/SLG at 260, 300 and 340 K and simulated peaks for Oh FeII and FeIII. The difference of the XAS of Fe L3 edge at  $\pm 1.5$  T defines the XMCD signal at B) 340 K C) 300 K and D) 260 K.<sup>44</sup>

To confirm the spin transition of  $[\text{Fe}(\text{qsal-I})_2]^+$ , temperature dependent X-ray absorption spectroscopy (XAS) and X-ray magnetic circular dichroism (XMCD) were carried out (Figure 4.10).

The XAS of Fe  $L_{2,3}$  edge<sup>45,46</sup> of  $2p_{3/2}$  at temperatures 260, 300 and 240 K is shown in Figure 4.10A. It can be seen a peak associated with  $O_h$   $\text{Fe}^{\text{III}}$  complex at 709.3 eV (98%) and a small shoulder related with  $O_h$   $\text{Fe}^{\text{II}}$  complex (2%).<sup>47,48</sup> The  $L_3$  edge moves 0.6 eV to higher photon energies along with decreasing temperature, indicating the transition from LS to HS state.

The XAS of  $[\text{Fe}^{\text{III}}(\text{qsal-I})_2]\text{NTf}_2$  in powder shows a LS-HS transition at lower temperatures in comparison with the SCO compound on the Cu/SLG substrate. Nonetheless, the transition temperatures are comparable with the previously reported<sup>49</sup> ( $T_{1/2,\text{cool}}=248$  K,  $T_{1/2,\text{heat}}=278$  K).

XMCD measurements with magnetic field  $\pm 1.5$  T and temperature dependence of Fe  $L_3$  edge are shown in figure Figure 4.10B-D. A negative XMCD signal at 340 K is presented in Figure 4.10B at 710.3 eV, indicating a spin-polarised  $O_h$   $\text{Fe}^{\text{III}}$  ion<sup>50</sup>. At 260 K (Figure 4.10D) it is shown a very weak signal, thus demonstrating that the SCO complex switches from HS ( $S=5/2$ ) to LS ( $S=1/2$ ) since the LS state has a smaller number of unpaired electrons.<sup>51</sup>

After the characterisation, charge transport measurements of the  $[\text{Fe}^{\text{III}}(\text{qsal-I})_2]\text{NTf}_2$  monolayer on Cu/SLG were performed using EGaIn top electrode.<sup>52-54</sup> 50 different junctions were measured, being 88% of them successful. A heatmap of the recorded  $J(V)$  (bias  $\pm 1.0$  V) indicates that the junction is highly stable and reproducible<sup>55-59</sup> (Figure 4.11A).

The charge transport also revealed the spin-transition of  $[\text{Fe}^{\text{III}}(\text{qsal-I})_2]\text{NTf}_2$  when it was measured for different temperatures (Figure 4.11B

## 4 Study of Large Area EGaIn Magnetic Junctions

and C). The density current changes an order of magnitude with temperature, being the HS being more conductive than the LS. The SCO property is more gradual with the average transition temperature  $T_{1/2}$ , around 300-330 K, in agreement with the results obtained from XAS and XMCD.

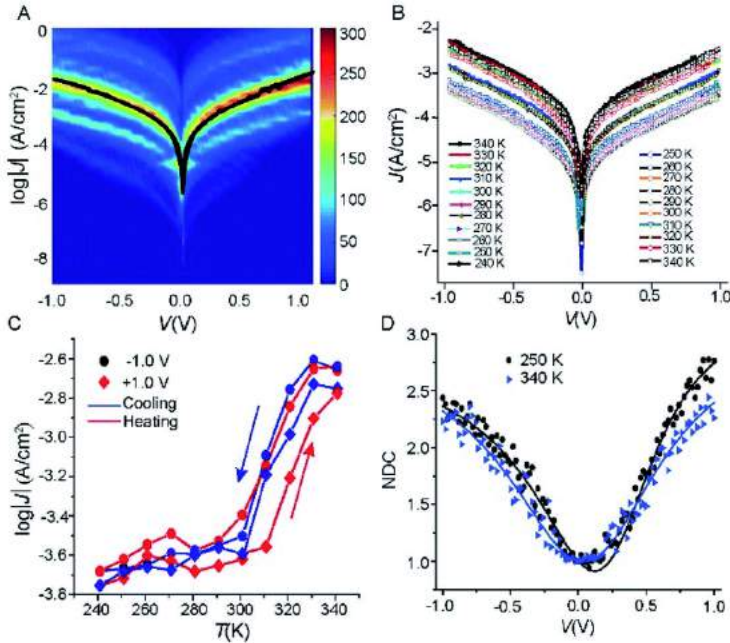


Figure 4.11. A) Heatmap of  $\log|J(V)|$  vs  $V$  curves. The black curve indicates the average. B)  $J(V)$  curves as a function of temperature from 340 to 240 K. C)  $J(V)$  hysteresis D) NDC at 340 and 250 K.<sup>44</sup>

As previously reported, the hysteresis is intimately associated with a conformation change of the anion  $\text{NTf}_2^-$ . Moreover, the cooperativity is reduced because of the presence of a single layer of  $[\text{Fe}^{\text{III}}(\text{qsal-I})_2]^+$ , leading to an increase of the  $T_{1/2}$  and a loss of hysteresis in the junction.<sup>60</sup> Compared to other junctions the spin-transition temperature is not strongly shifted when the SCO compound is placed within electrodes,<sup>61</sup> showing Cu/SLG as a promising substrate to conserve the SCO property without eroding the stability of the junction (Figure 4.11C).

Finally, Figure 4.11D plots the normalised differential conductance (NDC) of the junction. The parabolic behaviour is a characteristic sign of the coherent tunnelling charge transport mechanism.<sup>62,63</sup>

### 4.2.3 Computational details

Geometries were optimised using FHI-AIMS<sup>64</sup> code with GGA functional PBE.<sup>65</sup> The light basis set<sup>66,67</sup> and only gamma point was employed due to the large number of atoms involved. Dispersion effects were included using Tkachenko and Scheffer method<sup>68</sup> using Hirschfeld partitioning of the electron density to analyse the relative stability of the interaction between the Cu/SLG substrate and the SCO compound.

All-electron calculations were performed for high and low-spin states except when  $[\text{Fe}^{\text{III}}(\text{qsal-I})_2]\text{NTf}_2$  was placed between electrodes, where frozen-core approach was employed for orbitals below -500 eV.

Furthermore, the hybrid meta-GGA TPSSh functional<sup>69,70</sup> implemented in Gaussian09<sup>71</sup> with TZVP basis set<sup>72,73</sup> to calculate the transition metal complex electronic structure.

The charge transport properties were obtained using a combination of SIESTA<sup>74,75</sup> and GOLLUM<sup>76</sup> codes. The wavefunction was expanded using DZP basis set for all atoms except the atoms involved in the electrodes: Cu, Ag, Ga and In, in which SZ basis set was employed instead to reduce the computational time. Hubbard correction over  $\text{Fe}^{\text{III}}$  atom with  $U=4.0$  eV to improve the energy position of the 3d orbitals was taken into account. Because of the large size of the system, the transport calculations are restricted to gamma point.

### 4.2.4 Results

Before placing  $[\text{Fe}^{\text{III}}(\text{qsal-I})_2]\text{NTf}_2$  within the electrodes, different binding conformations onto Cu/SLG substrate were considered. Mainly, the relative energies of the optimised Cu/SLG// $[\text{Fe}^{\text{III}}(\text{qsal-I})_2]\text{NTf}_2$  with none, one and two iodine atoms pointing towards the graphene layer are calculated within a many-body approach (see section 4.2.3). Here, a many-body approach was chosen over classic dispersion models to obtain better numerical accuracy.

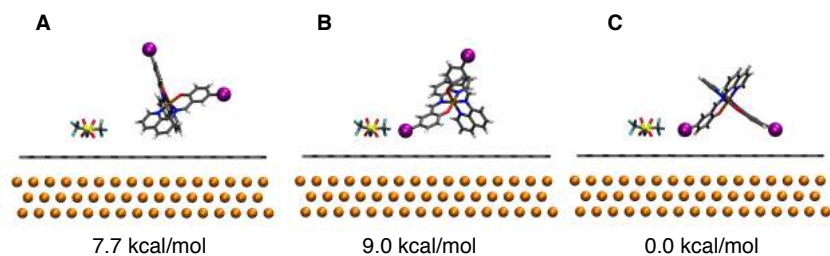


Figure 4.12. Conformations of low-spin  $[\text{Fe}^{\text{III}}(\text{qsal-I})_2]\text{NTf}_2$  considered with zero (A) one (B) and two (C) iodine atoms interacting directly with the graphene single layer. Colours for Cu: orange, C: Gray, S: yellow, F: Light green, N: Blue, O: Red, I: Purple, Fe: Ochre, H: White. Adapted figure.<sup>44</sup>

Figure 4.12 presents the three different conformations considered. As it can be seen, the conformation with both iodine atoms pointing towards the graphene layer is the most stable, in agreement with the ARXPS discussed before (Figure 4.9). Hypothetically, the combination of anion... $\pi$  and I... $\pi$  interactions aids to the non-covalent attachment of the SCO compound to the SLG.

The low-spin state was found to be the ground state. Meta-GGA TPSSh functional was used to compute the spin state of  $[\text{Fe}^{\text{III}}(\text{qsal-I})_2]\text{NTf}_2$  in the monolayer. The obtained HS-LS energy difference is 13.8 kcal/mol (0.59 eV), in close agreement with the value measured in the XAS spectrum (Figure 4.10A).

To introduce the electrode interaction, the first challenge to tackle is the model of EGaIn top electrode. In the previous contribution, the problem was circumvented by replacing the top electrode by a Au(111) electrode (section 4.1.4). However, as it will be shown in this section, a realistic model of the EGaIn electrode can be important for a correct interpretation of the charge transport.

The X-ray structure of  $\alpha$ -gallium [100] was chosen as starting point.<sup>77</sup> In that surface, a monolayer of O<sub>2</sub> molecules was placed. Randomly positioned In atoms keeping the experimental stoichiometric ratio of EGaIn (75.5% Ga and 24.5% In in weight) were introduced. Afterwards, the model was fully optimised. O<sub>2</sub> molecules were dissociated during the optimisation resulting in the formation of Ga<sub>2</sub>O<sub>3</sub> oxide. To match the experimental thickness of GaO<sub>x</sub> layer (0.7 nm),<sup>78</sup> a similar distribution of oxygen atoms was included in the first four layers.

Finally, the whole junction except the electrodes was optimised with the [Fe<sup>III</sup>(qsal-I)<sub>2</sub>]<sup>+</sup> iodine groups pointing towards the graphene layer, as shown before, for high (S=5/2) and low-spin (S=1/2) states (Figure 4.13).

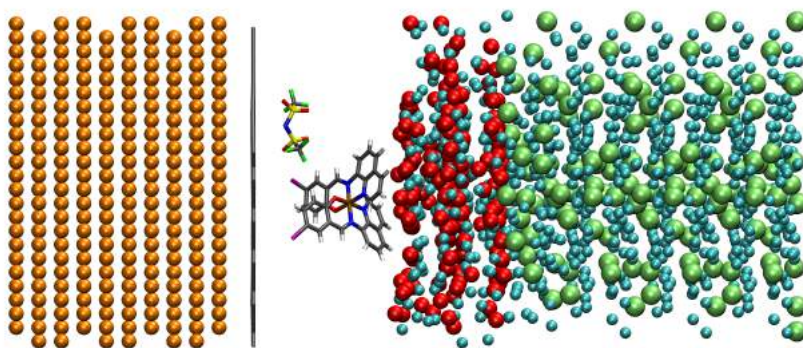


Figure 4.13. Cu/SLG/[Fe<sup>III</sup>(qsal-I)<sub>2</sub>]NTf<sub>2</sub>/GaO<sub>x</sub>/EGaIn junction. Colours for Cu: orange, C: Gray, S: yellow, F: Light green, N: Blue, O: Red, I: Purple, Fe: Ochre, H: White, Ga: light blue, In: Green.

Adapted figure.<sup>44</sup>

## 4 Study of Large Area EGaIn Magnetic Junctions

Almost 1800 atoms are involved in the nanojunction model. To expand the wavefunction and to calculate the charge transport properties of such big amount of atoms is a computational challenge but above all, very time consuming.

The projected density of states (PDOS) and transmission spectra of the high and low-spin states of the full system are shown in Figure 4.14.

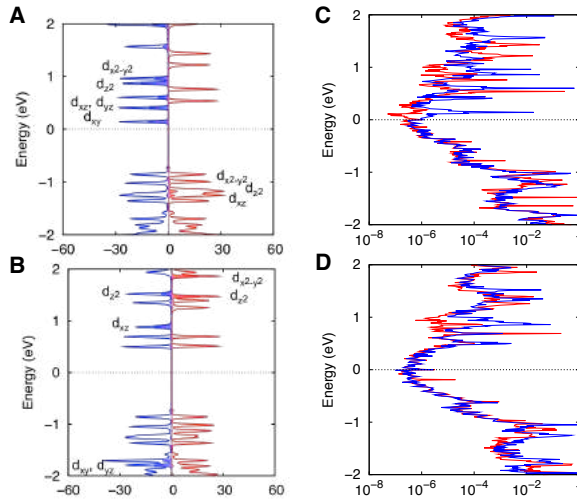


Figure 4.14. PDOS (A and B) and Transmission spectra (C and D) of high-spin (top panel) and low-spin (bottom panel) of Cu/SLG//[Fe<sup>III</sup>(qsal-I)<sub>2</sub>NTf<sub>2</sub>]/GaO<sub>x</sub>/EGaIn junction. Red and blue curves represent alpha and beta spinorbitals. Filled curves on the PDOS plots represents the Fe<sup>III</sup> orbital contribution.<sup>44</sup>

A quick method to obtain the conductance from transmission spectra (Figure 4.14C and D) is to approximate it to the zero-voltage limit<sup>79</sup>  $G = T(E)G_0$ . Within this approximation, the LS state conductance is  $2.94 \cdot 10^{-6} G_0$ , slightly larger than the obtained  $1.08 \cdot 10^{-6} G_0$  for the high-spin state. This result is in disagreement with the experimental observation, where the HS is a more conducting state. Nevertheless, in the transmission spectrum of high-spin state (Figure 4.14C) there is a transmission peak 0.1 eV above the Fermi energy related with Fe<sup>III</sup>  $\beta$   $d_{xy}$  spinorbital (Figure 4.14A). Other d-shell metal orbitals are 0.25-0.5 eV

above the Fermi energy, which can have some contribution for big bias voltages. Since the experimental bias window goes from -1 to 1 V, the small bias approximation is not suitable, as it has been shown.

When a  $V = 0.25$  V bias is considered in the calculation, it is obtained a higher conductance of  $2.03 \cdot 10^{-6} G_0$  for the high-spin state in comparison to  $4.37 \cdot 10^{-7} G_0$  conductance for low-spin state, now matching the experimental trend and the order of magnitude conductance difference observed. As announced, the bias applied during the experiments permits the spinorbital  $\beta d_{xy}$  to have an actual contribution in the electron transport of the high-spin state. In the case of the low-spin state (Figure 4.14B and C), there are no orbitals mediating the electron transport until 0.5 eV above the Fermi energy, thus having a very limited contribution to the transmission.

The influence of the anion  $\text{NTF}_2$  in the conductance was also explored by changing the relative position to the graphene layer. The anion was forced to remain perpendicular to the graphene layer, in order to induce a radical change in the interaction with the graphene layer. As Harding and Nijhuis have shown in their previous work,<sup>60</sup> the anion is strongly related with the hysteresis of the SCO compound (section 4.2.2). However, the projected density of states of the junction with a lying down and standing up  $\text{NTF}_2$  anion show no difference, thus it is inferred that although the anion has an important role in the hysteresis process, it remains passive relative to the electron transport for a large bias window (Figure 4.15).



## 4 Study of Large Area EGaIn Magnetic Junctions

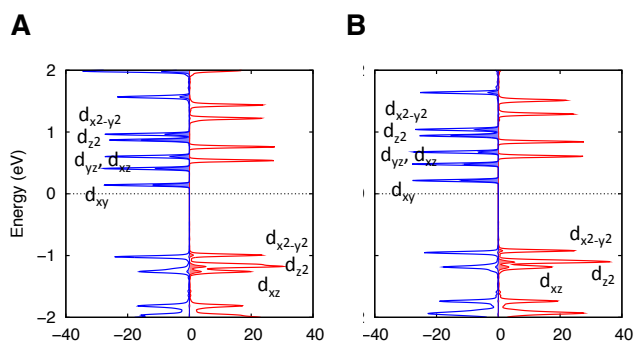


Figure 4.15. Projected Density of States (PDOS) of  $[\text{Fe}(\text{qsal-I})_2]$  and the anion  $\text{NTf}_2$  in a) lying-down and b) standing up orientation. Alpha and beta spinorbitals are represented as red and blue curves.

The filled curves represent the contribution of  $\text{Fe}^{\text{III}}$  centre.<sup>44</sup>

The model of EGaIn electrode turns out to be successful to explain the phenomena observed for  $[\text{Fe}^{\text{III}}(\text{qsal-I})_2]\text{NTf}_2$  junction. However, because it is the first time such electrode is considered explicitly in a quantum transport calculation, inconsistencies were checked by substituting the EGaIn top electrode by a Ag(111) lead. Silver is chosen because it has a similar workfunction to the EGaIn electrode (4.7 eV<sup>80</sup> and 4.3 eV<sup>78</sup>) and it is easily modelled (Figure 4.16).

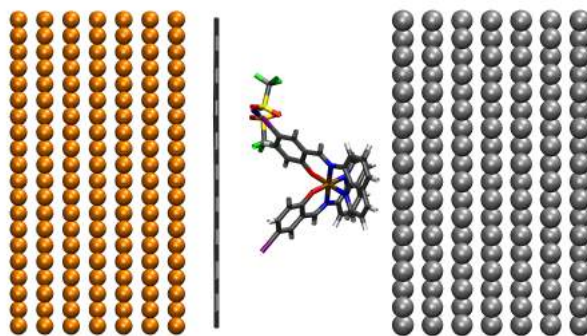


Figure 4.16.  $[\text{Fe}^{\text{III}}(\text{qsal-I})_2]\text{NTf}_2$  model sandwiched between Cu/SLG bottom electrode and Ag(111) top electrode in substitution of the actual EGaIn top electrode. Colours for Cu: orange, C: Gray, S: yellow,

F: Light green, N: Blue, O: Red, I: Purple, Fe: Ochre, H: White, Ag: Silver. Adapted figure.<sup>44</sup>

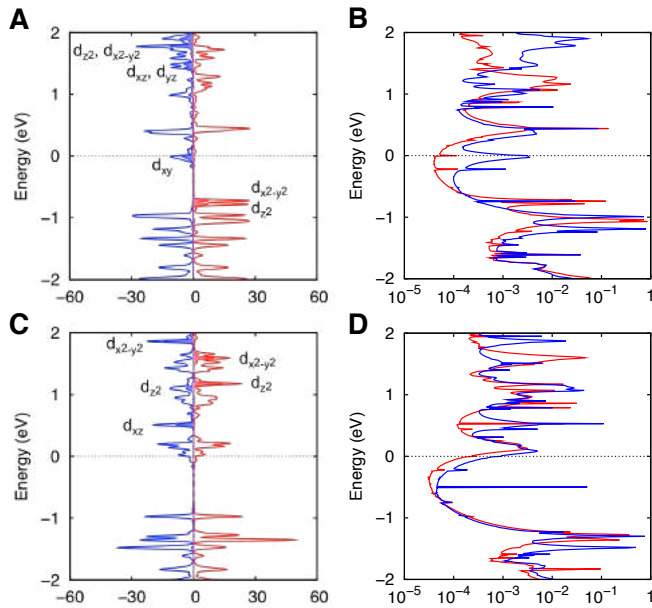


Figure 4.17. PDOS and Transmission spectra of  $[\text{Fe}^{\text{III}}(\text{qsal-I})_2]\text{NTf}_2$  sandwiched between Cu/SLG and Ag(111) electrodes for high (A and B) and low-spin states (C and D). Alpha and beta spinorbitals are represented as red and blue curves. The filled curves represent the contribution of  $\text{Fe}^{\text{III}}$  centre. Adapted figure.<sup>44</sup>

As it was done for EGaIn lead, the PDOS and the transmission spectra of high and low-spin states of the junction are calculated and shown in Figure 4.17. Using the zero-voltage approximation, with Ag(111) top electrode it is obtained a larger conductance value for the high-spin state ( $1.65 \cdot 10^{-3} G_0$ ) compared to the low-spin state ( $6.00 \cdot 10^{-4} G_0$ ) in correspondence with the experiments. Notice that the conductance values obtained using the silver electrode are three orders of magnitude bigger than the ones obtained with the actual EGaIn electrode. Qualitatively, it is easy to understand that the oxide  $\text{GaO}_x$  layer of EGaIn electrode will block the electron flow. Such layer is absent on silver, which is an excellent conductor. However, a closer examination of the PDOS of the HS state (Figure 4.17A) reveals that  $\beta$   $d_{xy}$  spinorbital is right below the Fermi energy. No filled  $d$   $\beta$  spinorbital of  $\text{Fe}^{\text{III}}$  is expected in the HS state.

## 4 Study of Large Area EGaIn Magnetic Junctions

---

This suggest a charge transfer from the Ag(111) electrode to the  $[\text{Fe}(\text{qsal-I})_2]^+$  moiety leading to a formal reduction of  $\text{Fe}^{\text{III}}$  to  $\text{Fe}^{\text{II}}$ . This is not observed when employing the EGaIn electrode (Figure 4.14A).

Notwithstanding, it is worth noting that  $\beta$   $d_{xy}$  spinorbital is very close to the Fermi energy for HS state even when the actual EGaIn electrode is considered. Luckily, EGaIn is able to keep the correct oxidation state. This reveals the difficulty of ensuring that the SCO complex remains in the  $\text{Fe}^{\text{III}}$  oxidation state when it is placed within electrodes.

### 4.2.5 Conclusions

It is demonstrated that  $[\text{Fe}(\text{qsal-I})_2]\text{NTF}_2$  is the first successful  $\text{Fe}^{\text{III}}$  spin crossover molecular junction begin fully functional at room temperature conductance switching. The junction is shown to be easy to fabricate, highly reproducible, robust and working in the tunnelling regime for both spin states.

Good balance between too weak and too strong interaction is found when Cu/SLG bottom electrode and EGaIn top electrode are employed. This combination ensures the survival of the SCO behaviour. Theoretical calculations highlight the critical role of the top electrode in stabilising the  $\text{Fe}^{\text{III}}$  oxidation state. To do so, an explicit model of EGaIn electrode is optimised using  $\alpha$ -Ga[100] crystal structure as a starting point.

The zero-voltage conductance approximation was found to be unsuccessful in predicting the experimental observations. This is somewhat expected because the experimental biases are from -1 to 1 V. When the conductance is obtained taking into account a bias of 0.25 V, HS state scores a higher conductance than LS state, as experimental results show.

The comparison to Ag(111) top electrode leads to an effective charge transfer that reduces the Fe<sup>III</sup> centre to Fe<sup>II</sup>. Although substitution of EGaIn by other metallic electrodes has been successful, it must be carefully checked to obtain and understand the correct results.

### 4.2.6 References

- 1 K. Senthil Kumar, M. Ruben, *Coord. Chem. Rev.* **2017**, *346*, 176.
- 2 A. Bousseksou, G. Molnár, L. Salmon, W. Nicolazzi, *Chem. Soc. Rev.* **2011**, *40*, 3313.
- 3 C. Lefter, V. Davesne, L. Salmon, G. Molnár, P. Demont, A. Rotaru, A. Bousseksou, *Magnetochemistry* **2016**, *2*, 18.
- 4 M. Atzori, F. Artizzu, *Functional Molecular Materials*, Jenny Stanford Publishing, **2018**.
- 5 O. Sato, *Nat. Chem.* **2016**, *8*, 644.
- 6 O. Sato, *Acc. Chem. Res.* **2003**, *36*, 692.
- 7 W. Fujita, K. Awaga, *Science* **1999**, *286*, 261.
- 8 I. Ratera, J. Veciana, *Chem. Soc. Rev.* **2012**, *41*, 303.
- 9 I. Boldog, A. B. Gaspar, V. Martínez, P. Pardo-Ibañez, V. Ksenofontov, A. Bhattacharjee, P. Gütllich, J. A. Real, *Angew. Chemie - Int. Ed.* **2008**, *47*, 6433.
- 10 B. L. Feringa, *Angew. Chemie - Int. Ed.* **2017**, *56*, 11060.
- 11 A. Fert, *Uspekhi Fiz. Nauk* **2008**, *178*, 1336.
- 12 C. Chappert, A. Fert, F. N. Van Dau, *Nat. Mater.* **2007**, *6*, 813.
- 13 M. D. Manrique-Juárez, S. Rat, L. Salmon, G. Molnár, C. M. Quintero, L. Nicu, H. J. Shepherd, A. Bousseksou, *Coord. Chem. Rev.* **2016**, *308*, 395.
- 14 A. Coskun, J. M. Spruell, G. Barin, W. R. Dichtel, A. H. Flood, Y. Y. Botros, J. F. Stoddart, *Chem. Soc. Rev.* **2012**, *41*, 4827.
- 15 M. Verdaguer, *Science* **1996**, *272*, 698.
- 16 S. Sanvito, *Chem. Soc. Rev.* **2011**, *40*, 3336.
- 17 L. Bogani, W. Wernsdorfer, *Nat. Mater.* **2008**, *7*, 179.
- 18 E. Coronado, M. Yamashita, *Dalt. Trans.* **2016**, *45*, 16553.
- 19 A. Cornia, P. Seneor, *Nat. Mater.* **2017**, *16*, 505.
- 20 G. Salvan, D. R. T. Zahn, *Beilstein J. Nanotechnol.* **2017**, *8*, 2464.

- 21 L. Guo, X. Gu, X. Zhu, X. Sun, *Adv. Mater.* **2019**, *31*, 1805355.
- 22 L. Poggini, M. Gonidec, R. K. C. Balasubramanyam, L. Squillantini, G. Pecastaings, A. Caneschi, P. Rosa, *J. Mater. Chem. C* **2019**, *7*, 5343.
- 23 L. Poggini, M. Gonidec, J. H. González-Estefan, G. Pecastaings, B. Gobaut, P. Rosa, *Adv. Electron. Mater.* **2018**, *4*, 1800204.
- 24 M. Mannini, P. Sainctavit, R. Sessoli, C. Cartier Dit Moulin, F. Pineider, M. A. Arrio, A. Cornia, D. Gatteschi, in *Chem. - A Eur. J.*, **2008**, pp. 7530–7535.
- 25 A. Pronschinske, R. C. Bruce, G. Lewis, Y. Chen, A. Calzolari, M. Buongiorno-Nardelli, D. A. Shultz, W. You, D. B. Dougherty, *Chem. Commun.* **2013**, *49*, 10446.
- 26 S. Beniwal, X. Zhang, S. Mu, A. Naim, P. Rosa, G. Chastanet, J. F. Létard, J. Liu, G. E. Sterbinsky, D. A. Arena, P. A. Dowben, A. Enders, *J. Phys. Condens. Matter* **2016**, *28*, 206002.
- 27 T. Miyamachi, M. Gruber, V. Davesne, M. Bowen, S. Boukari, L. Joly, F. Scheurer, G. Rogez, T. K. Yamada, P. Ohresser, E. Beaurepaire, W. Wulfhekel, *Nat. Commun.* **2012**, *3*, 938.
- 28 V. Meded, A. Bagrets, K. Fink, R. Chandrasekar, M. Ruben, F. Evers, A. Bernard-Mantel, J. S. Seldenthuis, A. Beukman, H. S. J. van der Zant, *Phys. Rev. B* **2011**, *83*, 245415.
- 29 G. D. Harzmann, R. Frisenda, H. S. J. Van Der Zant, M. Mayor, *Angew. Chemie - Int. Ed.* **2015**, *54*, 13425.
- 30 Y. Zhang, I. Séguy, K. Ridier, V. Shalabaeva, M. Piedrahita-Bello, A. Rotaru, L. Salmon, G. Molnár, A. Bousseksou, *J. Phys. Condens. Matter* **2020**, *32*, 214010.
- 31 T. G. Gopakumar, M. Bernien, H. Naggert, F. Matino, C. F. Hermanns, A. Bannwarth, S. Mühlenberend, A. Krüger, D. Krüger, F. Nickel, W. Walter, R. Berndt, W. Kuch, F. Tucek, *Chem. - A Eur. J.* **2013**, *19*, 15702.

- 32 T. Jasper-Tönnies, M. Gruber, S. Karan, H. Jacob, F. Tucek, R. Berndt, *J. Phys. Chem. Lett.* **2017**, *8*, 1569.
- 33 G. Serrano, E. Velez-Fort, I. Cimatti, B. Cortigiani, L. Malavolti, D. Betto, A. Ouerghi, N. B. Brookes, M. Mannini, R. Sessoli, *Nanoscale* **2018**, *10*, 2715.
- 34 T. Jasper-Toennies, M. Gruber, S. Karan, H. Jacob, F. Tucek, R. Berndt, *Nano Lett.* **2017**, *17*, 6613.
- 35 N. Phukkaphan, D. L. Cruickshank, K. S. Murray, W. Phonsri, P. Harding, D. J. Harding, *Chem. Commun.* **2017**, *53*, 9801.
- 36 P. Song, C. S. S. Sangeeth, D. Thompson, W. Du, K. P. Loh, C. A. Nijhuis, *Adv. Mater.* **2016**, *28*, 631.
- 37 M. S. Alam, M. Stocker, K. Gieb, P. Müller, M. Haryono, K. Student, A. Grohmann, *Angew. Chemie Int. Ed.* **2010**, *49*, 1159.
- 38 L. Kipgen, M. Bernien, S. Ossinger, F. Nickel, A. J. Britton, L. M. Arruda, H. Naggert, C. Luo, C. Lotze, H. Ryll, F. Radu, E. Schierle, E. Weschke, F. Tucek, W. Kuch, *Nat. Commun.* **2018**, *9*, 2984.
- 39 M. Bernien, H. Naggert, L. M. Arruda, L. Kipgen, F. Nickel, J. Miguel, C. F. Hermanns, A. Krüger, D. Krüger, E. Schierle, E. Weschke, F. Tucek, W. Kuch, *ACS Nano* **2015**, *9*, 8960.
- 40 M. Bernien, D. Wiedemann, C. F. Hermanns, A. Kruüger, D. Rolf, W. Kroener, P. Müller, A. Grohmann, W. Kuch, *J. Phys. Chem. Lett.* **2012**, *3*, 3431.
- 41 B. Long, M. Manning, M. Burke, B. N. Szafrank, G. Visimberga, D. Thompson, J. C. Greer, I. M. Povey, J. MacHale, G. Lejosne, D. Neumaier, A. J. Quinn, *Adv. Funct. Mater.* **2012**, *22*, 717.
- 42 P. Song, S. Guerin, S. J. R. Tan, H. V. Annadata, X. Yu, M. Scully, Y. M. Han, M. Roemer, K. P. Loh, D. Thompson, C. A. Nijhuis, *Adv. Mater.* **2018**, *30*, 1706322.
- 43 L. M. Malard, M. A. Pimenta, G. Dresselhaus, M. S. Dresselhaus,

- Phys. Rep.* **2009**, *473*, 51.
- 44 S. K. Karuppanan, A. Martín-Rodríguez, E. Ruiz, P. Harding, D. J. Harding, X. Yu, A. Tadich, B. Cowie, D. Qi, C. A. Nijhuis, *Chem. Sci.* **2021**, *12*, 2381.
- 45 A. Bhattacharyya, E. Stavitski, J. Dvorak, C. E. Martínez, *Geochim. Cosmochim. Acta* **2013**, *122*, 89.
- 46 P. A. Van Aken, B. Liebscher, *Phys. Chem. Miner.* **2002**, *29*, 188.
- 47 E. Stavitski, F. M. F. de Groot, *Micron* **2010**, *41*, 687.
- 48 M. Sassi, C. I. Pearce, P. S. Bagus, E. Arenholz, K. M. Rosso, *J. Phys. Chem. A* **2017**, *121*, 7613.
- 49 W. Thammasangwan, P. Harding, S. G. Telfer, A. Alkaş, W. Phonsri, K. S. Murray, R. Clérac, M. Rouzières, G. Chastanet, D. J. Harding, *Eur. J. Inorg. Chem.* **2020**, *2020*, 1325.
- 50 E. Lee, D. H. Kim, J. Hwang, K. Lee, S. Yoon, B. J. Suh, K. Hyun Kim, J. Y. Kim, Z. H. Jang, B. Kim, B. I. Min, J. S. Kang, *Appl. Phys. Lett.* **2013**, *102*, 133703.
- 51 J. K. Kowalska, B. Nayyar, J. A. Rees, C. E. Schiewer, S. C. Lee, J. A. Kovacs, F. Meyer, T. Weyhermüller, E. Otero, S. Debeer, *Inorg. Chem.* **2017**, *56*, 8147.
- 52 W. F. Reus, C. A. Nijhuis, J. R. Barber, M. M. Thuo, S. Tricard, G. M. Whitesides, *J. Phys. Chem. C* **2012**, *116*, 6714.
- 53 C. A. Nijhuis, W. F. Reus, J. R. Barber, G. M. Whitesides, *J. Phys. Chem. C* **2012**, *116*, 14139.
- 54 C. S. S. Sangeeth, A. Wan, C. A. Nijhuis, *J. Am. Chem. Soc.* **2014**, *136*, 11134.
- 55 A. Krzykawska, M. Wróbel, K. Koziel, P. Cyganik, *ACS Nano* **2020**, *14*, 6043.
- 56 O. E. Castañeda Ocampo, P. Gordiichuk, S. Catarci, D. A. Gautier, A. Herrmann, R. C. Chiechi, *J. Am. Chem. Soc.* **2015**, *137*, 8419.



- 57 H. J. Um, G. D. Kong, H. J. Yoon, *ACS Appl. Mater. Interfaces* **2018**, *10*, 34758.
- 58 G. Bullard, F. Tassinari, C. H. Ko, A. K. Mondal, R. Wang, S. Mishra, R. Naaman, M. J. Therien, *J. Am. Chem. Soc.* **2019**, *141*, 14707.
- 59 K. S. Kumar, R. R. Pasula, S. Lim, C. A. Nijhuis, *Adv. Mater.* **2016**, *28*, 1824.
- 60 J. J. Whittaker, P. Harding, J. K. Clegg, D. J. Harding, *Cryst. Growth Des.* **2020**, *20*, 7006.
- 61 A. Gee, A. H. Jaafar, B. Brachňaková, J. Massey, C. H. Marrows, I. Šalitroš, N. T. Kemp, *J. Phys. Chem. C* **2020**, *124*, 13393.
- 62 A. Vilan, *J. Phys. Chem. C* **2007**, *111*, 4431.
- 63 S. K. Karuppanan, E. H. L. Neoh, A. Vilan, C. A. Nijhuis, *J. Am. Chem. Soc.* **2020**, *142*, 3513.
- 64 V. Blum, R. Gehrke, F. Hanke, P. Havu, V. Havu, X. Ren, K. Reuter, M. Scheffler, *Comput. Phys. Commun.* **2009**, *180*, 2175.
- 65 J. P. Perdew, K. Burke, M. Ernzerhof, *Phys. Rev. Lett.* **1996**, *77*, 3865.
- 66 K. Lejaeghere, G. Bihlmayer, T. Björkman, P. Blaha, S. Blügel, V. Blum, D. Caliste, I. E. Castelli, S. J. Clark, A. Dal Corso, S. De Gironcoli, T. Deutsch, J. K. Dewhurst, I. Di Marco, C. Draxl, M. Dułak, O. Eriksson, J. A. Flores-Livas, K. F. Garrity, L. Genovese, P. Giannozzi, M. Giantomassi, S. Goedecker, X. Gonze, O. Grånäs, E. K. U. Gross, A. Gulans, F. Gygi, D. R. Hamann, P. J. Hasnip, N. A. W. Holzwarth, D. Iușan, D. B. Jochym, F. Jollet, D. Jones, G. Kresse, K. Koepf, E. Küçükbenli, Y. O. Kvashnin, I. L. M. Locht, S. Lubeck, M. Marsman, N. Marzari, U. Nitzsche, L. Nordström, T. Ozaki, L. Paulatto, C. J. Pickard, W. Poelmans, M. I. J. Probert, K. Refson, M. Richter, G. M. Rignanese, S. Saha, M. Scheffler, M. Schlipf, K. Schwarz, S. Sharma, F. Tavazza, P.

- Thunström, A. Tkatchenko, M. Torrent, D. Vanderbilt, M. J. Van Setten, V. Van Speybroeck, J. M. Wills, J. R. Yates, G. X. Zhang, S. Cottenier, *Science* **2016**, *351*, aad3000.
- 67 S. R. Jensen, S. Saha, J. A. Flores-Livas, W. Huhn, V. Blum, S. Goedecker, L. Frediani, *J. Phys. Chem. Lett.* **2017**, *8*, 1449.
- 68 A. Tkatchenko, M. Scheffler, *Phys. Rev. Lett.* **2009**, *102*, 73005.
- 69 V. N. Staroverov, G. E. Scuseria, J. Tao, J. P. Perdew, *J. Chem. Phys.* **2003**, *119*, 12129.
- 70 J. Tao, J. P. Perdew, V. N. Staroverov, G. E. Scuseria, *Phys. Rev. Lett.* **2003**, *91*, 146401.
- 71 M. J. Frisch, G. W. Trucks, H. B. Schlegel, G. E. Scuseria, M. A. Robb, J. R. Cheeseman, G. Scalmani, V. Barone, B. Mennucci, G. A. Petersson, H. Nakatsuji, M. Caricato, X. Li, H. P. Hratchian, A. F. Izmaylov, J. Bloino, G. Zheng, J. L. Sonnenberg, M. Hada, M. Ehara, K. Toyota, R. Fukuda, J. Hasegawa, M. Ishida, T. Nakajima, Y. Honda, O. Kitao, H. Nakai, T. Vreven, J. A. Montgomery Jr., J. E. Peralta, F. Ogliaro, M. Bearpark, J. J. Heyd, E. Brothers, K. N. Kudin, V. N. Staroverov, R. Kobayashi, J. Normand, K. Raghavachari, A. Rendell, J. C. Burant, S. S. Iyengar, J. Tomasi, M. Cossi, N. Rega, J. M. Millam, M. Klene, J. E. Knox, J. B. Cross, V. Bakken, C. Adamo, J. Jaramillo, R. Gomperts, R. E. Stratmann, O. Yazyev, A. J. Austin, R. Cammi, C. Pomelli, J. W. Ochterski, R. L. Martin, K. Morokuma, V. G. Zakrzewski, G. A. Voth, P. Salvador, J. J. Dannenberg, S. Dapprich, A. D. Daniels, Ö. Farkas, J. B. Foresman, J. V. Ortiz, J. Cioslowski, D. J. Fox, *Gaussian, Inc. Wallingford CT* **2009**.
- 72 A. Schäfer, C. Huber, R. Ahlrichs, *J. Chem. Phys.* **1994**, *100*, 5829.
- 73 A. Schäfer, H. Horn, R. Ahlrichs, *J. Chem. Phys.* **1992**, *97*, 2571.
- 74 J. M. Soler, E. Artacho, J. D. Gale, A. García, J. Junquera, P. Ordejón, D. Sánchez-Portal, *J. Phys. Condens. Matter* **2002**, *14*, 2745.

## 4 Study of Large Area EGaIn Magnetic Junctions

---

- 75 A. García, N. Papior, A. Akhtar, E. Artacho, V. Blum, E. Bosoni, P. Brandimarte, M. Brandbyge, J. I. Cerdá, F. Corsetti, R. Cuadrado, V. Dikan, J. Ferrer, J. Gale, P. García-Fernández, V. M. García-Suárez, S. García, G. Huhs, S. Illera, R. Korytár, P. Koval, I. Lebedeva, L. Lin, P. López-Tarifa, S. G. Mayo, S. Mohr, P. Ordejón, A. Postnikov, Y. Pouillon, M. Pruneda, R. Robles, D. Sánchez-Portal, J. M. Soler, R. Ullah, V. W. Z. Yu, J. Junquera, *J. Chem. Phys.* **2020**, *152*, 204108.
- 76 J. Ferrer, C. J. Lambert, V. M. García-Suárez, D. Z. Manrique, D. Visontai, L. Oroszlany, R. Rodríguez-Ferradás, I. Grace, S. W. D. Bailey, K. Gillemot, H. Sadeghi, L. A. Algharagholy, *New J. Phys.* **2014**, *16*, 93029.
- 77 H. G. Von Schnering, R. Nesper, *Acta Chem. Scand.* **1991**, *45*, 870.
- 78 K. S. Wimbush, R. M. Fratila, D. Wang, D. Qi, C. Liang, L. Yuan, N. Yakovlev, K. P. Loh, D. N. Reinhoudt, A. H. Velders, C. A. Nijhuis, *Nanoscale* **2014**, *6*, 11246.
- 79 M. Di Ventra, *Electrical Transport in Nanoscale Systems*, Cambridge University Press, **2008**.
- 80 A. W. Dweydari, C. H. B. Mee, *Phys. status solidi* **1975**, *27*, 223.

### Work published in

S. K. Karuppanan, A. Martín-Rodríguez, E. Ruiz, P. Harding, D. J. Harding, X. Yu, A. Tadich, B. Cowie, D. Qi, C. A. Nijhuis, *Chem. Sci.* **2021**, *12*, 2381.

## 5 SPINTRONIC DEVICES BASED ON HOFMANN-TYPE CLATHRATE MONOLAYER

### 5.1 Introduction

In the last chapter, spin crossover (SCO) compounds were shown to be crucial in the development of spintronics. Among SCO materials, metal-organic frameworks (MOFs) consist on 3D coordination polymers with tuneable porosity and high surface area.<sup>1</sup> Originally developed for applications in gas storage and catalysis,<sup>2,3</sup> in the last years MOFs have exhibit a huge potential in nanotechnology and solid state physics.<sup>4,5</sup> In this context, electric,<sup>6-9</sup> thermoelectric,<sup>10</sup> magnetic<sup>11,12</sup> and memristive<sup>13-15</sup> properties of MOFs have been explored to their potential used in electronic devices.

Cyanide-bridged Hofmann-type MOFs or Hofmann Clathrates were first introduced by Hofmann and Küspert in 1897 with general formula  $[\text{Ni}(\text{NH}_3)_2\{\text{Ni}(\text{CN})_4\}] \cdot 2\text{C}_6\text{H}_6$ <sup>16</sup>. Spin crossover property was originally observed in  $[\text{Fe}(\text{py})_2\{\text{Ni}(\text{CN})_4\}]$  (py = pyridine) Hofmann clathrate analogue based on the reversible change of  $\text{Fe}^{\text{II}}$  ion between low-spin (LS) and high-spin (HS) states.<sup>17</sup> This class of compounds rapidly widened with

## 5 Spintronic Devices based on Hofmann-type Clathrate Monolayer

the general formula  $[M(L)_n\{M'(CN)_4\}]$  ( $M = Fe^{II}, Co^{II}, Cu^{II}, Zn^{II}, Cd^{II}, Mn^{II}$ ,  $M' = Pt^{II}, Pd^{II}, Ni^{II}$ ) composed of two-dimensional (2D) sheets of  $M^{II}$  ion coordinated by the square-planar tetracyanometallate ion and two N-terminated axial ligands. Neighbouring sheets interact via  $\pi$ - $\pi$  stacking of intercalated axial ligands, usually pyridine (Figure 5.1, left), or connecting two  $M^{II}$  ions by sharing the same axial ligand, for example, pyrazine (pz) or bipyridine (bipy) (Figure 5.1, right). Over the years, a wide variety of monodentate and bidentate pyridines have been used to occupy the axial position.<sup>18,19</sup>

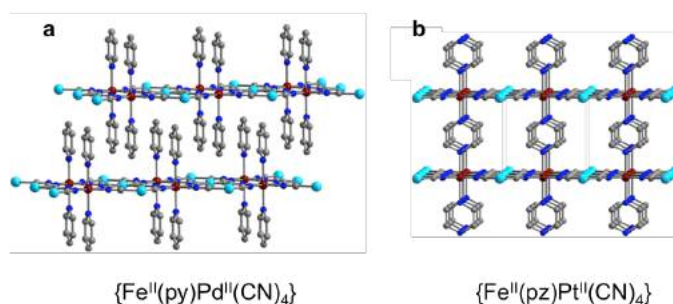


Figure 5.1. Structures of a)  $\{Fe(py)Pd^{II}(CN)_4\}$  (py = pyridine) and b)  $\{Fe(pz)Pt^{II}(CN)_4\}$  (pz = pyrazine).  
C: grey, N: dark blue, Fe: Brown, Pt and Pd: Light blue. Adapted figure.<sup>18</sup>

There are several methods available to build up a MOF on a substrate<sup>20</sup> such as spin coating,<sup>21</sup> electrochemical techniques<sup>22</sup> or chemical vapour deposition.<sup>23</sup> The most common bottom-up approach is layer-by-layer (LbL) synthesis achieved by alternating soaking of a substrate in solutions of the building blocks.<sup>24–30</sup> In this manner, tens to hundreds of 2D sheets can be accumulated in a cyanide-bridged Hofmann-type MOF.<sup>31</sup>

The objective for this chapter is to build a room temperature magnetoresistance monolayer of a Hofmann-type MOF of the form  $\{Co^{II}(PyrT)Pt^{II}(CN)_4\}$  (PyrT = 4-mercaptopyridine) optimising the LbL methodology to obtain a single sheet.  $Co^{II}$  in a high-spin state  $S=3/2$  in octahedral coordination have been reported to show large

magnetoresistance.<sup>32</sup> Further, the substitution of Fe<sup>II</sup> by Co<sup>II</sup> avoids the possible oxidation to Fe<sup>III</sup>, which should facilitate the synthesis conditions. Contrary to other monolayers (chapter 4), in a Hofmann-type monolayer the Co<sup>II</sup> centres are interconnected via the square-planar tetracyanometallate ions in the x-y plane. Those bonds are expected to improve the robustness, reproducibility and ordering of the monolayer in comparison to systems with discrete molecules while keeping a direct and short electron pathway through magnetic Co<sup>II</sup> centres.

## 5.2 Results

### 5.2.1 Synthesis and characterisation

The synthesis of {Co<sup>II</sup>(Pyr<sup>Γ</sup>)<sub>2</sub>Pt(CN)<sub>4</sub>} (Pyr<sup>Γ</sup> = 4-mercaptopyridine) Hofmann-type monolayer is inspired on the previous work of Mallouk<sup>31</sup> in 1994 and Real<sup>33</sup> in 2006. Overall, the synthesis is based on the successive exposition to the building blocks and cleaning of a chosen substrate. Several different temperatures (from original -60°C reported by Mallouk to room temperature), concentrations (typical values of 5-100 mM), cleaning and exposition times (within half and 10 minutes) are reported in the literature.<sup>30,34–37</sup> Here, it is shown the experimental conditions found for Hofmann-type single layer grown in a Au(111) monocrystalline substrate using the layer-by-layer (LbL) method (Figure 5.2).

The first step is to grow a 4-mercaptopyridine (Pyr<sup>Γ</sup>) monolayer finely spaced to keep the right distance between Co<sup>II</sup> ions to let the future lateral coordination via square-planar tetracyanoplatinate ion. This first monolayer is usually formed using an ethanolic solution. Nevertheless, it has been reported that Pyr<sup>Γ</sup> can suffer the rupture of the S-C bond under ethanol.<sup>38</sup> In order to grow a spaced Pyr<sup>Γ</sup> monolayer, the Au(111)

## 5 Spintronic Devices based on Hofmann-type Clathrate Monolayer

substrate is exposed to a EtS-PyrT 5 mM solution in  $\text{CH}_2\text{Cl}_2$  at room temperature. The cleavage of the S-S bond generates a monolayer of PyrT and ethanethiol. The latter has the passive but important role of spacing the PyrTs. Afterwards, the monolayer is cleaned by immersion during 30 s in  $\text{CH}_2\text{Cl}_2$ . The deposition of the monolayer is easily followed by ellipsometry, scoring an average height of 4.5 Å compatible to a slightly tilted PyrT (Figure 5.3, top panel).

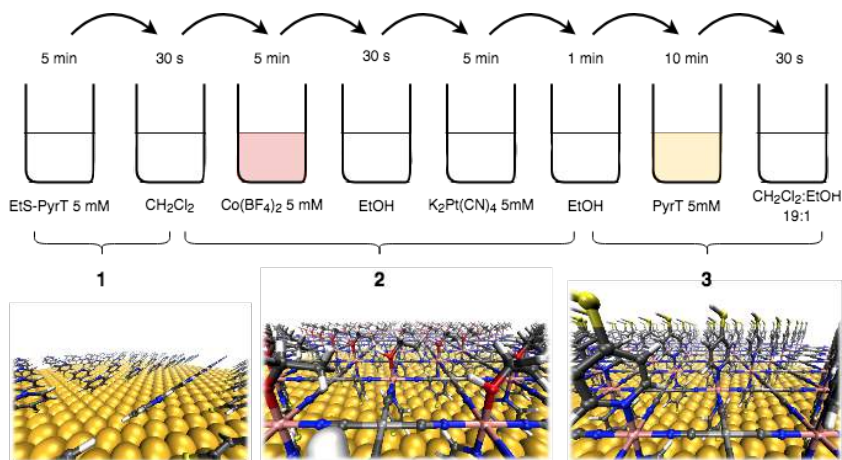


Figure 5.2. Synthesis of a  $\{\text{Co}^{\text{II}}(\text{PyrT})_2\text{M}^{\text{II}}(\text{CN})_4\}$  Hofmann-type monolayer using a layer-by-layer methodology. The Au(111) substrate is successively exposed to the building blocks and cleaned.

Then, it is exposed to  $\text{Co}(\text{BF}_4)_2$  5 mM in ethanol and cleaned in the same solvent during 30 s at 4°C. The operation is repeated for  $\text{K}_2[\text{Pt}(\text{CN})_4]$  and cleaned for 1 min. This step coordinates the  $\text{Co}^{\text{II}}$  ion to the PyrT and the tetracyanoplatinate ion interconnects the different  $\text{Co}^{\text{II}}$  centres. Although Mallouk reported that 2D counterparts of Hofmann-type MOF could be built at room temperature,<sup>31,33,36,37,39</sup> at 4°C it is found a good compromise between the coordination of the different chemical species and the desorption ratio under ethanol. The ellipsometry measures a height of 11.5 Å for this step (Figure 5.3, centre panel). This thickness is consistent with PyrT and ethanol working as axial ligands. Finally, the substrate is exposed to a PyrT 5 mM solution in 19 mL  $\text{CH}_2\text{Cl}_2$  and 1 mL of ethanol to

substitute the axial ethanol during 10 minutes. In this way, the solubility of PyrT in  $\text{CH}_2\text{Cl}_2$  is improved while keeping a low quantity of ethanol. Later, the excess of PyrT is washed during 30 s in pure  $\text{CH}_2\text{Cl}_2$ . The 16.7 Å height obtained in the ellipsometric measurements is in good agreement with the expected height for the fully-grown Hofmann-type monolayer (Figure 5.3, bottom panel).

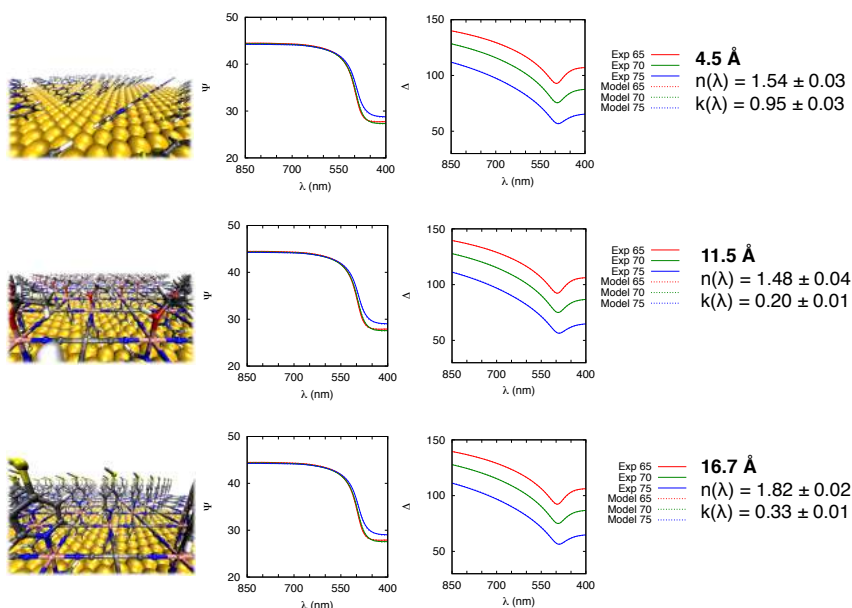


Figure 5.3. Ellipsometric measurements for PyrT monolayer (top panel), the intermediate step of interconnected  $\text{Co}^{\text{II}}$  ions via square-planar tetracyanoplatinate ions (centre panel) and fully-grown Hofmann-type monolayer (bottom panel) for angles of incidence 65°, 70° and 65°. The monolayer is modelled as a Cauchy optical layer with constant refractive index  $n(\lambda)$  and constant extinction coefficient  $k(\lambda)$ .

To corroborate the ellipsometry measurements, tapping mode AFM images have been obtained for the fully-grown monolayer in a Bruker Multimode 8 AFM with nanoscope V electronics (Figure 5.4). To obtain absolute thicknesses by AFM, the usual method is to scratch a hole on the surface to destroy part of the monolayer and check the section over the scratched area.<sup>40</sup> A 150x150 nm square was scratched on the surface to



## 5 Spintronic Devices based on Hofmann-type Clathrate Monolayer

remove the Hofmann-type monolayer and leave the bare Au(111) surface. By checking the section through the square it is possible to obtain the thickness of the deposited monolayer. For the last step, a thickness of 1.72 nm (17.2 Å) is obtained, in excellent agreement with the ellipsometry measurements (Figure 5.3, bottom panel).

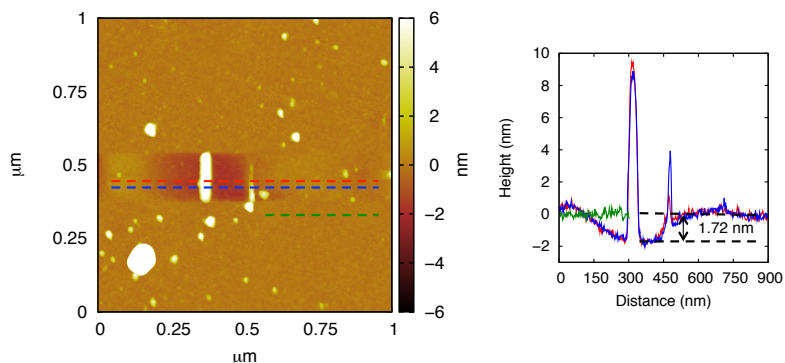


Figure 5.4. AFM image showing the thickness of the Hofmann-type monolayer. Blue and red curves show the section through the scratched 150x150 nm square to reveal a 1.72 nm thickness. Green curve shows the section variation over the monolayer.

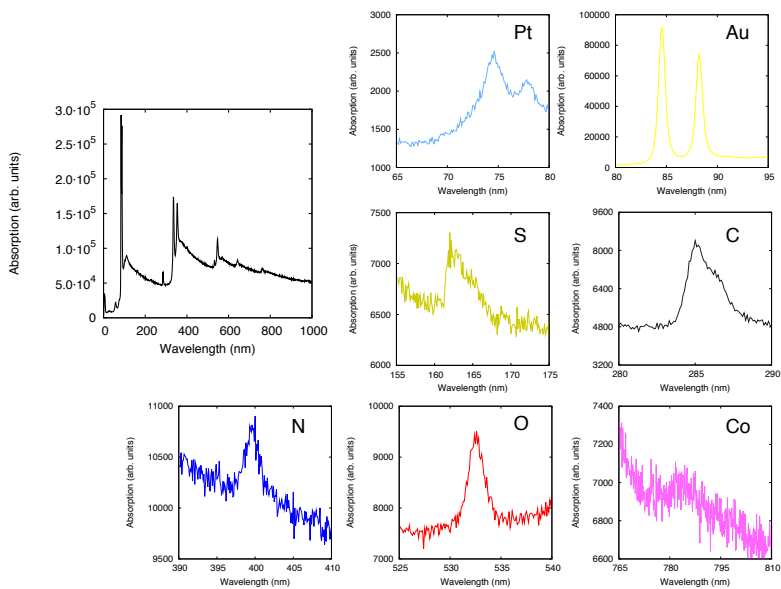


Figure 5.5. XPS spectrum of a fully-grown Hofmann-type monolayer and high-resolution spectra of relevant atoms: Pt, Au, S, C, N, O and Co.

The XPS for the fully-grown Hofmann-type monolayer shows a significant amount of oxygen, consistent with ethanol being the axial ligand and/or completing the coordination sphere of misplaced  $\text{Co}^{\text{II}}$  ions (Figure 5.5). An overall inspection of XPS spectra indicates that, although all the elements involved in the Hofmann-type monolayers are present, the small thickness of the monolayer makes difficult the data acquisition. Thus, quantitative information such as element ratio cannot be obtained.

### 5.2.2 C-AFM measurements

Conductive atomic force microscopy (C-AFM) can be employed to obtain contact mode topology images and, at the same time, current-position maps at a given bias. To do so, the fully-grown Hofmann-type monolayer was scanned using a CSI NanoObserver AFM and a doped diamond tip equipped with Resiscope module to obtain electrical information. Figure 5.6A shows the contact mode topology of the  $\{\text{Co}^{\text{II}}(\text{PyrT})_2\text{Pt}(\text{CN})_4\}$  Hofmann-type monolayer on Au(111). The blurred picture in combination of clear features indicates that a thin-film is on the substrate, as it was shown in the previous section.

Whilst topology images can be rather opaque regarding the coverage, to map the current can give better contrast to directly observe the extension of the monolayer. Bare Au(111) is expected to exhibit much higher conductance under bias than the Hofmann-type monolayer. Hence, to map the current against the position will show the coverage of  $\{\text{Co}^{\text{II}}(\text{PyrT})_2\text{Pt}(\text{CN})_4\}$  with excellent contrast (Figure 5.6B). Low current regions are marked in red and indicate the presence of the  $\{\text{Co}^{\text{II}}(\text{PyrT})_2\text{Pt}(\text{CN})_4\}$  monolayer. High current regions in blue are related to bare gold. Since most of the image is marked as a low current region, it suggest that the monolayer is covering gold to a very large extend.

## 5 Spintronic Devices based on Hofmann-type Clathrate Monolayer

Depressions of gold surface marked as blue dashed lines in Figure 5.6A show good correspondence to high current regions in Figure 5.6B. To further evidence the present of the  $\{\text{Co}^{\text{II}}(\text{PyrT})_2\text{Pt}(\text{CN})_4\}$  Hofmann-type monolayer,  $I(V)$  curves were measured on bare gold (blue curve) and on the monolayer (red curve) showing a much higher current on the bare gold, as it is expected (Figure 5.6C).

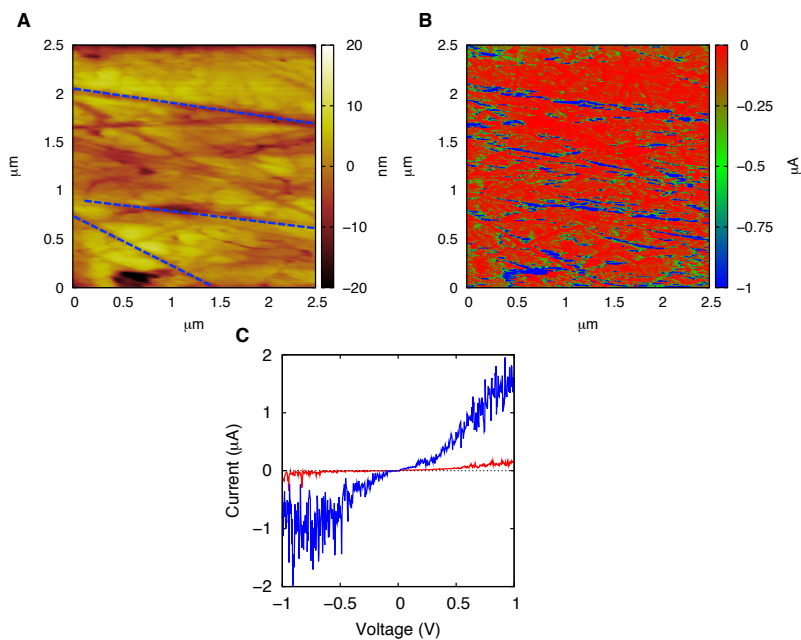


Figure 5.6. A) Contact mode topography of the Hofmann-type monolayer B) C-AFM image at bias -0.3 V C)  $I(V)$  curves obtained on bare gold (blue) and on the Hofmann-type layer (red).

### 5.2.3 Blinking STM experiments

To study the conductance of the Hofmann-type monolayer, it was carried out *blinking* STM measurements (section 1.2.1). Contact measurements as *tapping* usually employed for single molecule experiments are not suitable for extended junctions. The retraction of the STM tip would not be clean

because of the many interactions involved in a dense monolayer, hence making impossible the proper collection of molecular plateaus.

In the same fashion it was done in chapter 3, an STM tip was functionalised with PyrT. The monolayer was grown until step 2 (Figure 5.2). The actual Hofmann-type monolayer (Figure 5.2, 3) is created *in situ* when the PyrT on the STM tip bonds the Co<sup>II</sup> centre, displacing the axial ethanol (Figure 5.7).

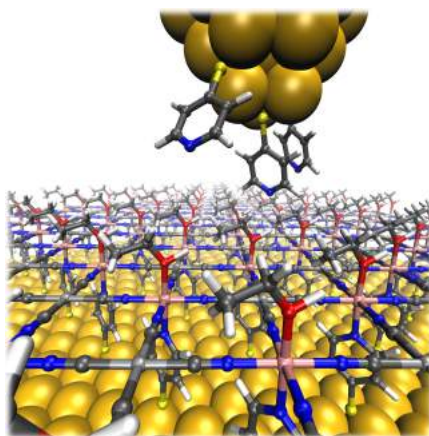


Figure 5.7. *Blinking* STM experiment recreation.

The data shown in this section are from a series of preliminary experiments with limited statistics. Nevertheless, very valuable information about the conductance and magnetoresistance of Hofmann-type clathrate monolayer can be inferred. When a PyrT bonds a Co<sup>II</sup> centre, a sudden jump or *blink* is observed in the conductance. These *blinks* (Figure 5.8, inset) are accumulated to generate a 2D heatmap (Figure 5.8). For a functionalised gold tip with PyrT (Figure 5.8, left), the lowest conductance signature is observed at  $5.62 \cdot 10^{-5} G_0$ . Higher conductance values are also recorded but no clear signature can be distinguished, forming a broad band. The same experiment carried out with a functionalised PyrT nickel tip (Figure 5.8, right) shows clearly differentiated conductance signatures

## 5 Spintronic Devices based on Hofmann-type Clathrate Monolayer

starting at  $4.16 \cdot 10^{-5} G_0$ , in consonance with what is found for the functionalised gold tip ( $5.62 \cdot 10^{-5} G_0$ ). Other conductance signatures at  $8.32 \cdot 10^{-5} G_0$  and  $1.23 \cdot 10^{-4} G_0$  (and higher) are roughly integer factors of the first conductance signature. This suggests that the conductance signature at  $4.16 \cdot 10^{-5} G_0$  can be attributed to the event of a single  $\text{Co}^{\text{II}}$ -Pyr $\Gamma$  bond formation and two and three  $\text{Co}^{\text{II}}$ -Pyr $\Gamma$  bond formation to  $8.32 \cdot 10^{-5} G_0$  and  $1.23 \cdot 10^{-4} G_0$ . Higher integer factors can also be understood in this fashion.

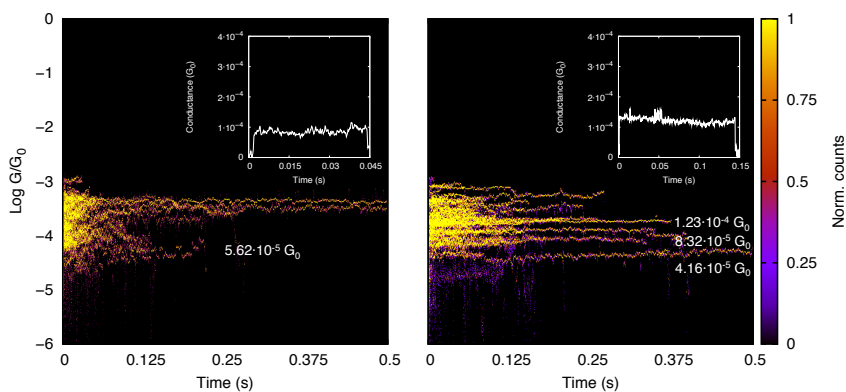


Figure 5.8. Accumulated 2D maps of Hofmann-type monolayer using gold (left) and nickel (right) tip and examples of *Blinking STM blinks* (insets) using a -50 mV bias and 0.8 nA setpoint.

The enhanced conductance signature resolution of Ni functionalised tip in comparison to Au tip could be related to the different electrode-monolayer interaction. However, Au and Ni have very similar workfunctions (5.1 and 5.0, respectively)<sup>41</sup> and previous experiments have shown during the thesis yielded similar resolution. Thus, the poor resolution obtained for gold tip is assigned to the small number of *blinks* recorded.

To explore the magnetoresistance of the Hofmann-type monolayer, Ni tips were freshly cut and exposed to Pyr $\Gamma$  solution. The rapid exposure to the Pyr $\Gamma$  solution and functionalization protects Ni of oxidation to a very

large extend. To polarise the tips, they were polarised *ex situ* by exposing them to a commercial 1 T NdFeB magnet after functionalization under N<sub>2</sub> atmosphere (section 3.2).

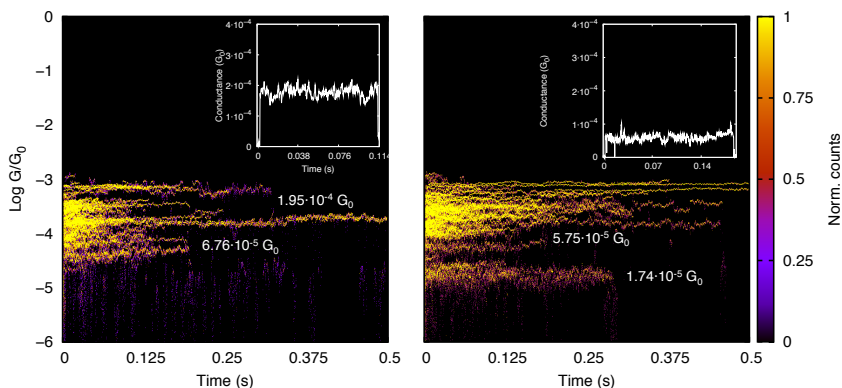


Figure 5.9. Accumulated 2D maps of Hofmann-type monolayer using alpha-polarised (left) and beta-polarised (right) Ni tip and examples of *Blinking* STM *blinks* (insets) using a -50 mV bias and 0.8 nA setpoint.

Alpha and beta-polarised Ni tips conductance 2D maps are shown in Figure 5.9 and an example of the selected *blinks* is shown in the respective insets. For an alpha-polarised Ni tip (Figure 5.9, left), a broad conductance signature at  $6.76 \cdot 10^{-5} G_0$  can be seen. The same broad signature is observed for a beta-polarised Ni tip (Figure 5.9, right) but at  $1.74 \cdot 10^{-5} G_0$ , scoring a magnetoresistance  $\alpha/\beta$  of 3.89. As observed for the non-polarised Ni tip, some integer factor signatures of a single Co<sup>II</sup>-PyrT bond can be intuited. While two Co<sup>II</sup>-PyrT bond formation is not clearly observed, three Co<sup>II</sup>-PyrT bond formations at  $1.95 \cdot 10^{-4} G_0$  (alpha-polarised) and  $5.75 \cdot 10^{-5} G_0$  (beta-polarised) yields a very similar magnetoresistance to the single Co<sup>II</sup>-PyrT bond formation case of 3.39. The magnetoresistance ratio of 3-4 fold is of the same order than the one observed for metalloporphyrins (chapter 3).

Although the big picture of the Hofmann-type clathrate monolayer can be understood with the experiments presented here, to rerun the experiments

with larger accumulation of *blinks* is of great importance to resolve the integer factor conductance signatures expected for Au, non-polarised and polarised Ni tips. Furthermore, to study if there is any effect of the bias sign on the conductance and/or magnetoresistance is also of interest to have a robust study.

### 5.2.4 Computational details

In the previous chapter, it was considered two different monolayers modelled as if it were single molecule experiments with no interaction with their neighbours. In both cases, there was experimental information pointing to a low interaction with their neighbours, hence making suitable the single molecule picture. For the Hofmann-type monolayer, this is no longer true and the model must replicate an actual monolayer using periodic boundary conditions (Figure 5.10).

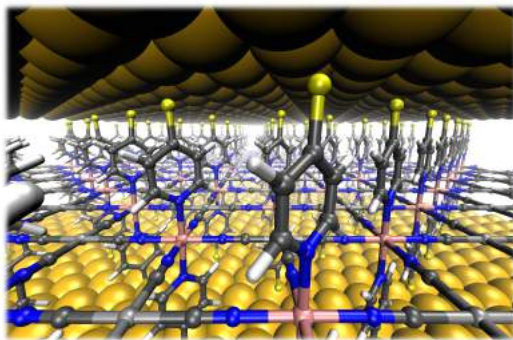


Figure 5.10. Computational model of  $\{\text{Co}^{\text{II}}(\text{PyrT})_2\text{Pt}(\text{CN})_4\}$  Hofmann-type monolayer.

The unit cell considered contains four  $\text{Co}^{\text{II}}$  centres and placed between electrodes (Figure 5.11). The scattering region was optimised until atomic forces were below  $0.04 \text{ eV}/\text{\AA}$  using SIESTA code.<sup>42–44</sup> The electrodes were kept fix but movement along the  $z$ -axis was permitted in order to optimise the interelectrode distance.

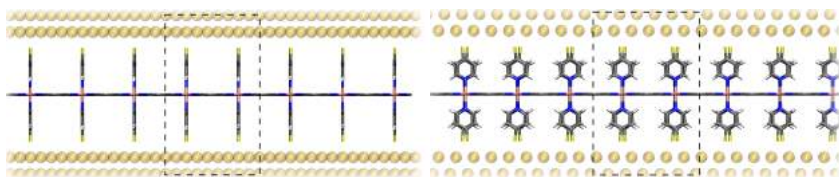


Figure 5.11. Computational model of  $\{\text{Co}^{\text{II}}(\text{PyrT})_2\text{Pt}(\text{CN})_4\}$  Hofmann-type monolayer. Views of the monolayer along the x-axis (left) and y-axis (right). The dotted line represents the unit cell considered, which consist of four  $\text{Co}^{\text{II}}$  ions.

The wavefunction was expanded using double- $\zeta$  polarised (DZP) basis set using valence pseudopotentials and PBE functional<sup>45</sup> for all atoms except for Co, in which semicore 3p orbitals were also included. For this atom, a Hubbard correction of  $U=4.0$  eV in the d-shell. A  $11e^-$  Au pseudopotential was used for the optimisation, whilst a  $1e^-$  pseudopotential and single- $\zeta$  polarised (SZP) was used to obtain the charge transport properties.<sup>46</sup> Using this light pseudopotential, it is possible to include a  $11 \times 11 \times 1$  and  $11 \times 11 \times 51$  k-point grids for the full system and for the isolated electrode, respectively.

The transport properties were obtained using GOLLUM code<sup>47</sup> within the EGF formalism (section 1.4.1). The conductance is approximated from the transmission spectrum as  $G = T(E_F)G_0$ , valid for small biases.

### 5.2.5 Theoretical study of $\{\text{Co}^{\text{II}}(\text{PyrT})_2\text{Pt}(\text{CN})_4\}$ monolayer

In the model considered, the unit cell connects both electrodes through 4 different channels (one channel for each  $\text{Co}^{\text{II}}$  centre).  $\text{Co}^{\text{II}}$  is a  $d^7$  ion and is found to have an experimental high-spin ground state ( $S=3/2$ ) in very similar systems.<sup>48</sup> Figure 5.12 shows the scheme, projected density of states (PDOS) and transmission spectrum of the  $\{\text{Co}^{\text{II}}(\text{PyrT})_2\text{Pt}(\text{CN})_4\}$  monolayer.



## 5 Spintronic Devices based on Hofmann-type Clathrate Monolayer

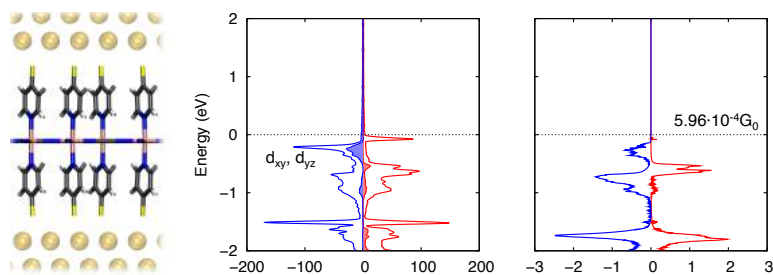


Figure 5.12. Scheme (left), projected density of states (centre) and transmission spectra (right) of Hofmann-type monolayer  $\{\text{Co}^{\text{II}}(\text{PyrT})_2\text{Pt}(\text{CN})_4\}$ . Red and blue colours stand for alpha and beta spinorbital contributions. Filled curves of the same colour indicate the  $\text{Co}^{\text{II}}$  contribution to the projected density of states.

The summation of the four  $\text{Co}^{\text{II}}$  centres scores a conductance of  $5.96 \cdot 10^{-4} G_0$  for low biases, in good agreement with the expected  $2.70 \cdot 10^{-4} G_0$  for the contact of four  $\text{Co}^{\text{II}}$  centres. The main metallic transmission channels lay 0.2 eV below the Fermi energy, corresponding to  $\beta d_{xy}$  and  $d_{yz}$  spinorbitals. The closest molecular orbital to the Fermi energy is from Pt centres, hence having negligible electron transmission.

In the figure below, an axial PyrT molecule is sequentially removed until a single PyrT is left, thus a single channel is open to the charge transport (Figure 5.13). The projected density of states (PDOS) indicates that all  $\text{Co}^{\text{II}}$  ions are, essentially, identical by symmetry, as it is expected. The transmission spectra are shrunk as long as axial PyrT molecules are removed. The conductance values obtained for three, two and only one open channel are  $3.70 \cdot 10^{-4} G_0$ ,  $2.25 \cdot 10^{-4} G_0$  and  $8.51 \cdot 10^{-5} G_0$ , respectively. The latter value, although slightly overestimated, is in consonance with the observed conductance during the PyrT functionalised Au tip *blinking* STM experiments.

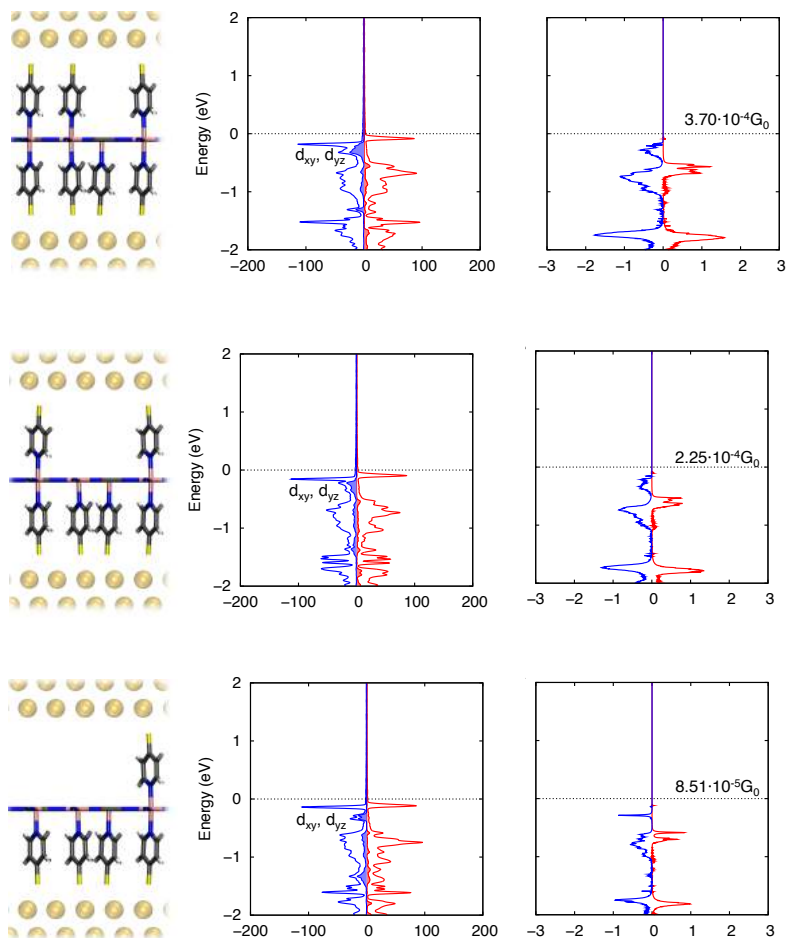


Figure 5.13. Scheme (left), projected density of states (centre) and transmission spectra (right) of Hofmann-type monolayer with four, three, two and one channels open. Red and blue colours stand for alpha and beta spinorbital contributions. Filled curves of the same colour indicates the  $\text{Co}^{\text{II}}$  contribution to the projected density of states.

Nearly integer factors of the single channel case (Figure 5.13, bottom panel) indicate that each channel is essentially working independently of its neighbours. Deviations from the perfect integer factor can be attributed to small asymmetries and weak interactions in the model, which can be also found in the actual experiment. The four channels in the unit cell are interconnected through the aforementioned tetracyanoplatinate equatorial

ligands. These connections are perpendicular to the charge transport direction and set the neighbouring PyrT molecules to a 7.4 Å distance. Because of that, it is expected that the total transmission is the sum of each Co<sup>II</sup> channel, with mild interactions between centres.

Regarding the magnetoresistance, the {Co<sup>II</sup>(PyrT)<sub>2</sub>Pt(CN)<sub>4</sub>} Hofmann-type monolayer shows a modest response to the magnetic Ni tip (3-4 fold magnetoresistance). Similarly to metalloporphyrins (section 3.3.2), the closest orbital to the Fermi energy with substantial transmission has a very small metallic contribution. Although there is a clear asymmetry in the alpha and beta transmission spectra (Figure 5.12, right and Figure 5.13, right), the broadening of those molecular orbitals is not sufficient to have a relevant contribution at the Fermi energy. Hence, alpha and beta contributions are very similar for low biases.

### 5.3 Conclusions

Based on previously reported layer-by-layer synthesis of Hofmann-clathrates of the form {Fe<sup>II</sup>(PyrT)<sub>2</sub>Pt(CN)<sub>4</sub>}, the synthesis is optimised to obtain a single sheet of {Co<sup>II</sup>(PyrT)<sub>2</sub>Pt(CN)<sub>4</sub>} on Au(111) in an easy, robust and reproducible manner. To follow the three different synthetic stages, the thickness of the monolayer was followed using ellipsometry and AFM imaging, showing a larger thickness on each step up to 16.7-17.2 Å, the expected height of the fully-grown Hofmann-type monolayer. The chemical composition of the resulting monolayer was extracted via XPS, despite no quantitative information could be inferred because of the small thickness of the sample. C-AFM measurements showed high coverage of {Co<sup>II</sup>(PyrT)<sub>2</sub>Pt(CN)<sub>4</sub>} over monocrystalline Au(111). Current-voltage curves further demonstrates that low current regions corresponds to {Co<sup>II</sup>(PyrT)<sub>2</sub>Pt(CN)<sub>4</sub>} and high current regions to bare gold.

*Blinking* STM measurements were performed to gain insight at molecular level. The conductance histogram of the *blinking* events obtained with a PyrT functionalised gold and nickel tip suggests that Co<sup>II</sup> centres can be understood as non-interacting channels, thus the different conductance peaks observed correlate to an integer number of Co<sup>II</sup>-PyrT bond formation. Theoretical studies confirm the independent channel picture and show good correspondence between the calculated ( $8.51 \cdot 10^{-5} G_0$ ) and observed ( $6.76 \cdot 10^{-5} G_0$ ) single Co<sup>II</sup>-PyrT bond formation.

The magnetoresistance of {Co<sup>II</sup>(PyrT)<sub>2</sub>Pt(CN)<sub>4</sub>} monolayer was explored polarising a functionalised nickel tip and repeating the *Blinking* STM measurements. The monolayer presented higher conductance for an alpha-polarised nickel tip being 3-4 larger than when measure with a beta-polarised tip. Theoretical calculations show small asymmetry between alpha and beta spinorbitals on the Fermi energy, thus in agreement with the modest magnetoresistance observed experimentally.

Overall, Hofmann-type clathrate monolayer offers the possibility to be easily integrated as a magnetoresistance device given the high coverage of the gold electrode. Thus, our results can be extended to generate spin valve-based devices with a heavy metal/Ni/2DHofmann/Gold layered structure (Figure 5.14). The Ni electrode works as a free layer. The direction of its magnetization is controlled via spin-orbit torque generated by the heavy atom electrode (i.e. tantalum). Furthermore, this kind of spin valve structures could be extended to memristor systems for neuromorphic devices (Figure 5.14).

## 5 Spintronic Devices based on Hofmann-type Clathrate Monolayer

---

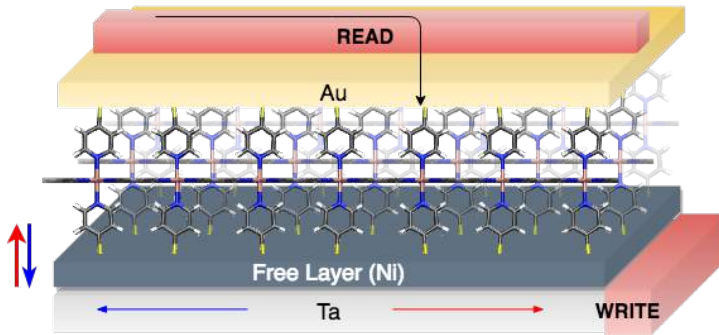


Figure 5.14. Spin valve-based devices with a heavy metal/Ni/2DHofmann/Gold scheme.

## 5.4 References

- 1 H. Furukawa, K. E. Cordova, M. O’Keeffe, O. M. Yaghi, *Science* **2013**, *341*, 1230444.
- 2 S. Kitagawa, R. Kitaura, S. I. Noro, *Angew. Chemie - Int. Ed.* **2004**, *43*, 2334.
- 3 G. Férey, *Chem. Soc. Rev.* **2008**, *37*, 191.
- 4 J. Liu, C. Wöll, *Chem. Soc. Rev.* **2017**, *46*, 5730.
- 5 I. Stassen, N. Burtch, A. Talin, P. Falcaro, M. Allendorf, R. Ameloot, *Chem. Soc. Rev.* **2017**, *46*, 3185.
- 6 A. A. Talin, A. Centrone, A. C. Ford, M. E. Foster, V. Stavila, P. Haney, R. A. Kinney, V. Szalai, F. El Gabaly, H. P. Yoon, F. Léonard, M. D. Allendorf, *Science* **2014**, *343*, 66.
- 7 V. Rubio-Giménez, S. Tatay, F. Volatron, F. J. Martínez-Casado, C. Martí-Gastaldo, E. Coronado, *J. Am. Chem. Soc.* **2016**, *138*, 2576.
- 8 M. G. Campbell, S. F. Liu, T. M. Swager, M. Dincă, *J. Am. Chem. Soc.* **2015**, *137*, 13780.
- 9 M. G. Campbell, D. Sheberla, S. F. Liu, T. M. Swager, M. Dincă, *Angew. Chemie - Int. Ed.* **2015**, *54*, 4349.
- 10 K. J. Erickson, F. Léonard, V. Stavila, M. E. Foster, C. D. Spataru, R. E. Jones, B. M. Foley, P. E. Hopkins, M. D. Allendorf, A. A. Talin, *Adv. Mater.* **2015**, *27*, 3453.
- 11 P. Jain, A. Stroppa, D. Nabok, A. Marino, A. Rubano, D. Paparo, M. Matsubara, H. Nakotte, M. Fiebig, S. Picozzi, E. S. Choi, A. K. Cheetham, C. Draxl, N. S. Dalal, V. S. Zapf, *npj Quantum Mater.* **2016**, *1*, 16012.
- 12 S. Friedländer, J. Liu, M. Addicoat, P. Petkov, N. Vankova, R. Rüger, A. Kuc, W. Guo, W. Zhou, B. Lukose, Z. Wang, P. G. Weidler, A. Pöppel, M. Ziese, T. Heine, C. Wöll, *Angew. Chemie - Int. Ed.* **2016**, *55*, 12683.

- 13 S. M. Yoon, S. C. Warren, B. A. Grzybowski, *Angew. Chemie - Int. Ed.* **2014**, *53*, 4437.
- 14 L. Pan, Z. Ji, X. Yi, X. Zhu, X. Chen, J. Shang, G. Liu, R. W. Li, *Adv. Funct. Mater.* **2015**, *25*, 2677.
- 15 Z. Wang, D. Nminibapiel, P. Shrestha, J. Liu, W. Guo, P. G. Weidler, H. Baumgart, C. Wöll, E. Redel, *ChemNanoMat* **2016**, *2*, 67.
- 16 K. A. Hofmann, F. Küspert, *Zeitschrift für Anorg. Chemie* **1897**, *15*, 204.
- 17 T. Kitazawa, Y. Gomi, M. Takahashi, M. Takeda, M. Enomoto, A. Miyazaki, T. Enoki, *J. Mater. Chem.* **1996**, *6*, 119.
- 18 O. I. Kucheriv, I. O. Fritsky, I. A. Gural'skiy, *Inorganica Chim. Acta* **2021**, *521*, 120303.
- 19 M. C. Muñoz, J. A. Real, *Coord. Chem. Rev.* **2011**, *255*, 2068.
- 20 K. Otsubo, T. Haraguchi, H. Kitagawa, *Coord. Chem. Rev.* **2017**, *346*, 123.
- 21 V. Chernikova, O. Shekhah, M. Eddaoudi, *ACS Appl. Mater. Interfaces* **2016**, *8*, 20459.
- 22 W. J. Li, M. Tu, R. Cao, R. A. Fischer, *J. Mater. Chem. A* **2016**, *4*, 12356.
- 23 I. Stassen, M. Styles, G. Greci, H. Van Gorp, W. Vanderlinden, S. De Feyter, P. Falcaro, D. De Vos, P. Vereecken, R. Ameloot, *Nat. Mater.* **2016**, *15*, 304.
- 24 G. Agustí, S. Cobo, A. B. Gaspar, G. Molnár, N. O. Moussa, P. Á. Szilágyi, V. Pálfi, C. Vieu, M. Carmen Muñoz, J. A. Real, A. Bousseksou, *Chem. Mater.* **2008**, *20*, 6721.
- 25 O. Shekhah, H. Wang, S. Kowarik, F. Schreiber, M. Paulus, M. Tolan, C. Sternemann, F. Evers, D. Zacher, R. A. Fischer, C. Wöll, *J. Am. Chem. Soc.* **2007**, *129*, 15118.
- 26 M. C. So, S. Jin, H. J. Son, G. P. Wiederrecht, O. K. Farha, J. T.

- Hupp, *J. Am. Chem. Soc.* **2013**, *135*, 15698.
- 27 K. Kanaizuka, R. Haruki, O. Sakata, M. Yoshimoto, Y. Akita, H. Kitagawa, *J. Am. Chem. Soc.* **2008**, *130*, 15778.
- 28 R. Makiura, S. Motoyama, Y. Umemura, H. Yamanaka, O. Sakata, H. Kitagawa, *Nat. Mater.* **2010**, *9*, 565.
- 29 S. Motoyama, R. Makiura, O. Sakata, H. Kitagawa, *J. Am. Chem. Soc.* **2011**, *133*, 5640.
- 30 T. Haraguchi, K. Otsubo, O. Sakata, S. Kawaguchi, A. Fujiwara, H. Kitagawa, *Chem. Commun.* **2016**, *52*, 6017.
- 31 C. M. Bell, M. F. Arendt, L. Gomez, R. H. Schmehl, T. E. Mallouk, *J. Am. Chem. Soc.* **1994**, *116*, 8374.
- 32 A. C. Aragonès, D. Aravena, F. J. Valverde-Muñoz, J. A. Real, F. Sanz, I. Díez-Pérez, E. Ruiz, *J. Am. Chem. Soc.* **2017**, *139*, 5768.
- 33 S. Cobo, G. Molnár, J. A. Real, A. Bousseksou, *Angew. Chemie - Int. Ed.* **2006**, *45*, 5786.
- 34 C. Bartual-Murgui, L. Salmon, A. Akou, C. Thibault, G. Molnár, T. Mahfoud, Z. Sekkat, J. A. Real, A. Bousseksou, *New J. Chem.* **2011**, *35*, 2089.
- 35 T. Haraguchi, K. Otsubo, O. Sakata, A. Fujiwara, H. Kitagawa, *J. Am. Chem. Soc.* **2016**, *138*, 16787.
- 36 T. Haraguchi, K. Otsubo, O. Sakata, A. Fujiwara, H. Kitagawa, *Inorg. Chem.* **2015**, *54*, 11593.
- 37 K. Otsubo, T. Haraguchi, O. Sakata, A. Fujiwara, H. Kitagawa, *J. Am. Chem. Soc.* **2012**, *134*, 9605.
- 38 E. A. Ramírez, E. Cortés, A. A. Rubert, P. Carro, G. Benítez, M. E. Vela, R. C. Salvarezza, *Langmuir* **2012**, *28*, 6839.
- 39 G. Molnár, S. Cobo, J. A. Real, F. Carcenac, E. Daran, C. Vieu, A. Bousseksou, *Adv. Mater.* **2007**, *19*, 2163.
- 40 K. S. Birdi, *Scanning Probe Microscopes: Applications in Science and Technology*, CRC Press, **2003**.



- 41 P. A. Tipler, R. Llewellyn, *Modern Physics*, W. H. Freeman, **1999**.
- 42 J. M. Soler, E. Artacho, J. D. Gale, A. García, J. Junquera, P. Ordejón, D. Sánchez-Portal, *J. Phys. Condens. Matter* **2002**, *14*, 2745.
- 43 M. Brandbyge, J. L. Mozos, P. Ordejon, J. Taylor, K. Stokbro, *Phys. Rev. B* **2002**, *65*, 165401.
- 44 A. García, N. Papior, A. Akhtar, E. Artacho, V. Blum, E. Bosoni, P. Brandimarte, M. Brandbyge, J. I. Cerdá, F. Corsetti, R. Cuadrado, V. Dikan, J. Ferrer, J. Gale, P. García-Fernández, V. M. García-Suárez, S. García, G. Huhs, S. Illera, R. Korytár, P. Koval, I. Lebedeva, L. Lin, P. López-Tarifa, S. G. Mayo, S. Mohr, P. Ordejón, A. Postnikov, Y. Pouillon, M. Pruneda, R. Robles, D. Sánchez-Portal, J. M. Soler, R. Ullah, V. W. Z. Yu, J. Junquera, *J. Chem. Phys.* **2020**, *152*, 204108.
- 45 J. P. Perdew, K. Burke, M. Ernzerhof, *Phys. Rev. Lett.* **1996**, *77*, 3865.
- 46 C. Toher, S. Sanvito, *Phys. Rev. B* **2008**, *77*, 155402.
- 47 J. Ferrer, C. J. Lambert, V. M. García-Suárez, D. Z. Manrique, D. Visontai, L. Oroszlany, R. Rodríguez-Ferradás, I. Grace, S. W. D. Bailey, K. Gillemot, H. Sadeghi, L. A. Algharagholy, *New J. Phys.* **2014**, *16*, 93029.
- 48 M. A. Palacios, I. F. Díaz-Ortega, H. Nojiri, E. A. Sutura, M. Ozerov, J. Krzystek, E. Colacio, *Inorg. Chem. Front.* **2020**, *7*, 4611.

## 6 SYSTEMATIC STUDY OF THERMOELECTRIC PROPERTIES ON MAGNETIC COMPLEXES

### 6.1 Introduction

Nowadays, there is an increasing interest and demand of sustainable development.<sup>1</sup> A major problem to overcome in this matter is to reduce the amount of wasted energy. Up to 80% of the generated energy is lost in the form of heated gas.<sup>2</sup> Hence, to recover and convert waste heat into available electrical energy is a compelling need. In this scenario, thermoelectric devices based on Seebeck effect (section 1.1.7) become valuable allies, reconverting waste heat into electricity.<sup>3,4</sup> An important class of thermoelectric materials are metal chalcogenides,<sup>5</sup> being Bismuth Telluride ( $\text{Bi}_2\text{Te}_3$ )<sup>6</sup> and its alloys extensively studied. Nevertheless, the low abundance of Bi and Te, the working temperature range and industrial scalability encourage the search of alternatives. Recently, SnSe has emerged as a new candidate being cheaper, high performing and less toxic than other metal chalcogenides.<sup>7</sup> Organic semiconductors have also attracted the attention of the community because they combine the semiconducting and soft-matter properties, making possible the

fabrication of flexible, light and biocompatible electronic devices.<sup>8</sup> However, the low performance of these materials limits their applications and only thermoelectric coolers based on Peltier effect are on the market.<sup>9</sup>

The figure of merit ( $ZT$ ) is the parameter that measures the efficiency of thermoelectric devices as  $ZT = S^2GT/(k_{el} + k_{ph})$ . It involves the Seebeck coefficient ( $S$ ), the conductance ( $G$ ), working temperature ( $T$ ) and phonon and electronic thermal conductance ( $k_{ph}$  and  $k_{el}$ ). Efficiency ( $\eta$ ) of thermoelectric devices is limited by the Carnot factor  $\Delta T/T_h$  in equation 1.2.<sup>10</sup> For very high  $ZT$  values, the efficiency at room temperature for a temperature gradient of 20 degrees is only 7%.

$$\eta = \frac{\Delta T}{T_h} \frac{\sqrt{1 + ZT} - 1}{\sqrt{1 + ZT} + T_c/T_h} \quad 6.1$$

Beyond  $ZT = 1$ , efficiency increases slowly and a figure of merit of  $ZT > 1$  is usually the milestone for practical applications.<sup>11</sup> One strategy to improve the thermoelectric performance is to exploit quantum confinement effects in low-dimensional materials.<sup>12,13</sup> In the light of that, many efforts have been dedicated to thermoelectrics of nanowires.<sup>14</sup> Down to molecular level, quantum interference can lead to huge thermoelectric efficiencies.<sup>15-17</sup> Whereas thermoelectric properties of many organic molecules have been already measured,<sup>11,18-20</sup> the inclusion of metal centres is rather left unexplored. Van der Zant *et al.* showed a completed mapping of thermoelectric properties of  $[\text{Gd}^{\text{III}}(\text{tpy-SH})_2(\text{SCN})_3]$  (tpy = terpyridine)<sup>21</sup> by electromigration with a figure of merit of 0.7. Agraït and co-workers<sup>22</sup> reported bi-thermoelectricity in endohedral  $\text{Sc}_3\text{N}@C_{60}$  by STM-BJ and, more recently, showed that the inclusion of a ruthenium or platinum atom in a series of 12 conjugated molecular wires leads to improved electric and thermoelectric properties.<sup>23</sup>

Although theoretical calculations of thermoelectric properties are easily accessible, organic molecule junctions have attracted much of the attention.<sup>9,24–27</sup>

Motivated by these works, in this last chapter the discussion goes back to single molecule junctions. The objective is to systematically study simple metallic complexes to elucidate common characteristics of high performing thermoelectric devices. To focus on high conductance metal complexes is very convenient because the power factor  $S^2G$  will be enhanced but more importantly, electrons will be the main heat carriers. This last statement is important from the computational point of view. If electrons are the main heat carriers, the figure of merit can be reduced to  $ZT = S^2GT/k_{\text{el}}$ . Hence, the phonon calculations associated to thermoelectric calculations can be skipped, shortening computational time without a sensible loss of accuracy, a priori.

Because of their simplicity and variety, metallocenes ( $V^{\text{II}}$ ,  $Fe^{\text{II}}$ ,  $Ni^{\text{II}}$  and  $Co^{\text{II}}$ ) are chosen for this study. Ferrocene has been reported to exhibit a  $0.25 G_0$  conductance, thus being an excellent candidate.<sup>28</sup> Lanthanide sandwich compounds ( $Gd^{\text{III}}$ ,  $Eu^{\text{II}}$ ) are also introduced to explore the effect of f-shell orbitals. Finally, the  $[M^{\text{II}}(\text{py})_{2+x}(\text{SCN})_{4-x}]$  ( $M^{\text{II}} = Fe^{\text{II}}$ ,  $Co^{\text{II}}$ ,  $\text{py} = \text{pyridine}$ ,  $x = 0-2$ ) family is studied to understand the effect of the ligand field and complex charge on the thermoelectric properties. Similar compounds have been studied previously showing sharp transmission peaks near the Fermi energy, potentially exhibiting an excellent thermoelectric performance.<sup>29</sup>

## 6.2 Results

### 6.2.1 Computational details

All the metallic complexes presented were placed within electrodes of five gold layers of different sizes according to the molecular size. The electrode size is of 4x2 surface unit cell for metallocenes ( $V^{II}$ ,  $Fe^{II}$ ,  $Co^{II}$ ,  $Ni^{II}$ ), 5x3 for  $Ln(COT)_2$  and  $Ln(COT)(Cp)$  ( $Ln = Gd^{III}$  and  $Eu^{II}$ ), 8x4 for  $Ln(Pc)_2$  ( $Ln = Gd^{III}$  and  $Eu^{II}$ ) and 6x4 for the  $[M^{II}(SCN)_{2+x}(py)_{4-x}]$  ( $M^{II} = Fe^{II}$ ,  $Co^{II}$ ,  $py =$  pyridine,  $x = 0-2$ ) family.

The nanojunctions were optimised up to atomic forces below 0.04 eV/Å keeping the farther three gold layers from the scattering centre of both ends rigid but letting them move along the  $z$  axis. In this manner, the periodic unit cell of bulk electrode is kept while the interelectrode distance is relaxed.

The wavefunction was expanded using a double- $\zeta$  polarised (DZP) basis set with valence pseudopotentials except for transition metals ( $V^{II}$ ,  $Fe^{II}$ ,  $Co^{II}$  and  $Ni^{II}$ ), in which semicore 3p orbitals were explicitly described, and PBE functional with SIESTA code.<sup>30-32</sup> For the optimisations, 11e<sup>-</sup> Au pseudopotential was employed and 1e<sup>-</sup> Au pseudopotential and single- $\zeta$  polarised (SZP) basis for thermoelectric properties calculations.<sup>33</sup> For the  $[M^{II}(SCN)_{2+x}(py)_{4-x}]$  family, PBE+U ( $U = 4.0$  eV) functional is chosen.

Similarly to the different electrode sizes, the k-point grid also varies depending on the nanojunction under study. A 19x19x1 k-point grid for metallocenes, 15x15x1 for  $Ln(COT)_2$ ,  $Ln(COT)(Cp)$ ,  $Ln(Pc)_2$  ( $Ln = Gd^{III}$  and  $Eu^{II}$ ) and  $[M^{II}(SCN)_{2+x}(py)_{4-x}]$  ( $M^{II} = Fe^{II}$ ,  $Co^{II}$ ,  $py =$  pyridine,  $x = 0-2$ ) family. The same k-point grid is chosen from the respective electrodes but with 51 k-points along the  $k_z$  axis.

Thermoelectric properties were computed at 298 K with GOLLUM code.<sup>34</sup> A proper calculation of the figure of merit would require a phonon computation to obtain the phonon thermal conductance  $k_{\text{ph}}$ . However, for high conductance nanojunctions, the electronic thermal conductance will be much larger than the phonon contribution, thus the figure of merit can be reduced to  $ZT = S^2GT/k_{\text{el}}$ . This reduces sensibly the computational time to obtain thermoelectric properties.

### 6.2.2 Metallocenes ( $\text{V}^{\text{II}}$ , $\text{Fe}^{\text{II}}$ , $\text{Co}^{\text{II}}$ and $\text{Ni}^{\text{II}}$ )

The first family of compounds to discuss is metallocenes of  $\text{V}^{\text{II}}$ ,  $\text{Fe}^{\text{II}}$ ,  $\text{Co}^{\text{II}}$  and  $\text{Ni}^{\text{II}}$ . Metallocenes typically consist of two cyclopentadienyl anions ( $\text{C}_5\text{H}_5^-$ ) and the metal centre, a subset of a broader class of compound called sandwich compounds. Many of the common metallocenes are commercially available in large quantities for years. Ferrocene ( $\text{Fe}(\text{Cp})_2$ ) and its derivatives are the most studied members of the family both theoretically and experimentally.<sup>35</sup> The HOMO of ferrocene lies very close to the Fermi energy of the most common metallic electrodes making it a very convenient choice for molecular electronics applications.<sup>36</sup> It has been employed as building blocks to construct molecular rectifiers<sup>35</sup> and rotatory molecular switches.<sup>37</sup>

## 6 Systematic Study of Thermoelectric Properties on Magnetic Complexes

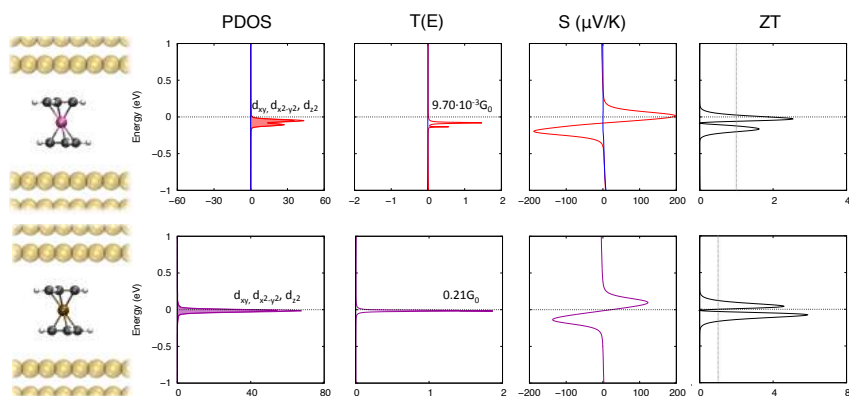


Figure 6.1. Vanadocene (top panel) and Ferrocene (bottom panel) projected density of states (PDOS), transmission spectra (T(E)), thermopower (S) and figure of merit (ZT). Colours in the scheme, Au: Gold, C: Grey, H: White, V: Pink, Fe: Ochre. Red and blue colours stand for alpha and beta spinorbitals. Purple curves represents both alpha and beta spinorbitals of ferrocene. Shaded curves on the PDOS represent the metallic contribution. Vertical dotted line indicates ZT > 1 milestone.

Vanadocene and ferrocene have shown experimental conductance values of up to  $10^{-2} G_0$ <sup>38</sup> and  $0.25 G_0$ <sup>28</sup> respectively, making possible to skip the phonon calculation to obtain the figure of merit. The calculated conductance for these two metallocenes is  $9.70 \cdot 10^{-3} G_0$  and  $0.21 G_0$  is very good agreement. Figure 6.1 shows the projected density of states (PDOS), transmission (T(E)), thermopower (S) and figure of merit (ZT) of vanadocene and ferrocene. V<sup>II</sup> ion in vanadocene is a S=3/2 ion with the lowest energy d orbitals, d<sub>xy</sub>, d<sub>x<sup>2</sup>-y<sup>2</sup></sub> and d<sub>z<sup>2</sup></sub> alpha spinorbitals occupied and very close to the Fermi energy. Fe<sup>II</sup> in ferrocene have the same metallic orbitals occupied but for both spin states, thus having S=0. Since thermopower (S) is proportional to log<sub>e</sub>[T(E)] derivative, it is greatly improved when the transmission peaks are very sharp and thereafter the figure of merit (ZT). Transmission peaks will be sharp when the interaction with the electrodes is low, reducing the broadening of the molecular orbital. The transmission spectra for both metallocenes (T(E)) shows very sharp transmission peaks for d<sub>xy</sub>, d<sub>x<sup>2</sup>-y<sup>2</sup></sub> and d<sub>z<sup>2</sup></sub> molecular

orbitals. Low broadening is expected for these three metallic orbitals, since they do not mix effectively with the Cp $\pi$  orbitals and thus, the mixing with the electrodes is very low as well. Vanadocene and ferrocene score a striking figure of merit of  $\approx 2$  and  $\approx 5$ , respectively. Roughly the double, because alpha and beta molecular orbitals are involved in the transmission of ferrocene compared to only alpha molecular orbitals of vanadocene. Because both metallocenes surpass the  $ZT > 1$  milestone, they become interesting candidates for thermoelectric experiments. Although ferrocene should have a better performance, vanadocene gives the opportunity of combining spintronic and thermoelectric properties because of its spin-polarised Fermi energy.

When cobaltocene and nickelocene are considered, alpha spinorbital  $d_{yz}$  and alpha spinorbitals  $d_{xz}$  and  $d_{yz}$  are occupied. Those antibonding metallic orbitals point towards the  $\pi$  cloud of Cp $\pi$  ligands, hence achieving a much larger mixing with the electrodes. This is reflected into the PDOS of cobaltocene and nickelocene (Figure 6.2, PDOS) showing wiggly and low density of states of the molecule due to the rather constant DOS of gold around the Fermi energy. This is translated into a much smaller thermopower (and  $ZT$ ) close to the Fermi energy, as it is shown in Figure 6.2. While cobaltocene scores the largest conductance of the metallocenes, on nickelocene the addition of the second alpha electron stabilises the  $d_{yz}/d_{xz}$  pair, resulting in a reduction of the conductance up to 0.14  $G_0$ . However, cobaltocene and nickelocene do not exceed the  $ZT$  threshold of 1 in an energy range of  $\pm 1$  eV, chosen as a sensible gate voltage window in which the metallocene might not oxidise or reduce.



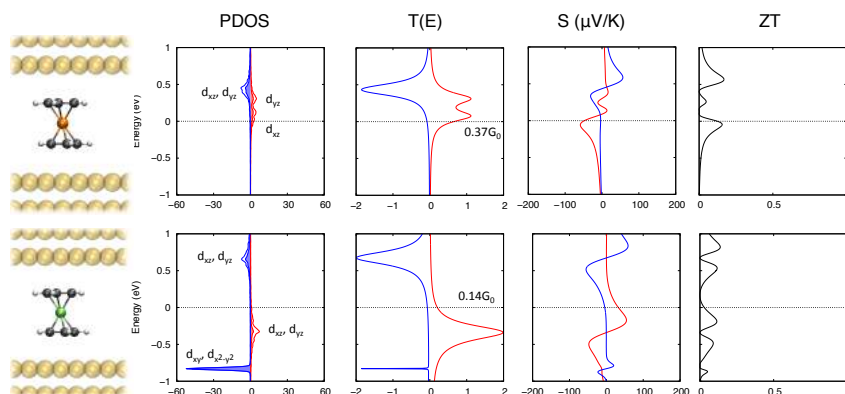


Figure 6.2. Cobaltocene (top panel) and Nickelocene (bottom panel) projected density of states (PDOS), transmission spectra ( $T(E)$ ), thermopower ( $S$ ) and figure of merit ( $ZT$ ). Colours in the scheme, Au: Gold, C: Grey, H: White, Co: Orange, Ni: Green. Red and blue colours stand for alpha and beta spinorbitals. Shaded curves on the PDOS represent the metallic contribution.

### 6.2.3 Sandwich compounds of Gd<sup>III</sup> and Eu<sup>II</sup>

Following on the sandwich compounds started with first row transition metal metallocenes, now it is explored the f-shell through gadolinium and europium.  $[\text{Gd}(\text{tpy-SH})_2(\text{SCN})_3]$  (tpy = terpyridine) is a precedent of lanthanides employed for thermoelectricity presented by van der Zant exhibiting a  $ZT = 0.7$ .<sup>21</sup> As shown in chapter 4, the single determinant nature of DFT cannot describe the degenerated ground states of lanthanides. Exceptionally, some oxidation states can be described as a single determinant. For this reason, sandwich compounds of Gd<sup>III</sup> and Eu<sup>II</sup>, isoelectronic  $f^7$  ions, are considered. The f-shell is an inner metallic shell and because of that, the interaction with the electrodes should be lower, yielding sharper transmission peaks. Figure 6.3 shows the electric and thermoelectric properties of  $[\text{Gd}(\text{COT})_2]^-$  (COT = cyclooctatetraene),  $\text{Gd}(\text{COT})(\text{Cp})$  (Cp = cyclopentadienyl) and  $[\text{Gd}(\text{Pc})_2]^-$  (Pc = phthalocyanine). The negatively charged complexes have been

counterbalanced with ammonium in the unit cell, which is not participating in the transport.

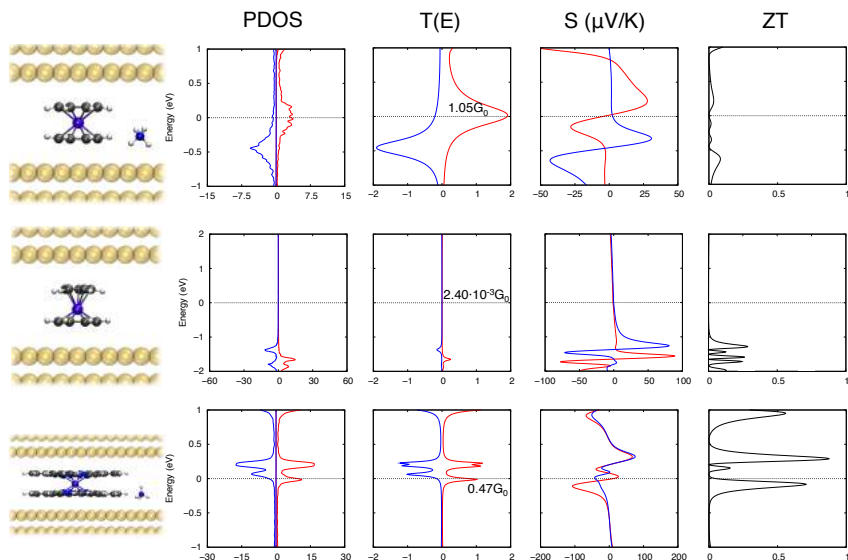


Figure 6.3.  $[\text{Gd}(\text{COT})_2]$  (top panel) and  $\text{Gd}(\text{COT})(\text{Cp})$  (central panel) and  $[\text{Gd}(\text{Pc})_2]$  (bottom panel) projected density of states (PDOS), transmission spectra ( $T(E)$ ), thermopower ( $S$ ) and figure of merit ( $ZT$ ). Colours in the scheme, Au: Gold, N: Blue, C: Grey, H: White, Gd: Purple. Red and blue colours stand for alpha and beta spinorbitals. Shaded curves on the PDOS represent the metallic contribution.

At first glance, the trivalent positive charge of  $\text{Gd}^{\text{III}}$  pushes the  $f$ -shell well below the Fermi energy; hence no metallic contribution is seen in the selected energy window. However, some interesting results arise when considering the charge of the complex. Negatively charged  $[\text{Gd}(\text{COT})_2]^-$  (Figure 6.3, top panel) and  $[\text{Gd}(\text{Pc})_2]^-$  (Figure 6.3, bottom panel) present more than one ligand molecular orbitals on the Fermi energy that are very effective transmission channels, giving surprisingly high conductance of  $1.05 G_0$  and  $0.47 G_0$ . This is highlighted when observing the PDOS non-charged  $\text{Gd}(\text{COT})(\text{Cp})$  (Figure 6.3, central panel), in which first molecular orbitals are below  $-1$  eV apart from the Fermi energy. The high number of unpaired electrons in  $\text{Gd}^{\text{III}}$  ion triggers an alpha/beta energy position asymmetry more pronounced than in the metalloporphyrin case (section

## 6 Systematic Study of Thermoelectric Properties on Magnetic Complexes

3.2), hence it is expected a greater magnetoresistance under a spin-polarised electrode. Unluckily, the high interaction with the electrodes broadens the transmission peaks yielding poor to modest thermoelectric performance.

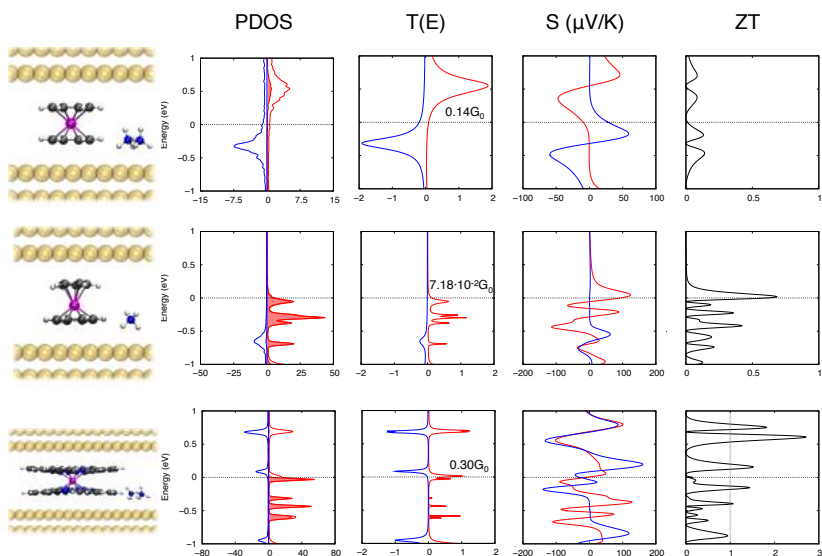


Figure 6.4.  $[\text{Eu}(\text{COT})_2]^{2-}$  (top panel) and  $[\text{Eu}(\text{COT})(\text{Cp})]^-$  (central panel) and  $[\text{Eu}(\text{Pc})_2]^{2-}$  projected density of states (PDOS), transmission spectra (T(E)), thermopower (S) and figure of merit (ZT). Colours in the scheme, Au: Gold, N: Blue, C: Grey, H: White, Eu: magenta. Red and blue colours stand for alpha and beta spinorbitals. Shaded curves on the PDOS represent the metallic contribution. Vertical dotted line indicates  $ZT > 1$  milestone

Figure 6.4 shows the analogous sandwich complexes for  $\text{Eu}^{\text{II}}$  ion. The reduction of the charge of the lanthanide pushes the f-shell closer to the Fermi energy. For  $[\text{Eu}(\text{COT})(\text{Cp})]^-$  (Figure 6.4. central panel), f-shell molecular orbitals are now the main transmission channels available. The transmission spectrum (Figure 6.4. central panel, T(E)) reveals sharper transmission peaks for f-shell orbitals with  $ZT \approx 0.7$ , but below the  $ZT > 1$  milestone. In comparison to its analogue  $\text{Gd}(\text{COT})(\text{Cp})$ , the conductance value is more than an order of magnitude larger, scoring  $7.18 \cdot 10^{-2} G_0$ .  $[\text{Eu}(\text{COT})_2]^{2-}$  and  $[\text{Eu}(\text{Pc})_2]^{2-}$  show very similar results than

their Gd<sup>III</sup> analogue but with smaller conductance values (0.14  $G_0$  and 0.30  $G_0$ ) and better thermoelectric performance. In the case of [Eu(Pc)<sub>2</sub>]<sup>2-</sup>, an alpha spinorbital below the Fermi energy and an unoccupied beta spinorbital above the Fermi energy presents a figure of merit of  $\approx 1.4$ . Potentially, the spin polarisation of the Fermi energy could be tuned with a gate voltage while keeping the thermoelectric performance, converting [Eu(Pc)<sub>2</sub>]<sup>2-</sup> a very interesting candidate to combine thermoelectricity and spintronics.

Given that [Gd(COT)<sub>2</sub>]<sup>-</sup>, for example, exhibits high conductance and a broad transmission peak (Figure 6.3, top panel,  $T(E)$ ) on the Fermi energy, it might be of interest to reduce the interaction with the electrodes in order to sharpen the transmission peak and hence improve the thermoelectric performance. Experimentally, coating the electrode with graphene can do the reduction of the interaction, as it is shown in chapter 4. Another possibility is the chemical substitution of COT with voluminous groups to increase the COT-Au(111) distance. To illustrate it, both COT-Au(111) distances have been systematically increased in Figure 6.5. As expected, as long as the interaction with the electrodes is reduced, the thermoelectric performance is enhanced. In the case of [Gd(COT)<sub>2</sub>]<sup>-</sup>, the figure of merit increases faster than the consequent reduction of the conductance because of the smaller molecule-electrode interaction. The conductance and ZT at relaxed COT-Au(111) distance are 1.05  $G_0$  and  $\approx 0.15$ , respectively. When the electrodes are +1.0 Å apart from the relaxed COT-Au(111) distance, the conductance is reduced by a half (0.42  $G_0$ ) but the figure of merit is improved by an order of magnitude, up to  $\approx 1.5$ .

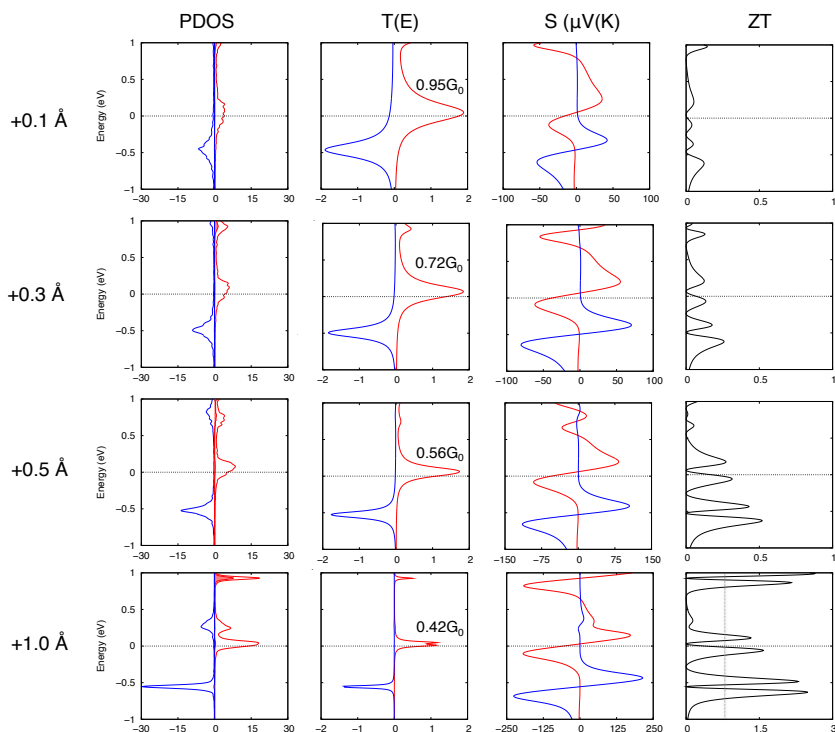


Figure 6.5.  $\text{Gd}(\text{COT})_2$  projected density of states (PDOS), transmission spectra (T(E)), thermopower (S) and figure of merit (ZT) for +0.1, +0.3, +0.5 and +1.0 Å relaxed COT-Au(111) distance.

### 6.2.4 $[\text{Co}^{\text{II}}(\text{SCN})_{2+x}(\text{py})_{4-x}]$ and $[\text{Fe}^{\text{II}}(\text{SCN})_{2+x}(\text{py})_{4-x}]$ families

Sandwich compounds studied in the previous sections showed some interesting results but to chemically modify them to refine their thermoelectric properties can be challenging. To easily shift a molecular orbital closer to the Fermi energy or reduce the broadening of a specific molecular orbital via chemical design is crucial to generate new potential candidates. Octahedral coordination compounds can be easily tuned by chemical substitution or exchange of the ligands. For this last study, it is selected  $[\text{Co}^{\text{II}}(\text{SCN})_{2+x}(\text{py})_{4-x}]$  ( $x = 0-2$ ,  $\text{py} = \text{pyridine}$ ) family because of

the simplicity of the ligands involved, chemical stability and permits the sequential substitution of py ligand by SCN<sup>-</sup>. The SCN<sup>-</sup> ligand works as an anchoring group to gold electrodes. Hence, the interaction with the electrodes and the charge of the complex are tuned with the number of SCN<sup>-</sup> in the complex. As it was done for the lanthanide sandwich compounds, the negative charges are counterbalanced with ammonium.

Co<sup>II</sup> is a d<sup>7</sup> ion in its high-spin state S=3/2 in the [Co<sup>II</sup>(SCN)<sub>2+x</sub>(py)<sub>4-x</sub>] family at room temperature.<sup>39</sup> Figure 6.6 shows the projected density of states (PDOS), transmission spectra (T(E)), thermopower (S) and figure of merit (ZT) of Co(SCN)<sub>2</sub>(py)<sub>4</sub>, [Co(SCN)<sub>3</sub>(py)<sub>3</sub>]<sup>-</sup> and [Co(SCN)<sub>4</sub>(py)<sub>2</sub>]<sup>2-</sup> complexes. [Co<sup>II</sup>(SCN)<sub>2+x</sub>(py)<sub>4-x</sub>] (x = 0-2) family do not show any molecular orbitals in the nearby of the Fermi energy. Occupied d orbitals lie below -1 eV whereas unoccupied d orbitals lie above 1 eV. In the case of Co(SCN)<sub>2</sub>(py)<sub>4</sub>, alpha d spinorbitals are placed at -3.88 eV, -3.74, -3.36 - 2.55 and -1.78 eV and beta d spinorbitals at -2.21, 1.24, 2.12 and 2.59 being the occupied degenerated in energy. As expected, molecular orbitals are pushed towards the Fermi energy with increasing negative charge Co(SCN)<sub>2</sub>(py)<sub>4</sub>, < [Co(SCN)<sub>3</sub>(py)<sub>3</sub>]<sup>-</sup> < [Co(SCN)<sub>4</sub>(py)<sub>2</sub>]<sup>2-</sup> (Figure 6.6, PDOS). Also, the broadening of the transmission spectra (Figure 6.6, T(E)) is increased with the number of SCN<sup>-</sup> ligands, as it was predicted. Because of the inexistence of sharp transmission peaks in the energy window, modest thermoelectric performance is observed (Figure 6.6, S and ZT).

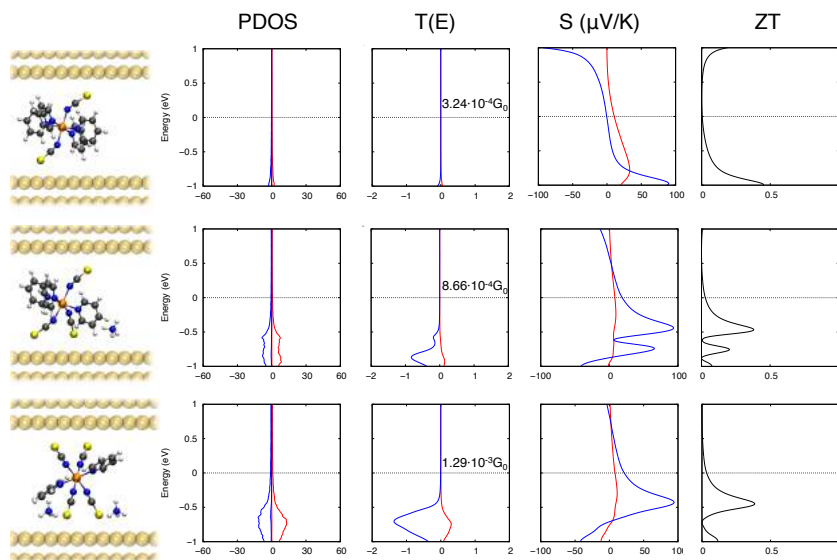


Figure 6.6.  $\text{Co}(\text{SCN})_2(\text{py})_4$  (top panel),  $[\text{Co}(\text{SCN})_3(\text{py})_3]^-$  (central panel) and  $[\text{Co}(\text{SCN})_4(\text{py})_2]^{2-}$  projected density of states (PDOS), transmission spectra ( $T(E)$ ), thermopower ( $S$ ) and figure of merit ( $ZT$ ).

Colours in the scheme, Au: Gold, N: Blue, C: Grey, H: White, Fe: Ochre, S: Yellow. Red and blue colours stand for alpha and beta spinorbitals. Shaded curves on the PDOS represent the metallic contribution.

In order to shift molecular orbitals towards the Fermi energy, the same three complexes for  $\text{Fe}^{\text{II}}$  are considered, similarly as it was done for the  $\text{Gd}^{\text{III}}$  and  $\text{Eu}^{\text{II}}$  sandwich compounds. As found for  $\text{Co}^{\text{II}}$ ,  $\text{Fe}^{\text{II}}$  is its high-spin state  $S=2$  in the  $[\text{Fe}^{\text{II}}(\text{SCN})_{2+x}(\text{py})_{4-x}]$  family at room temperature.<sup>40</sup> Figure 6.7 shows the projected density of states (PDOS), transmission spectra ( $T(E)$ ), thermopower ( $S$ ) and figure of merit ( $ZT$ ) of complexes.  $\text{Fe}(\text{SCN})_2(\text{py})_4$  shows  $d_{xy}$  beta spinorbital at 0.5 eV below the Fermi energy with a very sharp transmission peak scoring an striking figure of merit close to 5 (Figure 6.7, top panel,  $ZT$ ), being a good candidate if a gate voltage can be applied. In comparison to  $\text{Co}^{\text{II}}$ , the removal of  $d_{yz}$  beta spinorbital pushes  $d_{xy}$  beta spinorbital close the Fermi energy due to exchange energy of identical electrons and weaker nuclear attraction. When adding  $\text{SCN}^-$  ligands, the negative charge is increased and the ligand field splitting is reduced, thus the  $d_{xy}$  beta spinorbital is shifted towards the

Fermi energy. The interaction with the electrode is enlarged because the added SCN<sup>-</sup> ligand work as new anchoring groups. As a consequence, [Fe(SCN)<sub>3</sub>(py)<sub>3</sub>]<sup>-</sup> scores a conductance value of  $4.10 \cdot 10^{-2} G_0$  and [Fe(SCN)<sub>2</sub>(py)<sub>4</sub>]<sup>2-</sup> 0.18 G<sub>0</sub>. However, figures of merit are equal or below the milestone ZT > 1.

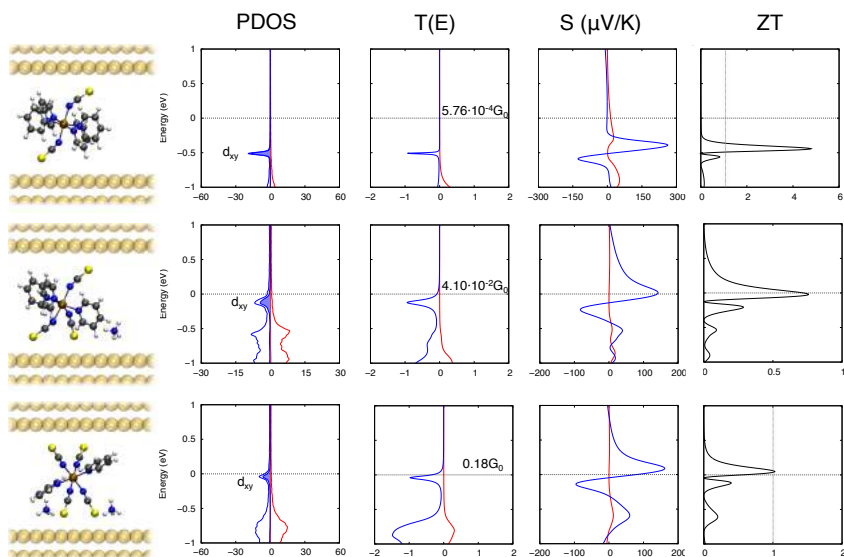


Figure 6.7. Fe(SCN)<sub>2</sub>(py)<sub>4</sub> (top panel), [Fe(SCN)<sub>3</sub>(py)<sub>3</sub>]<sup>-</sup> (central panel) and [Fe(SCN)<sub>4</sub>(py)<sub>2</sub>]<sup>2-</sup> projected density of states (PDOS), transmission spectra (T(E)), thermopower (S) and figure of merit (ZT). Colours in the scheme, Au: Gold, N: Blue, C: Grey, H: White, Fe: Ochre, S: Yellow. Red and blue colours stand for alpha and beta spinorbitals. Shaded curves on the PDOS represent the metallic contribution.

## 6.3 Conclusions

In this last chapter, thermoelectric properties of simple metal coordination complexes have been studied systematically to obtain some insight on which common characteristics should have a potential candidate. From metallocenes M(Cp)<sub>2</sub> (M = V<sup>II</sup>, Fe<sup>II</sup>, Co<sup>II</sup> and Ni<sup>II</sup>), it is observed that molecular orbitals with sharp transmission peaks close to the Fermi energy translates into high thermopower and high figure of merit. In



metallocenes,  $d_{xy}$ ,  $d_{z^2}$  and  $d_{x^2-y^2}$  molecular orbitals weakly interacts with the gold electrodes, thus keeping a low broadening. Ferrocene ( $d_{xy}^2 d_{x^2-y^2}^2 d_{z^2}^2$ ) exhibits the best thermoelectric performance with  $ZT = 5$  of the studied metallocenes followed by vanadocene ( $d_{xy}^1 d_{x^2-y^2}^1 d_{z^2}^1$ ) with  $ZT = 2$ . When  $d_{xz}$  and  $d_{yz}$  orbitals are occupied in cobaltocene and nickelocene, the thermoelectric performance is repressed.

The f-shell is explored through the study of  $Gd^{III}$  and  $Eu^{II}$  sandwich compounds. The f-shell is an inner atomic shell in comparison to the d-shell and should exhibit a better thermoelectric performance. For  $[Gd(COT)_2]^-$ ,  $Gd(COT)(Cp)$  and  $[Gd(Pc)_2]^-$  no f orbital is found within 1 eV above and below the Fermi energy. However, a stunning  $1.05 G_0$  and  $0.47 G_0$  conductance values are calculated for  $[Gd(COT)_2]^-$  and  $[Gd(Pc)_2]^-$  due to frontier molecular orbitals lying on the Fermi energy. The same sandwich compounds of  $Eu^{II}$  showed f orbitals close the Fermi energy. The increased metallic character of the f-shell lead to a better thermoelectric performance of this shell, specially for  $[Eu(Pc_2)]^{2-}$  complex ( $ZT = 1.5$ ) in which the  $ZT > 1$  milestone was surpassed in the surroundings of the Fermi energy. Negatively charged sandwich compounds seem to have molecular orbitals very close of the Fermi energy, thus being an interesting characteristic to design molecular devices.

A possibility to systematically improve the thermoelectric performance is to reduce the molecule-electrode interaction introducing voluminous groups. The interaction with the electrode of  $[Gd(COT)_2]^-$  was artificially tuned by increasing the COT-Au(111) distance showing a larger figure of merit as the interaction is reduced. In order to tune easily tune the charge of the complex and the interaction with the electrodes,  $[Co^{II}(SCN)_{2+x}(py)_{4-x}]$  and  $[Fe^{II}(SCN)_{2+x}(py)_{4-x}]$  ( $x = 0-2$ ) octahedral complexes were also studied. Both  $Co^{II}$  and  $Fe^{II}$  ions are in their high-spin state. While  $Co^{II}$ ,

does not show any metal orbital close the Fermi energy due to exchange energy of identical electrons and stronger nuclear attraction, beta  $d_{xy}$  of  $\text{Fe}(\text{SCN})_2(\text{py})_4$  lies at 0.5 eV below the Fermi energy with an excellent figure of merit of 5. By substituting py ligand by  $\text{SCN}^-$ , the charge and the interaction with the electrode is enhanced, shifting  $d_{xy}$  orbital towards the Fermi energy and enlarging the broadening of the transmission peak. This results in conductance value of  $0.18 G_0$  and a ZT of roughly 1 for  $[\text{Fe}(\text{SCN})_4(\text{py})_2]^{2-}$ .

## 6.4 References

- 1 A. Grubler, C. Wilson, N. Bento, B. Boza-Kiss, V. Krey, D. L. McCollum, N. D. Rao, K. Riahi, J. Rogelj, S. De Stercke, J. Cullen, S. Frank, O. Fricko, F. Guo, M. Gidden, P. Havlík, D. Huppmann, G. Kiesewetter, P. Rafaj, W. Schoepp, H. Valin, *Nat. Energy* **2018**, *3*, 515.
- 2 D. M. Rowe, *Thermoelectr. Handb. Macro to Nano* **2005**, *80*, 1014.
- 3 C. J. Vineis, A. Shakouri, A. Majumdar, M. G. Kanatzidis, *Adv. Mater.* **2010**, *22*, 3970.
- 4 D. Beretta, N. Neophytou, J. M. Hodges, M. G. Kanatzidis, D. Narducci, M. Martin-Gonzalez, M. Beekman, B. Balke, G. Cerretti, W. Tremel, A. Zevalkink, A. I. Hofmann, C. Müller, B. Dörling, M. Campoy-Quiles, M. Caironi, *Mater. Sci. Eng. R Reports* **2019**, *138*, 100501.
- 5 I. Pallecchi, N. Manca, B. Patil, L. Pellegrino, D. Marré, *Nano Futur.* **2020**, *4*, 1.
- 6 I. T. Witting, T. C. Chasapis, F. Ricci, M. Peters, N. A. Heinz, G. Hautier, G. J. Snyder, *Adv. Electron. Mater.* **2019**, *5*, 1800904.
- 7 L. Xie, D. He, J. He, *Mater. Horizons* **2021**, Advanced Article.
- 8 M. Lindorf, K. A. Mazzio, J. Pflaum, K. Nielsch, W. Brütting, M. Albrecht, *J. Mater. Chem. A* **2020**, *8*, 7495.
- 9 R. Gupta, N. Kumar, P. Kaur, C. Bera, *Phys. Chem. Chem. Phys.* **2020**, *22*, 18989.
- 10 G. J. Snyder, A. H. Snyder, *Energy Environ. Sci.* **2017**, *10*, 2280.
- 11 L. Rincón-García, C. Evangeli, G. Rubio-Bollinger, N. Agraït, *Chem. Soc. Rev.* **2016**, *45*, 4285.
- 12 L. D. Hicks, M. S. Dresselhaus, *Phys. Rev. B* **1993**, *47*, 12727.
- 13 J. Ding, W. Zhao, W. Jin, C. an Di, D. Zhu, *Adv. Funct. Mater.* **2021**, 2010695.

- 14 R. Chen, J. Lee, W. Lee, D. Li, *Chem. Rev.* **2019**, *119*, 9260.
- 15 C. J. Lambert, *Chem. Soc. Rev.* **2015**, *44*, 875.
- 16 J. P. Bergfield, C. A. Stafford, *Nano Lett.* **2009**, *9*, 3072.
- 17 M. Strange, J. S. Seldenthuis, C. J. O. Verzijl, J. M. Thijssen, G. C. Solomon, *J. Chem. Phys.* **2015**, *142*, 84703.
- 18 L. Cui, R. Miao, C. Jiang, E. Meyhofer, P. Reddy, *J. Chem. Phys.* **2017**, *146*, 92201.
- 19 J. R. Widawsky, P. Darancet, J. B. Neaton, L. Venkataraman, *Nano Lett.* **2012**, *12*, 354.
- 20 Y. Li, L. Xiang, J. L. Palma, Y. Asai, N. Tao, *Nat. Commun.* **2016**, *7*, 11294.
- 21 P. Gehring, J. K. Sowa, C. Hsu, J. de Bruijkere, M. van der Star, J. J. Le Roy, L. Bogani, E. M. Gauger, H. S. J. van der Zant, *Nat. Nanotechnol.* **2021**, *16*, 426.
- 22 L. Rincón-García, A. K. Ismael, C. Evangeli, I. Grace, G. Rubio-Bollinger, K. Porfyrakis, N. Agraït, C. J. Lambert, *Nat. Mater.* **2016**, *15*, 289.
- 23 M. Naher, D. C. Milan, O. A. Al-Owaedi, I. J. Planje, S. Bock, J. Hurtado-Gallego, P. Bastante, Z. M. Abd Dawood, L. Rincón-García, G. Rubio-Bollinger, S. J. Higgins, N. Agraït, C. J. Lambert, R. J. Nichols, P. J. Low, *J. Am. Chem. Soc.* **2021**, *143*, 3817.
- 24 C. C. Kaun, Y. C. Chen, *J. Phys. Chem. C* **2018**, *122*, 12185.
- 25 L. O. Jones, M. A. Mosquera, G. C. Schatz, M. A. Ratner, *J. Phys. Chem. B* **2019**, *123*, 8096.
- 26 N. Mosso, H. Sadeghi, A. Gemma, S. Sangtarash, U. Drechsler, C. Lambert, B. Gotsmann, *Nano Lett.* **2019**, *19*, 7614.
- 27 A. Droghetti, I. Rungger, *Phys. Chem. Chem. Phys.* **2020**, *22*, 1466.
- 28 A. C. Aragonès, N. Darwish, S. Ciampi, L. Jiang, R. Roesch, E. Ruiz, C. A. Nijhuis, I. Díez-Pérez, *J. Am. Chem. Soc.* **2019**, *141*, 240.
- 29 A. C. Aragonès, D. Aravena, F. J. Valverde-Muñoz, J. A. Real, F.

- Sanz, I. Díez-Pérez, E. Ruiz, *J. Am. Chem. Soc.* **2017**, *139*, 5768.
- 30 J. M. Soler, E. Artacho, J. D. Gale, A. García, J. Junquera, P. Ordejón, D. Sánchez-Portal, *J. Phys. Condens. Matter* **2002**, *14*, 2745.
- 31 M. Brandbyge, J. L. Mozos, P. Ordejon, J. Taylor, K. Stokbro, *Phys. Rev. B* **2002**, *65*, 165401.
- 32 A. García, N. Papior, A. Akhtar, E. Artacho, V. Blum, E. Bosoni, P. Brandimarte, M. Brandbyge, J. I. Cerdá, F. Corsetti, R. Cuadrado, V. Dikan, J. Ferrer, J. Gale, P. García-Fernández, V. M. García-Suárez, S. García, G. Huhs, S. Illera, R. Korytár, P. Koval, I. Lebedeva, L. Lin, P. López-Tarifa, S. G. Mayo, S. Mohr, P. Ordejón, A. Postnikov, Y. Pouillon, M. Pruneda, R. Robles, D. Sánchez-Portal, J. M. Soler, R. Ullah, V. W. Z. Yu, J. Junquera, *J. Chem. Phys.* **2020**, *152*, 204108.
- 33 C. Toher, S. Sanvito, *Phys. Rev. B* **2008**, *77*, 155402.
- 34 J. Ferrer, C. J. Lambert, V. M. García-Suárez, D. Z. Manrique, D. Visontai, L. Oroszlany, R. Rodríguez-Ferradás, I. Grace, S. W. D. Bailey, K. Gillemot, H. Sadeghi, L. A. Algharagholy, *New J. Phys.* **2014**, *16*, 93029.
- 35 M. E. Welker, *Molecules* **2018**, *23*, 1551.
- 36 K. S. Wimbush, W. F. Reus, W. G. Van Der Wiel, D. N. Reinhoudt, G. M. Whitesides, C. A. Nijhuis, A. H. Velders, *Angew. Chemie - Int. Ed.* **2010**, *49*, 10176.
- 37 I. B. Sivaev, *Molecules* **2017**, *22*, 2201.
- 38 A. N. Pal, D. Li, S. Sarkar, S. Chakrabarti, A. Vilan, L. Kronik, A. Smogunov, O. Tal, *Nat. Commun.* **2019**, *10*, 5565.
- 39 J. Boeckmann, C. Näther, *Dalt. Trans.* **2010**, *39*, 11019.
- 40 Y. Suffren, F. G. Rollet, O. Levasseur-Grenon, C. Reber, *Polyhedron* **2013**, *52*, 1081.

## FINAL CONCLUSIONS

Throughout this thesis, theoretical calculations and experimental work have been done to further understand molecular-based magnetoresistance devices at room temperature.

### **Chapters 2 and 3: Supramolecular landscape of CoDPP and Study of magnetoresistance on metalloporphyrin devices**

Theoretical calculations on  $M^{II}$ -5,15-diphenylporphyrin (MDPP,  $M^{II} = Co^{II}, Ni^{II}, Cu^{II}$  and  $Zn^{II}$ ) have provided valuable insight about the supramolecular interactions of these metallodiphenylporphyrins when both electrodes are functionalised using pyridine-4-yl-methanethiol (PyrMT) and 4-mercaptopyridine (PyrT). The high conductance signature of  $M^{II}$ DPP lies on the range of  $10^{-2}$ - $10^{-1}$   $G_0$ .  $Co^{II}$ ,  $Ni^{II}$  and  $Cu^{II}$ DPP junctions show a highly distorted octahedral coordination junction while  $Zn^{II}$ DPP produces a distorted pentacoordinated junction. Because of the shorter tunneling gap due to pentacoordination,  $Zn^{II}$ DPP exhibits the highest conductance of the studied metallodiphenylporphyrins.  $Co^{II}$ DPP and  $Cu^{II}$ DPP present magnetoresistance and show 4-6 fold higher conductance for alpha-polarised nickel tip with respect to beta-polarised tip. Magnetoresistance is qualitatively understood in theoretical calculations based on alpha and beta spinorbital energy asymmetry.

Contrary to what it is expected, Ni<sup>III</sup>DPP does not show magnetoressitance because of the stabilised low-spin state (S=0), which can be attributed to its highly distorted octahedral coordination. The theoretical calculations on MDPP suggest an exciting supramolecular landscape, paving the way to Supramolecular Electronics.

#### **Chapter 4: Study of large area EGaIn magnetic junctions**

Large area magnetic junction [CuLn(L·SMe)<sub>2</sub>(OOCMe)<sub>2</sub>(NO<sub>3</sub>)] · x MeOH (x = 0.75-1) (Ln = Gd<sup>III</sup>, Tb<sup>III</sup>, Dy<sup>III</sup> and Y<sup>III</sup>) measured using eutectic gallium and indium (EGaIn) top electrode showed current independence on the lanthanide. The computational model with gold electrodes corroborates the experimental observation and shows that Cu<sup>II</sup> β d<sub>x<sup>2</sup>-y<sup>2</sup></sub> molecular spinorbital is the main transmission channel, thus being independent of the lanthanide. A second large area magnetic junction of [Fe<sup>III</sup>(qsal-I)<sub>2</sub>]NTf<sub>2</sub> (qsal-I = 4-iodo-2-[(8-quinolylimino)methyl]phenolate) is the first Fe<sup>III</sup> spin crossover junction at room temperature. In this study, the bottom Cu/SLG (SLG = Single layer graphene) and top EGaIn electrodes are explicitly taken into account. EGaIn electrode is optimised computationally from α-gallium [100] crystal structure. The inclusion of explicit EGaIn top electrode permits the correct description of the [Fe<sup>III</sup>(qsal-I)<sub>2</sub>]NTf<sub>2</sub> junction with higher conductance high-spin state at V = 0.25 V. The substitution of EGaIn top electrode by a Ag(111) electrode led to a formal reduction of Fe<sup>III</sup> to Fe<sup>II</sup>, hence not being accurate.

#### **Chapter 5: Spintronic devices based on Hofmann-type clathrate monolayer**

Synthesis, characterisation and preliminary measurements on Hofmann-type clathrate {Co<sup>II</sup>(PyrT)<sub>2</sub>Pt(CN)<sub>4</sub>} monolayers on Au(111) are described. Ellipsometry, XPS, AFM and C-AFM measurements show that {Co<sup>II</sup>(PyrT)<sub>2</sub>Pt(CN)<sub>4</sub>} monolayer presents a high coverage on Au(111).

*Blinking* STM measurements in conjunction with computational calculations picture an integer number of Co<sup>II</sup>-PyrT<sup>I</sup> connections during *blinking* experiments (conductance of  $5.62 \cdot 10^{-5} G_0$  for one Co<sup>II</sup>-PyrT<sup>I</sup> connection). The study of magnetoresistance with polarised nickel tips showed a 3-4 fold magnetoresistance ratio, similar to metallodiphenylporphyrins. Our results can be extended to generate spin valve-based devices with a heavy metal/Ni/2DHofmann/Gold layered scheme. Furthermore, this kind of spin valve structures could be extended to memristor systems for neuromorphic devices.

## **Chapter 6: Systematic study of thermoelectric properties on magnetic complexes**

As a final remark, computational studies on metallocenes (V<sup>II</sup>, Fe<sup>I</sup>, Co<sup>II</sup> and Ni<sup>III</sup>), Gd<sup>III</sup> and Eu<sup>II</sup> sandwich compounds and  $[M^{II}(\text{SCN})_{2+x}(\text{py})_{4-x}]$  ( $M^{II} = \text{Co}^{II}$  and  $\text{Fe}^{II}$ ,  $x = 0-2$ ) complexes were carried out to extract common characteristics of high thermoelectric performance magnetic junctions. Sharp transmission peaks close to the Fermi energy exhibit high thermopower. Hence it is convenient to have small molecule-electrode interaction. Because of the more atomic character, f-shell orbitals present sharper transmission peaks than d-shell orbitals. Negatively charged metal complexes exhibit molecular orbitals closer to the Fermi level. In the wake of these characteristics, vanadocene ( $ZT = 2$ ), ferrocene ( $ZT = 5$ ),  $[\text{Eu}(\text{Pc}2)]^{2-}$  ( $ZT = 1.5$ ) and  $\text{Fe}(\text{SCN})_2(\text{py})_4$  ( $ZT = 5$ ) are excellent candidates to further thermoelectric measurements.